Manufactured and laboratory tested scaled blades and parts of the blade

Authors:

Sonell Shroff (TUDelft), A. Makris (CRES), G. Roukis (CRES), A. Croce (PoliMI), Anargyros Karakalas (University of Patras), Theodoros Machairas (University of Patras), Dimitris Saravanos (University of Patras), Nikolaos Chrysochoidis (University of Patras), Theodosis Theodosiou (University of Patras), Peter Berring (DTU), Kim Branner (DTU), Vladimir Fedorov (DTU)

Edited by: Andreas Makris (CRES), Georgios Roukis (CRES)

Deliverable 2.24

Agreement n.:	308974
Duration	November 2012 – October 2017
Co-ordinator:	Mr Peter Hjuler Jensen
Supported by:	EU 7th Framework Programme

Document information

Document Name:	Manufactured and laboratory tested scaled blades and parts of the blade
Confidentiality Class	PU
Document Number:	D2.24
Author:	Sonell Shroff (TUDelft), A. Makris (CRES), G. Roukis (CRES), A. Croce (PoliMI), Anargyros Karakalas (University of Patras), Theodoros Machairas (University of Patras), Dimitris Saravanos (University of Patras), Nikolaos Chrysochoidis (University of Patras), Theodosis Theodosiou (University of Patras), Peter Berring (DTU), Kim Branner (DTU), Vladimir Fedorov (DTU)
Review:	Andreas Makris (CRES), Georgios Roukis (CRES)
Date:	07/10/2016
WP:	WP2: Lightweight Rotor
Task:	Task 2.2: Lightweight structural design

Executive Summary

The main objective of Task2.2 is to **define and assess innovative structural concepts** in order to achieve lightweight rotor blades with adequate stiffness and strength, but also new requirements for the implementation of smart/adaptive rotor blade concepts. Towards that direction, different solutions were defined and reported in D2.2.2 and D2.2.3. Three promising solutions are here evaluated by manufacturing and testing scaled prototypes of the predefined designs. The performed work for these three concepts is described in individual chapters in the present document. Section 2 discusses the concept using the bend twist coupling (BTC), section 3 describes the concept using the shape memory alloys (SMA) and section 4 presents a new manufacturing technique for the implementation of grid stiffeners in the rotor blade. The detailed characteristics of these concepts are discussed in the individual sections, while an overall assessment is available in the last session of the report.

This manuscript aims to summarize the efforts made by the partners within subtask 2.2.3 entitled "Scaled manufacturing and laboratory testing" to **manufacture and test in laboratory, scaled blades or parts of the innovative designs proposed within WP2** for active and passive load alleviation and for reduction of the blade weight. The manufacturing processes, the design of the tests and the obtained results are highlighted. A combination of calculations and experiments is used, to evaluate the performance of the new technologies and prove the feasibility of each solution.

More specifically, within this subtask, three different blade parts were fabricated:

• Three scaled blades with a bend-twist coupling by POLIMI and DTU
• A morphing scaled blade section equipped with Shape Memory Alloys by University of Patras
•A scaled blade part with trailing edge panels reinforced with grid-stiffeners instead of the commonly used sandwich structure by TUD

In the work described in chapter 2, POLIMI designed and manufactured three scaled blades equipped with bend-twist coupling. The effect of the bend-twist coupling on the structural behaviour of the reference blade was extensively studied and presented in D2.2.2. The work in the current document covers the manufacturing and characterization of the scaled blades using different testing methods performed both in POLIMI and in DTU testing facilities, study of the aerodynamic behaviour of the blades and an investigation on the blades' load alleviation capabilities. Dynamic and static tests were performed, while the blades were equipped with Fiber Bragg Grating (FBG) sensors embedded inside the structure during the manufacturing process in order to evaluate potentialities of the HUMS (Heath and Usage Monitoring Systems) based on the fiber optics. Three manufactured blades were finally assembled on a scaled tower-nacelle model. The resulting wind turbine model was tested in the wind tunnel of Polimi (GVPM) with the absolute goal to investigate the load alleviation capabilities of the BTC and its synergy with the active pitch control system. To evaluate the manufacturing, the blade was characterized at bench, by the use of static tests both at PoliMI and DTU and by modal tests using an impact hammer at PoliMI and a Scanning Laser Vibrometer at DTU. The modal analysis shows that the natural eigenfrequencies and the Lock number remain close to design, with mismatches around 10%. A test campaign for assessing the load reduction capability was performed in the boundary layer section of the GVPM. Tests were performed in no wake/partial wake conditions. The model was tested for three configurations: RGD, (i.e. with rigid blades), BTC, hybrid BTC+IPC (BTC blades and cyclic pitch controller). Examining the shaft and tower base bending moments, the BTC seemed capable of mitigating the peaks within a bandwidth up to the first blade flapping frequency. The inertial loads were not affected by the BTC, therefore their contribute may increase the peak at the 1xRev, and hence the equivalent fatigue load of the shaft bending moment. Finally, the hybrid BTC+IPC model seemed to recover this aspect since the 1xRev is cutout by the cyclic pitch control.

The work performed in University of Patras consists of two main parts: i) the experimental characterization of Shape Memory Alloy wire actuators and ii) the experimental characterization of a scaled morphing section. The first part of the work included the material characterization of the SMA actuators in wire form. The second part of this work consisted of the manufacturing and testing of a scaled morphing section prototype using SMA wire actuators. The design of the prototype is the outcome of the D2.2.3 while a proper scale of a reference blade's section was selected in order to facilitate the manufacturing and the laboratory testing. The morphing functionality of the prototype was assessed under zero loads as well as aerodynamic loads. The SMA material properties have been successfully extracted after a test campaign conducted by the University of Patras. Additionally the fatigue life of the material in the envisioned working stress level has been estimated. Furthermore, the scaled morphing section has been designed, fabricated and successfully tested in the laboratory in order to assess and demonstrate its morphing capabilities. The prototype proved its capability to morph its trailing edge to target shapes with and without the presence of simulated aerodynamic loads calculated by NTUA.

TUD used an innovative manufacture technique to fabricate a scaled 2m section of a wind turbine blade. This section was designed using an optimization tool presented in D2.2.2, where weight savings of up to 20% were illustrated when the traditional sandwich structure is replaced with a proposed grid stiffened structure, of a particular height to thickness ratio, solely in the trailing edge panel. Considering the upscaling of this method, the automated fiber placement process can be used to produce extremely large parts with the use of multiple robots with the fiber placement heads mounts on them in a bilinear track arrangement with minimum difficulty. However many practical problems should be solved before this method can be used in massive production of blades.

In conclusion, three concepts, the first one aiming for load alleviation using passive load control, the second one aiming for load alleviation using active load control and the last one aiming for weight reduction of the blade using an innovative fabrication technique, were manufactured and tested in laboratory using scaled blades or parts of the blade. Considering the scaled blade with the bend-twist coupling the blade was characterized, using static and dynamic tests both at PoliMI and at DTU. A good agreement between the two labs and the design values was observed. Moreover, the tests in the wind tunnel showed that the synergy of the BTC with IPC led to the most promising results for the load reduction on the blade. The experimental campaign regarding the SMA technology proved that the morphing section prototype is capable to operate both as a single flap of length equal to 10% and 30% of the chord and as morphing trailing edge offering a smooth shape change, matching the specified target shapes that achieve the maximum increase of the lift coefficient in almost all of the considered cases. Finally using the grid stiffeners method, a scaled blade was fabricated, however the upscaling of this method still is limited due to practical issues.

TABLE OF CONTENTS

1 INTRODUCTION

In order to achieve the primary objectives of the INNWIND project, i.e. the high performance innovative design of a beyond the state-of-the-art 10-20MW offshore wind turbine and hardware demonstrations of some of the key components, new concepts and technologies are investigated within WP2 "Lightweight rotor". Towards that direction, three promising solutions are in the current work assessed by manufacturing and testing scaled prototypes of predefined designs which were extensively described in previous documents D2.2.2 and D2.2.3. The first concept opts for load alleviation using passive load control of the blade, the second one aims for load alleviation using active load control and the last one targets for weight reduction of the blade using an innovative fabrication technique and optimization algorithms.

More specifically within subtask 2.2.3, three different blade parts were fabricated:

• Three scaled blades with a bend-twist coupling (BTC) by POLIMI and DTU
• A morphing scaled blade section equipped with Shape Memory Alloys (SMA) by University of Patras
• A scaled blade part with trailing edge panels reinforced with grid-stiffeners instead of the commonly used sandwich structure by TUD

The present document includes three main chapters where the different concepts are explained separately by the partners of subtask 2.2.3. The emphasis is given on the manufacturing process of each concept and on the evaluation of each solution against the set targets through dedicated mechanical testing and calculations.

Chapter 2 summarizes the efforts made from POLIMI and DTU regarding the design, manufacture and testing of three scaled blades equipped with bend-twist coupling. The effect of the bend-twist coupling on the structural behaviour of the reference blade was extensively studied and presented in the previous work of D2.2.2. The work in the current chapter begins with details on the material selection and manufacture process. Next, the characterization of the scaled blades using different testing methods performed both in POLIMI and in DTU testing facilities, study of the aerodynamic behaviour of the blades and an investigation on the blades' load alleviation capabilities are presented. Dynamic and static tests are performed, while the blades are equipped with Fiber Bragg Grating (FBG) sensors embedded inside the structure during the manufacturing process in order to evaluate potentialities of the HUMS (Heath and Usage Monitoring Systems) based on the fiber optics. Three manufactured blades are then assembled on a scaled tower-nacelle model. The resulting wind turbine model is tested in the wind tunnel of Polimi (GVPM) with the absolute goal to investigate the load alleviation capabilities of the BTC and its synergy with the active pitch control system. The model was tested for three configurations: RGD, (i.e. with rigid blades), BTC, hybrid BTC+IPC (BTC blades and cyclic pitch controller). Finally the chapter ends with a comparison between the obtained results from the two different labs and the design values.

Chapter 3 contains the work performed in University of Patras including two main parts: i) the experimental characterization of Shape Memory Alloy wire actuators and ii) the experimental characterization of a scaled morphing section. The material characterization consists of the thermomechanical properties determination and estimation on the fatigue life of the SMA wire. Special testing apparatus for SMA materials cannot be found in market, thus two in-house devises, oriented in testing SMA wires, were designed and manufactured. The first one is an existing device that has been used by UPATRAS for material characterization in the past, but due to the limitations encountered a second device was designed to perform the experiments needed in the framework of this project.
To acquire the full set of material properties there are four categories of experimental tests that must be conducted and can be summarized as follows:
• Determination of zero stress transformation temperatures through Differential Scanning Calorimetry (DSC)
• Stabilization of material properties under cyclic isothermal or isobaric loading (training)

- Isothermal mechanical loading
- Isobaric thermal loading

Each test provides different information and is used for different properties extraction. It should be noted that the stabilization of the material's properties (training) is performed under isothermal or isobaric conditions according to the further use of the material. If the SMA is used for actuation, then the training procedure is performed under isobaric conditions. All the experiments conducted on SMA wires in the framework of this project took place in the facilities of University of Patras using wire specimens extracted from an 80 m spool of NiTi bought from Nimesis Technology.

The second part of chapter 2 consists of the manufacturing and testing of a scaled morphing section prototype using SMA wire actuators. The design of the prototype is described in D2.2.3 while a proper scale of a reference blade's section was selected in order to facilitate the manufacturing and the laboratory testing. The target shape of the morphing section has been defined through aeroelastic analysis conducted by National Technical University of Athens (NTUA) in the framework of INNWIND.EU project. A first approach considers a single flap with variable length. The morphing functionality of the prototype was assessed under zero loads as well as under aerodynamic loads. This chapter finishes with a comparison of flap testing with no loads and under simulated aerodynamic loading where the prototype proved its capability to morph its trailing edge to target shapes with and without the presence of the simulated aerodynamic loads.

Chapter 4 presents the efforts made from TUD for the demonstration of a manufacture technique using grid stiffeners to replace the trailing edge sandwich structure. The chapter begins with the project plan where the reasons for the selection of the particular blade part and scale are stated. The production process with detailed description of the molds and the used materials are following. Finally a cost analysis of this concept is given and the report finishes with a paragraph on the possibility for upscaling this technique. Considering the upscaling of this method, the automated fiber placement process can be used to produce extremely large parts with the use of multiple robots with the fiber placement heads mounts on them in a bilinear track arrangement with minimum difficulty. However many practical problems should be solved before can be used in massive production of blades.

2 MANUFACTURING AND TESTING OF A SCALED BLADE WITH BUILD IN COUPLINGS (POLIMI & DTU)

2.1 Brief description of the work

This task is focused on the design and manufacturing processes for the realization of the scaled aeroelastic blades equipped with bend-twist coupling (BTC). The characterization and structural testing of the scaled blades using different testing methods is also part of the task. The blades were equipped with Fiber Bragg Grating (FBG) sensors embedded inside the structure during the manufacturing process in order to evaluate potentialities of the HUMS (Heath and Usage Monitoring Systems) based on the fiber optics, since the continuous increase of the wind turbine dimensions needs improvement of safety and reduction of the inspection time, achieved through load detection capabilities to the composite structure as explained in [35].

Three manufactured blades are finally assembled on a scaled tower-nacelle model. The resulting wind turbine model is tested in the wind tunnel with the goal of investigating the load alleviation capabilities of the BTC and its synergy with the active pitch control system.

2.2 Design and manufacturing of the scaled blades

It is well known that the non-dimensional parameters that drive the dynamics of the wind turbines are the tip-speed-ratio λ, the Reynolds number Re, the Froude number Fr, the Mach number Ma and the Lock number Lo, as well as the non dimensional natural frequency Ω and the non-dimensional time τ. Even if the ideal scaling would involve the matching of all the aforementioned non-dimensional parameters, it is readily demonstrated that this situation never can occur. Hence, there isn't a unique criterion to be followed for a correct scaling, but instead, the method should be set-up in order to fulfill some driving requirements that depend on the application and on the field where the model will be tested. The method used here is based on the loose scaling criteria derived by [20] that required the exact-matching of the aerodynamic kinematics, i.e. the same tip-speed-ratio, the exact-scaling of the structural dynamics, i.e. the same non-dimensional natural frequencies, and the enforcement to have the same ratio between the aerodynamic and inertial properties, i.e. the same Lock number, which amounts to have the same scaled aeroelastic stiffness properties.

The rotor model has been design to be a loose scaled-representation of some multi-megawatt machines in the range of 2-10 MW. To understand the designing solutions for the aerodynamics of the scaled blades, additional considerations should be taken in mind. 1. Being the tests conducted in the wind tunnel, the size of the test chamber constraints the rotor diameter. Additionally it may introduce wake blockage affects that became important with the increasing of the rotor dimensions; 2. The limitation of the rotor size would require a scaled-up of the time in order to satisfy the scaling requirements, and therefore scaled-up of the bandwidth for the controls with consequent possible excessive increase of the actuators workload; 3. Limiting the scaled-up of the bandwidth and the velocity, together with the limited rotor dimensions, brings to have an unavoidable high mismatch with reference full-scaled machines in terms of Reynolds' number, that changes the physics of the fluid-structure interactions and therefore reduces the energy conversion quality.

Keeping in mind the previous considerations, the scaled rotor was conceived so as to match with the following driving requirements:

- Limited rotor size, in order to limit blockage effects due to the interference with the wind tunnel walls, but large enough not to lower too the Reynolds numbers. Based of previous experience, a good trade off value of the rotor diameter was considered $\approx$ 2m.

- Limited scaled-up of the time in order to avoid an excessive increase in the pitch control bandwidth and a reasonable rendering of the principal dynamic effects of servo-actuators, mainly due to time delays and maximum attainable rates. For this purpose, the nominal rotor speed was chosen $\approx$ 380 rpm, which translates in *Re* around 4.5-6.5x10^4.

- A realistic energy conversion process, which translates into the same full-scale and model aerodynamic kinematics (i.e. same tip-speed ratio) as well as into realistic aerodynamic thrust and power. For this purpose, the blade is designed using special airfoils developed for Reynolds around 5-60000 and equipped with transition strip. The AH79-100C [2] and WM006 [32] airfoils were used, with the former airfoil extending for η = [0.146,0.451] and the latter for η = [0.697,1]. The choice of these profiles was dictated by the fact that their capability in providing good aerodynamic performance at low Reynolds was proved previously [20]. In the blade inner region, the inboard airfoil is smoothly deformed into the blade root cylinder, which extends for η = [0.0,0.021].

In order to account for the limitations induced by the scaling, the following expedients were considered:

- the chord distribution has been selected accordingly to have Reynolds number around 5-60000 for a large part of the span, that, with the chosen airfoils, guarantees good performances in terms of aerodynamic thrust and power coefficients. At the same time a reasonable rotor solidity according to the reference multi-MW machines was also provided;

- to account for the choice of the airfoils and for the chord length distribution, the twist was accurately chosen in order to have an optimal axial induction distribution.
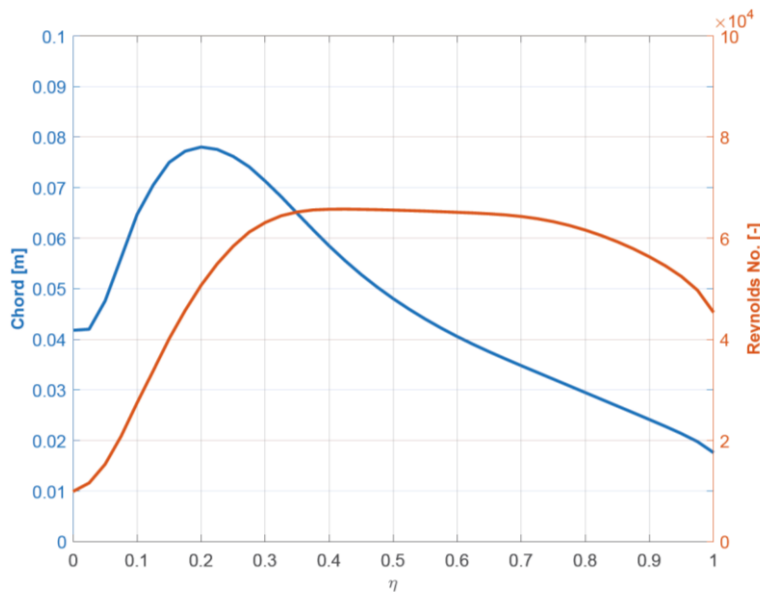
Figure 1 Chord and airfoils Reynolds distribution for the designed blade

2.2.1 Blade layout

The realization of the aeroelastic blades is a complex challenge. The design process should identify optimal structural layout, choice of materials and sizing of the structural members to ensure the fulfilment of the requirements.

According to the scaling, the shape of the blade passes from the root cylinder of diameter around 40 mm to airfoils whose thickness is around 1-2 mm. The required total mass is about 50 [g], while the first flap-wise frequency is slightly greater than the 3xRev.

Table 1 Scaling factors for the model characteristics with respect to 2 MW, 5 MW [26] and 10 MW [1] Reference Wind Turbines (RWTs)

	SF	RWT 2 MW	RWT 5 MW	RWT 10 MW
Length	n_l	1:48.09	1:65.87	1:93.25
Rotor speed	n_Ω	25.3:1	31.4:1	39.5:1
Wind speed	$n_l n_\Omega$	1:1.90	1:2.10	1:2.36
Rotor power	$n_l^5 n_\Omega^3$	1:1.58x10^4	1:4.00x10^4	1:1.14x10^4

Looking at the layout of the modern wind turbine blades, they are typically realized with a D-spar structure: a carrying-box made up of two shear webs connected to the spar-caps, which are made of epoxy resin reinforced with glass fiber and/or carbon fiber and designed with the primary function of withstanding the aerodynamic and inertial loads, while an external shell, usually made of epoxy resin reinforced with glass fiber, provides the necessary torsional stiffness and gives the desired aerodynamic shape to the blade.

Since the goal is producing a scaled version of a multi-megawatt machine, the most obvious solution would be to directly scale all the structural elements using the ratios of Table 1. This would involve scaling the blade geometry, as well as the structural thicknesses, with the factor $n_l \approx 1/50 \div 100$ and using materials whose Young's modulus is scaled with the factor $n_l^2 n_\Omega^2 \approx 1/5 \div 10$. This solution appears to be unfeasible because the scaling of the original structural elements

INNWIND.EU, Deliverable 2.24, Manufactured and laboratory tested scaled blades and parts of the blade

would require the manufacturing of components whose thicknesses would be in the order of a few hundreds of microns, resulting in huge technological complications, as well as high fragility and difficult handle-ability of the manufactured components.

On the basis of all the aforementioned considerations, some driving requirements for design and manufacturing of the blades can be deduced:

- The external shape should be consistent with the rotor model geometry and with good surface finishing, in order to guarantee a realistic energy conversion process;

- The bending stiffness consistent to the one specified by the scaling factors, together with a blade mass distribution and external shape such that requirements on the placement of the blade natural frequencies and of the Lock Number are fulfilled.

- The manufacturing process should allow the embedment of Fiber Optic Sensors (FOs) in desired positions inside of the blade structure.

Fiber Optics with embedded *FBG* sensor

Carbon fibers spar:
- Made up with *HM M50J 100 EU334 32.5% epoxy* prepeg + carbon fibers, with layer thickness = 0.0903 mm (nominal)

Scotch Weld AF 163-2K external film:
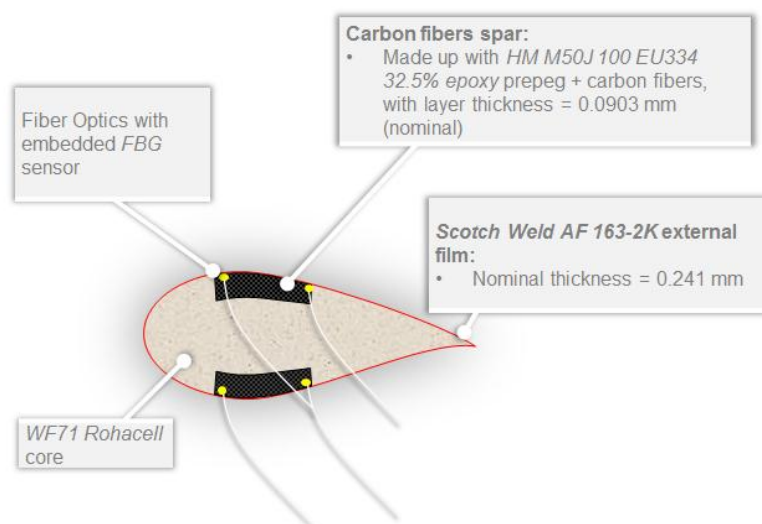- Nominal thickness = 0.241 mm

WF71 Rohacell core

Figure 2 Blade layout

The blade layout is shown in Figure 2. As done in other applications (see [11] and [25]), a Rohacell® [3] core is used to avoid any deformation of the airfoils shape due to the forces exerted by the aerodynamic pressure. Instead of the more classical D-configuration, which by the way would imply an unacceptably higher bending stiffness for the chosen thinner airfoils, two properly sized composite spars are selected and located far from the airfoil mean line, in order to obtain adequate edge to flap wise stiffness ratios. The spars are made of non-symmetric and non-balanced stacking sequences of prepreg UD carbon fibers, which provide the desired bend-twist coupling and guarantee sufficient level of stability to the whole blade. Finally, this solution allows FOs integration during the hand lay-up of the spars exploiting embedment techniques especially developed for composite laminates [34], which ensure high load transfer capability between FOs and host structure, minimally invasive as well high accuracy of embedded sensors. As underlined in Figure 2, four FOs, equipped each with one FBG sensor, are embedded from the blade root. The sensors are placed at about one third of the blade span. The four application points within the section are chosen as those with higher strains (two on suction and two on pressure side), so as to maximize their sensitivity and their accuracy.

All the aforementioned requirements are achievable with this layout using a very small and predictable fraction of the blade target mass and with little increase of the cross-section stiffness; furthermore, the Rohacell exhibits good deformability properties if subjected to conveniently high level of pressure, and resists at high cure temperature. On the other hand, it is necessary to pre-form the Rohacell before its inclusion in the model blade, as well as conveniently sized grooves must be realized for housing the carbon spars. Moreover, the high fragility of the material requires the use of appropriate techniques for its machining and handling during the lamination phase.

Finally, an uncured polymeric layer is used to cover the blade surface and to provide good and smooth finishing by filling the Rohacell pore. At the same time, it contributes to increase the torsional stiffness with small effect on the bending stiffnesses. This solution allows to precisely know the modest amount of mass added to the blade, which is not possible in the case, for example, of manual application of epoxy resin or similar; furthermore, during the curing process the adhesive film becomes very fluid allowing its homogeneous distribution all over the blade surface.

2.2.2 Material selection and characterization

The *HM M50J 100 EU334 32.5%* [4] unidirectional (UD) high-modulus graphite/epoxy prepreg (layer thickness equal to 0.0903~mm) was selected for the production of the carbon spars on the basis of its very high module to density ratio. With regard to the filler, Rohacell WF71 with nominal density of 71 kg/m^3 was chosen, which is a good compromise between low density and not excessive cells size. For the external skin a film of *Scotch Weld® AF 163-2K* [6], with nominal thickness equal to 0.241 mm was used; this epoxy structural adhesive has a curing temperature equal to that of the UD prepreg and its supporting carrier provides good drapability, which is fundamental given the complex and doubly curved blade surface, avoiding, at the same time, excessive deformation of the resin film during its application on the blade surface.

The *HM M50J* and AF163-2K mechanical properties were measured by performing standard tensile tests on sample coupons of the materials, following the requirements imposed by rules [5] and using a *MT S793* Materials Test Machine. The measured longitudinal tensile modulus in the direction of the fiber orientation E_{11}, the tensile modulus transverse to the fiber direction E_{22}, the in plane shear modulus G_{12} and the major Poisson ratio v_{12} of the *HM M50J* and *AF163-2K* are reported in Table 2.

Table 2 Measured mechanical properties of the *HM M50J* and *AF163-2K*.

	HM M50J	AF 163-2K
E_{11} [MPa]	245019	2887
E_{22} [MPa]	5936	2887
G [MPa]	4151	1024
v	0.324	0.41

As explained in the following section, the Rohacell core must be oversized in order to provide a sufficient level of pressure during the curing process; consequently, the material density can be much greater than the nominal one and variable along the blade span. The characterization of the Rohacell WF71 mechanical properties was therefore done by realizing several specimens with different density. Specimens with measured density equal to 72, 97 and 110 kg/m^3 were

produced with ad-hoc molds used to compress small blocks of different thickness into the desired shape.

The specimen Young's and shear modulus are characterized as function of the temperature, using the DMA 2980 Dynamic Mechanical Analyzer. The measured modulus is shown in Figure 3.
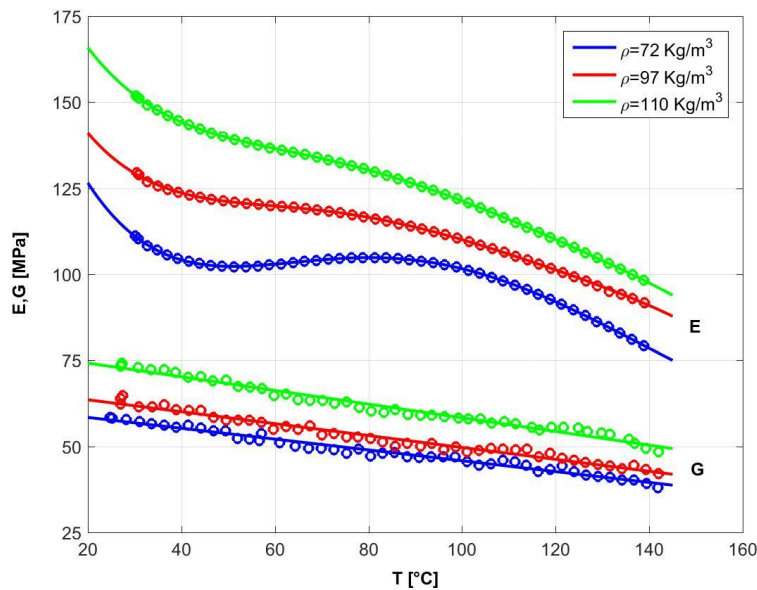

Figure 3 *Rohacell WF71 modulus as function of the specimen density and temperature.*

2.2.3 Design optimization of the anisotropic composite structure

The problem of sizing was performed by looking at the following objectives. First, the correct aero-elastic scaling, i.e. the correct matching of the Lock Number and the lowest N_Ω non-dimensional blade frequencies, i.e. $\hat{\omega}_i/\hat{\Omega} = \tilde{\omega}_i/\tilde{\Omega}$ for i = 1 : N_Ω, where N_Ω is an appropriate number that selects all modes up to a certain frequency. Second, the anisotropic composite structure should be realized in a way of creating an effective bend-twist coupling. The bend-twist coupling is reached by rotating the carbon fibers in the spar of a certain angle so as to guarantee a sufficient coupling, quantified at section level with the coefficient $\alpha_s = K_{ft}/\sqrt{K_{flap}K_{tor}}$ (defined as in [30], where K_{flap} is the local flap-wise bending stiffness, K_{tors} the torsional one and K_{ft} the coupled bend-twist stiffness).

The structural design of the blade is made by solving the aforementioned issues one per time. At this purpose, a first sizing is made without bend-twist coupling, i.e. considering the carbon fibers in the spar aligned with pitch axis. But given the different layout between the scaled blade and the reference D-spar structure, the problem of matching many frequencies becomes hard and even impossible. On the other hand, being the final purpose to demonstrate the capability of the bend-twist coupling in reducing the fatigue loads, it was considered enough to match only the lowest three frequencies, i.e. the first two flap modes and the first edge.

The structural design is made with a fast design tool that accounts for all the requirements listed and, at the same time, to capture the local effects in complex 3D structures made with anisotropic composite materials. The approach here proposed is based on the works published in [16,19] and consists of a multi-level design procedure that conducts the design with a high level of integration and automation. Figure 4 illustrates the proposed multi-level constrained structural design optimization of the blade, which will be described in detail later on.

INNWIND.EU, Deliverable 2.24, Manufactured and laboratory tested scaled blades and parts of the blade

As a starting point, a guess configuration of the blade structure is required at section level. The primary design variables are defined at selected span-wise sections while intermediate values are interpolated using shape functions. Based on this, a beam-like multibody model of the blade is developed in the *Cp-Lambda* multibody environment, and the automatic computation of the beam eigenvalues allows the evaluation of the first three natural frequencies. The cost function is the error on the edgewise stiffness (distributed along the blade-span) with respect to the scaled reference blade. The reason associated with the use of this cost function is related to the chosen airfoils, that being much thinner than those used in the target blade, the achievable ratio K_{edge}/K_{flap}, i.e the ratio between the blade edge-wise and flap-wise stiffness, will be greater than target one. With this cost function, the optimization problem seeks the best configuration with the minimum (unavoidable) descrepancy on the edgewise stiffness.

A 3D CAD model is than directly generated from the optimal blade geometry which precisely accounts for all components of the blade (spar caps, external skin, *Rohacell* core and blade root insert) as well as their associated material properties and laminate characteristics. The meshing of the blade is performed with the commercial pre-processing software *HyperMesh* [7], which provides macro-based facilities for automatic mesh generation, using either shell and solid elements, and the subsequent export of the model data in the form of input files compatible with various commercial FEM solvers.

The 3D FEM model provides the framework for a fine-level verification of the design constraints, as the detailed model reveals effects that may have been overlooked by the coarse-level (multibody level) modeling. For example, local effects at regions with rapidly changing geometry in the span-wise direction cannot be correctly represented by beam models. In case that constraint violations are detected at the fine-level, the coarse optimization loop is repeated with constraint bounds that are tightened proportionally to the violation amount; coarse and fine-level iterations are repeated until an optimal design satisfies all the constraint conditions at the finest description level.
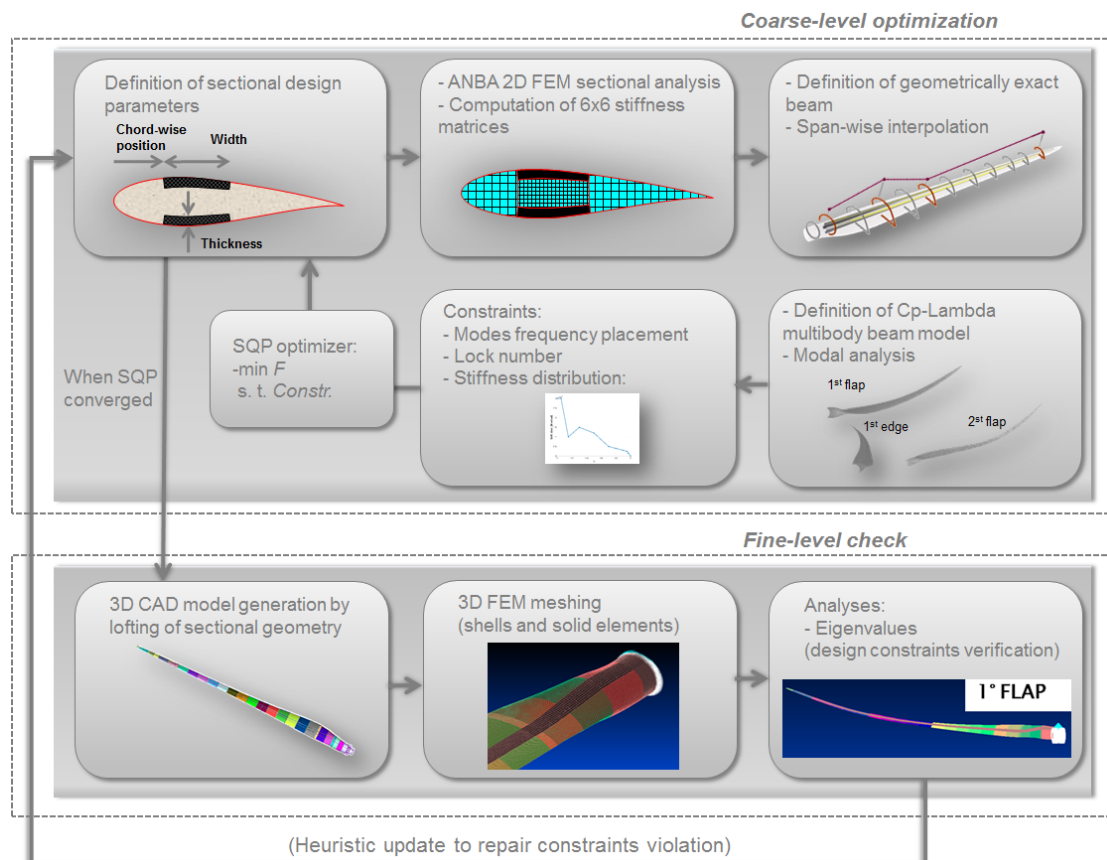
Figure 4 Multi-level structural blade design tool

Coarse-level optimization

The numerical problem of finding the structural configuration to meet the design requirements has been formulated in order to minimize differences between model and target edge-wise bending stiffness, subjected to some constraints. The constrained optimization procedure requires the ability to define parametric beam models of the blade, as well as to numerically evaluate the blade natural frequencies. The beam models are based on the multibody formulation reviewed in [16]. The structural parameterization used by the optimization problem is based on detailed cross-sectional models of the blade at a certain number of span-wise locations; from these models, equivalent cross sectional stiffness and inertial data are generated using the approach of [24], which leads to the definition of the beam sectional data. The structural model of the blade comprises the following elements:

- a description of the external shape of the blade, which is obtained by providing the airfoil data coordinates at each span-wise location. This information, together with the curved and twisted aerodynamic reference line and its associated chord length data, fully defines the external blade geometry;

- a description of the blade cross section and span-wise internal geometry. The cross section definition requires, at a number of stations along the span, to define the chord-wise location, the chord extension and thickness of the spars, as well as the thickness of the external blade skin. The cross section is modeled using: 1) panels made of equivalent materials for modeling the spars, which involves a discretization of the mid-thickness line

with 1D elements, and the external skin; 2) 2D quad elements for modeling the Rohacell core. The mesh density parameters are associated to the structural elements to support the computation of beam-like equivalent structural blade properties.;

- for each cross section, a description of the lay-up of composite laminates of skin and spars, together with the definition of all the necessary material properties. In this regard, the carbon and skin-glue properties are constant for each cross section, while the Rohacell properties may vary from section to section due to the fact that the amount of core compression, as explained hereinafter, changes along the blade span.

The code *ANBA* [24] is used for defining the structural and inertial characteristics of the cross sections along the blade span, which are used as inputs for the definition of the beam model. The computation of a possibly fully populated sectional stiffness matrix, which hence accounts for all possible couplings (flap-torsion, flap-lag, extension-torsion, etc.), is performed starting from a detailed finite element mesh of the cross section using the anisotropic beam theory. The analysis also yields all other data of interest, including location of centroid and elastic center, orientation of principal axes, sectional inertia and mass. The analysis is conducted for each section along the blade span, whose number and location can be selected by the user, in order to provide for an accurate representation of the blade characteristics.

Fine-level check of the requirements conformity
The next step to the coarse-level optimization is checking the fulfillment to the design constraints, i.e. natural frequencies and Lock number. This was done by performing structural analysis on a detailed 3D FEM blade model. Indeed, the effect on blade structural properties, produced by regions with rapidly changing geometry in the span-wise direction cannot be correctly represented by beam models, which is used in the multibody environment.
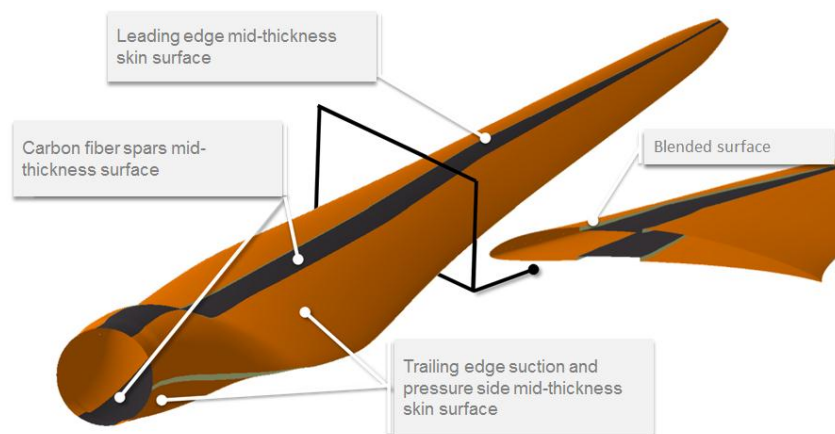

Figure 5 NURBS surfaces for CAD model generation

For the FEM modeling of the blade, mid-thickness layered shell elements are used for modeling the glue-made blade skin and the carbon fiber reinforcements, while solid tetra elements are used for modeling the *Rohacell* core and the metal part placed at the root of the blade during the lamination process.

The structural constraints are therefore investigated through the detailed 3D FEM model. The Lock number is evaluated by looking at the flapping moment of inertia, while the blade modal frequencies by performing a linear modal analysis in *MSC Nastran*, in the same way as described for the coarse optimizer.

Since the mass distribution is directly moved into the 3D FEM environment from the multibody model, no significant mismatches are expected in terms of Lock number. If, instead, the verification of the constraint conditions on the fine level model reveals that design inequalities on frequency placement are not satisfied, a heuristic approach is applied in which the constraints are modified proportionally to the violation amount.

2.2.4 Aero-elastic blades design with BTC

As previously mentioned, once designed the scaled blade, the next step is to generate a sufficient bend-twist coupling by rotating the carbon fibers on the spars. For this purpose, the best approach is to introduce BTC to twist the blade sections so as to decrease the angle of attack, the so called twist-to-feather concept shown in Figure 6, more suitable for load reduction applications, as discussed in [18,29,30].
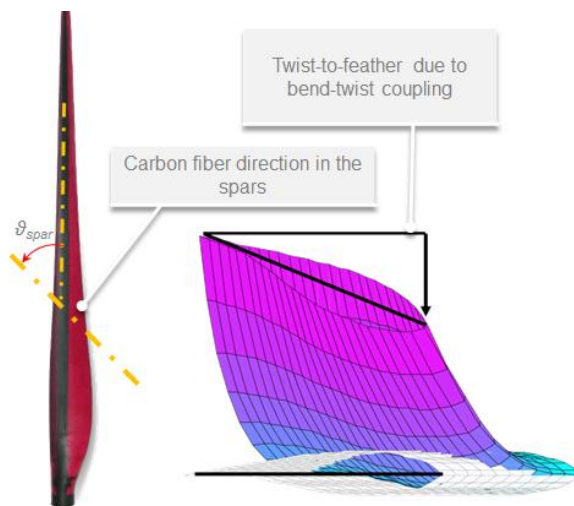

Figure 6 Coupling coefficient α_s as function of the carbon fiber rotation ϑ_{spar}.

Fully coupled design, where fibers are rotated in the spar of an angle equal to ϑ_{spar} and for the whole span-wise extension of the blade, was considered. Starting from the design of the blade without coupling, the coefficient $\alpha_s = K_{ft}/\sqrt{K_{flap}K_{tor}}$ (defined as in [30], where K_{flap} is the local flap-wise bending stiffness, K_{tors} the torsional one and K_{ft} the coupled bend-twist stiffness) was computed with ANBA for several cross-sections along the blade span and for different amount of fibers rotation ϑ_{spar}.

The design of the coupled blade was carried using the design tool previously described, whose working process is depicted if Figure 4. To better understand how the most suitable optimization problem was figure out, the following considerations should be kept in mind:

- From a design point of view, the rotation of the carbon fibers away from the blade axis leads mainly to a reduction of the out-of-plane bending stiffness; this would imply a redesign of the spar in order to match with the scaling constraints;

- on the other hand, as well explained hereinafter, the spars are manufactured with an ad-hoc mold, thought to be flexible for the realization of spars with generic ϑ_{spar}-oriented carbon fibers. This requests a constrained spar-shape, i.e. a constrained spar width and chord wise position along the span;

- since the width and the chord-wise position of the spar should be kept frozen for the previous consideration, a redesign of the spars to compensate for the loss of the flap bending stiffness would imply an increase of the spars thickness, which in turn would bring to an increase (even if moderate) of the blade weight and, therefore, a reduction of the modes frequencies, which would require an increase of the bending stiffness to compensate for it, with a consequent loss in matching the Lock number.

To account for all the aforementioned considerations, the width $s_w(\eta)$, and the chord-wise position $s_c(\eta)$ of the spars are not considered optimization variables anymore. They are taken from the design of the scaled blade without bend-twist coupling and added to the given data list, together with the carbon fibers orientation: $D_4 = \{R, AF, c(\eta), \vartheta(\eta), s_w(\eta), \vartheta_{spar}\}$. The design was carried out constraining the placement of the blade natural frequencies $\widehat{\omega}_i$ and with the goal of minimizing the Lock number mismatch due to the unavoidable increase of the spars thickness.

Few iterations of the overall algorithm were required until the final configuration was obtained. Figure 7 shows the spar distribution along the span in terms of width, chord-wise position and thickness, for the case with and without BTC.

In the case with BTC it is possible to observe that the thickness is increased to compensate for the loss of stiffness due to the rotation of the fibers. The beam properties, including frequencies and Lock Number remain very close to the case without BTC, therefore the choice of freezing the spar shape while leaving the thickness to be optimized is revealed to be successful. Table 3 shows the first three scaled-up frequencies and the Lock number of the designed blade with BTC in comparison to the RWT 5MW. The three natural frequencies are very close to the reference value, since the differences are below 6% and still acceptable for our purpose.
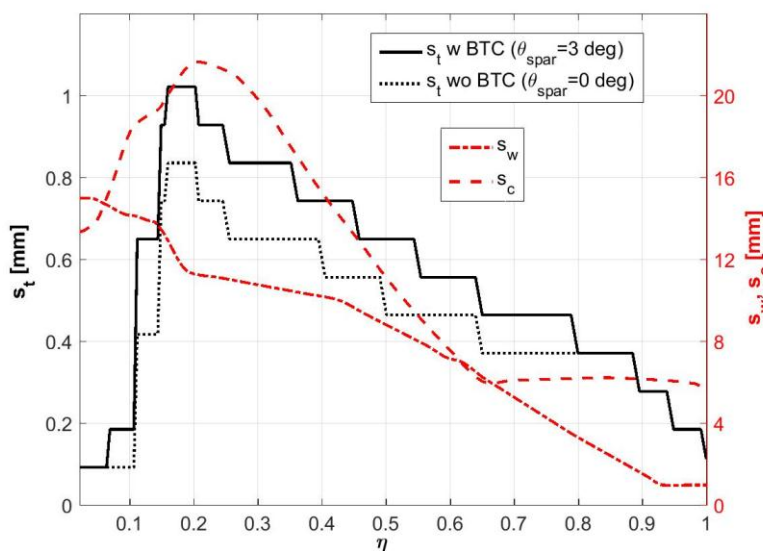

Figure 7 Dimensions of the spars along the span for the scaled blade.

Table 3 Computed frequencies of the scaled-up designed blade (3D FEM analysis). A comparison with the baseline.

	Baseline	BTC blade (scaled up)	Diff.
1st flapwise freq.	0.702	0.742	+5.7%
1st edgewise freq.	1.088	1.137	+4.5%
2nd flapwise freq.	1.960	1.981	+1.0%
Lock number	21.79	20.25	-6.9%

2.2.5 Blade manufacturing

The entire manufacturing process was set up for realizing, with a high level of reproducibility, good quality blades capable to fulfill the design requirements. Since the shape of the blade in very complex, as well as the technology was totally new, all possible critical aspects were unknown. Hence, the process was built step by step in order to acquire a certain confidence level of all aspects. It was debugged by the realization of several not-tapered and not-twisted specimen samples with chord equal to 50 mm, equipped with two optical fibers and one FBG sensor per each. The specimens were designed with the design tool and then manufactured. Experimental modal analyses were also set-up and performed in order to see if the manufacturing process was capable to satisfy the design requirements. The results, compared with the design expectations, showed a good quality of the process, since the mismatches in terms of frequencies were lower than 6%.
The final manufacturing process consists of the following parts:

- **Blade core shaping.** The core part of the blade is made with Rohacell *WF 71* whose defines the overall shape of the blade that should match the designed geometry. For this reason, the 3D CAD model was used to seed a CNC machine tool that provided for the realization of the desired shape. The thickness distribution of the machined core is slightly greater than the blade one. With this stratagem, once closed the mold, the core is forced to lay in a lesser volume which results in an increase of the Rohacell density and pressure that the core exerts on the inner mold surfaces. The mold is therefore put in the hoven, and once the curing process reached the glass transition temperature, the inner pressure favors the homogenous distribution of the resin, which meanwhile become fluid over the blade, providing good surface finishing. Furthermore, the core is conveniently machined in order to create, over its external surface, the grooves where the carbon spars were laid down during the assembly process. In the end, the filler root is worked up to allow the connection with a steel part, which was opportunely worked for housing the pitch motor.

- **Carbon fiber plies realization.** The plies with carbon fiber rotated of 3 degs are produced from the material roll and starting from the mathematics of the plies flat pattern, an automatic cutting tools was used, which allows to obtain reproducible plies with a good finishing.

- **Spars lamination.** This process is carried out before the final assembly, with the goal of having the plies correctly stacked in accordance to the ply-book. During the lamination process the optical fibers are embedded between the two outer plies while the FBG sensors are placed at the desired location, by means of a printout of the spar layout. The

spars curing process is carried out through the aid of an ad-hoc mold, specifically designed to avoid damage of the optical fibers, as shown in Figure 8.

- **Blade assembly.** Once all the blade sub-components are available, it was possible to proceed with the final assembly and, immediately after, with the final curing process. An aluminum alloy female mold, made up of two Computer Numerical Control (CNC) machined and polished halves, was designed by taking into account for the thermal expansion of the carbon fibers and the alloy itself. The two halves of the mold perfectly match at the leading edge parting plane, while there is a small gap of 0.1~mm at the trailing edge parting plane, so as to allow excess resin to squeeze out. Finally, some support blocks allow the fixing of the blade root to the mold.

Once spread a thin layer of release agent on the mold, the assembly is characterized by the phases shown in Figure 9 and listed below:

1. a thin film of glue is used for sticking together the *Rohacell* core and the metal part on which are assembled the bearings and the pitch motor;
2. both spars laminates are laid down on the *Rohacell* core surfaces and a thin layer of glue is used to ensure the bonding between the two parts;
3. one single layer of glue is laid up over the core using the mold as support base, so as to avoid breaking the fragile core; the resin film is laid on one side of the blade, wrapped around the leading edge and then laid on the other side, so as to form a continuous and homogeneous coating;
4. finally, such an artifact is placed over one half of the mold, with the second half successively fixed to the first one using several uniformly spaced screws: in this way high and uniform pressure is generated thanks to the *Rohacell* compression. The metal root part is fixed, by means of small screws, at the mold support blocks, where small holes allow the optical fibers to going out from the mold without causing damage.
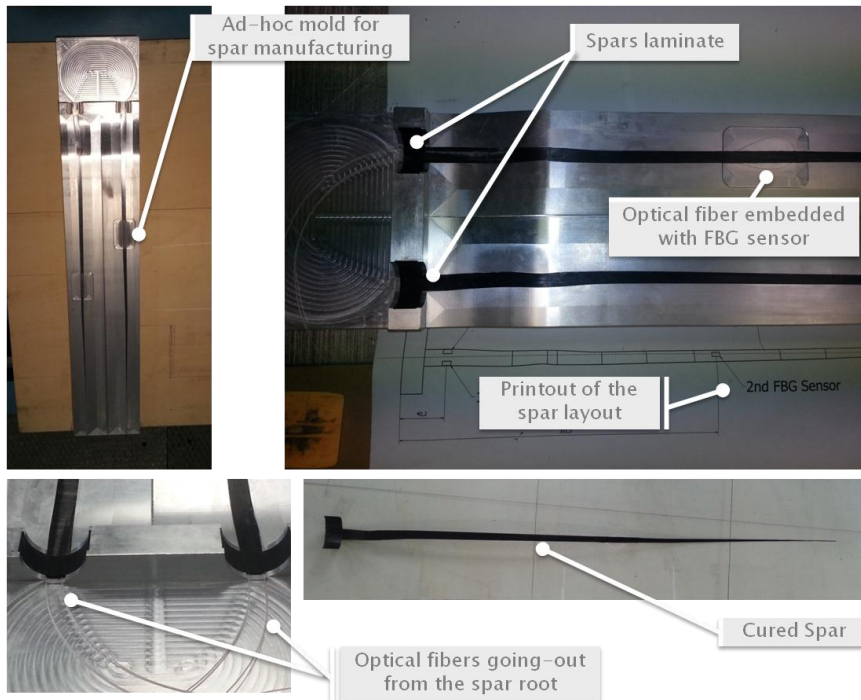
Figure 8 The mold used for the spar curing process.

Once finished the assembly procedure the polymerization process takes place in the oven with monitored temperature. At the end of the production process, modest finishes are necessary to obtain a high-quality aero-elastic blade.

Figure 9 Blade sub-components assembly.

2.3 Testing and characterization at PoliMI

This section describes the tests made for a complete characterization of the rotor equipped with scaled bend-twist coupled blades. The section is articulated by following: First, the structural characterization of the blade is described, including the tests description and the results. Second, a brief description of the scaled experimental facilities is made, which were useful to characterize the rotor from the aerodynamic point of view. Third, the test for aerodynamic characterization are described, before showing the results in terms of power coefficient and thrust coefficient. Then, the last part is dedicated to the application of the BTC technology in reducing the fatigue load. There will be an exhaustive description of the configurations tested and a detailed analysis of the results.

2.3.1 Structural characterization

The structural characterization is made at the blade level, once the realization process is complete. The structural characterization consisted of the following items: 1. verify the compliance to the design requirements; i.e. verify the modes frequencies and the Lock number; 2. verify the presence of the bend-twist-coupling.

Experimental modal analyses were carried out to characterize the dynamic properties. With a certain level of confidence on the reproducibility of the manufacturing process, the test was conducted on only one blade. The root was constrained rigidly to a steel-made plate fixed to the floor, thus ensuring a perfectly rigid constraint. The modal analysis was performed with the procedure debugged through some sample specimens, and consisted in some impact hammer tests to excite the structure; then, through miniaturized and lightweight (0.5 g) *PCB 352C22* accelerometer and exciting the structure at almost 20 different locations using a hammer instrumented with a load cell *PCB 086B03* (see Figure 10), was possible to reconstruct, with a good accuracy, the eigen-shape associated to out-of-plane and torsional modes.
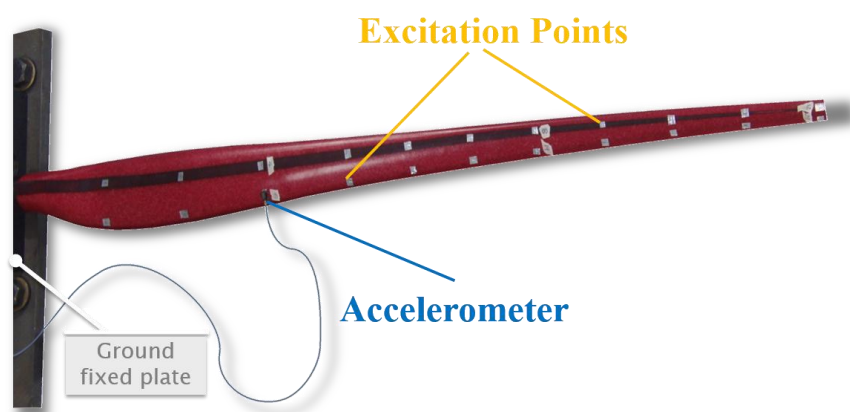

Figure 10 Modal testing with hammer.

Based on the measured Frequency Response Functions FRFs, eight out-of-plane and torsional natural frequencies $\tilde{\omega}$, related damping ζ and eigenvectors Φ, were identified, and two in-plane natural frequencies with related damping values were observed, despite their eigen-shape could not be reconstructed with the used setup.

Table 4 Measured natural frequencies, and related damping, identified on the basis of the measured FRFs and compared with the one computed on the 3D FEM model.

Mode	$\breve{\omega}$ [Hz]	$\breve{\zeta}$	$\widehat{\omega}_{[3]st}^{(3D-FEM)}$[Hz]	$\Delta\omega$ [%]	MAC
1st Flap-wise	20.7	0.86	23.3	-11.2	0.99
1st Edge-wise	33.73	-	35.7	-5.6	-
2nd Flap-wise	55.1	0.74	62.2	-11.4	0.978
2nd Edge-wise	109.69	-	112.5	-2.5	-
3rd Flap-wise	115.9	0.85	132.5	-12.5	0.917
1st Torsional	155.5	1.52	162.1	-4.1	0.563
4th Flap-wise	194.2	1.25	227.5	-14.6	0.969
2nd Torsional	240.6	1.51	254.4	-5.4	0.539
5th Flap-wise	286.8	1.35	335.5	-14.5	0.824
3rd Torsional	366.2	1.45	389.3	-5.9	0.463

Table 4 reports the comparison between the experimental and numerical natural frequencies, as well as the value of the MAC($\widehat{\Phi}_i^{(3D-FEM)}$, $\widehat{\Phi}_i$) operator, where $\widehat{\Phi}_i^{(3D-FEM)}$ is the ith eigenvector computed with the 3D FEM model. The comparison is quite satisfactory and especially the measured eigen-shape of the flap-wise modes well matches the corresponding numerical ones. Also the numerical values of the natural pulsations of the torsional and edge-wise modes well match the measured ones, while the 3D FEM model overestimates of around 15% the natural frequencies of the flap-wise modes.

Table 5 Measured blade mass and center of gravity span-wise position, variation with respect to the design.

	$\breve{m}[g]$	$\breve{r}_g[mm]$	Δm [%]	Δr_g [%]	ΔLo [%]
1st Blade	76.7	190.6	+1.05	+3.38	-7.40
2nd Blade	76.5	190.5	+0.78	+3.32	-7.06
3rd Blade	76.0	191.2	+0.13	+3.70	-7.14

To evaluate for Lock number mismatch, the three blades were checked in terms of mass $\breve{m}$ and center of gravity span-wise position $\breve{r}_g$. Table 5 reports the measurements adjusted by the mass of the blade root steel part. The results effectively highlight the good reproducibility of the manufacturing process and the good match with the design.

The static tests were performed with two main goals: 1. verifying the presence of the bend-twist coupling; 2. calibrating the FBG sensors. The bend-twist coupling is verified by loading the blade opportunely and evaluating the cinematic coupling between the flapping and the twisting. The blade was fixed from its root at a rigid steal-made structure and was equipped with four saddles placed at $\eta \approx [0.2, 0.5, 0.8, 0.93]$. The blade was then rotated in a position with the suction side facing down and the saddles in the horizontal position. Dead loads were applied at each saddle by some hooks located at three different points: the central point aligned with the pitch axis, while the other two aligned respectively with the trailing edge and the leading edge. Three laser *LAS8010* displacement transducers were used at each saddle to measure the vertical and horizontal deflections, as well as to evaluate the torsions. The blade was subjected to various loads inducing either mostly pure flap or flap-torsional deformations. For the pure flap-wise tests saddles were loaded at central point. Similarly, for the flap-torsional tests, saddles were loaded at both lateral points, which result in a leading edge pull-down case and a trailing edge pull down

case. Thus allows to separate the deformation due to the torsional flexibility from that one due to bend-twist coupling.

For the calibration of the FBG sensors, additional tests were needed. The blade is then rotated in a vertical position, with the trailing edge facing down. Dead loads were applied at each saddle by hooks located at a point aligned with the trailing edge.
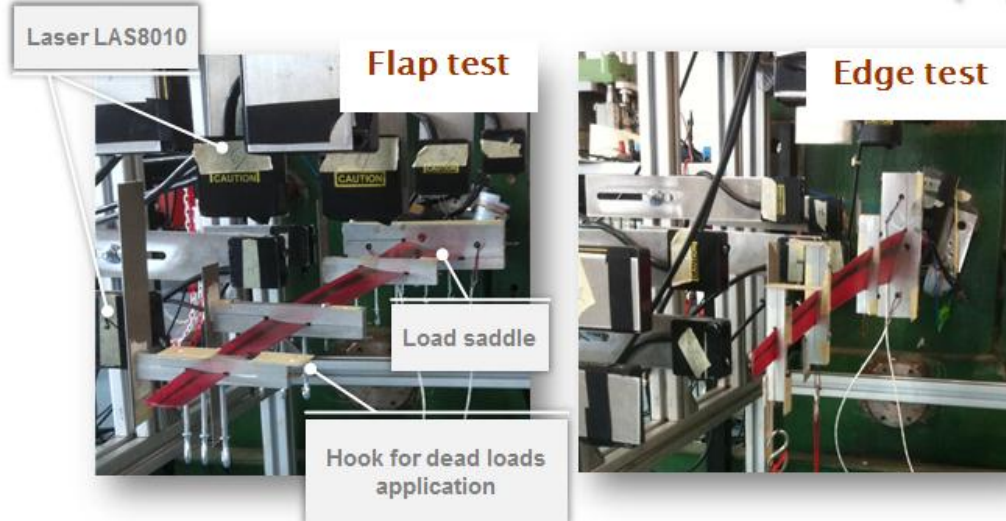

Figure 11 Static testing set-up.

Figure 11 shows the static tests configurations, with the twelve laser installed to acquire the four saddles displacements. Left-top picture shows the set-up for the flap tests, i.e. with the blade suction side facing down. In this configuration, for each saddle, two lasers were mounted at the top of the castle, in order to acquire the vertical displacement of two distant points: in this way it was possible to estimate the twisting of the blade at the saddle station by difference of the two measures. A further laser is then mounted laterally to acquire the edge displacement. Right-top picture shows the set-up for the edge tests, i.e. with the blade trailing edge facing down. With the same scope of estimating the twisting, for each saddle two lasers were mounted laterally, while for capturing the edge displacement, one laser is used at the top. Left-bottom and right-bottom pictures show two flap test cases, respectively a leading edge pull-down and a trailing edge pull-down.
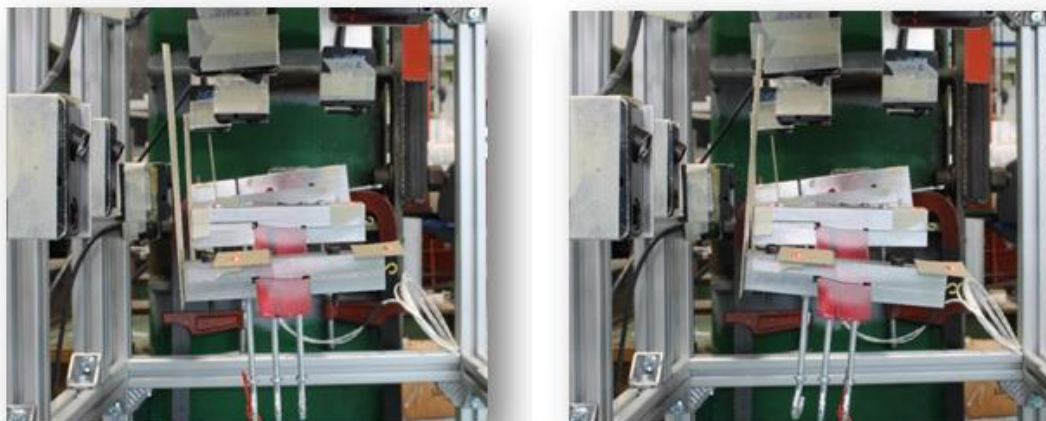

Figure 12 Leading edge pull-down to the left side, Trailing edge pull-down to the right side.
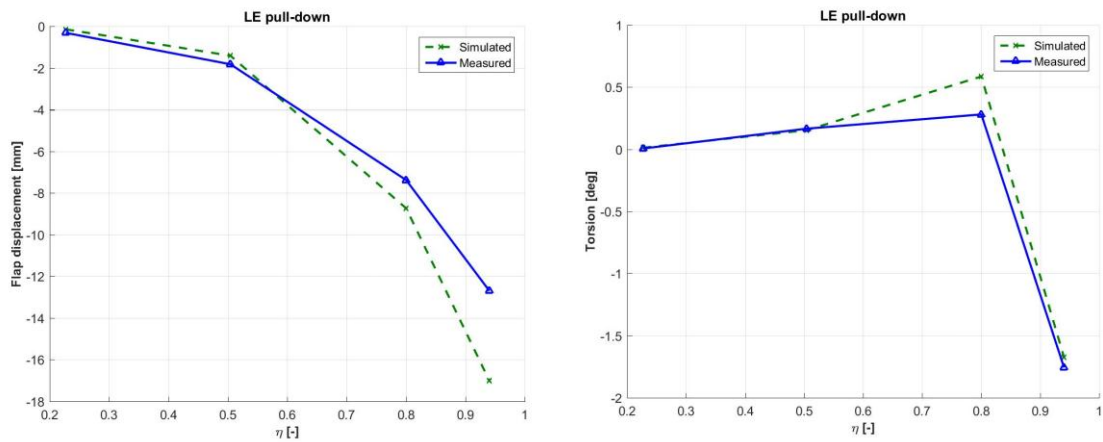
INNWIND.EU, Deliverable 2.24, Manufactured and laboratory tested scaled blades and parts of the blade

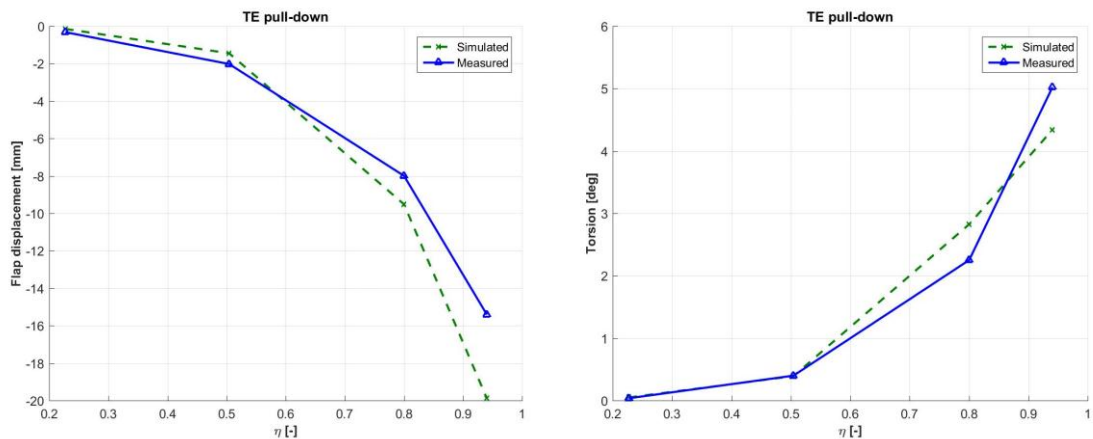**Figure 13** Leading edge pull-down.

Figure 14 Trailing edge pull-down.

The experiment set-up was also modeled in the *Cp-Lambda* multibody environment, by using the blade design, while rigid bodies are used to model the saddles. All the tests were simulated and the laser measurements opportunely reconstructed.

Figure 13-14 show the vertical ΔY at the left side, and the torsion $\Delta \vartheta$ at right side, evaluated at each saddle as the arctangent of the ratio between the two in-plane laser measurements difference and the their inter-axis. Two test cases are proposed here, respectively a leading edge pull down and a trailing edge pull down case.

The comparison with the numerical displacements of the beam-like multibody model highlights some differences. The manufactured blade shows a higher tendency-to-twist, especially for the inner sections (around η = 0.5). In the three tests the BTC twist-to-feather is observed, since the torsion for most of the span is always in a pitch-up sense, even when a leading edge pull is applied.

Although the matching between experimental and simulated data, especially for the flap-wise displacements, seems acceptable, an updating procedure for the beam like structural properties is necessary in order to have a comprehensive validated model, which can capture correctly also

the coupled bend-to-twist behavior. The updating procedure based on a system identification approach is described in § 2.3.1.1, *Beam-like structural model identification*.

Beam-like structural model identification

Improving the fidelity of the blade beam structural model is a key aspect in order to obtain a comprehensive validated model of any wind turbine. In fact, although modern wind turbine models are able to capture the coupled aero-servo-structural behavior of the machine, having a correct tuning of structural (and aerodynamic) properties is still a challenge. This issue becomes even more pronounced when considering a complicated structural behavior like the one involved in BTC blades.

From the structural point of view, the BTC blade can be modeled with the geometrically exact beam formulations [36] having fully populated sectional stiffness matrices.

With the goal of updating such structural beam properties so as to reduce the small mismatch between measured and simulated torsion in Figure 13-14, an updating procedure has been employed.

Using the measurements of the tests already described in §2.3.1, the estimation procedure (described in Ref. [37]) has been carried out. Figures 15 and 16 show the agreement between predicted and measured vertical displacement and torsion for two trials, respectively a leading edge pull down and a trailing edge pull down. It is clear that the identified model (solid red lines) is improved with respect to the nominal baseline (green dotted lines) and results to be well correlated with the measurements (triangle blue markers) especially in the half outer part of the blade. From the results obtained, it is possible to appreciate the goodness of the identified model outputs and, on the other side, to assess the ability of the beam model employed to characterize the behavior of a BTC blade.
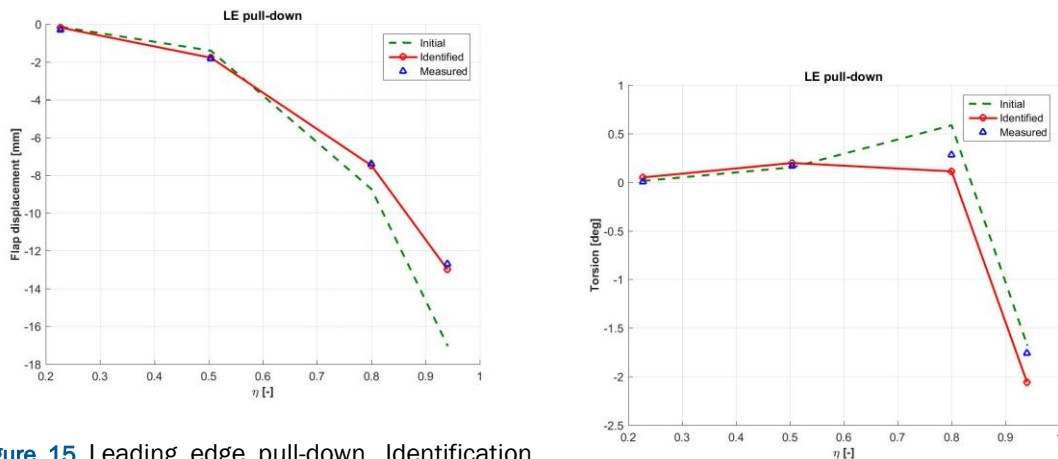

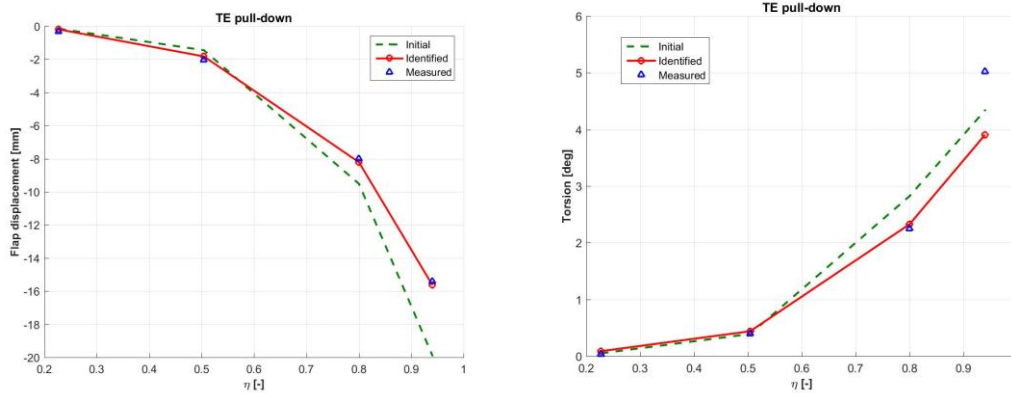**Figure 15** Leading edge pull-down. Identification results.

Figure 16 Trailing edge pull-down. Identification results.

FBG sensors calibration

The FBG sensors were calibrated by using the aforementioned static tests, with the goal of evaluating the loads in terms of bending moment at one third of the blade span.

In order to acquire all the FBG sensors through only one optical channel (requirement for wind tunnel tests, as explained hereinafter), the four optical fibers embedded in the blade were connected to a miniaturized 4x1 optical coupler. The four FBG sensors work at different wavelengths, respectively at 1582, 1564, 1529 and 1547 nm. For this reason, the four signals remain separated in the light beam thanks to the Wavelength Division Multiplexing (WDM). Sensors were acquired by a *MICRON OPTICS SM130* interrogator system at a sample rate of 1kHz.

The position of the sensors is known with an uncertainty ε_{FBG} = ± 10 mm. Since the sensors are placed at approx. η = 0.3 and the four saddles at η = [0.2,0.5,0.8,0.93], only the outer three were loaded to this scope. Twelve load cases were acquired:

- Three flap (flap test config., central hook)
- Three trailing edge pull-down (flap test config., right hook)
- Three leading edge pull-down (flap test config., left hook)
- Three edge (edge test config., edge hook)

For the twelve loads conditions, the associated flap-wise and edge-wise bending moment components at the sensor positions were evaluated, by accounting of its uncertainty ε_{FBG}. Later, the calibration problem of finding the two sets (one per each bending moment component) of four weight coefficients associated to the four FBG outputs was formulated as two least squares problems.

During the static test, one FBG signal was lost, therefore the weight coefficient associated to that measure was imposed null. The sensors position was estimated at η = 0.337. Table 6 reports a comparison between the applied loads and the estimates. The errors always remain below 1.1% in the flap direction and 1.2% in the edge direction. The use of four signals would have guaranteed more accuracy, anyway the results were considered enough satisfactory.

Table 6 Estimated dead loads with FBG sensors in the static tests.

Load Case	$\tilde{M}_{\text{flap}}$ [Nm]	$\tilde{M}_{\text{flap}}$ [Nm]	ΔM_{flap}[%]	$\tilde{M}_{\text{edge}}$ [Nm]	$\tilde{M}_{\text{edge}}$ [Nm]	ΔM_{edge}[%]
1st Flap	2.1714	2.1760	0.09	0	-0.0130	-
2nd Flap	2.0225	2.0292	0.33	0	-0.0125	-
3rd Flap	0.7799	0.7748	-0.65	0	-0.0202	-
1st TE pull-down	1.4623	1.4726	0.71	0	-0.0063	-
2nd TE pull-down	1.6946	1.6895	-0.30	0	-0.0205	-
3rd TE pull-down	0.6570	0.6500	-1.06	0	0.0173	-
1st LE pull-down	1.4623	1.4469	-1.05	0	0.0467	-
2nd LE pull-down	1.6946	1.6964	0.11	0	0.0193	-
3rd LE pull-down	0.6570	0.6616	0.70	0	0.0021	-
1st Edge	0	0.0019	-	4.6984	4.6991	0.02
2nd Edge	0	-0.0039	-	5.7655	5.7587	-0.12
3rd Edge	0	0.085	-	1.6399	1.6594	1.19

2.3.2 Scaled wind tunnel facilities

In order to perform the aerodynamic and loads characterization, the three blades with BTC were mounted on the hub of a scaled tower-nacelle system by two bearing, and a zero-backlash pitch motor with built in relative encoder housed at the root is used for pitching. This system is realized with the goal of supporting such activities of validating aeroelastic models and control laws. All its sub-components are also capable of representing the mutual interaction of aerodynamic, elastic and inertial forces, as required by the scaling lows. Table 7 reports the main geometrical dimensions of the model.

Table 7 Main dimensions of the wind turbine model.

Rotor diameter	1.913 m
Up-tilt angle	6°
Cone angle	4°
Over-hang	≈ 80 mm
Nacelle height	≈ 90 mm
Nacelle width	≈ 90 mm
Nacelle length	≈ 215 mm
Tower height	1.723 m

The shaft is mounted on other two bearings, held by a rectangular carrying box that features the main structural member of the nacelle. Behind the nacelle carrying box, the three electronic control boards of the pitch actuators are mounted on the shaft and therefore rotate with it. A 36-channel slip ring occupies the aft part of the nacelle, held in place by a plate and connected to the main carrying box by four rods. The tower is realized with a tube whose stiffness was designed so that the first fore-aft and side-side natural frequencies of the nacelle-tower group of the scaled model is close to the ones of the multi-megawatt machines. At the top of the tower is housed the

torque actuator connected to the shaft through a pair of conical spiral gears, with a reduction ratio of 0.5.

At the tower base, the model is mounted on a balance, that provides measurements of three force and three moment components. Finally, aerodynamic covers of the nacelle and hub ensure a satisfactory quality of the flow in the central rotor area. At the root of one blade, strain gauge bridges provide measures of the bending moments and their output voltages are conditioned and A/D converted by an electronic board placed in front of the rotor hub.

The presence of the 4x1 optical coupler (installed in a special composite reel frame on the rotor hub) allows the transmission of the optical signals of the embedded FBGs from the rotating part to the fixed one of the model through a special Fiber Optic Rotary Joint (FORJ) mounted coaxially with the electrical sleep ring.
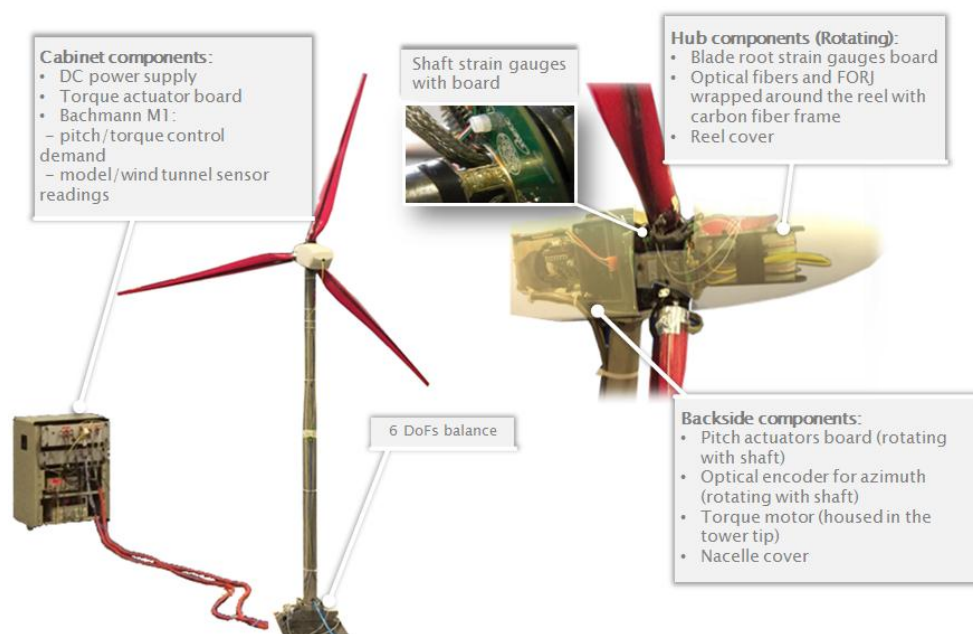
Figure 15 Wind turbine model with its main features.

Onboard sensors provide the ability to measure, with sufficient accuracy, the aerodynamic torque and the bending loads on the shaft by means of strain gauges, whose output voltages are conditioned and A/D converted by the electronic board placed among the rotor and the nacelle. An optical rotary encoder disk dragged from the shaft, mounted behind the two bearings, provides for rotor azimuth position. The model is controlled by a hard real-time module implementing a supervisor of the state machine and the pitch-torque control laws. The control action is performed by varying the blades pitch and the electrical torque provided by the generator. For each blade, the pitch actuation is demanded to a small brushed motor driven by its own control board mounted on the shaft and rotating with it. The feedback is based on the motor built-in encoder measures. The torque actuation is instead provided by a brushless motor lodged in the tower top and driven by a 4-quadrant control board, so as to allow the motor operating also as a generator. These actuation devices enable the testing of modern control strategies with appropriate bandwidth and a reasonable rendering of the principal dynamic effects of servo actuators. The electrical onboard sensors signals, together with the wind flow measurements from the wind tunnel, are sampled by the analog acquisition modules of the industrial Bachmann M1 hard-real-time system at the sampling frequency of 250 Hz. The machine states and the pitch-torque control laws are compiled

to the M1 CPU, while the control outputs, represented by pitch and torque demands, are sent to the actuators control boards via the M1 CAN module.

The overall model is illustrated in Figure 15, where the main features are highlighted.

The tests were performed in the wind tunnel of the Politecnico di Milano, arranged in a vertical layout, whose Figure 16 shows the configuration for testing of wind turbine models. At the bottom level, the aeronautical section was used for the aerodynamic characterization of the rotor. It is featured of a low turbulence (<0.1%) level and a wide flow velocity range (up to 55~m/sec), with a cross sectional chamber of 4m x 3.84m. At the top level, there is the boundary layer section with a wider cross area of 13.84m x 3.84m and a length of 35m. This feature allows to perform tests with low blockage effects. In this test chamber, that is mainly used for civil and wind engineering applications, the boundary layer and the high turbulence level (>25%) are introduced with the use of appropriate turbulence generators installed at the inlet of the chamber. The dimensions of the chamber allow testing of multiple wind turbines so as to be able to simulate wind farm configurations.

The wind tunnel is equipped with wide range of devices for measuring the physical quantities of the environment and for controlling the flow conditions, as well as with control rooms that allow to supervise the models and conducting the tests.
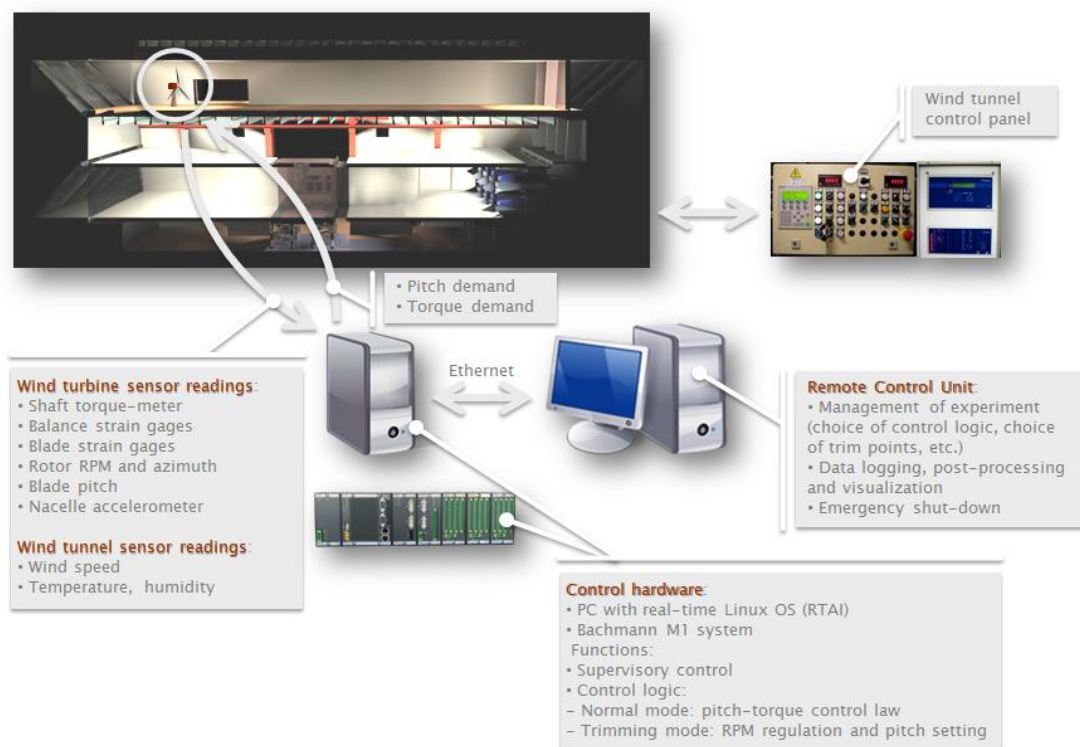

Figure 16 Wind tunnel layout with testing management system.

A Remote Control Unit is used for managing the model during the experiments through an GUI interface directly linked to the Bachmann M1 of the model. The interface allows the visualization of the main measurements, i.e. signals from shaft strain gauges, blade strain gauges, azimuth position and rotor speed, pitch position, wind speed, environment temperature, density etc., but also to switch among the several operation modes. A wind tunnel operator is capable of controlling the wind tunnel environment through the wind panel control unit.

2.3.3 Aerodynamic characterization

A first test campaign was performed in the aeronautical section of the PoliMI's wind tunnel, with the goal of evaluating the aerodynamic characteristics of the model with the bend-twist coupled blades. This step was necessary for at least three reasons: 1. To evaluate the impact of the BTC technology on the performances, mainly in terms of power production capability and thrust; 2. Creating the aerodynamic database that is useful for setting correctly the control strategy; 3. Comparing the results with those obtained by simulating the multibody model in the numerical environment.

The model was put in the test chamber on a 6 DOFs balance, used to acquire the thrust force. The balance was installed on a turntable that allows for a precise orientation of the rotor in the airflow direction. A laser system was used to align correctly the nose to the middle position of the flow inlet section.

The camber was equipped with distributed pressure probes and temperature sensors, and a pitot tube was installed in a position ahead of the model. While the thrust measurement was provided by the balance, strain gauges on the shaft were used to acquire the torque. The torque and thrust were evaluated in several static wind conditions, by combining different wind speeds, rotor speeds and pitch angles, with the goal of characterizing the C_F-λ-β and C_P-λ-β curves in the following way:

$$C_F = \frac{F}{\frac{1}{2}\rho\pi(R\,\cos\gamma)^2(V\,\cos\theta)^2}$$

$$C_P = \frac{T}{\frac{1}{2}\rho\pi(R\,\cos\gamma)^2(V\,\cos\theta)^3}$$

where T is the torque moment measured at the shaft, F the thrust force, λ is the tip speed ratio, ρ the density chamber, V the wind speed of the undisturbed flow, two Diameters in front of the turbine, R the radius of the rotor, γ is the cone angle of the rotor, while θ is the up-tilt.

In order to set-up the test matrix, i.e. to choose the wind speeds, the pitch angles and the TSRs for testing, the *Cp-Lambda* multibody simulation environment was used. This tool, previously used to perform the eigenvalues analysis and to compute the loads for the correct sizing of the sub-components of the scaled tower-nacelle system, for the hub, etc., is based on finite-element multibody formulation (see [10] and references therein). The aeodynamic model consists in the classical BEM method with corrections that account for unsteady phenomena. More details on formulation and implementation can be found in [15].

The experiment was first performed in the multibody environment, in order to understand the most significant λ-β points to be tested, so as to capture the maximum power coefficient, i.e. to find which is the power production capability of the model. Then a testing grid was determined for the wind tunnel tests. The results in terms of thrust and power coefficient are shown in Figure 18, with thick solid lines, both corrected from non-negligible blockage effects ($\pi R^2/A_{chamber}$=0.189) with the disk actuator method presented in [9]. The maximum power coefficient is approximately 0.39, reached with tip speed ratio around 7.5 and blade pitch around -5°. The curves trend is in accordance with those of the multibody simulations, whose results are reported in the same graphs in dot-dashed lines, with a mismatch that becomes quite important at higher tip speed ratios values and low pitch angles. This mismatch is caused by the differences between the effective structural properties and those from the design (implemented in the multibody model), results in an increased torsion angle (as also shown in Figure 13-14, where the higher tendency to twist is visible for the beam-like model) and therefore the local incidence of the blade airfoils. For

this reason, a complete identification of the blade structure would be helpful in order to have better matching between simulations and experiments.

The power coefficient is compared with that from a rigid rotor (RGD), i.e. without BTC, and with the same diameter and blade shape, whose results are reported in Figure 17. This rotor, equipped with low-flexible (without BTC) blades in carbon fibers, showed a maximum power coefficient of about 0.4, reached with a tip speed ratio around 7.5, and with a pitch angle around -1.7°. The comparison highlights what was expected: the BTC does not affect the power production capabilities, and the maximum performance is obtained at lower pitch angles, since the twist-to-feather reduces the local incidence of the blade airfoils.
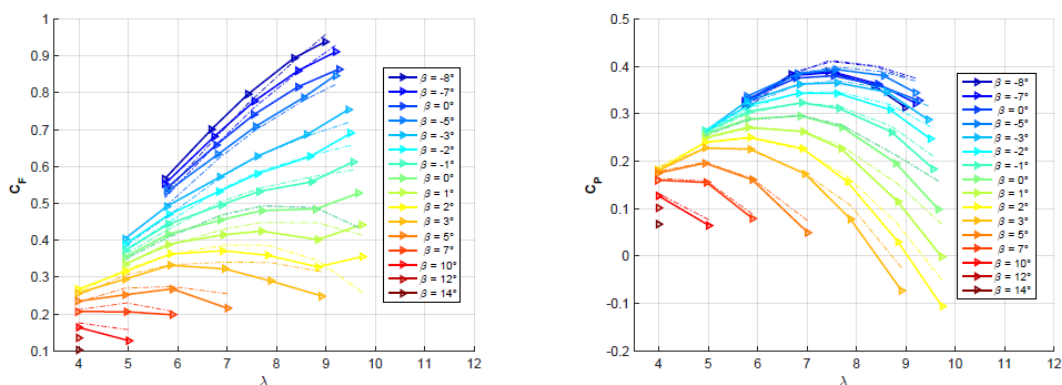
Figure 17 Aerodynamic characterization of the rotor with bend-twist coupling. Experimental with solid line vs. numerical with dot-dashed line.
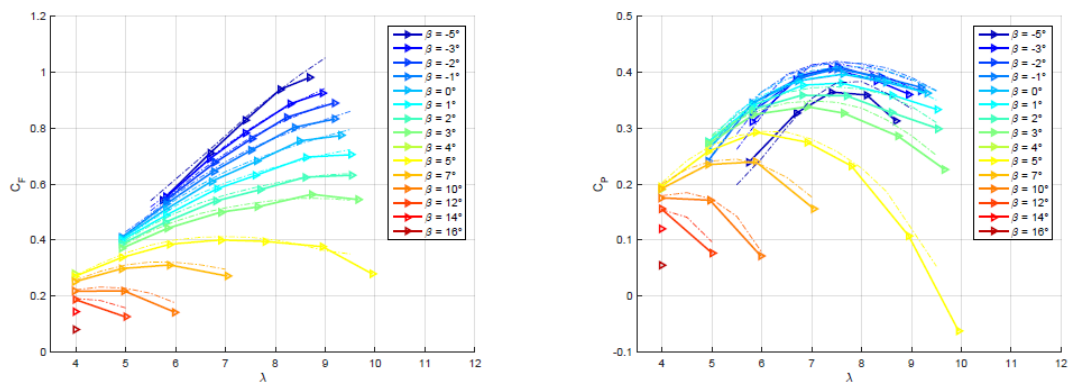
Figure 18 Aerodynamic characterization of the rigid rotor without bend-twist coupling. Experimental with solid line vs. numerical with dot-dashed line.

2.3.4 Loads characterization

A second test campaign was performed in the boundary layer section of the PoliMI's wind tunnel. The goal of these tests were to characterize the model in terms of fatigue loads, in order to assess the capability of the BTC. For this scope, realistic 'scaled' environment conditions are generated. First, the use of a partialized wind tunnel engines power allows to reproduce a scaled atmospheric boundary layer; second, the use of the vortex generators at the inlet allowed the introduction of a turbulence level between 5% and 8%, as requested by the international standards on the HAWT.
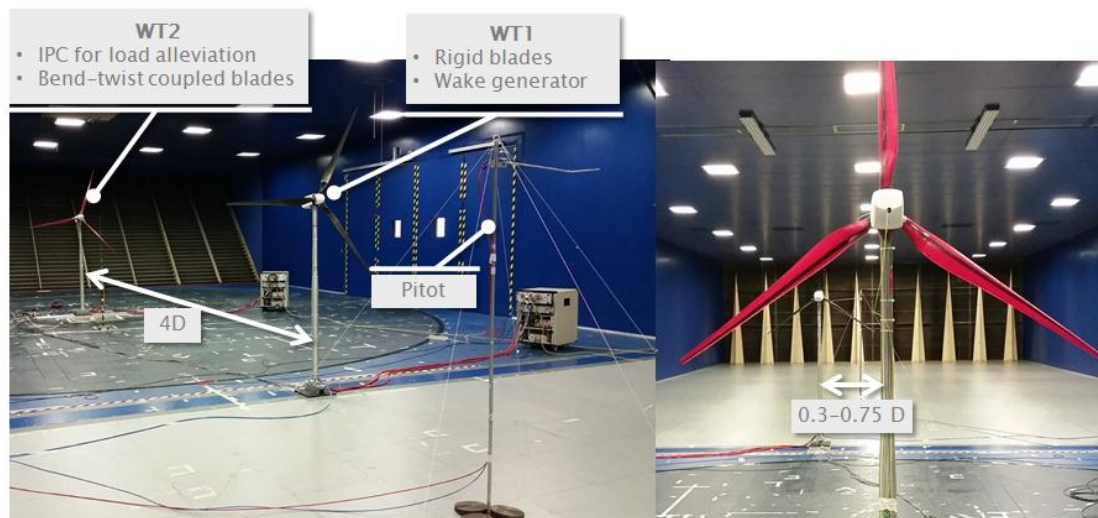
Figure 19 Partial wake tests configuration: RGD in front, BTC model in downwind position

Figure 19, shows the general arrangement of the tests. The scaled wind turbine with BTC is mounted on the 6-DOFs balance, fixed at the floor of the camber. By the use of the laser system, an accurate alignment with the wind flow is guaranteed. In front of the model, approximately half diameter ahead, a pitot tube was installed at the height of the hub, in order to measure the wind speed. The cabinet providing the hardware equipment for the control system was also put in the test chamber far enough to not aerodynamically interface with the tests. A model with RGD blades was put in test camber ahead at a distance of four diameters, with the scope of generate wake conditions.

The 6-DOFs balance was used to acquire the thrust, the bending moment and the yawing moment at the tower root. The strain gauges at the shaft provided the torque and the bending moment measurements, while the FBG sensors measured the loads of one blade at approximately one third of the span.

The experiment consisted in several tests at different wind speeds and partial wake conditions, with the goal of exploiting the loads in some relevant points of the operative envelope.

The wind turbine models were set in power production mode: from the knowledge of the rotor aerodynamics it was possible to set-up the controller. A look-up table is used for controlling the generator torque in region II, whose values are scheduled in function of the rotor speed, following the feed-forward low: $T = k_{opt}\Omega^2$, where the constant $k_{opt} = \frac{1}{2}\rho\pi R^5 C_{Pmax}/\lambda^3_{C_{Pmax}}$ is imposed using the data of the rotor aerodynamics. In order to allow a smooth transition between region II and region III, where the torque reached the rated value, a rotor speed PI controller with anti-wind-up scheme within upper and lower bounds is implemented.

In a similar manner was managed the collective blade pitch control. In region II the value of the pitch is set to that allowing the maximum power coefficient C_{Pmax}, therefore assuring the maximum aerodynamic performances. In region III the pitch motion is governed by the rotor speed throw a PI controller with anti-wind-up scheme, permitting to reject the excessive wind power. The maximum value is set to the value $\bar{\beta}$ corresponding to the flag position, in order to allow the recovery procedure from an emergency shutdown. Table 8 reports the values used for the control system. The rated values are scaled from the NREL 5 MW wind turbine model.

Table 8 Models controller settings.

Model:	RGD	BTC
Rated wind speed	5.4	5.4
Rated rotor speed	380	380
Rated power	124.9	124.9
Rated torque	3.14	3.14
Torque Look-Up k_{opt} [Nm/(rad/s)^2]	1.45x10^{-3}	1.45x10^{-3}
Min. pitch β_{CpMax} [deg]	-1.7	-5
Max. pitch $\bar{\beta}$ [deg]	90	90

The downwind model was tested in several no-wake/partial-wake conditions. For the no-wake (NW) cases the upwind turbine was kept turned off and the rotor was invested by the turbulent wind generated with the spires. Two wind speeds were used, 5 m/s and 6.5 m/s, corresponding respectively to region II and region III scenarios. For the partial-wake (PW) cases the downwind model was placed in four different positions away from the wake axis: By referring to Figure 19, 0.30, 0.45, 0.60 and 0.75 diameters.

All the cases were tested twice, by then including the active individual pitch controller (IPC). In this way it was also possible to verify the synergic effect of the integrated passive (BTC) / active (IPC) load reduction systems.

For a comprehensive comparison and a complete load characterization, combined NW/PW tests were also re-conducted by placing another RGD model in the downwind position, so as to have a reference baseline.

Each test was run for 60 seconds. Figure 20 shows the mean power produced by the downwind models in the test cases selected for the comparison. Blue bars represent the RGD model, the red bars refer to the BTC, while the yellow bars are related to the hybrid model BTC+IPC. In these test cases the mean power mismatch remains under 1%.
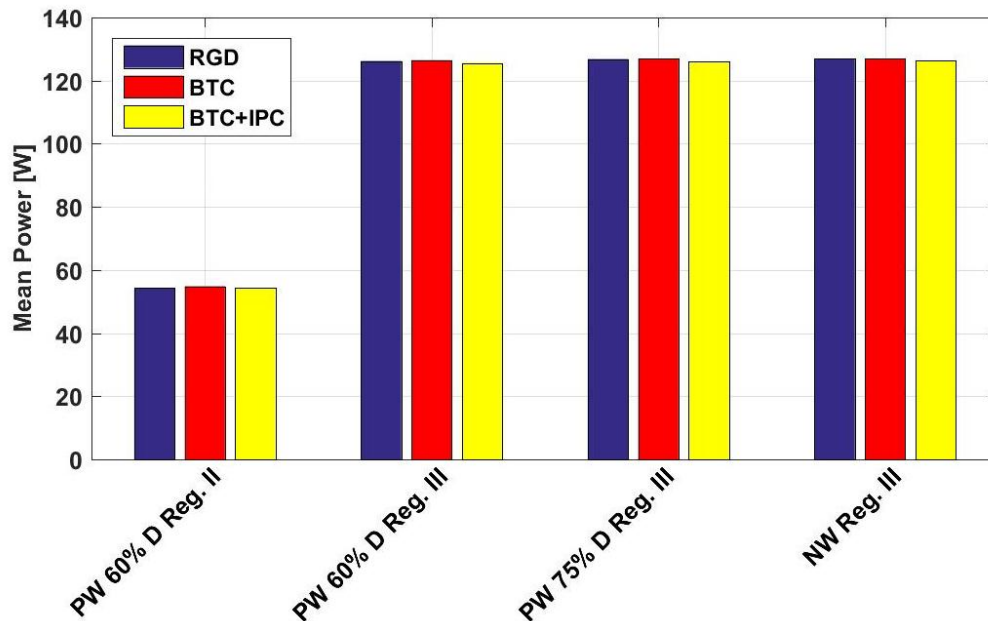

Figure 20 Mean power produced by the downwind model.

Fatigue loads

The BTC acts mainly on the fatigue loads. A comparison between the RGD and BTC models is first carried out, then the hybrid BTC+IPC is also considered. The data related to the hub come from the strain gauges at the shaft, while the tower loads are acquired through the balance. The BTC blade loads coming from the FBG sensors are next analyzed by a comparison with the hybrid model. All the loads signals are pre-processed with a low-pass Butterworth filter of the 8-th order at a cut-out frequency of 50 Hz, which is sufficient high to guarantee the spectra analysis for up to the 8xRev.
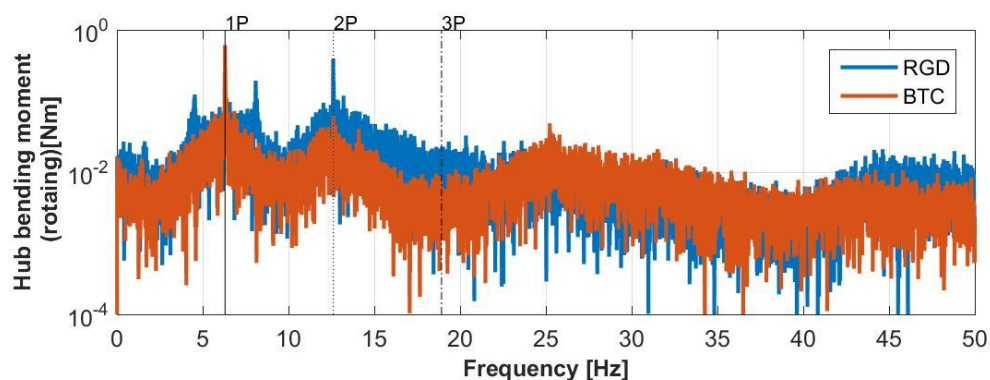
Figure 21 NW Reg. III test. Bending moment components on the shaft (rotating). Frequency response.

Figure 21-22-23 refer to the NW test case. Figure 21 represents the frequency response of the shaft bending moment in the direction of the computed highest Damage Equivalent Load (DEL). Here, many characteristics of the models are highlighted. Looking at the RGD, marked with blue line, the 1st and 2nd xRev frequencies are clearly visible. The others emerging peaks are in correspondence of the spurious tower frequencies: ω_T, $\omega_T \pm \Omega_R$, $\omega_T \pm 2\Omega_R$, $\omega_T \pm 3\Omega_R$, where the tower frequency ω_T in side-side direction is 7.8 Hz. In fore-aft direction the resonant frequency is slightly higher (around 8.6 Hz), but is highly damped, and therefore the associated peaks do not emerge. Looking at BTC model, marked with red line, most of the peaks associated to the tower resonant frequency are not visible, therefore the BTC acts as a damper for them. It is also possible to observe that the bending moment is mitigated over the bandwidth up to the first blades flapping mode frequency (around 23 Hz, higher with respect to the bench tests, because of the centrifugal stiffening). This feature is quite understandable, because since the twist to feather characteristic is related to the flapping, its effectiveness is guaranteed within the bandwidth limited to the modal frequency. At the 1xRev the peak related to the BTC seems higher. This because the rotor weight with its arm with respect to the strain gauges' position generates a bending moment at this frequency. It was verified that by removing this load source from the measures of both the RGD and the BTC models, the 1xRev peak of the latter becomes slower. This is due to the fact that the BTC has the capability of mitigating the aerodynamic load sources. Since at 1xRev the main aerodynamic load is the wind shear and is phased of 180° respecting to the rotor weight, whether the sensing point on the shaft is far enough from the hub, the two load sources are similar in magnitude, and tend to compensate each other. When the wind shear effect is lessened by the BTC, the rotor weight induced moment is not opposed anymore, causing an increment of measured load.

The nodding and yawing moment, i.e. the hub bending moment components in the fixed reference system, are evaluated starting from the strain gauges of the shaft: the signals are first

INNWIND.EU, Deliverable 2.24, Manufactured and laboratory tested scaled blades and parts of the blade

filtered from the mean value, which brought a little of rotor inertial unbalances, therefore rotated by using the transformation of coordinates into the fixed hub reference system. Figure 22 shows the frequency response of the combined hub bending moment, (i.e. in the direction of the highest DEL) in the fixed reference system. The direction of the combined moment is close to the nodding direction for both the models. As expected, the higher peaks are multiples of 3xRev frequencies. Looking at the RGD model, there are some peaks corresponding to the 1xRev and 2xRev frequencies due to some small pitch misalignments and the turbulence instability, and the peaks at the tower resonant Ω_T frequency with related spurious at $\omega_T \pm n\Omega_R$. The BTC seems to damp out some of the peaks and reduce the loads in almost over the spectrum.

Figure 23 reports the combined bending moment measured at the tower base. It should be remarked that for tower base measures a notch filter was applied at 1xRev frequency with the scope of not considering the rotor inertial unbalances on the DEL calculation. In this case the direction of the combined moment between the two models is different. For this reason, the RGD model manifests a higher tower side-side resonant frequency, since the direction is close to the side-side component, while the spectrum of the BTC model shows higher loads component at lower frequencies, being close to the fore aft direction. As shown hereinafter, the resulting fatigue load appears to be lower in the cases with BTC.
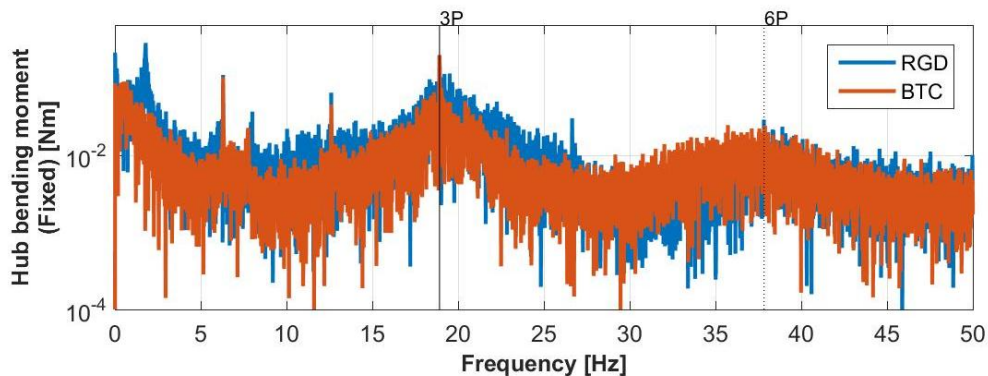
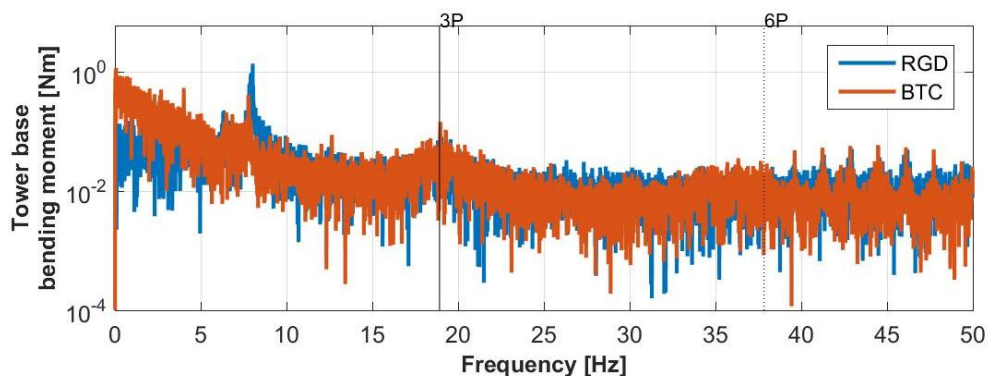Figure 22 NW Reg. III test. Combined bending moment on the shaft (fixed). Frequency response.

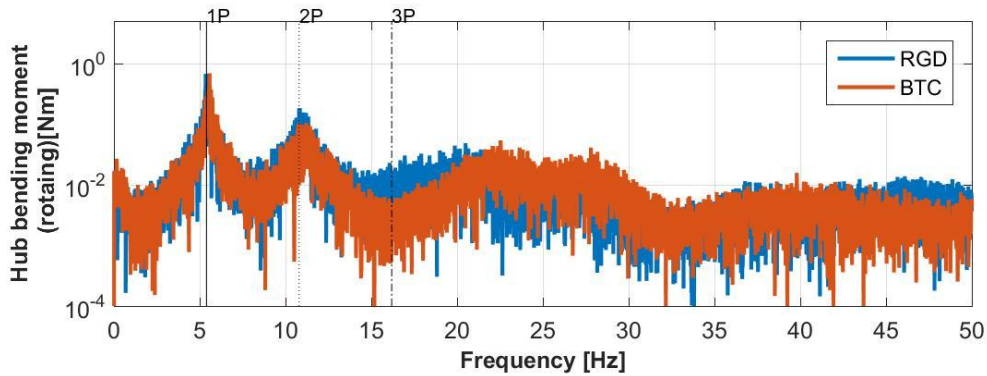Figure 23 NW Reg. III test. Combined bending moment at the tower base. Frequency response.

INNWIND.EU, Deliverable 2.24, Manufactured and laboratory tested scaled blades and parts of the blade

Figure 24 PW 0.60 D Reg. II test. Shaft bending moment. Frequency response.

Figure 24 reports the spectrum of the combined shaft bending moment for the PW 0.60 D Reg. II test. Here the load attenuation capability of the BTC seems to be lessened at low frequencies, i.e. behind the 2xRev frequency, but still remains important at higher frequencies (up to 23 Hz, where the blades first flapping frequency is placed).
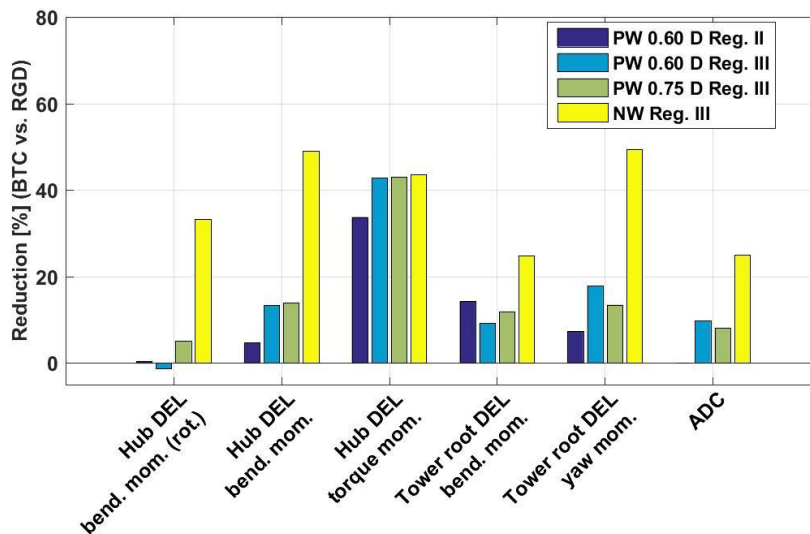

Figure 25 NW/PW tests. DEL results.

Figure 25 reports the amount of Damage Equivalent Load (DEL) and Actuator Duty Cycle (ADC) reduction in all the test configurations considered. The DEL is calculated by applying the *Rainflow* counting algorithm. For the bending moment DEL (at the hub and tower root) the measures are first projected in different directions over the section. Then, per each direction the DEL is calculated and then the higher is selected, i.e. the DEL in the most critical direction. The results related to the NW tests show important reductions (between 20% and 50%) for all the loads considered, which translates in an increased life-time of the components, and a significant saving of ADC, denoting a good synergy with the collective pitch system. The results related to the PW tests confirm that the BTC effectiveness is here lessened. PW 0.60 D Reg. II shows practically no reduction on the rotating shaft bending moment DEL, since the low frequencies loads component, i.e. those with the higher load energy, are not touched by the BTC, which seems to be still effective

INNWIND.EU, Deliverable 2.24, Manufactured and laboratory tested scaled blades and parts of the blade

in reducing the moments in the fixed reference system of around 5-15%. PW 0.60 D Reg. III and PW 0.75 D Reg. III show similar results: in the case of PW 0.60 D Reg. III the rotating shaft bending moment is slightly increased, due to the higher 1xRev peak, while for the bending moments in the fixed reference system a reduction of around 10-20% is observed.

In all the cases there is an important reduction on the shaft torque, which may also be translated in an improved power quality.

As shown previously, the BTC has an intrinsic fatigue load reduction capability up to the blade first flapping mode frequency. The twist to fear of the blade due to the flapping deformations reduces the effective angle of attack of the airfoils and therefore the excess aerodynamic load. It appears that in some components, mitigating the aerodynamics may not be beneficial in terms of the overall load. Indeed, it was readily demonstrated that in some cases the inertial loads, e. g. the rotor weight, are also important and work in contrast to the aerodynamic ones, causing drawbacks. As the BTC does not have the ability of rejecting the overall load, but the aerodynamic only, a possible improvement of the load reduction capability is done by integrating with the IPC active system, which is capable of sensing and rejecting the overall load sources.

The IPC implemented here has the primary goal of cutting out the 1xRev load on the shaft. The implementation, whose details can be found in [20], follows the method presented in [13]. The feedback here is taken from the shaft bending moment components, that are first rotated in the fixed reference system and then filtered out from peaks over 0.5 Hz. For its intrinsic working principle of cutting out the 1xRev, the active IPC system should show a good synergy with the BTC.
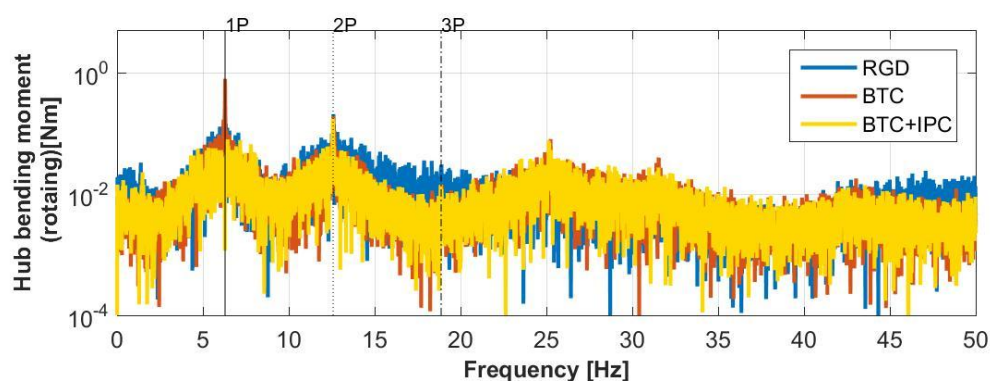

Figure 26 PW 0.60 D Reg. III test with the hybrid BTC+IPC model. Shaft bending moment. Frequency response.

In Figure 26 the frequency response of the shaft bending moment at PW 0.60 D Reg. III case is proposed with the hybrid BTC+IPC model. It is possible to see how the load spectrum is almost overlapped to the BTC-only model, except at 1xRev, where the peak is canceled out. The synergic effect of the BTC with the IPC is then clearly visible here. The 1xRev is the frequency where act the most energetic load sources, therefore the effect on the fatigue is relevant. The synergy determines a consistent DEL reduction in the shaft bending moment, as shown in Figure 27, with also some little improvements on the other components, at the expenses of the increased ADC.
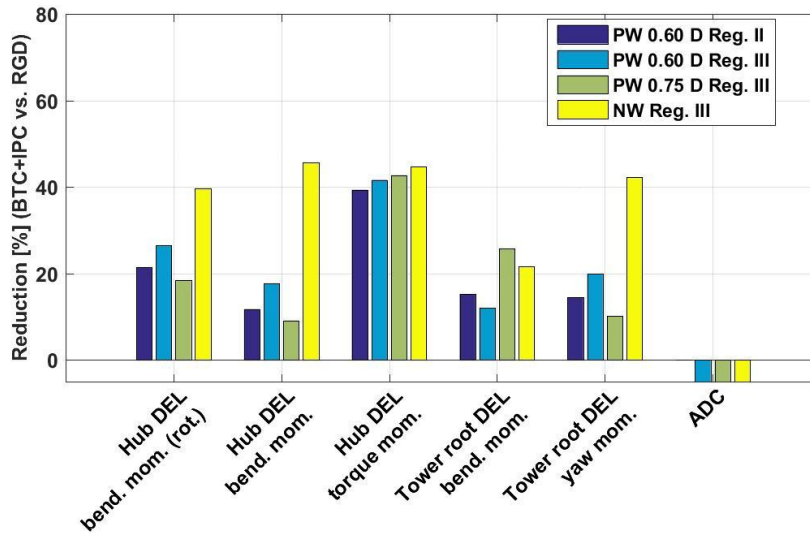
Figure 27 NW/PW tests with IPC. DEL results.

Figure 28 shows the blade bending moment measured with the FBG sensors for the hybrid BTC+IPC and the BTC-only model. Here the multiples of the 1xRev are clearly visible up to the 8th, with also the first flapping frequency that is located at about 23 Hz. The spectra are quite close and the hybrid model seems to slightly mitigate in the overall.
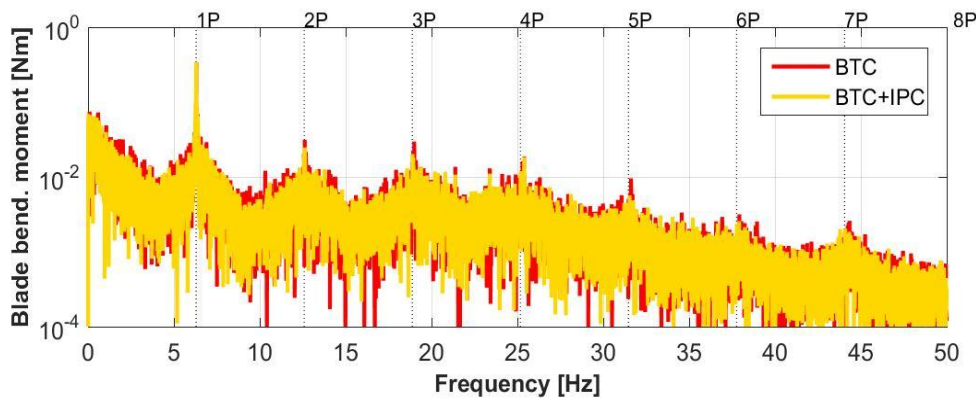

Figure 28 PW 0.60 D Reg. III test with the BTC and hybrid BTC+IPC model. Blade bending moment. Frequency response.

The 1xRev is instead increased: since the IPC system works with the goal of cutting out the 1xRev load at the shaft, a possible way to do it would be to overload the blade so as to mitigate the inertial load by increasing the aerodynamics. This way of working may impact on the blades lifecycle, since the fatigue loads may be increased, as shown here by Figure 29, where in three test configurations shows an increased DEL.
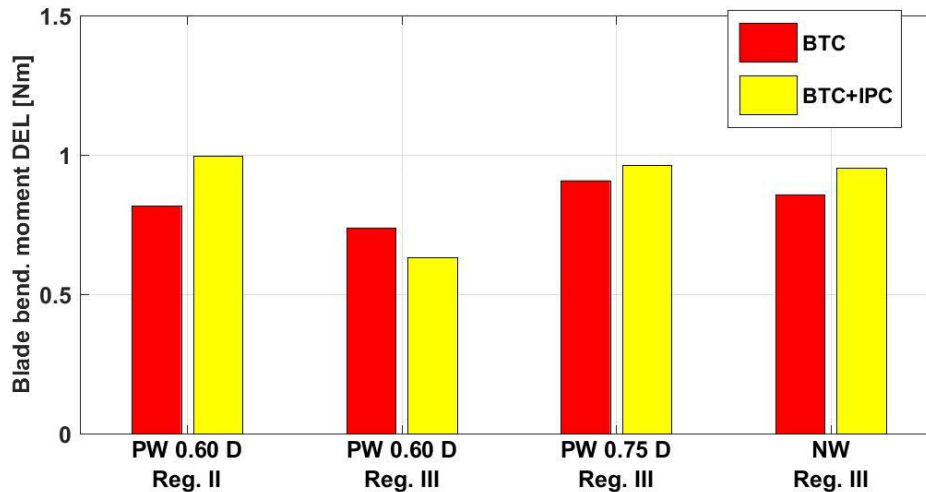
Figure 29 Blade bending moment DEL for BTC and the hybrid BTC+IPC model.

Possible ways to mitigate this phenomenon are: 1) using the blade loads as feedback for the IPC, instead of the shaft bending moments. This would require the installation of strain gauges at the three blades root, that were not available for these tests. 2) Even when the shaft bending moments are used, tuning the IPC finely by looking also at the blade loads.

It should be remarked that the cost of using the IPC is an increasing of the ADC. Since the BTC-only helps to reduce the ADC, as shown in Figure 26, a possible better synergy could be reached by tuning the IPC so as to fill this ADC margin done by the BTC. For this reason, further experimental investigations are strongly recommended.

2.4 Modal and static testing of blade at DTU

2.4.1 Experimental modal analysis

Experimental modal analysis of one of the PoliMI blades was done at DTU using a Polytec PSV 500 Scanning Laser Vibrometer. A laser Doppler vibrometer (LDV) is a scientific instrument that is used to make non-contact vibration measurements of a surface. The laser beam from the LDV is directed at the surface of interest, and the vibration amplitude and frequency are extracted from the Doppler shift of the reflected laser beam frequency due to the motion of the surface [1].

The blade was mounted on the special root connection L-shaped plate provided by PoliMI, which again was mounted on a block and a plate provided by DTU. Two concrete slabs were used to make boundary conditions very stable so only the blade will experience vibrations. See Figure 30.
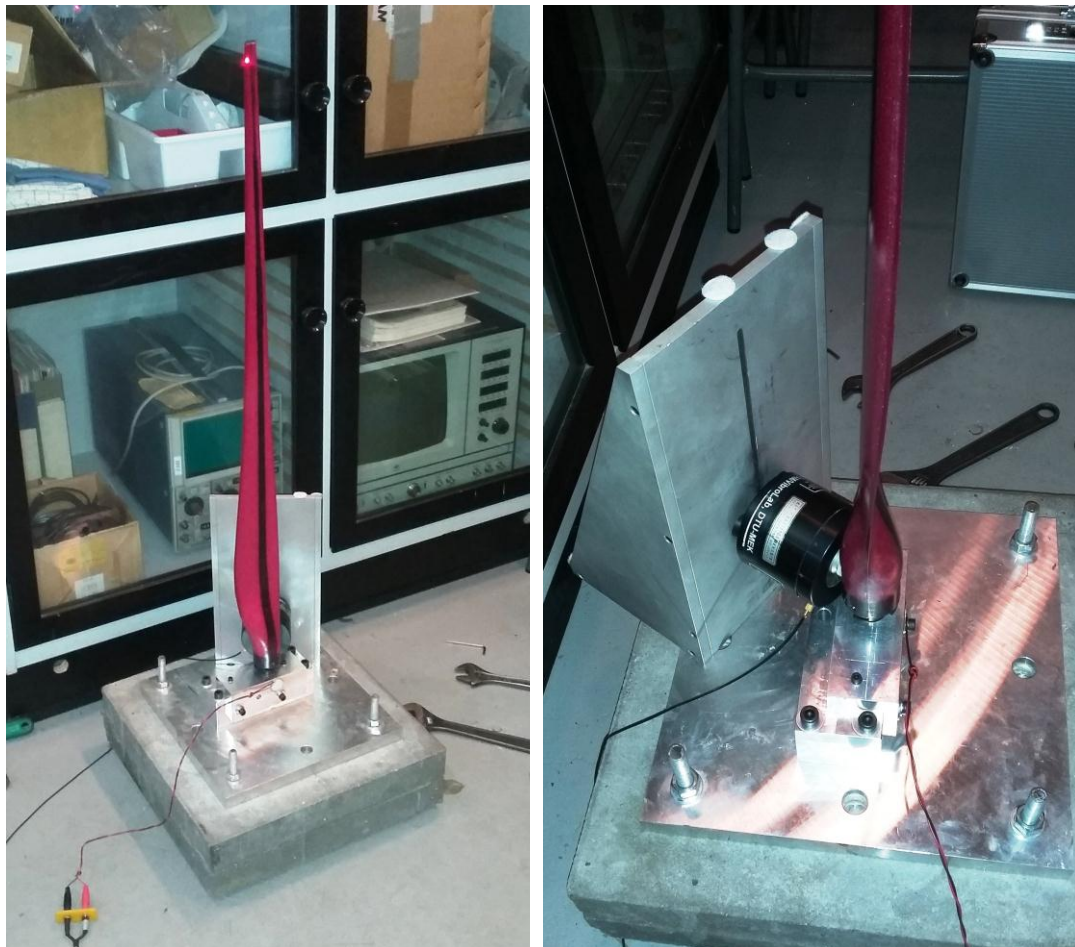
Figure 30 Blade test setup with piezoelectric actuator in front of root connection block and shaker on the back of the root.

The blade was excited with white noise by placing a piezoelectric actuator on the root connection block, but this setup was found not to provide enough energy the blade in order to make reliable measurements. In order to provide enough energy the blade was excited with white noise by placing a shaker on the blade root.

In order to measure the Eigen frequencies and Eigen modes of the blade the laser Doppler vibrometer was scanning the blade and measuring vibration amplitudes and frequencies at a number of grid points along the blade. Two methods were used. One method (grid) where the grid points where placed in a grid over one side of the entire blade. And another method (lines) where the grid points where placed in two lines on one side of the blade. The frequency response plot using the grid method can be seen in Figure 31.

INNWIND.EU, Deliverable 2.24, Manufactured and laboratory tested scaled blades and parts of the blade
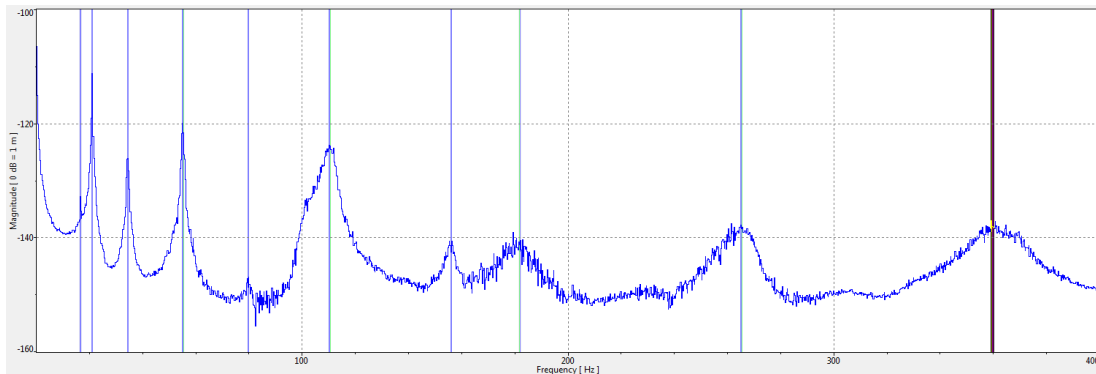
Figure 31 Frequency response plot from laser Doppler vibrometer measurements using the grid method.

The laser Doppler vibrometer generally measure the amplitudes and frequencies at the grid point perpendicular to the surface and it is therefore difficult with the performed setup to measure edgewise vibrations. In Table 9 is shown the measured Eigen frequencies using the grid and lines methods. By looking at video of the grid point motions the modes corresponding to the Eigen frequencies can be determined as listed in Table 9. As it is difficult to measure edgewise vibrations with the performed setup the first edgewise mode can only be seen as it couple with flapwise motion. Some of the higher frequency modes cannot be determined due to the missing edgewise component.

Table 9 Measured natural frequencies using the grid and lines methods.

Mode	Freq. [Hz], lines	Freq. [Hz], grid
1st Flapwise	20.75	21.00
1st Edgewise	34.25	34.50
2nd Flapwise	55.00	55.00
?	78.25	79.75
3rd Flapwise	110.75	110.25
1st Torsional		156.00
4th Flapwise	183.00	182.25
?	267.50	265.00
?	364.00	359.25

The 1st flapwise mode is shown in Figure 32 using the grid method and in Figure 33 using the lines method. Figure 34 shows the 1st edgewise mode using the grid method. Figure 35 shows the 2nd flapwise mode and Figure 36 the 1st torsional mode.
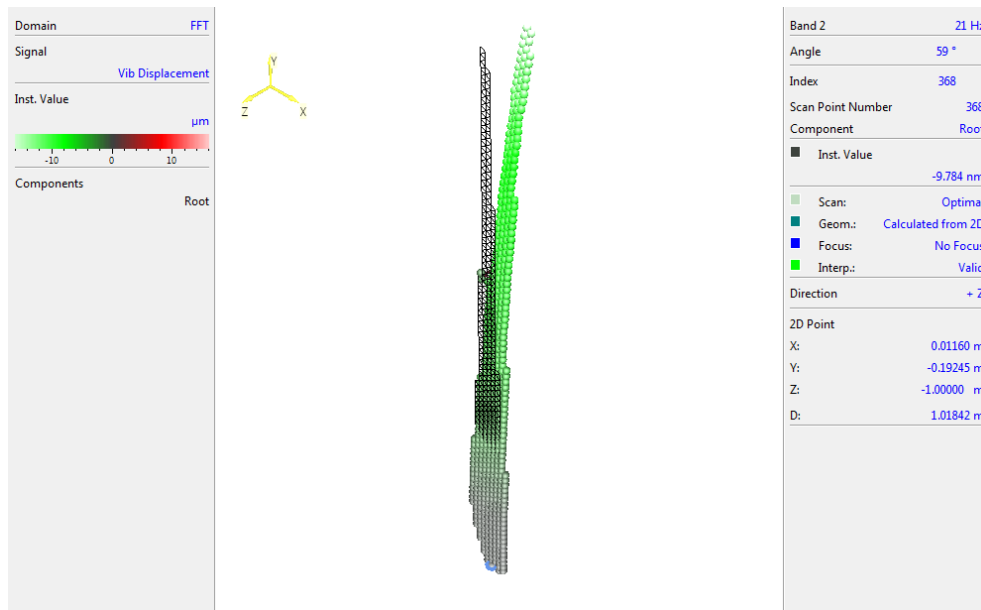
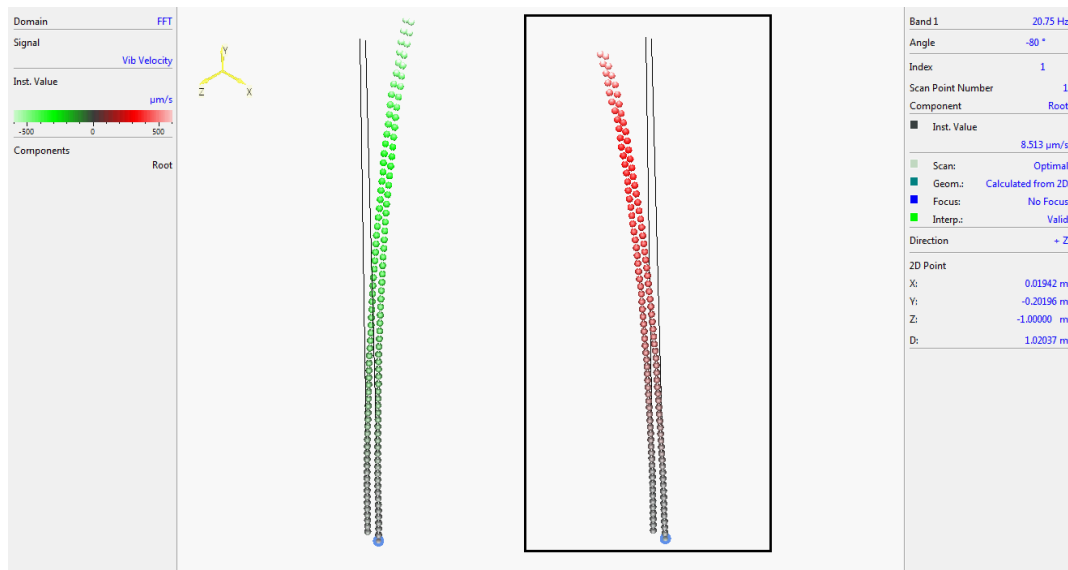**Figure 32** Plot of 1st flapwise mode using the grid method.

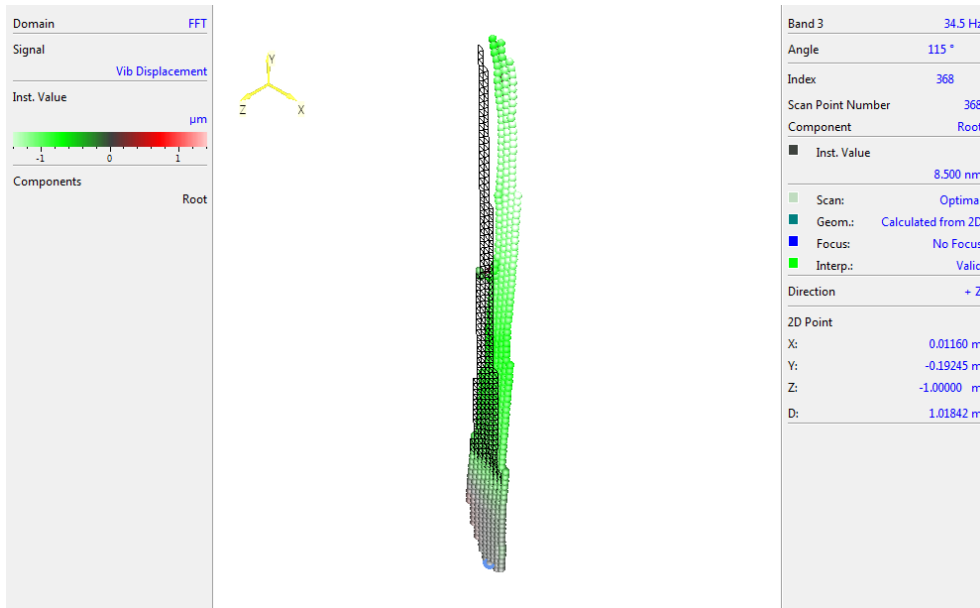**Figure 33** Plot of 1st flapwise mode using the lines method.

Figure 34 Plot of 1st edgewise mode using the grid method. Note that the edgewise mode couple with flapwise motion.
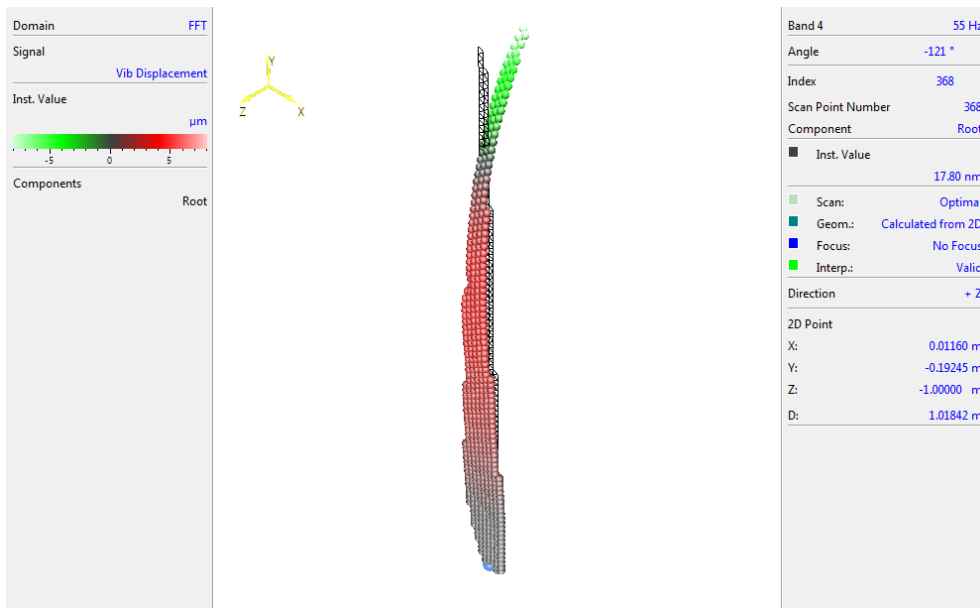

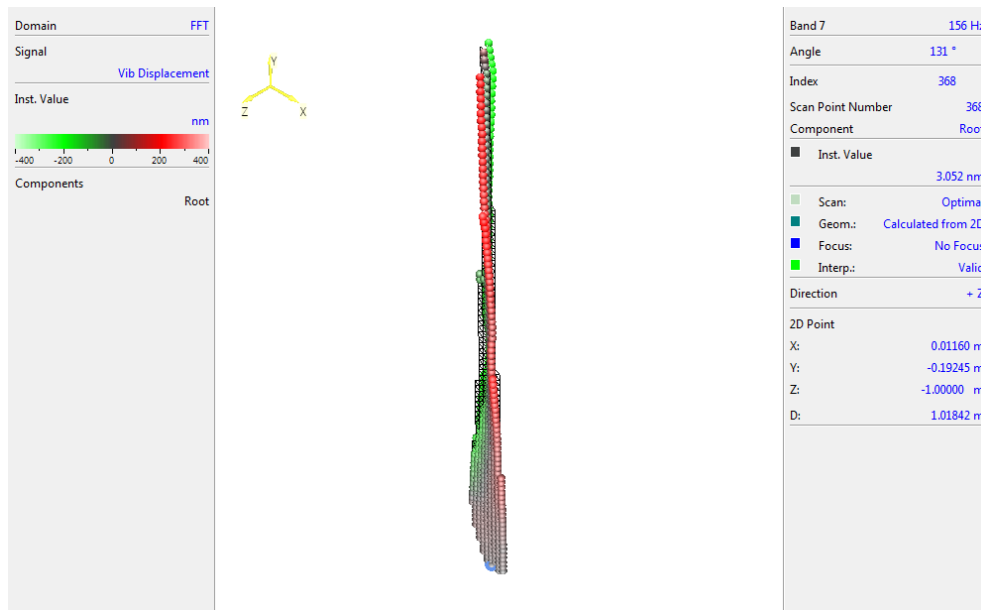**Figure 35** Plot of 2nd flapwise mode using the grid method.

Figure 36 Plot of 1st torsional mode using the grid method.

2.4.2 Static tests

2.4.2.1 Test setup

Static tests on one of the PoliMI blades were done at DTU. The blade was mounted on the special root connection L-shaped plate provided by PoliMI, which again was mounted on a block and a plate provided by DTU. The whole setup is then bolted to a large steel plate in the lab to obtain an almost perfectly rigid constraint. See Figure 39.

Loading of the blade was done using a specially designed system of two clamps and a frame. Due to low magnitude of the applied loads the clamps were printed with PLA material using a 3D printer available at DTU. As the coupled response of the blade was of a primary interest, the system of clamps is aimed at accurate application of bending moment and twisting to the blade.

The two clamps are designed to fit the shape of the blade and to be mounted at the following positions: 714 mm from the blade root – so-called "root clamp", and 845 mm – so-called "tip clamp". Hereby, the distance of 131 mm between the clamps allows of bending moment application to 714 mm long part of the blade by applying two opposite shear forces to the root and tip clamps accordingly. The clamp design allowed for using them for torque and single shear force application as well. The clamps are depicted in Figure 37.
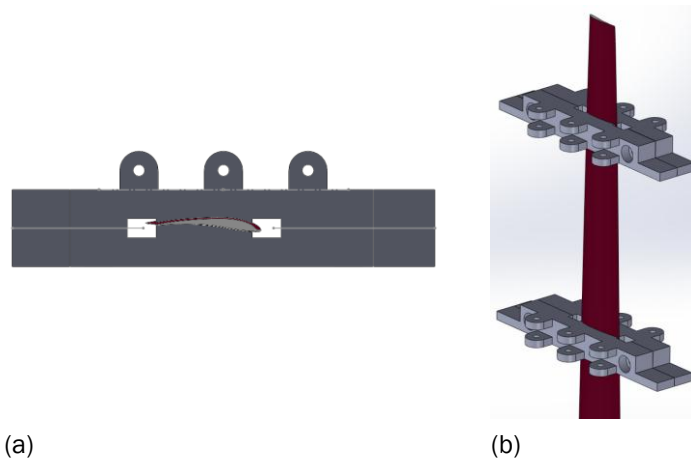
(a)	(b)

Figure 37 3D model of load clamps. (a) - Clamp top view. (b) - Clamp positions on the blade.

A special load frame was developed in addition to the clamps to implement a special way of bending moment application. In this configuration the frame is used to move the point of load application at the clamp and create a pushing force in contrast to pulling force that is commonly used. This configuration with one clamp with pulling and one clamp with pushing force allows alignment of the points of the two shear forces which prevents unwanted torque generated by this couple of forces when blade starts to twist. The load configuration with two clamps and a frame is shown in Figure 38.
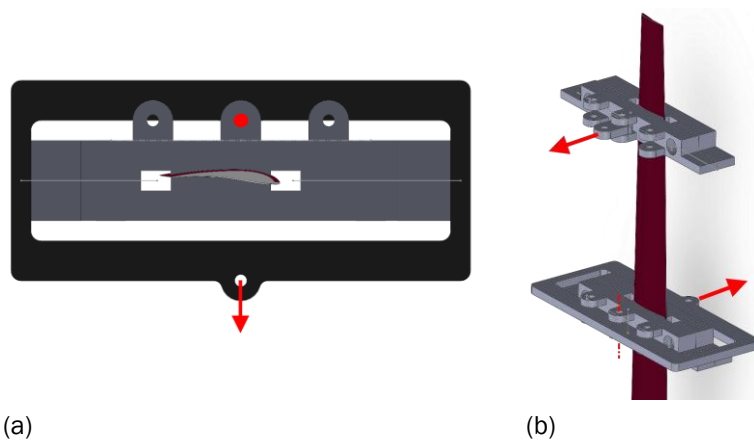

(a)	(b)

Figure 38 (a) - Load frame transferring the load application point from pressure side to suction side. (b) – Bending load case with load frame.

Loading is made through a thin carbon wire (Fire line) connected to the loading clamps by a small hook. The carbon wire runs through a low friction pulley connected to a steel bar on the wall in the lab and dead weights are applied to the end of the carbon wire. This setup was made at two opposite walls in the lab with the blade mounted in the centre between these walls. Since the distance between the wall and the blade is approximately 50 times bigger that the size of the loading clamps, then the loading direction can be assumed to be the same independent of where the carbon wire is hooked to the loading clamps. This assumption is even more true for the blade deflections as they are much smaller than the size of the loading clamps.

Deflections of the blade are measured by a Digital Image Correlation (DIC) system. An ARAMIS 3D 12M system from GOM mbH is used in this test campaign. The DIC system records the surface of an object throughout the entire load history using two CCD cameras. The digital images are then

INNWIND.EU, Deliverable 2.24, Manufactured and laboratory tested scaled blades and parts of the blade

used to measure the full-field 3D displacements of the object by digital image processing. An example is shown in Figure 40. As an aid for the digital image processing, a speckle pattern (black spray paint on a white background) was applied to the surface of the object. As we should not paint the blade in this case, the speckle pattern was applied to thin tape which then was applied to the blade on the pressure side only.
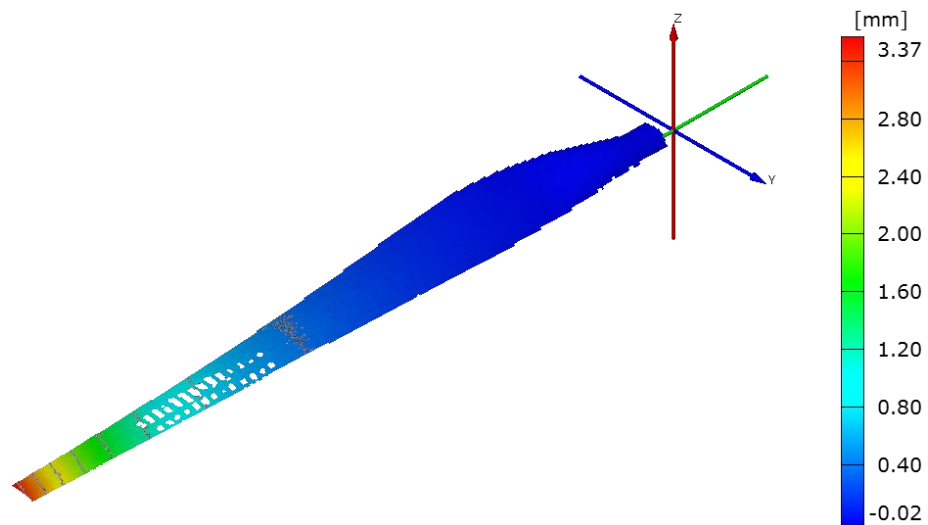

Figure 39 Static blade test setup with DIC camera boom in front.

Figure 40 3D view of DIC measurements on the blade surface. Bending load case.

2.4.2.2 Load cases

In this experimental test campaign 7 different load configurations are utilized to evaluate the structural response of the blade. These load configurations are the following:

- Shear force bending by applying a point load
- Shear force bending and torsion (counterclockwise) by applying a point load with an offset
- Shear force bending and torsion (clockwise)by applying a point load with an offset
- Pure bending towards suction side by applying a force couple
- Pure bending towards suction side by applying a force couple and special loading frames
- Pure torsion (counter clockwise)by applying a force couple around the blade axis
- Pure torsion (clockwise)by applying a force couple around the blade axis

The different load configurations are also shown in Figure 38 and Figure 41. The pure bending and torsion test was reproduced 3 times to ensure reproducibility. The thin tape with the painted speckle pattern was gradually removed during these studies to evaluate if the tape had an influence on the structural response.
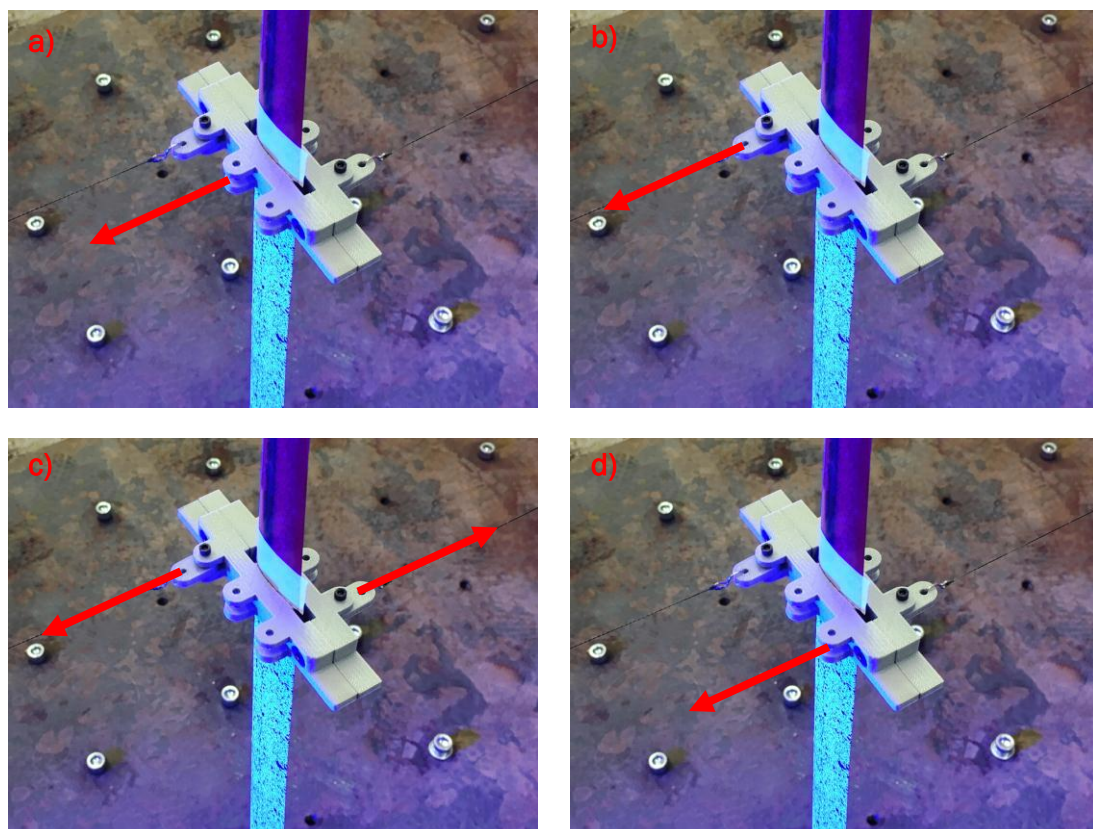

Figure 41 Loading of the blade through the lower clamp only. a) Shear force bending. b) Shear force bending and torsion counterclockwise. c) Pure torsion. d) Shear force bending and torsion clockwise.

2.4.2.3 Results

The objective with this experimental work is to create a comprehensive comparison bases for models of the blade. In the different test a special focus was on the coupling between bending

INNWIND.EU, Deliverable 2.24, Manufactured and laboratory tested scaled blades and parts of the blade

and torsion which is one of the reasons that pure bending and torsion is applied as the main load configurations.

Shear force bending by applying a point load

In this load configuration was a point load of 3.338N applied 0.707m from the root. The load was introduced at the middle of the load clamp, which is as close as possible to the blade pitch axis. Based on the DIC results the y-z-displacements and the twist angle are plotted below.
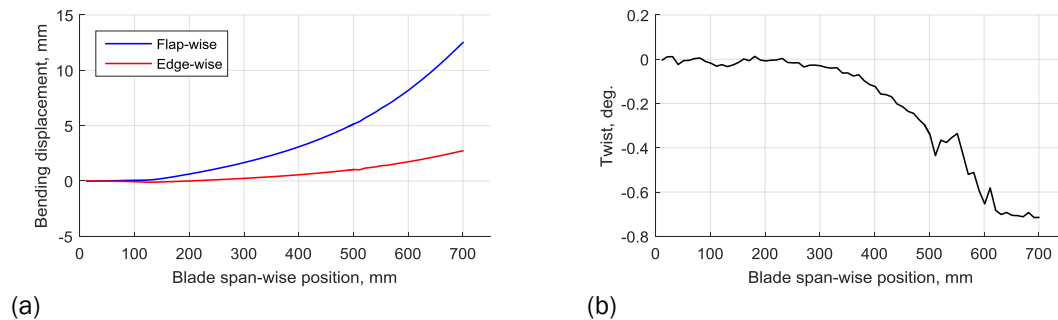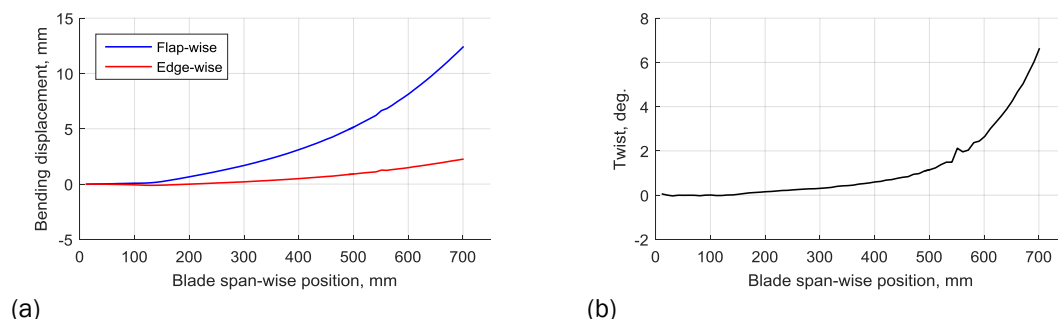

(a)   (b)

Figure 42 Structural response of Shear force bending by applying a point load.

Comments

Based on the displacements response it seems, in the particular loading direction, that the blade is also loaded in the edgewise direction, as the blade deforms approximately 2.5mm in the y-direction (edgewise direction). The result of the twist angle is affect by noise but it can still clearly be seen that the blade twists clockwise. The twist angle is very sensitive to the location of the point load and therefore is the results of the twist angle subjected to significant uncertainties. The sign of the twist angle fits with the results of the pure bending case where the special frames were utilized. Furthermore, also a slightly bigger twist angle is observed in the *clockwise shear force bending and torsion case* than in the *counter clockwise load case,* which also would be expected based on the results of this load case where the twist is clockwise.

Shear force bending and torsion (counter clockwise)

In this load configuration was a point load of 3.338N applied 0.707m from the root. This load was introduced at the outer hole (towards the leading edge) creating a 22 mm offset from the blade pitch axis. This generates a combination of bending and torsion. Based on the DIC results are the y-z-displacements and the twist angle plotted below.
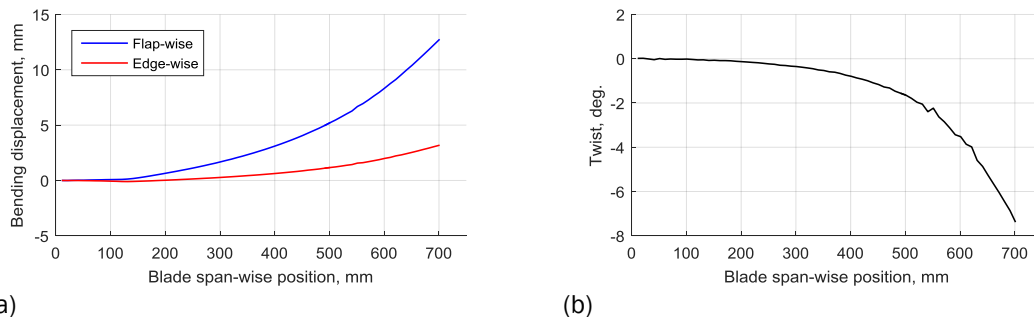

(a)   (b)

Figure 43 Structural response of Shear force bending and torsion (counter clockwise).

Comments

The y-z displacement response of this load configuration is very similar to the *Shear force bending load case.* The blade twist counter clockwise and the twist angle a 700mm from the root is approximately 6.5˚.

Shear force bending and torsion (clockwise)

In this load configuration was a point load of 3.338N applied 0.707m from the root. This load introduced at the outer hole (towards the trailing edge) creating a 22 mm offset from the blade axis. This generates a combination of bending and torsion. Based on the DIC results are the y-z-displacements and the twist angle plotted below.
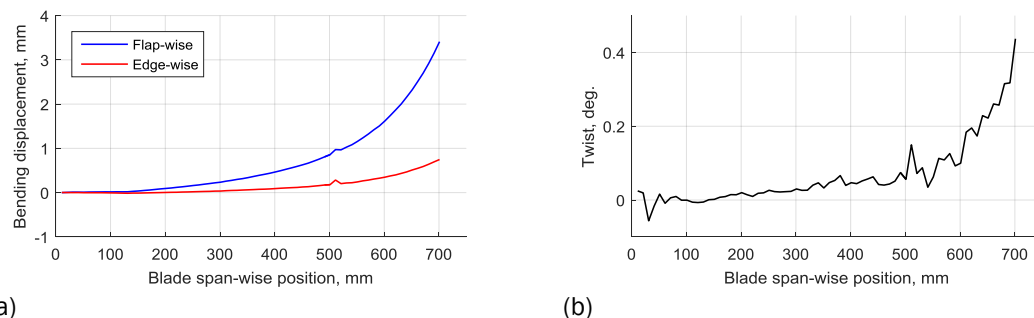

(a)   (b)

Figure 44 Structural response of Shear force bending and torsion (clockwise).

Comments

The y-z displacement response of this load configuration is again very similar to the *Shear force bending load case.* The blade twist counter clockwise and the twist angle is approximately 7.5˚ which is approximately 1˚ larger than the magnitude for the counter clockwise load case. This was also expected as the blade twists approximately 1˚ clockwise in the *Shear force bending* load case were the load is assumed to be introduced at the blade pitch axis.

Pure bending towards suction side by applying a force couple

In this load configuration was a force couple of 2.144N applied with an internal distance of 131 mm. The two loads were introduced at the middle of the two load clamps generating a "pure bending moment" of -0.281 Nm. As the blade twists the loads will in theory move away from blade axis and thereby create a small torsional moment as well. This is assumed to be small compared to the main loading but can have an effect on the twist angle and will therefore be evaluated in these studies. This will be performed by comparing the response of this load configuration with the one where the special load frames are used. Based on the DIC results are the y-z-displacements and the twist angle plotted below.

(a)   (b)

Figure 45 Structural response of the pure bending case.

Comments

The y-z displacement response of this load configuration is similar to the *Pure bending case* were the special frames are used. The twist angle on the other hand is very different and even has opposite sign, as the blade in this load configuration twists counter clockwise while in the pure bending case with the frame twists clockwise. In this setup the results are very sensitive to the location of the loads with respect to the blade axis and furthermore as the blade starts twisting a small torsional moment will be generated as the loads moves away from the blade axis.

Pure bending towards suction side by applying a force couple and special loading frames

In this load configuration was a force couple of 2.144N applied with an internal distance of 131 mm. The two loads were introduced at the blade axis utilizing the special loading frames with is designed to account for cross sectional rotations/twist and still applying only a pure bending moment of -0.281 Nm. Based on the DIC results are the y-z-displacements and the twist angle plotted below.
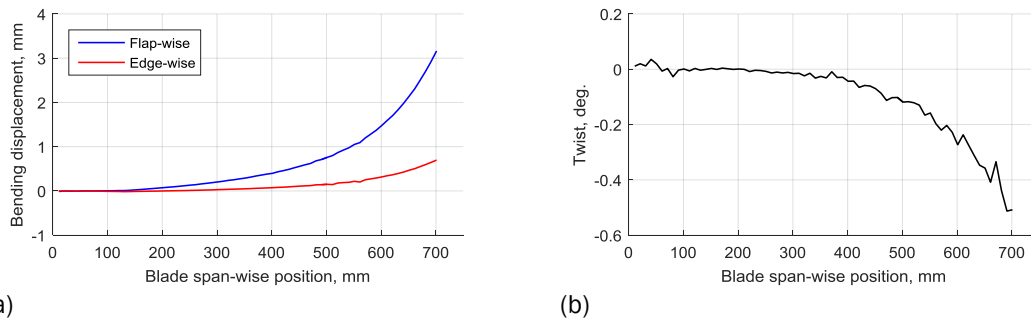

(a)   (b)

Figure 46 Structural response of the pure bending case with special loading frames.

Comments

The y-z displacement response of this load configuration is similar to the previous *pure bending case* without the special loading frames. This setup was designed to limit the effect of the location of the point loads with respect to the blade axis and also to account for cross sectional rotations during loading as stated above. In this load case the blade twist clockwise which is very different from the results of the pure bending without the frames as a counter clockwise response was observed during that test. It is assumed that the results of this load case a much more reliable due to the above-mentioned reasons. This particular load case was performed 3 times and was found to be very reproducible.

Pure torsion (counter clockwise) by applying a force couple around the blade axis

In this load configuration was a force couple of 2.677N applied with an internal distance of 44 mm around the blade axis at 0.707m from the root. These loads were introduced at the two outer holes of the load lower clamp creating a counter clockwise torsional moment of 0.0124 Nm. Based on the DIC results are the y-z-displacements and the twist angle plotted below.
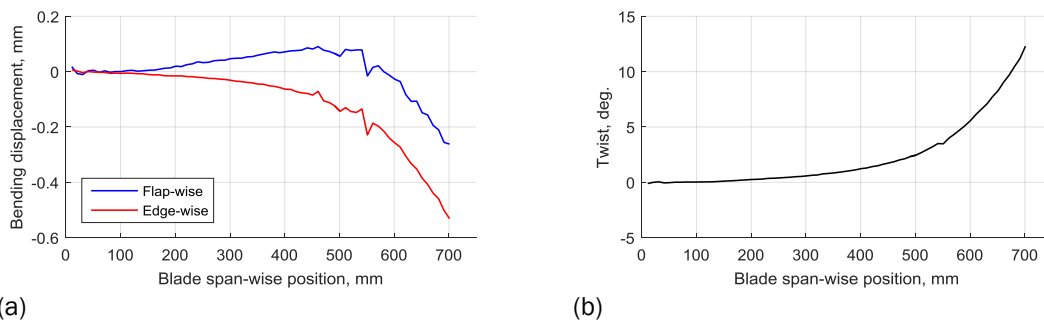

(a)   (b)

Figure 47 Structural response of the pure torsion (counter clockwise).

Comments

The y-z displacement response of this load configuration is subjected to significant uncertainties as displacements depend on where on the cross section they are reported. The flapwise displacements in this load case have the opposite sign compared to the *pure torsion clockwise load case* which also fits with the expected results when the effect of the bend-twist-coupling is taken into consideration.

In this load case the blade twists counter clockwise approximately 12˚. The magnitude of the twist angle fits well with the expected results if superposition of the two *shear force bending and torsion cases* are utilized to compute the twist angel (need to account for different load levels).

Pure torsion (clockwise) by applying a force couple around the blade axis

In this load configuration was a force couple of 2.677N applied with an internal distance of 44 mm around the blade axis at 0.707m from the root. These loads were introduced at the two outer holes of the load lower clamp creating a clockwise torsional moment of 0.0124 Nm. Based on the DIC results are the y-z-displacements and the twist angle plotted below.
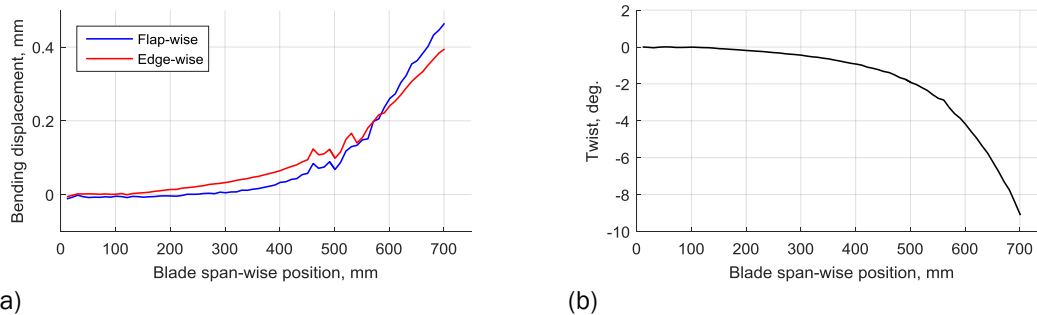

(a)   (b)

Figure 48 Structural response of the pure torsion (clockwise).

Comments

The y-z displacement response of this load configuration is again subjected to significant uncertainties as displacements depend on where on the cross section they are reported.

In this load case the blade twists clockwise approximately 9˚. The magnitude of the twist angle is smaller than expected if it is compared to the *pure torsion counter clockwise load case* and it is also too small if it compared with results from superposition of the two *shear force bending and torsion cases* (need to account for different load levels). It is not clear what causes this deviation between measured results and the expected results, but based on the study where the influence of the painted tape was evaluated it can be seen that the results a consistent.

Evaluation of the structural influence of the thin speckle pattern painted tape

Presented below are the results of studies performed to evaluate is the tape has a measurable effect on the bending or torsional stiffness.
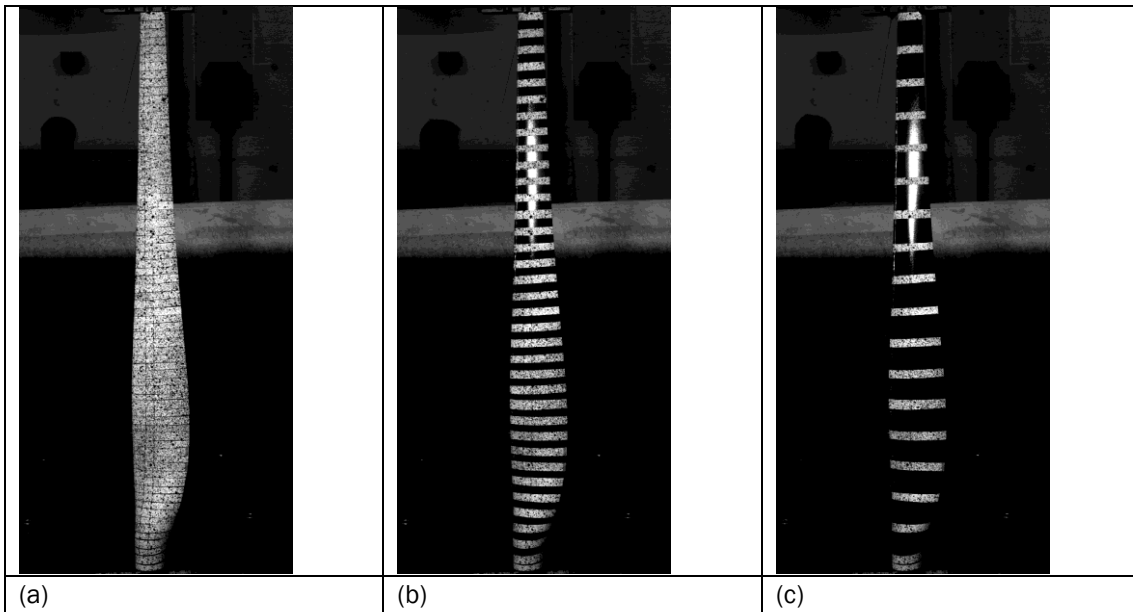
Figure 49 Tape with stochastic pattern on the suction side of the blade. Full - (a), half - (b) and quarter - (c) of the blade surface is covered with tape to investigate effect of blade stiffening due to tape application.
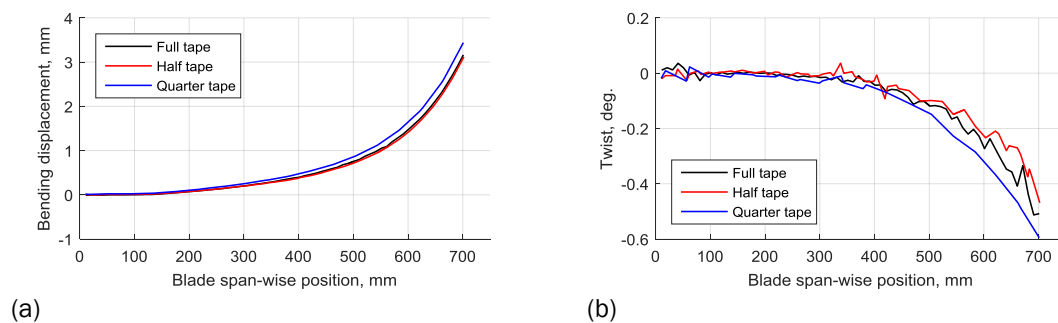

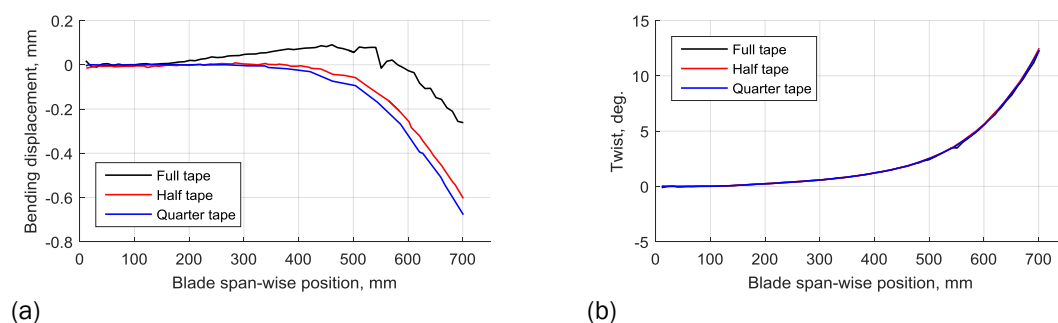**Figure 50** Tape effect in bending load case.

Figure 51 Tape effect in torsion load case.

Comments

Comparing the structural response from the bending load case of the half and full tape it seem that the influence is very limited. But some difference can be seen when the blade is tested with only a quarter of the tape. The difference in bending displacements is below 10%. There might also be an effect of the bending induced twist but that is more uncertain.

Comparing the results of the torsion load case it seems that there is no effect on the twist angle. But is looks like the tape has an effect on the twist induced bending.

Evaluation of the effect of special loading frame

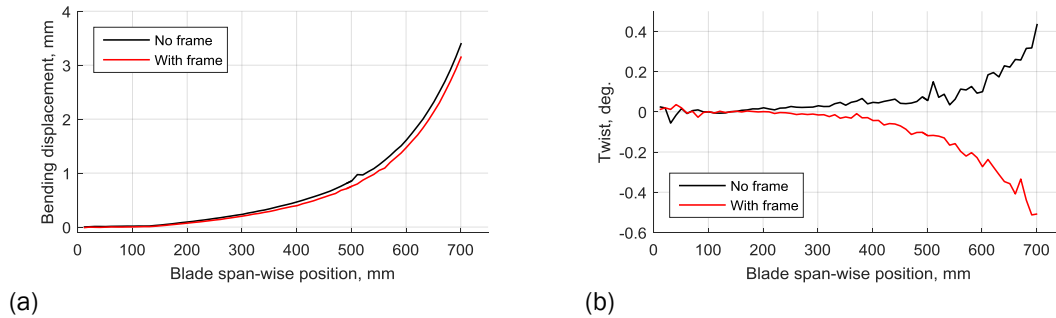Below is a comparison between the pure bending with and without the special loading frames presented.

(a)   (b)

Figure 52 Effect of special loading frames.

Comments

The y-z -displacement response are not identical but still similar. On the other hand the twist angle deviates a lot as expected as the loading without the frames very much depend on the location of the point loads with respect to the blade axis and furthermore creates a torsional moments as the blade starts to twist. These problems with the pure bending load case seem to be overcome with the new loading clamps/frames.

2.5 Comparison between DTU and POLIMI modal analyses

Experimental modal analyses were carried out both at PoliMI and DTU. At PoliMI the experimental modal response was measured by lightweight (0.5 g) accelerometers and an impact hammer instrumented with a load cell was used to excite the blade. At DTU a Scanning Laser Vibrometer was used to measure the modal response and a shaker was used to excite the blade with white noice.

The measurements from PoliMI and DTU are compared in table 10 where the difference is calculated relative to the PoliMI measurements. There is generally very good agreement for the lower Eigen frequencies, while the difference is larger for the higher Eigen frequencies. As discussed earlier it is difficult with the used setup with the Scanning Laser Vibrometer to measure edgewise vibrations. Therefore can some of the higher frequency modes not be determined due to the missing edgewise component. This is indicated with a question mark in table 10 and the very large difference in Eigen frequency in these cases is very likely due to the fact that it is not the same modes that are compared.

Table 10 Comparison of measured natural frequencies by PoliMI using and DTU using the grid method. The difference is related to the PoliMI measurements.

Mode	Freq. [Hz], PoliMI	Freq. [Hz], DTU	Difference
1st Flapwise	20.7	21.00	1.4%
1st Edgewise	33.7	34.50	2.4%
2nd Flapwise	55.1	55.00	-0.2%
2nd Edgewise / ?	109.7	79.75	-27.3%
3rd Flapwise	115.9	110.25	-4.9%
1st Torsional	155.5	156.00	0.3%
4th Flapwise	194.2	182.25	-6.2%
2nd Torsional / ?	240.6	265.00	10.1%
3rd Torsional / ?	366.2	359.25	-1.9%

2.6 Conclusions and recommendations

Ad-hoc design and manufacturing processes have been set-up for the realization of scaled multi-megawatt blades with bend-twist coupling, testable in the wind tunnel. The possibility of embedding low-intrusive, high-accuracy FBG sensors with the scope of monitoring the load at some stations along the blade span was also successfully exploited. The blade shape was chosen so as to minimize the reduction of the power conversion quality due to lower Reynolds numbers. The blade layout was set-up with the scope of allowing the design of the small structural components for meeting the scaling requirements, and to facilitate the embedment of the Fiber Optic sensors. The structural design, prepared with a multi-level structural blade design tool, showed good accuracy in matching the scaling requirements, since the errors of the scaled-up modal frequencies and the Lock Number remain below 7%. To evaluate the manufacturing, the blade was characterized at bench, by the use of static tests both at PoliMI and DTU and by modal tests with hammer at PoliMI and with a Scanning Laser Vibrometer at DTU. The modal analysis shows the modal frequencies and the Lock number remain close to design, with mismatches around 10%. The two experimental modal methods generally showed very good agreement for the lower Eigen frequencies, while the difference was larger for the higher Eigen frequencies. Some uncertainty on defining the measured modes was observed between the two methods. The static tests showed the twist-to-feather capability evaluated through the Kinematic Coupling Coefficient. It was encountered a more coupling in the manufactured blades with respect to the design. To quantify the mismatch an accurate characterization of the blade structural properties, i.e., the identification of the mass distribution and the structural matrix of the blade beam-like model will be provided successively.

The FBG sensors were calibrated from the static tests by solving two least squares problems (one per each bending moment direction), which allow to estimates also the FBGs position uncertainty. The calibration showed an estimation error below 7% in the flapping direction and 8% in the edge direction. The error is not particularly low, since the calibration was done on only three of the four FBG sensors, due to the unavailability of one, but is considered enough for the goal of evaluating the fatigue loads variation vs. different configurations.

The tests in the aeronautical section of GVPM showed little or no reduction in the power coefficient for the rotor with BTC blades if compared with the one with identical shape but without BTC. The main difference is the minimum collective pitch, which is lower since the twist to feather causes a higher effective angle of attack to the airfoils.

A tests campaign for assessing the load reduction capability was performed in the boundary layer section of the GVPM. Some no wake/partial wake conditions were tested. The model was tested in three configurations: RGD, (i.e. with rigid blades), BTC, hybrid BTC+IPC (BTC blades and cyclic pitch controller). Looking at the shaft and tower base bending moments, the BTC seemed capable of mitigating the peaks within a bandwidth up to the first blade flapping frequency. The inertial loads are not affected by the BTC, therefore their contribute may increase the peak at the 1xRev, and hence the equivalent fatigue load the shaft bending moment. The hybrid BTC+IPC model seemed to recover this aspect since the 1xRev is cut-out by the cyclic pitch control.

The cost of using the IPC is an increased ADC. The analysis of the blade load measured by the FBG sensors conducted on the BTC and hybrid BTC+IPC models showed that the IPC implemented here by doing feedback on the shaft bending moments may have negative impact on the blades fatigue loads.

A possible improvement would be a fine tuning of the IPC gains, by taking into account the impact on the blade loads and on the ADC increasing. May be of relevant interest to conduct a new test campaign where the IPC is tuned so as to fill the ADC saving margin achieved by the BTC.

3 MANUFACTURE AND TESTING OF A MORPHING BLADE SECTION PROTOTYPE (UPATRAS)

This section gives a summary of the work performed by the University of Patras under the framework of Task 2.2 of the INNWIND.EU project. A description of the conducted and ongoing work is presented and the main results are provided.

3.1 Brief description of the work

The work described in this deliverable consists of two main parts: i) the experimental characterization of Shape Memory Alloy (SMA) wire actuators and ii) the experimental characterization of a scaled morphing section. The first part of the work includes the material characterization of the SMA actuators in wire form. Both the mechanical properties and the transformation related properties were extracted through isothermal and isobaric tests respectively. Additional tests were performed to estimate the fatigue life of the material. To fulfil this task, a special testing setup was designed and realized, able to operate in a temperature range between sub-ambient (~−100ºC) and elevated (~+150ºC) temperatures. A temperature controller was used to drive the process by either keeping constant the temperature level or performing thermal cycles under constant stress level. Custom fixtures were fabricated to realize the experimental set up while Virtual Instrument developed in National Instrument LabVIEW software were collecting the experimental data through data acquisition systems. Post processing of the acquired experimental data resulted in the SMA material properties.

The second part of this work consists of the manufacturing and testing of a scaled morphing section prototype using SMA wire actuators. The design of the prototype is the outcome of the D2.23 while a proper scale was selected in order to facilitate the manufacturing and the laboratory testing. A special test jig was used for the prototype mounting while the instrumentation required for the testing included a programmable power supply, a laser Doppler vibrometer for the displacement recording and data acquisition systems. The morphing functionality of the prototype was assessed under zero and representative aerodynamic loads.

Behaviour of Shape Memory Alloys

The special behaviour of SMAs relies on the solid state diffusionless martensitic transformation which is activated either by thermal or mechanical loading [39], [40]. During the martensitic transformation the transition from the stable phase of austenite (*A*) to the stable phase of martensite (*M*) occurs. Martensite is a low symmetry phase which is stable at low temperatures while contrary the high symmetry phase of austenite is stable at high enough temperatures [41].The transformation from austenite to martensite can occur either through thermal or mechanical load. While austenite is cooled below a critical temperature it transforms to twinned martensite without any generation of macroscopic strain. Transformation of austenite to detwinned martensite through mechanical load is accompanied by a large inelastic macroscopic strain (>4%) that is not recovered upon unloading. Both these procedures are referred to as forward or martensitic transformation. The transformation of martensite (either twinned or detwinned) back to austenite can only occur through heating above a critical temperature. If martensite is at detwinned form during this reverse transformation the inelastic strain, called transformation strain, is recovered and the material gains its initial configuration. The behaviour described above is called *Shape Memory Effect* (SME) and is the one out of the two special behaviours of SMA. Figure 53 presents schematically the SME in stress – strain – temperature space. Starting from austenitic phase (point A) the subsequently cooling of the material results in the transformation to twinned martensite (point B) without generation of any macroscopic strain. Loading of the material it makes it transform to detwinned martensite configuration (point C) with a simultaneous strain generation. During unloading of the material the elastic strain is recovered with no transformation process taking place (point D). The heating of the material above a certain temperature transforms it back to austenite returning to its initial shape. In the case of

constrained recovery, the exerted forces from the actuator to the interconnected structure can be sufficient high to deform it. This effect is usually exploited for the design and development of morphing structures.
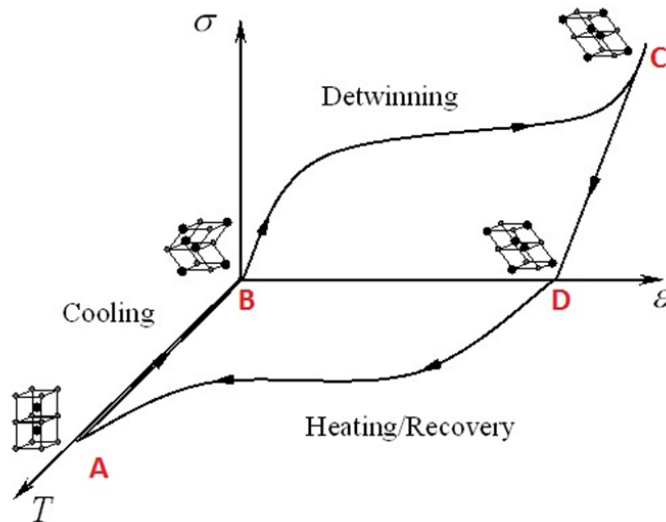

Figure 53: Representation of Shape Memory Effect

Pseudoelasticity is the second special behaviour related to Shape Memory Alloys, which effectively results in its functionality as an actuator. It is associated with recovery of the transformation strain while temperature is above a specific value. Starting from austenitic phase, the material is stressed and transformed to detwinned martensite developing the transformation strain. Upon unloading the transformation strain is recovered and the material transforms back to austenite gaining its initial shape. A schematic representation is showed at Figure 54.
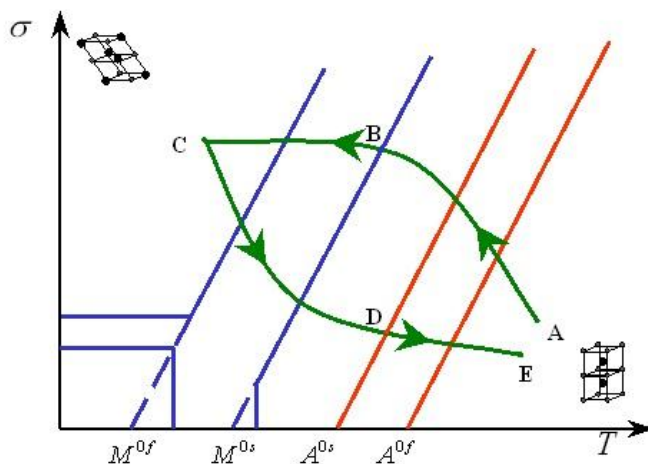
Figure 54: Representation of pseudoelastic behaviour

3.2 Material characterization

The thermomechanical characterization of a SMA material requires special instrumentation and fixtures to extract the distinct material properties. Although the characterization of these materials is based on the same principles with the tests on other common materials, their complex thermomechanical response and its dependence on the loading path account for dedicated

testing procedures. Special testing apparatus for SMA materials cannot be found in market, thus two in-house devises, oriented in testing SMA wires, were designed and manufactured. The first one is an existing device that has been used by UPAT for material characterization in the past (Figure 136), but due to the limitations encountered a second device was designed to perform the experiments needed in the framework of this project.

Both apparatuses were designed based mainly on research activities [52]–[60] and partially on ASTM standards. It should be noted though that there no ASTM standards specially for SMA materials characterization. Most of the available standards refer to medical devices and/or surgical implants, but can provide an insight for testing procedures for these materials. Hereby the main standards are listed:

- ASTM F 2004-05 Standard Test Method for Determination of Transformation Temperature of Nickel-Titanium Shape Memory Alloys by Thermal Analysis
- ASTM F 2005-05 Standard Terminology for Nickel-Titanium Shape Memory Alloys
- ASTM F 2063-05 Standard Specification for Wrought Nickel-Titanium Shape Memory Alloys for Medical Devices and Surgical Implants
- ASTM F 2633-07 Standard Specification for Wrought Nickel-Titanium Shape Memory Alloys Tube for Medical Devices and Surgical Implants
- ASTM F 2082-06 Standard Test Method for Determination of Transformation Temperature of Nickel-Titanium Shape Memory Alloys by Bend and Free Recovery
- ASTM F 2516-07e1 Standard Test Method for Tension Testing of Nickel-Titanium Superelastic Materials

The material characterization of the SMA material requires testing in both sub-ambient and elevated temperatures. In order to achieve sub ambient temperature a liquid nitrogen container of 35lt capacity (Figure 140) equipped with a regulating valve and an electro-vane was used. Heating phase was achieved either by use of heating elements that heated the air inside the chamber or by letting current pass through the specimens. For the first method a programmable power supply (Figure 143) was used while for the second a simple computer power supply was utilized. A temperature controller equipped with PID and PLC units (Figure 141) was used to maintain constant temperature for isothermal testing and perform the thermal cycles when required. Special extensometers (Figure 148) capable to measure up to 25% strain at extreme temperature conditions (−265°C to +200°C) were also used. Additionally, a Laser Doppler Vibrometer (Figure 133) was used to record the displacement of the wire due to transformation. In order to avoid slippage of the 1mm diameter SMA wire custom grips (Figure 146 and Figure 145) with special configuration were designed and manufactured. Displacement, strain and temperature were monitored and recorded by using National Instrument (NI) signal conditioning and DAQ cards as well as special Virtual Instrument (VI) interfaces. The DAQ cards and NI equipment as well as all the major experimental fixtures and equipment is described in Appendix A.

3.2.1 Required experimental tests and testing setups

In this section the required testing procedures are described followed by the experimental setups used for the extraction of material's properties.

As mentioned in the previous sections, SMAs have two stable solid phases (Austenite and Martensite) that present different and distinct thermo-mechanical properties. Transformation and transition from one phase to the other is achieved through following particular thermomechanical paths in the stress-temperature space. In order to characterize the transition from one phase to the other, temperature and stress threshold values must be derived. Furthermore, as the material changes its behaviour through cyclic loading a stabilization (training) procedure is essential. During the aforementioned procedure the material's properties stabilize according to the load induced. Specific loading input leads to a specific output from the material. To acquire the full set of material properties there are four categories of experimental tests that must be conducted and can be summarized as follows:

- Determination of zero stress transformation temperatures through Differential Scanning Calorimetry (DSC)

- Stabilization of material properties under cyclic isothermal or isobaric loading (training)

- Isothermal mechanical loading

- Isobaric thermal loading

Each test provides different information and is used for different properties extraction. It should be noted that the stabilization of the material's properties (training) is performed under isothermal or isobaric conditions according to the further use of the material. If the SMA is used for actuation, then the training procedure is performed under isobaric conditions.

All the experiments conducted on SMA wires in the framework of this project took place in the facilities of University of Patras using wire specimens extracted from an 80 m spool of NiTi bought from Nimesis Technology.

Isothermal test setup

In order to perform the isothermal experiments a rectangular testing chamber insulated with stone miner wool (Figure) was fitted on the frame of a MTS universal testing machine. The chamber provides the control volume for constant temperature conditions. Temperature is maintained in a predefined value and controlled by a PLC and two digital controllers (Figure 138 and Figure). Control input is the temperature which is obtained using Type K thermocouples and the output is voltage which is applied to heating units. If cooling is needed the controller lets gases from the liquid nitrogen supply to pass through a pipe suitable for transferring cryogenic fluids and cool the control volume of the chamber. During this test the wire specimen is secured between the custom made grips (Figure 138) suitable for this device with the extensometer (Figure 148) attached and the thermocouples securely glued on it with thermal conductive paste.
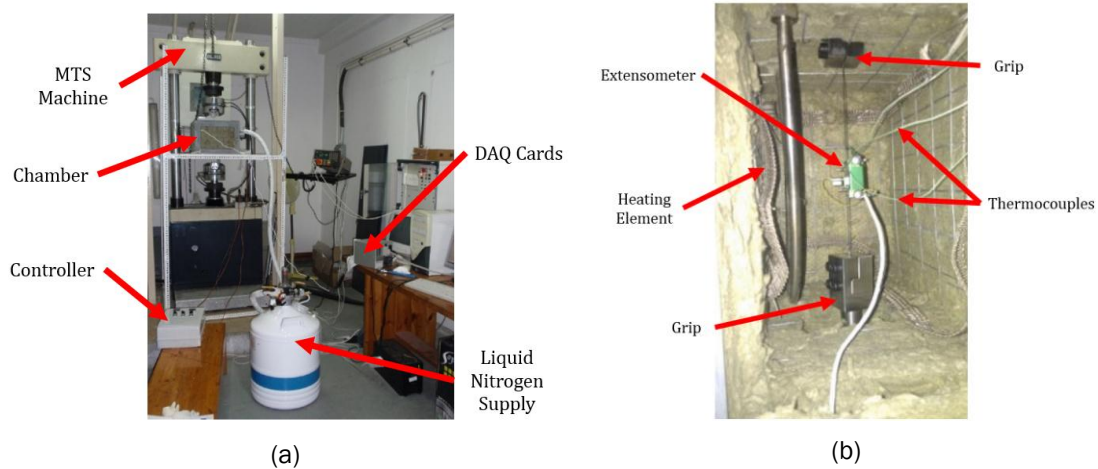
INNWIND.EU, Deliverable 2.24, Manufactured and laboratory tested scaled blades and parts of the blade

(a)   (b)

Figure 55: Isothermal testing (a) general setup and (b) internal view of the chamber

Isobaric and fatigue test setup

In the framework of this project two isobaric test setups were used. The first setup includes the rectangular testing chamber described in the previous section while the second one constitutes an optimized version of this setup with improved capabilities. In Figure 56 the existing general setup of the isobaric experiment is outlined. The rectangular chamber is placed on the frame of a tension machine. On this machine the fixed grip was also attached and secured. On the moving grip an axle was fitted to provide the required configuration for the suspension of the dead weights. Configuration of measuring instruments and heating and cooling elements remained the same inside the chamber. The dead weights were used to set the required stress level while the controller was used to adjust the temperature by either activating the heating elements or by letting gases of liquid nitrogen enter the chamber. Data acquisition was achieved using the required cards and a proper VI of LabVIEW software.
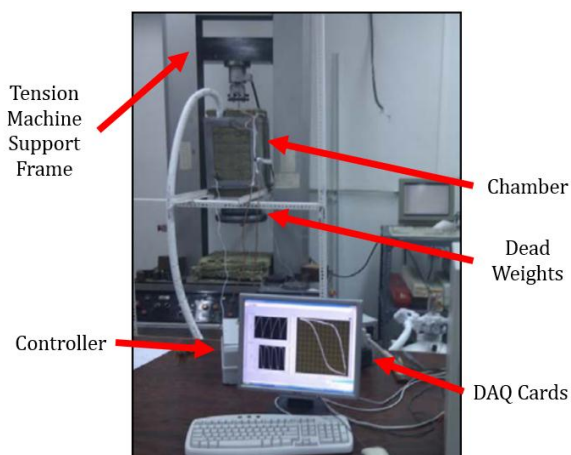
Figure 56: Existing isobaric testing general setup

The optimized version of the isobaric experimental setup was created in order to make better use of the consumables (especially nitrogen) during cycling operations in order to increase the number specimens that can be tested simultaneously, reduce the control volume of the chamber and to increase the number of testing cycles (duration of the experiment), in comparison to the existing setup. The before mentioned aspects were crucial for the fatigue testing of SMAs as large number of isobaric cycles was envisioned to be performed till failure of the specimen. Therefore, this

compact testing device with improved operational characteristics was used to expedite the fatigue testing procedure. In Figure 57 a photorealistic view of the new testing device is presented.
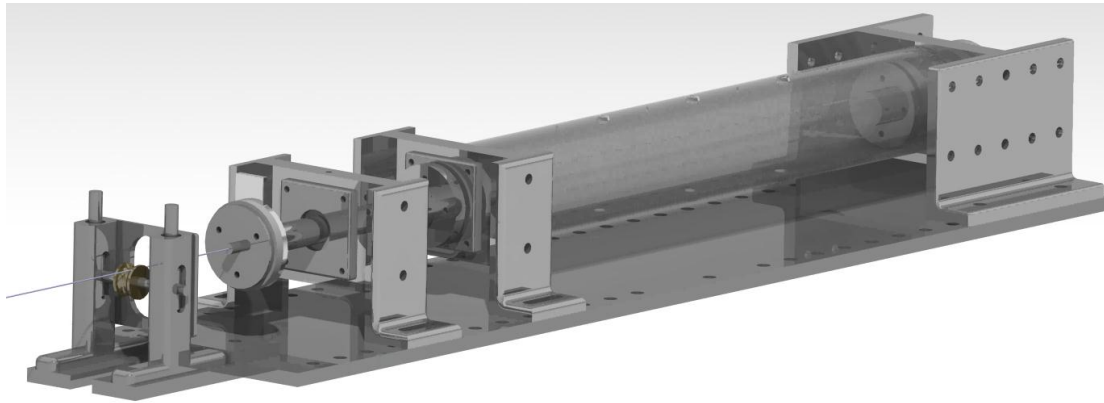

Figure 57: Photorealistic view of the new isobaric testing device

As it can be seen the configuration of the chamber is altered. In this case the specimens are placed horizontally and parallel to the ground level allowing the whole specimen to be under the same temperature level. This proves to be a great improvement especially for determination of SME where the changes in temperature are slow. If the chamber has a vertical configuration and the specimens are placed perpendicular to the ground level, then during slow temperature changes the lighter hot air will accumulate on the top of the chamber while the heavier colder air is accumulated on the lower surface of the chamber which may lead in wide temperature variations across the length of the specimen. When the specimen is under a wide temperature variation across its length then it is possible to have a non-uniform presence of austenite and martensite in its structure.

The horizontal layout of the chamber along with the most important components of the device is outlined in Figure 58. All the parts are connected to a steel device plate that provides rigidity. Again there are two custom made grips which are identical (Figure 139) and can hold up to four (4) wire specimens. Each grip is connected to an axle which have different length. The short axle is fixed on the fixed end support while the axle which is longer is the moving axle that rests on two (2) supports (indicated as "Moving End Supports" in Figure 58). The number of the supports was set to two in order to assist for the adequate alignment of the axle and its positioning to minimize bending moments acting on the specimens. In each support, between the axle and the support structure there are rings made of Teflon to minimize friction between the axle and the support and also electrically insulate the parts in contact.

In this configuration isobaric loading is achieved by loading mechanically the wire rope that is fixed on the end of the moving axle. To adequately adjust and align the wire rope a pulley is placed on a frame with the capability to adjust its height. On the other end of the wire rope there is an axle holding the dead weights during an isobaric test. For safety reasons there are secure lock plates. If the specimens or other component fail the aforementioned locks will stop the moving grip from escaping the device and cause further damages or hurt laboratory personnel.
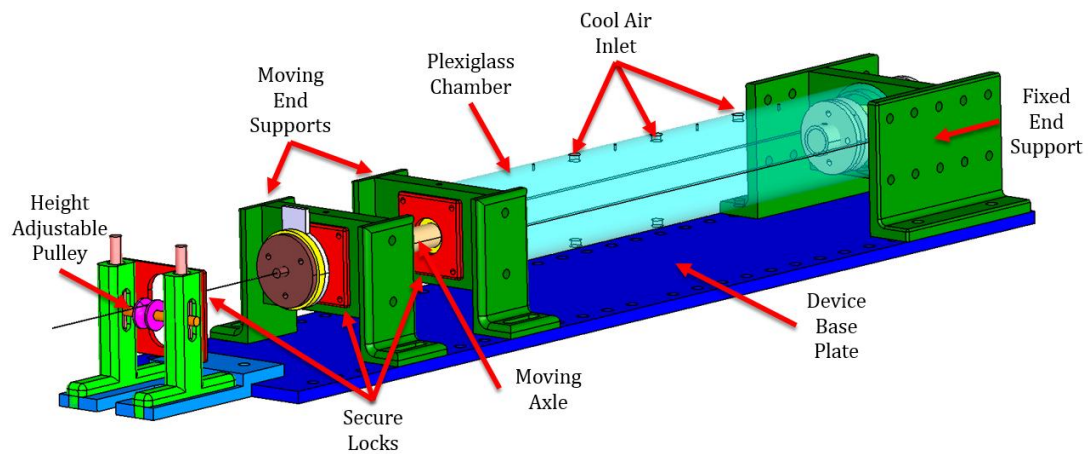
Figure 58: The main components of the new isobaric testing device

A major change on the new testing device is its chamber which is cylindrical and without any insulation. The cylindrical shape offers better circulation of air when its flow gets through the inlet. Moreover, plexiglass as a material can provide a level of thermal insulation as well as electrical insulation. Electrical insulation is crucial because the specimens are heated using Joule effect. Joule heating is achieved by applying a voltage on the ends of the specimens. Due to the electrical resistance of the SMA material the applied voltage creates an electrical current that passes through the specimen and elevates its temperature.

It should be noted that there is no equipment inside the chamber except for the thermocouple wires and the wires that are attached on the grips to create the voltage difference. The aforementioned wires are passed through small holes created on the chamber parts. Additional holes are created to fit the hoses for air inlet and air outlet. Because of the small space inside the chamber there is no extensometer for strain measurement. The deformation of the specimens is measured using telemetry methods. A laser Doppler vibrometer points on a surface of a part (called "Measurement Disk") placed on the end of the moving axle. In Figure 59 the Measurement Disk is shown along with the other parts that are assembled together. The moving axle is manufactured from stainless steel, a material that is electrically conductive, thus its end has to be insulated. To electrically insulate the moving axle a Teflon insulation cap (yellow colour in Figure 59) is connected with it. On this cap the measurement disk is mounted. The shape of the measurement disk is designed in way that allows the laser beam of the laser vibrometer to track it. Along with the Teflon insulation and the measurement disk there is also the load disk (dark red colour in Figure 59) which has a threaded protrusion to allow screw connection with the wire rope. All of the three parts are connected together with three screws that secure them.
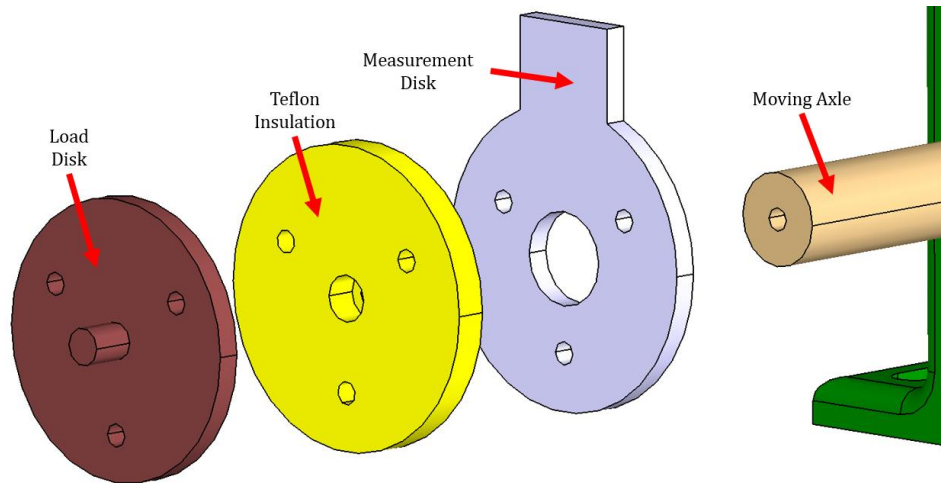
Figure 59: The attached parts on the end of moving axle

In Figure 60 the experimental setup is summarized through a schematic representation. The main controller is used to regulate the phases. Controller commands are transferred to two on/off controllers that are responsible for the heating and cooling phase. Heating is achieved through electrical current provided by a power supply while cooling is performed using the nitrogen gases from the LNG container. Finally, the isobaric conditions are achieved using dead weights connected through wire rope with the specimen
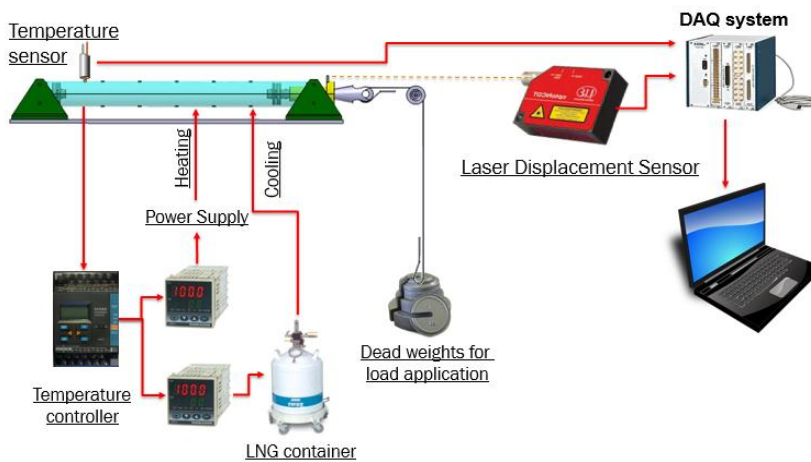
Figure 60: Schematic representation of experimental setup

INNWIND.EU, Deliverable 2.24, Manufactured and laboratory tested scaled blades and parts of the blade

3.2.2 Thermomechanical characterization

Differential Scanning Calorimetry

Differential Scanning Calorimetry is a basic step for the following experimental procedure as it provides an estimation of the crucial temperature values that define the onset and the completion of transformation processes and allows for the design of the whole testing campaign. A small portion of SMA wire was cut and placed at the aluminium pan of the DSC machine. The SMA material was heated from room temperature up to 120°C to recover any remaining strains. Cooling down to -30°C the forward transformation of austenite to martensite occurs giving an exothermal reaction. When the cooling has been completed a heating up to 120°C follows to provoke the reverse endothermic transformation from martensite to austenite. A peak with opposite direction of the previous one is now generated. From these two peaks the transformation temperatures were specified by using the method of tangent lines. The heating and cooling rate was set to be 10°C/min as proposed by ASTM [61] standards while helium was used as the purge gas for the sample chamber. In Figure 61 the DSC test results can be shown while Table 11 summarizes the crucial transformation temperatures. The transformation temperature M_s refers to the temperature where martensitic transformation (A→M) during cooling starts and M_f to the point where the transformation is completed. Respectively A_s refers to the critical temperature for the initiation of reverse transformation (M→A) while heating and the A_f to the temperature where the transformation ends. The R_s and R_f refer to the respective critical temperatures for the transformation from austenite to the intermediate R-phase during specimen cooling.
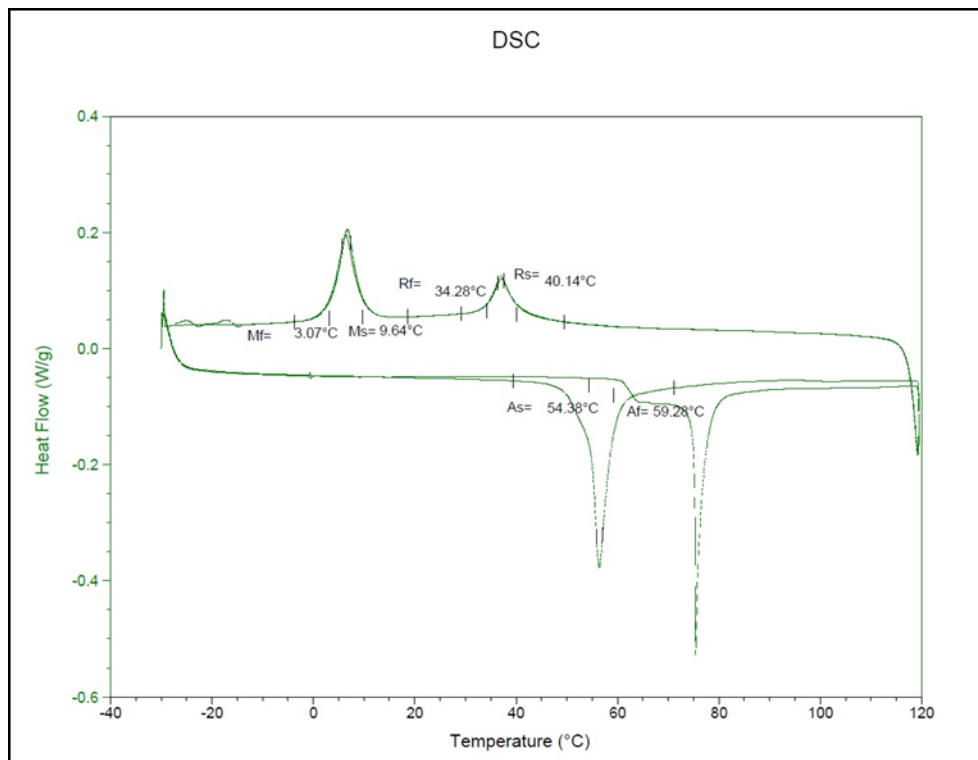

Figure 61: DSC results

INNWIND.EU, Deliverable 2.24, Manufactured and laboratory tested scaled blades and parts of the blade

Table 11: DSC transformation temperatures

Transformation Temperatures [°C]	
M_s	9.67
M_f	3.45
A_s	54.39
A_f	59.19
R_s	40.40
R_f	34.26

Stabilization of material's response (training procedure)

A SMA can exhibit repeatable shape changes when cyclic thermal load is applied under a constant stress level. This behaviour is called Two-way Shape Memory Effect (TWSME). If the thermomechanical loading is repeated the microstructure is affected and will consequently affect the observable macroscopic response. The recommended procedure for SMAs intended to be used as actuators, entails the execution of numerous isobaric thermal cycles at a stress level equal or greater to the one foreseen to be developed during SMA operation in the application. Due to this phenomenon the stabilization of a SMA is a required process that aims to saturate the hysteretic behaviour of the material. The temperature range should ensure the transformation from the fully austenitic phase austenite to the fully martensite during cooling and the transition from the fully martensite to fully austenite during heating. Depending on the alloy composition and the maximum stress it is foreseen that the material's response will be stabilized after a number of 80-100 isobaric thermal cycles (Lagoudas, 2008,Hartl, Lagoudas, Calkins, & Mabe, 2010).

For the characterization of material's properties and the other experiments included in the framework of this project a number of SMA wires has been trained. The total number of trained wires depending on the type of use is summarized in Table 12.

Table 12: Summary of training procedures

Intended Usage	Number of Specimen Wires	Experimental Device Used
Isobaric Experiments for Material's Characterization	5	Rectangular Chamber
Isothermal Experiments for Material's Characterization	5	Rectangular Chamber
Actuator Wires for the Prototype Operation	12	Cylindrical Chamber
Total Number of Trained Wires	22	

In Figure 62 the variation diagrams of temperature (Figure 62a) and strain (Figure 62b) with respect to time are presented. Temperature limits were set to the controller as -50°C for the cooling phase and +150°C for the heating phase. The three first cycles were completed in a larger time period because during the two first cooling phases the pipes transferring liquid nitrogen gases had to reach a sub-ambient temperature. Moreover, as it can be observed in Figure 62b maximum transformation strain saturate in a certain level.
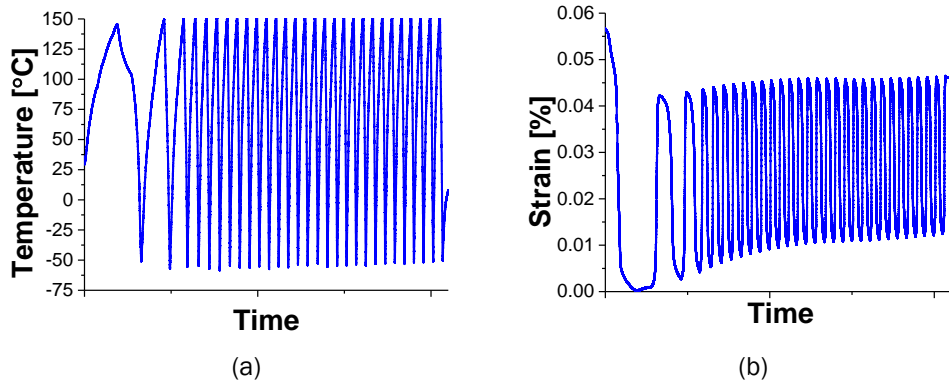
INNWIND.EU, Deliverable 2.24, Manufactured and laboratory tested scaled blades and parts of the blade

Figure 62: Diagrams of (a) temperature and (b) strain variation during a typical training procedure

The most indicative diagram for a training procedure is the strain vs. temperature diagram which is presented in Figure 63. In this figure the first and the last cycle of the procedure are highlighted with red and green colour respectively. During the first thermal cycle, only a partial recovery of the strain generated during cooling is observed upon heating with some irrecoverable strain generated during the cycle. It can be noticed that after the completion of a thermal cycle a small amount of irrecoverable strain remains. This amount of permanent strain gradually decreases as the cycles increase until it practically ceases to further accumulate.
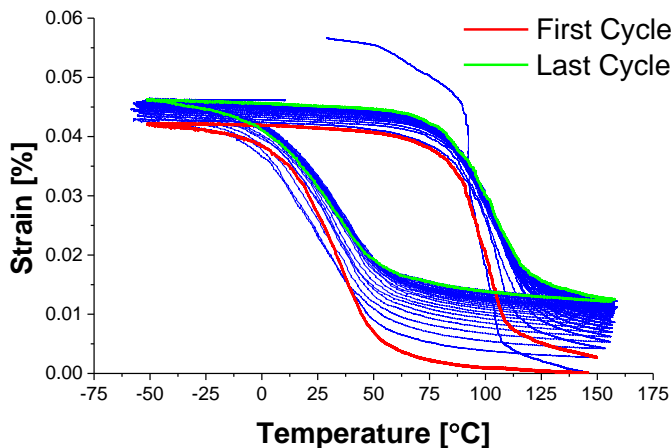
Figure 63: Typical strain vs. temperature curve of a training procedure

The number of cycles performed during training procedure and other information were obtained automatically using an in-house multi-purpose Graphics User Interface (GUI) developed by UPAT using MATLAB software.

Isothermal tests

Isothermal mechanical loading tests are required to extract the elastic properties of each stable phase. Monotonic loading and unloading of the specimen is performed in temperatures lower than M_f or higher than A_f to determine either martensitic or austenitic response, respectively.

To extract the elastic properties of austenite a temperature level, 25˚C greater than the A_f determined by the DSC was selected to ensure that the austenite elastic region will be a large part

of the response during loading. To avoid force jumps near the transformation region, displacement control was selected for the loading with a strain rate of 0.01%. Such a low loading rate was necessary to achieve isothermal conditions due to the endothermic/exothermic nature of the phase transformations. In Figure 64 the response of the SMA during loading is depicted and the elastic modulus of austenite is found to be E^A=66.2 GPa. Additionally, the ultimate stress of SMA specimen under this thermal conditions exceeds the stress levels of 780 MPa.
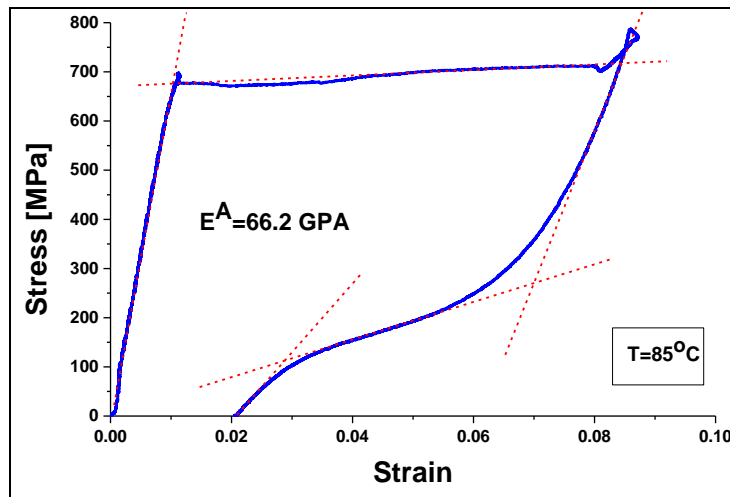
Figure 64: Isothermal testing for extraction of austenite elastic properties

The extraction of the martensite elastic modulus was performed under isothermal testing in sub-ambient conditions with a constant temperature of -25˚C. In Figure 65 presents the stress – strain response of the isothermal test. It must be noted that throughout the test the material remains at the martensite phase, in twinned martensite form before the stress plateau initation and in detwinned martensite form after the end of the stress plateau. Using tangent lines the elastic modulus of martensite has be found to be almost the same during loading and unloading (25.6 GPa for loading and 26.6 GPa for unloading) proving that the elastic properties of martensite are independent of the orientation of its microstructure. The average value E^M=26.1 GPa is considered to be the final martensitic elastic modulus.
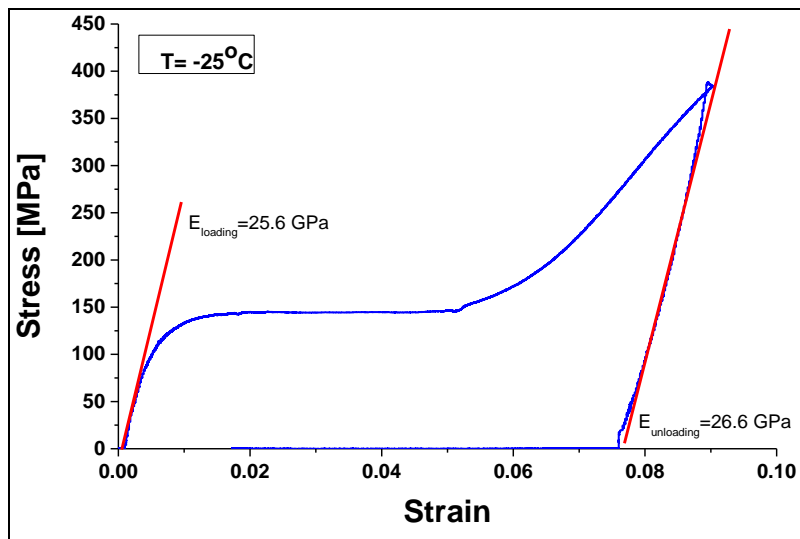
INNWIND.EU, Deliverable 2.24, Manufactured and laboratory tested scaled blades and parts of the blade

Figure 65: Isothermal testing for the extraction of martensite elastic properties

Isobaric tests

Out of the five (5) specimens that were trained for the extraction of the material's properties during isobaric tests three (3) were selected as more suitable for further testing. These specimens undergone thermal cycles under constant mechanical load using combinations of dead weights to achieve five different stress levels. The masses used for loading and the developed stress on the wire specimen of 0.5 mm radius are summarized in Table 13.

Table 13: Stress levels in Isobaric Tests

Level	Nominal Mass [kg]	Weighted Mass [kg]	Total Mass [kg] (including connection parts etc.)	Force [N] $F = m\,g$	Developed Stress [MPa] $\sigma = F / (\pi\, r^2)$
1	0	0	2.4	23.52	29.95
2	5	4.9	7.3	71.54	91.09
3	10	9.9	12.3	120.54	153.48
4	15	14.7	17.1	167.58	213.37
5	20	20.3	22.7	222.46	283.25

To address the transformation temperatures and determine the shape memory effect, the trained specimens are subjected to thermal cycles under constant stress. During this experimental procedure the variation rate of temperature is about 15˚C per minute. In Figure 66 a qualitative thermal cycle under constant stress is presented. The cycle can be divided into two phases that represent cooling and heating phase. Each phase presents two linear regions, one almost parallel to the temperature axis and one after the initiation of the respective transformation. These linear regions are indicated in Figure 66 using their tangent lines that are represented with red dashed lines for the heating phase and with blue dashed lines for the cooling phase. The transformation

INNWIND.EU, Deliverable 2.24, Manufactured and laboratory tested scaled blades and parts of the blade

temperature thresholds are calculated by addressing the junction points between the tangent lines and by projecting each junction point on the horizontal axis as shown in Figure 66.
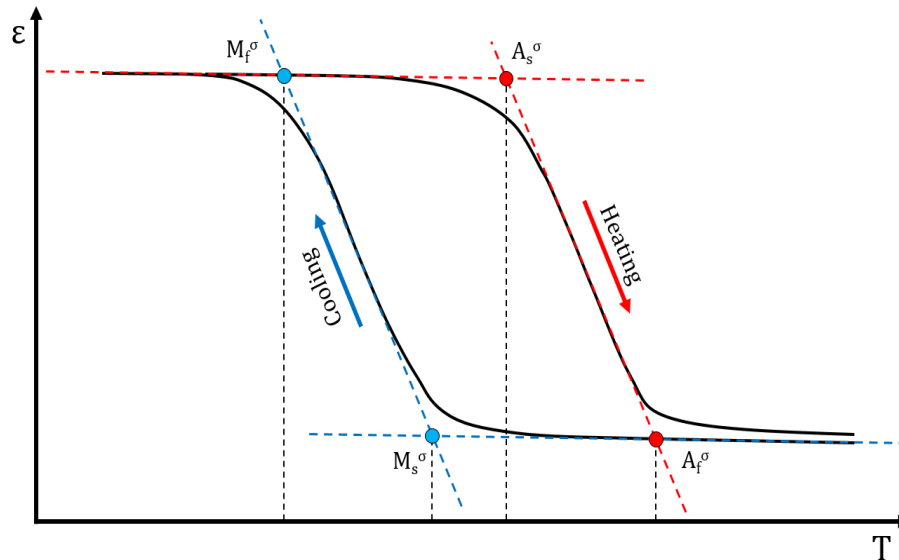

Figure 66: Strain vs. Temperature graph under isobaric conditions

For each specimen the procedure included at least two thermal cycles to validate that the subsequent cycles coincide (no need for further training) and confirm that during these cycles the extracted properties do not deviate. To extract the transformation temperatures, the in-house GUI was used for the experimental data of each specimen.

Two successive thermal cycles under isobaric conditions (91.09 MPa) are presented in Figure 67. It is clear that the cycles coincide so no further training is needed.
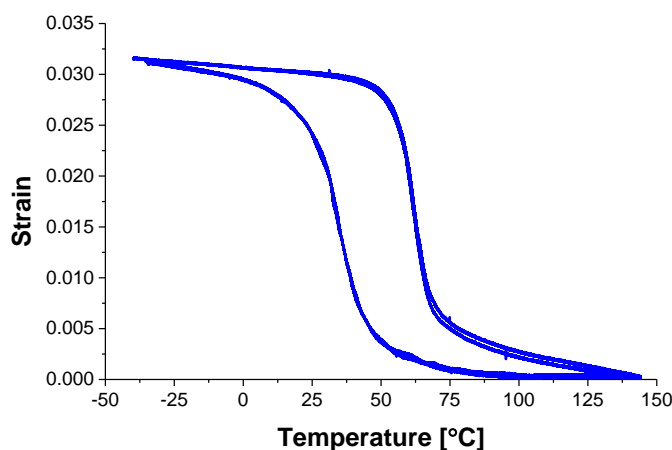
Figure 67: Typical Strain vs. Temperature curve for SME determination

Each cycle was isolated and processed to address the transformation temperature thresholds, the slopes of the tangent lines of the linear regions of cooling and heating phase and calculate the maximum transformation strain for the current stress level. In Figure 68 the separated phases and the tangent lines of the considered linear regions are presented.
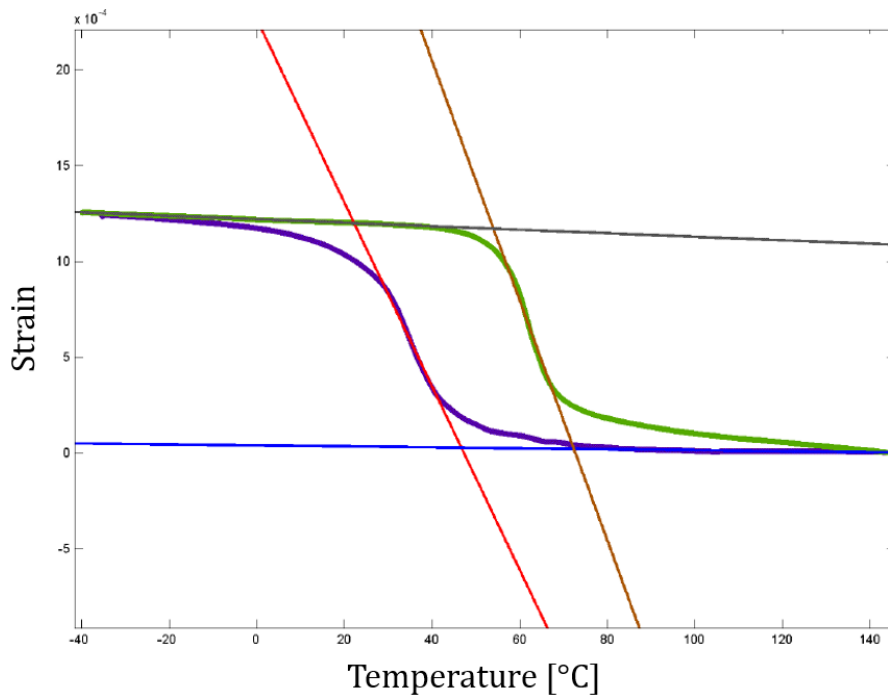
Figure 68: Separation of cooling and heating phase and drawing of tangent lines using MATLAB GUI

The procedure described above was performed for all the three specimens and after prover processing of the results and statistical averaging the transformation properties of the SMA material were extracted. In

Table 14 the transformation temperature thresholds for each stress level are summarized.

Table 14: Transformation temperature thresholds for each stress level

Applied Stress [MPa]	Temperature [°C]			
	M_s	M_f	A_s	A_f
29.95	33.98	14.31	49.29	64.75
91.09	45.46	17.51	54.39	72.28
153.48	59.24	24.27	61.40	78.16
213.37	63.69	39.62	65.14	88.67
283.24	69.47	40.48	75.03	94.72

Using the data from Table 14 the phase diagram of the SMA material is constructed. Because of the two phases consisting the SMA, the phase diagram shows the limits in the stress-temperature space over which transformation takes place.
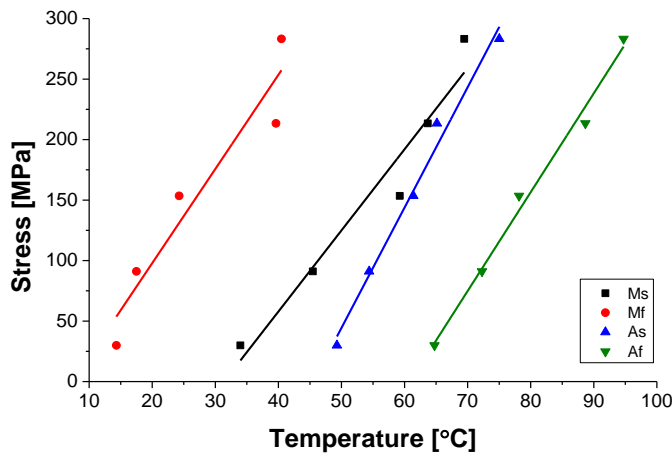
Figure 69: Phase diagram of NiTi wire specimens

The transformation temperatures at zero stress level are calculating by using the equation expressions after linear fitting of the experimental data. To this end, the calculated intersection points between the limits of the transformation regions and horizontal temperature axis are summarized in Table 15.

Table 15: Transformation temperatures at zero stress level

M_s [°C]	M_f [°C]	A_s [°C]	A_f [°C]
31.37	7.42	45.54	60.84

Finally, from isobaric experiments the association of maximum transformation strain with the applied stress level is extracted. The experimental procedure described so far is followed for 5 different stress levels. For each level the maximum transformation strain is calculated and the values are presented in the diagram of Figure 70 where it can be seen that the experimental plot follows an exponential form.
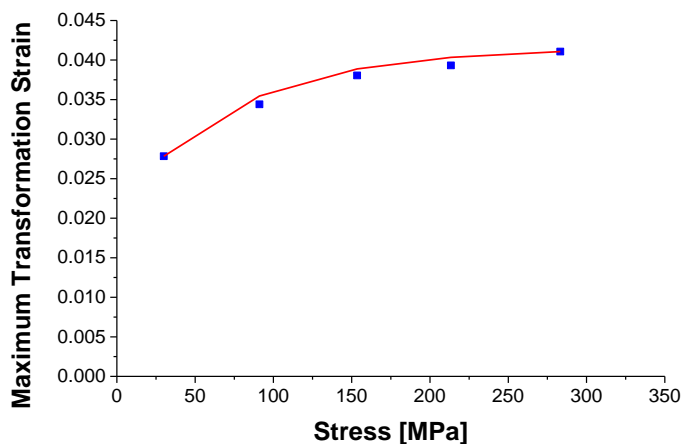
Figure 70: Maximum transformation strain vs. applied stress

3.2.3 Fatigue life estimation

Fatigue life of Shape Memory Alloys

Knowledge of fatigue life of SMAs is crucial, especially when the application entails the use of these materials as actuators. During actuation the material is subjected to cyclic thermomechanical loads. Cyclic loading can be associated with structural and functional fatigue that both affect the operational life of a component manufactured by a SMA material. Functional fatigue refers to repeated actuation with the maximum recoverable strain being of order of three to five per cent (in most common polycrystalline SMAs) which results in gradual accumulation of transformation-induced plasticity and low cycle fatigue [42].

Eggeler et al. have considered structural and functional fatigue of NiTi SMAs in four different cases [43]. One of these cases is the use of SMA spring actuators where the generic features of their functional fatigue are studied. It was observed that during the first 100 cycles the actuator spring suffers irreversible plastic deformation which saturates and its performance stabilizes without failure up to 1000 cycles. The first 100 cycles can be considered as the training procedure for the stabilization of material's response under predefined thermomechanical stimuli.

Bigeon and Morin reported on the thermoelastic fatigue of CuZnAl and TiNiCu SMA wire specimens under slow and fast cycles [44]. Based on the results of their experiments they reported that CuZnAl fails immediately when applied stress exceeds 200 MPa. Their tests proved that for the TiNiCu specimens failure didn't occur after more than 11.000 cycles when stress level was around 50 MPa while for the CuZnAl the developed stress was about 10 MPa. For both cases the transformation strain exhibited was 2% for the CuZnAl and 1% for the TiNi. Hornbogen relates training with fatigue, because during training microstructure of the martensitic domain is affected and therefore an optimum strain exists along with a number of cycles [45]. If this optimum combination of strain and number of cycle is surpassed fatigue starts.

An experimental investigation of Bertacchini et al. was conducted to account for the thermomechanical transformation fatigue of TiNiCu SMA actuators under a corrosive environment [46]. The wire specimens were tested under isobaric mechanical loading conditions and they were thermally activated under temperature variations. Due to the temperature variations the wires were actuated repeatedly, something that lead to accumulation of transformation induced plasticity and reduced fatigue limit of the material to a low-cycle fatigue regime. The experimental setup in this study is similar to the testing fixture used by UPAT in framework of InnWind.EU project. In the work of Bertacchini et al. the mechanical load was applied in five different levels. The results show that increasing stress level above 100 MPa decreases the amount of actuation strain. The higher the stress level, the more damage is generated upon cycling.

Fatigue testing and extraction of fatigue limit can be challenging due to lack of standards and protocols about these experiments and also due to the large number of parameters influencing the material's response such as environment of testing, gripping mechanism, applied loading path and frequency of actuation etc. Lagoudas and coworkers have published a table that summarizes the fatigue life results for some of the NiTi alloys based on different studies [47]. The table is presented below.

Table 16: Fatigue life of different shape memory alloys reported in various research studies

Reference	Cycles to Failure	Alloy Type	Cycle Loading
[48]	$10^3 \leq Nf \leq 10^4$	$Ni_{50}Ti_{49.9}$ & $Ni_{50.7}Ti_{49.7}$	Pseudoelastic
[48]	$7 \times 10^3 \leq Nf \leq 2 \times 10^5$	$Ni_{50}Ti_{50}$	Thermal
[49]	$10^2 \leq Nf \leq 10^5$	$Ni_{50}Ti_{50}$ & $Ni_{50}Ti_{40}Cu_{10}$	Pseudoelastic

[44]	$10 \leq Nf \leq 10^4$	$Ni_{48.8}Ti_{45.2}Cu_6$	Thermal
[50]	$10^2 \leq Nf \leq 10^4$	$Ni_{50.2}Ti_{49.8}$	Pseudoelastic
[51]	$10^3 \leq Nf \leq 5x10^4$	$Ni_{50}Ti_{40}Cu_{10}$	Thermal

In the study of Lagoudas et al. the conducted experiments refer to both full and partial transformation of SMAs and the Manson-Coffin relation is used to associate the plastic strain generated with the cycles to failure.

Fatigue testing

For the experimental characterization of material's fatigue life, a NiTi equiatomic SMA material was used in wire form (same as the wires for characterization experiments). The diameter of the wire was 1 mm and the mean net length of the specimen 80mm. Heating phase was achieved by driving electrical current through the specimen while cooling phase was performed by using an inflow of liquid nitrogen gases. For the estimation of SMA fatigue life the testing device presented in Figure 57 and Figure 58 was used.

The nominal dead weight used to simulate isobaric load conditions was 30 kg and it was applied to a pair of specimens. Thus developed stress for each specimen is calculated to be equal to 198.84 MPa. Controller settings were properly adjusted to let temperature reach up to 100°C during the heating phase and -95°C during the cooling phase to ensure that transformation is complete. The following table summarizes the required times for each phase to complete and the frequency of each thermal cycle.

Table 17: Heating/cooling phase times and thermal cycle frequency

Cooling time	14 seconds
Heating time	15 seconds
Cycle Frequency	0.0345 Hz

The duration of each fatigue test is approximately two weeks. In Figure 71 the diagrams of temperature variation (Figure 71a) and strain variation (Figure 71b) vs. time are presented. The peaks in temperature variation diagram occurred after inconsistences presented during cooling phase because the flow of nitrogen gases during the last cycles required manual regulation. Furthermore, transformation strain is calculated to 6.4% during the initialization of fatigue testing procedure and tend to saturate to 6.2% towards the completion of the test.
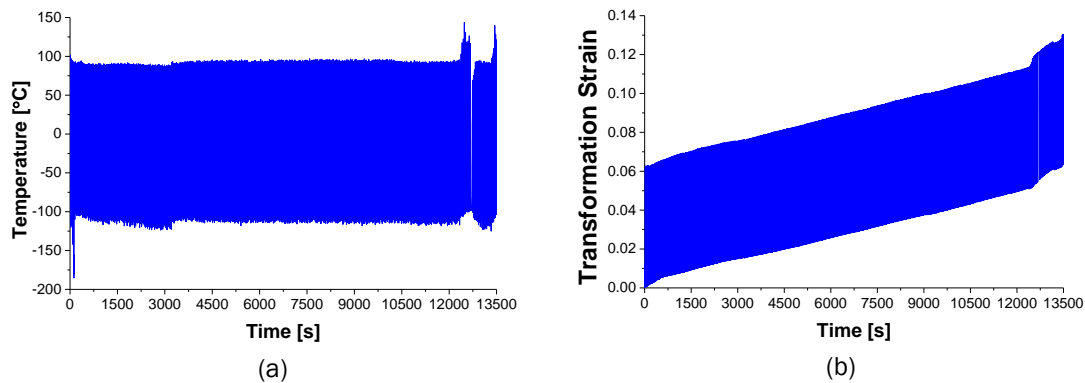
Figure 71: Fatigue testing diagrams of (a) Temperature vs. Time and (b) Strain vs. Time

Figure 72 shows the diagram of transformation strain related with the temperature of the specimen wires. It is clear that after the completion of each thermal cycle a small portion of plastic strain accumulates and this leads to a swift of the hysteresis loop during the positive direction of transformation strain axis.
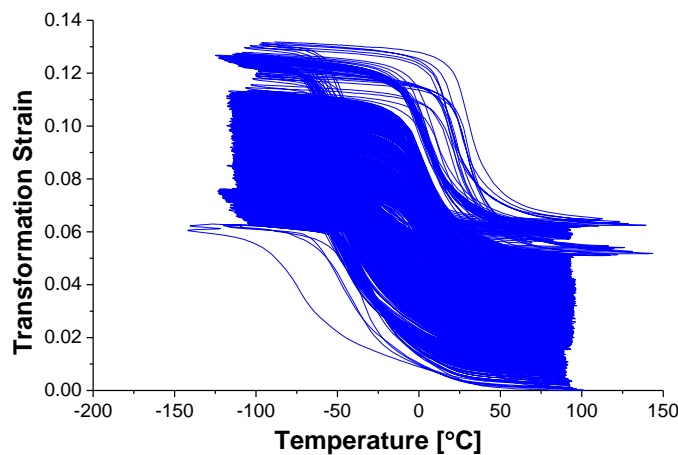

Figure 72: Strain vs. Temperature diagram during fatigue testing procedure

Specimens failed after the completion of approximately 1600 cycles. In Figure 73 the specimens are presented after failure happens. As shown in Figure 73a the specimens have failed along their free length and not on their supports on the grips. This proves that the grips do not affect substantially the evolution of fatigue failure. Moreover, the close up photo presented in Figure 73b proves that the specimen failed while presenting a ductile behavior due to the exhibited neck.

(a)	(b)
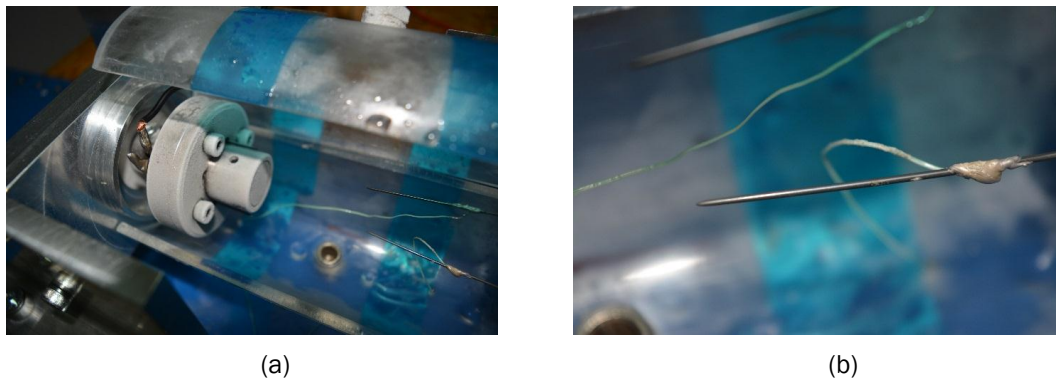
Figure 73: Failure of SMA wire specimens during fatigue testing: (a) chamber view of the specimens and (b) close up view of the specimens

Although the specimen that failed first exhibited a ductile failure the other specimen of the pair failed while presenting brittle behaviour. This can be explained if it is considered that after the failure of the first specimen of the pair the developed stress on the remaining specimen is instantly doubled. In the photos of Figure 74 the two failed specimens are presented. Figure 74a shows the specimen that failed in a ductile manner while in Figure 74b the brittle failure of the other specimen is depicted.

(a)	(b)
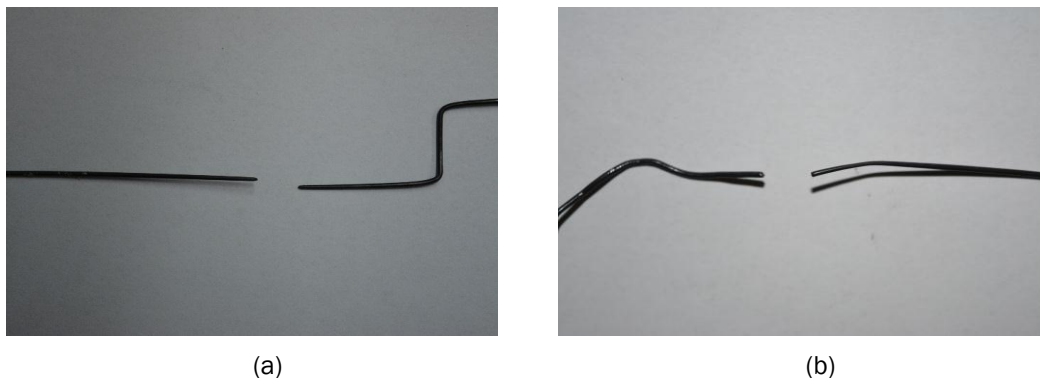
Figure 74: Failure of the specimens' pair: (a) ductile failure and (b) brittle failure.

The obtained fatigue life of 1600 actuation cycles to full transformation under the load of approximately 200 MPa agrees slightly with the results presented in other studies. The main variables that affect the fatigue life and might be vague when comparing the results published by other research are the exact composition of the alloy, the heat treatments or other procedures entailed and the heating/cooling rates applied. Heating and especially cooling rates are very difficult to be controlled and kept to be consistent during the experimental procedure. In order to address the effect of heating rate while using Joule heating several specimens where subjected to various electrical current values. During these tests it was proved that if the heating procedure is faster than 30°C/s then the material with fail before reaching 50 thermal cycles. In some of the cases tested the specimen failed after performing only 6 cycles. Because of the time required for the experimental procedure and the various variables that need to be controlled to obtain consistent results, fatigue life testing is an ongoing procedure.

3.3 Manufacturing of the prototype

3.3.1 Specifications and target functionalities

The target shape of the morphing section has been defined through aeroelastic analysis conducted by National Technical University of Athens (NTUA) in the framework of INNWIND.EU project. A first approach considers a single flap with variable length. NTUA has provided charts that relate the percentage of chordal moving length represented by the flap and the angular rotation β with the variation of coefficient of lift at a given reduced angular velocity (k) of the blade and a known angle of attack (a.o.a.). Table 18 presents the required flap rotation (*β*) in order to achieve a specific change in lift coefficient for flaps with length (*C*) equal to 10%, 30% and 50% of the chord length. The design parameters are graphically represented in Figure 75.
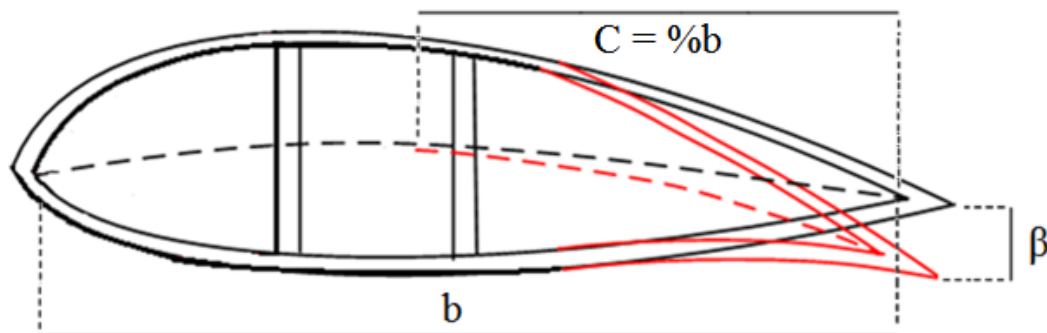
Figure 75: Airfoil design parameters 9Courtesy of NTUA)

These results have been acquired considering a 4 degrees angle of attack and a reduced angular velocity of 0.1. In Figure 76 the dependency of the variation of the lift coefficient on the flap length and the rotation angle is graphically illustrated. Apparently the same variation of the coefficient of lift can be achieved either by rotating a small flap by a big angle or by rotating a bigger flap by a smaller angle. More details can be found in deliverable 2.31 entitled "New concepts to control the load along the span of the blade, passive, active or mixed" and deliverable 2.23 entitled "New morphing blade section designs and structural solutions for smart blades".

Table 18: Dependency of ΔCL on flap length and rotation angle

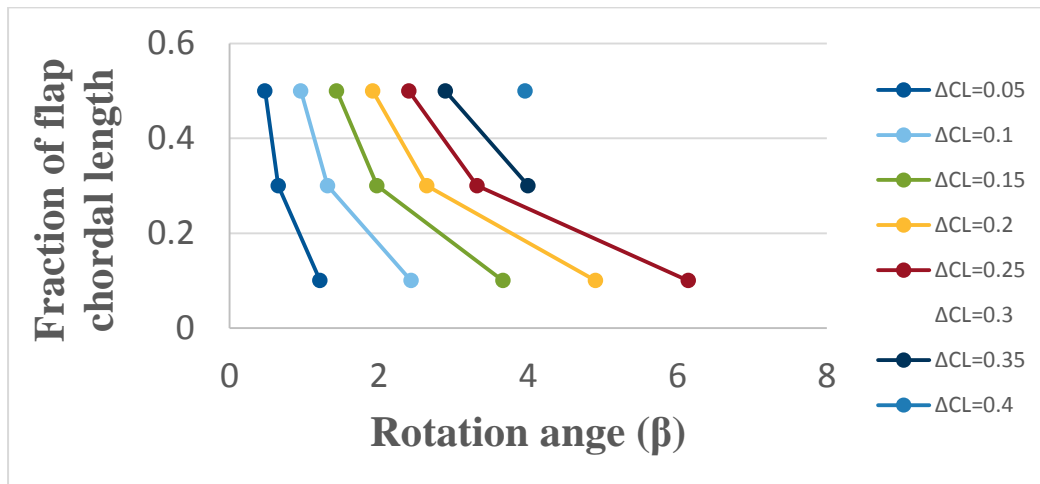| ΔCL(frq0.1,4deg)	β(deg)		
	C=10%	C=30%	C=50%
0.05	1.214024181	0.653732	0.476472
0.1	2.433357837	1.313568	0.956258
0.15	3.663361188	1.975362	1.436287
0.2	4.904238813	2.642064	1.917821
0.25	6.1454726	3.315998	2.401998
0.3	-	3.998429	2.891498
0.35	-	-	3.393049
0.4	-	-	3.961339

Figure 76: Chart relating percentage of chord length and angular rotation β to the variation of coefficient of lift (provided by NTUA)

Using the above mentioned target flap rotation the Table 19 that summarizes the maximum required trailing edge rotation for a single flap is derived.

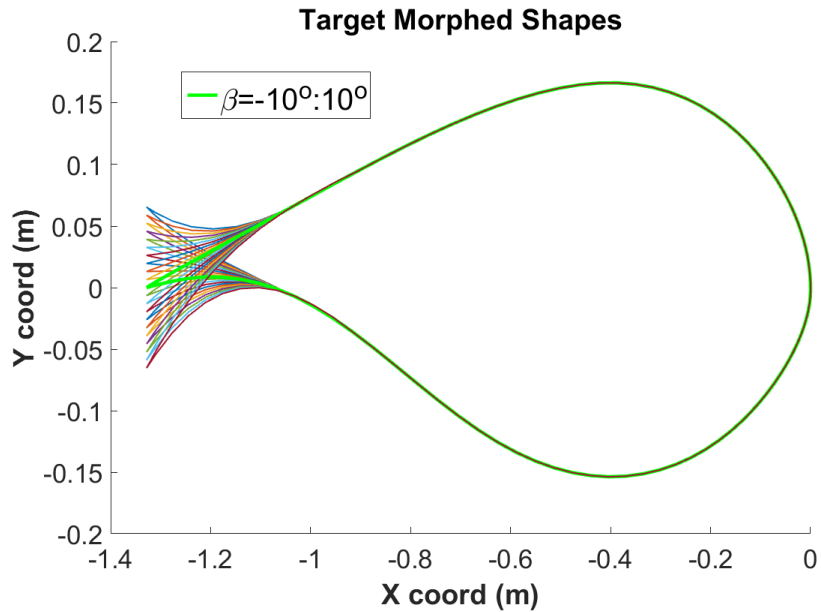**Table 19:** Maximum deflection values of the morphing flap

Flap length as chord percentage (%)	Maximum rotation angle β (degrees)
10	±6.145
30	±3.998
50	±3.961

A second approach defines the target morphed shape by considering a smooth change at a portion of the camberline profile instead of a single flap. The aeroelastic investigations conducted by NTUA resulted in the morphed shapes presented in Figure 77. The y coordinate of the airfoil's target camberline is given by equation (1) while for a moving segment with length equal to 30% of the chord, the function $f(x)$ is given by equation (2):

$$y(x) = y_0(x) + f(x) \cdot c \cdot \beta \tag{1}$$

$$f(x) = \left(0.095 \frac{df}{dx}|_{x=c} - 0.2087 \right) + \left(0.778 - 0.3665 \frac{df}{dx}|_{x=c} \right) x +$$
$$\left(0.4654 \frac{df}{dx}|_{x=c} - 0.9445 \right) x^2 + \left(0.3703 - 0.19391 \frac{df}{dx}|_{x=c} \right) x^3 \tag{2}$$

where y_0 is the y coordinate of the undeformed camberline, β is the rotation angle of the moving segment in degrees; c is the chord length, $x = \dfrac{x_2}{c}$, x2 is the x coordinate of the moving segment and $\dfrac{df}{dx}$ is the slope of the moving segment at the trailing edge.

INNWIND.EU, Deliverable 2.24, Manufactured and laboratory tested scaled blades and parts of the blade

Target Morphed Shapes

(a)
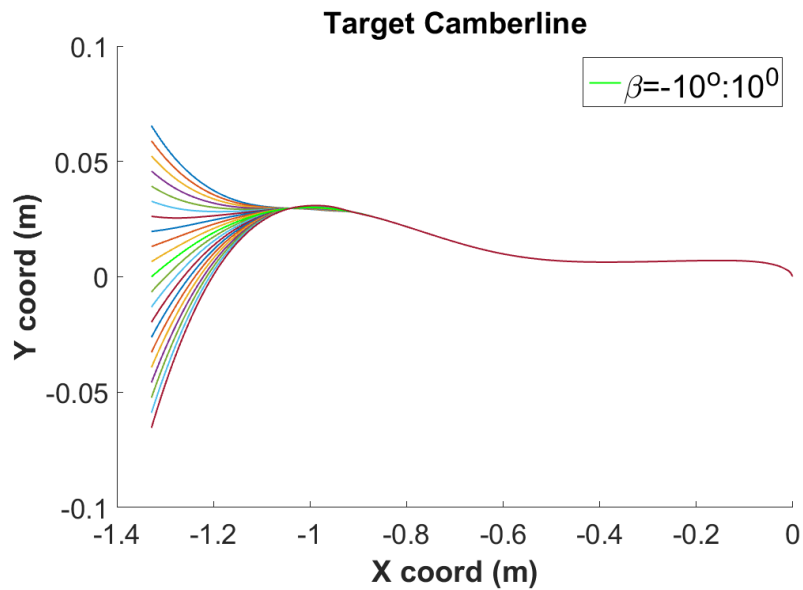
Target Camberline

(b)

Figure 77: Smooth curvature change of airfoil. a) Target airfoil profile and b) target camberline profile

The target dimensionless morphed shapes presented in Figure 77 have been derived using a slope of 3 degrees $\frac{df}{dx} = 3^o$ for rotation angles β in a range from -10 up to 10 degrees while the chord of the scaled prototype has been used *c=1.32m*. Using the aforementioned equations the trailing edge displacement for each rotation angle is calculated and presented in Table 20.

Table 20: Trailing edge displacement for the concept of the smooth curvature change

Rotation angle (degrees)	Trailing edge displacement (m)
±0	±0
±1	±0.0065
±2	±0.0131
±3	±0.0196
±4	±0.0262
±5	±0.0327
±6	±0.0393
±7	±0.0458
±8	±0.0524
±9	±0.0589
±10	±0.0655

Aim of the conducted tests on the prototype is to achieve the defined trailing edge tip deflection in each case and the displacement of the rotation point of the flap with length equal to 10% of the chord. The first set of tests was performed without the presence of aerodynamic loads while in the second one representative aerodynamic loads were applied. In order to calculate the representative aerodynamic loads, the pressure coefficient (C_P) distribution provided by NTUA and the scaled geometry of the airfoil were used. To calculate the relative pressure, equation (3) was used:

$$Pressure = C_P \cdot \frac{d_{air}}{2} \cdot \omega^2 \tag{3}$$

where d_{air} is the air density and is equal to 1.2 kg/m³, while ω^2 is given by :

$$\omega^2 = (omega \cdot R)^2 + v_{wind}^2 \tag{4}$$

where v_{wind} is the air velocity and consider to be equal to 10 m/s, R is distance of the section from the rotor hub and *omega* is calculated by

$$omega = 2 \cdot \pi \cdot f \tag{5}$$

where *f* is the 1P rotation frequency of the rotor and is equal to 0.16 Hz.

Using the chord length of the scaled prototype and the width of the section the pressure distribution presented in Figure 78 is derived. In Figure 79 the pressure distribution on the isolated segment located at the back of the shear box is illustrated.
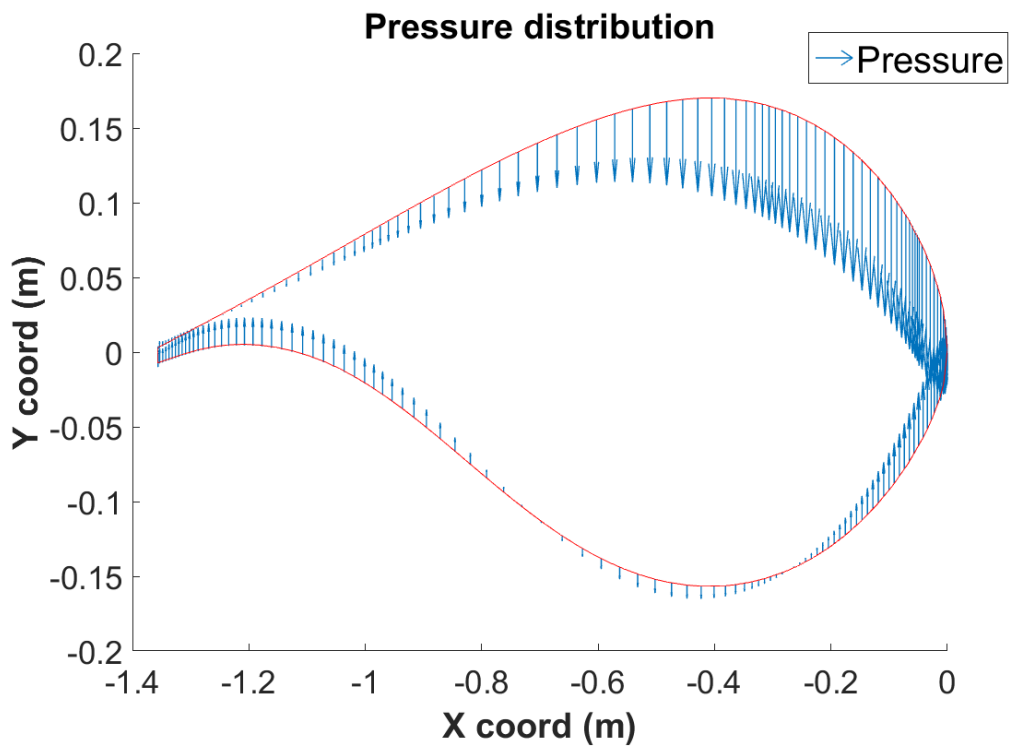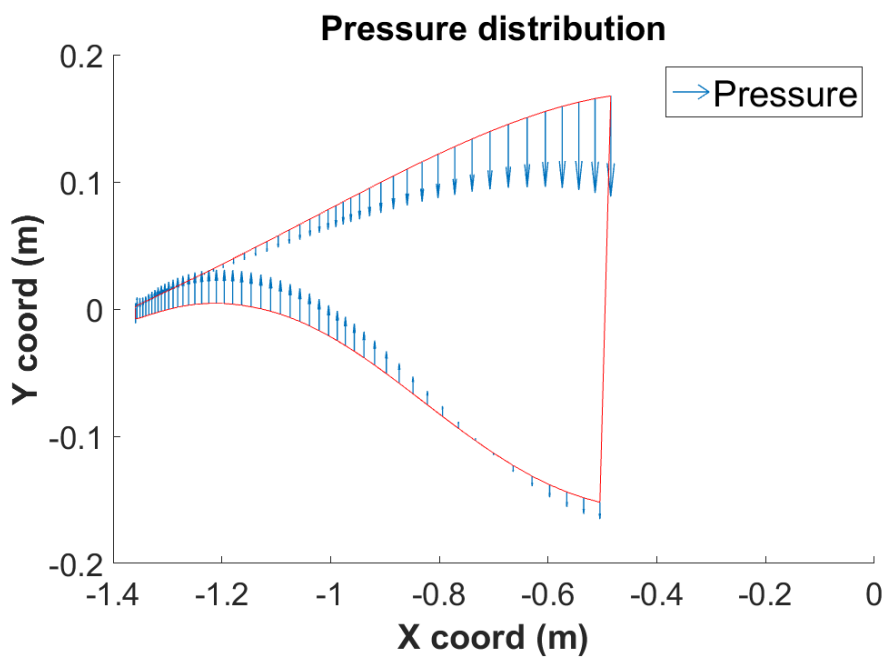
Figure 78: Pressure distribution in scaled prototype

Figure 79: Pressure distribution for the moving part

INNWIND.EU, Deliverable 2.24, Manufactured and laboratory tested scaled blades and parts of the blade

Using the derived pressure distribution and the geometry of the scaled prototype, the respective aerodynamic loads on the moving segments of 10%, 30% and 50% of the chord length are calculated and presented in Table 21.

Table 21: Calculated forces applied on each moving segment

Moving Segment (C%)	Applied Force (N)
0-10	0.624
10-30	26.316
30-50	206.3

3.3.2 Design of the prototype

In this section the prototype manufacturing is described. The baseline concept is the outcome from the deliverable D2.23 "New morphing blade section designs and structural solutions for smart blades". The morphing concept considers the geometry of the airfoil section located at x/l=0.772 of the blade span with a chord length equal to 3.32m. In the initial concept three morphing segments were adopted, capable to move to both directions by using SMA wire actuators (Figure 80). In this concept either the 50%, the 30% or the 10% of the chord length was able to move.
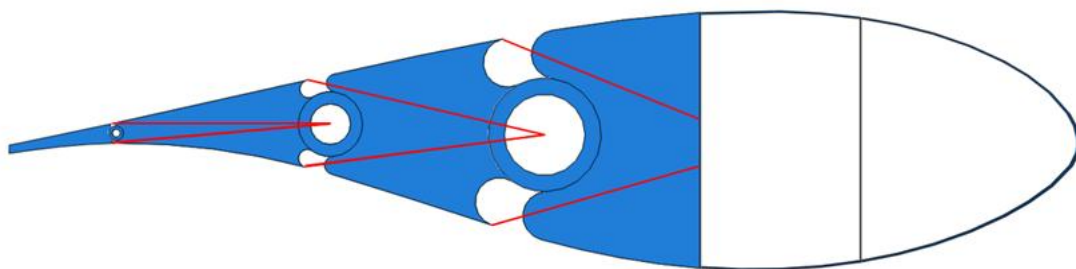
Figure 80: Downselected morphing concept

The baseline geometry of the morphing section was scaled down by a factor of 2.5 resulting in a chord length equal to 1.33m , in order to fabricate its components and test it in the laboratory facilities. For the prototype fabrication of the morphing section, only the trailing edge, behind the shear webs was designed and manufactured (Figure 81). The morphing section consists of two ribs which entail SMA wire actuators for clockwise and counter-clockwise rotation. The scaled distance between the two ribs is equal to 0.35m. On each rib, the actuators that are responsible for the clockwise rotation are located on the one side while the actuators responsible for the counter-clockwise movement are located on the other side of the camberline. The diameter of each SMA wire actuator is equal to 1mm. In order to interconnect the two ribs and synchronize their movement, glass rods were used. An overview of the prototype design is given in Figure 82.
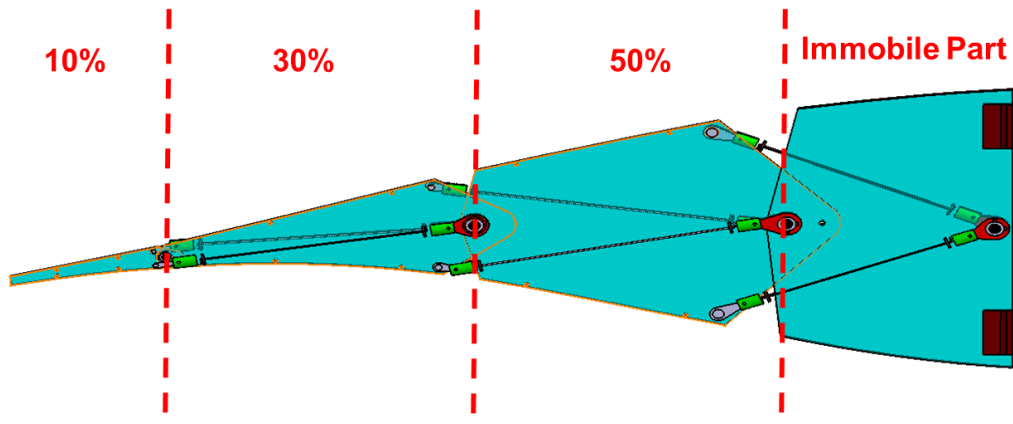
Figure 81: Morphing rib with moving and immobile segments
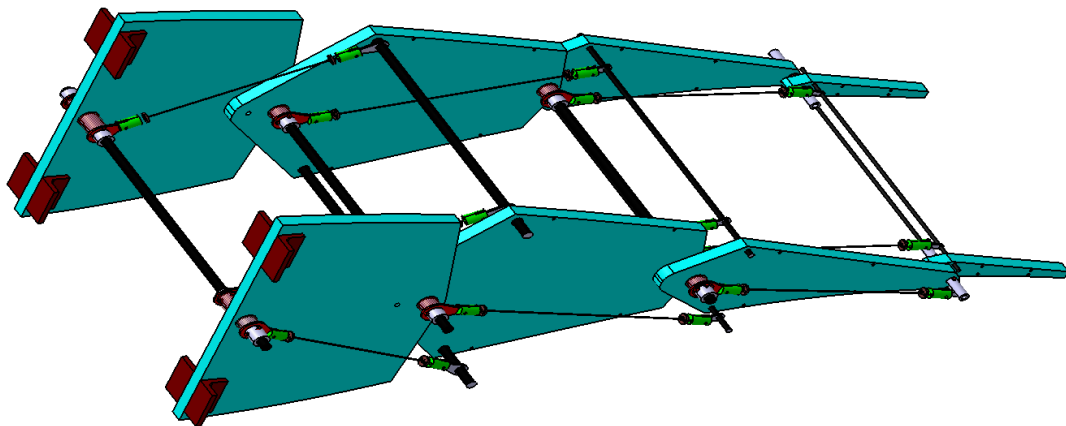

Figure 82: Overview of the morphing section design

In order to attach the SMA wire actuators to the host structure and avoid any slippage during actuation, special consideration was given in the design of the jigs (Figure 83). The two front components of the jig were fastened together via bolts that provided adequate friction to clamp the SMA wire between them. The main body of the jig is pinned to the lug allowing the relative rotation between the wire axis and the supporting axis that connects the two ribs. This configuration is repeated at both ends of each actuator for attachment purposes.
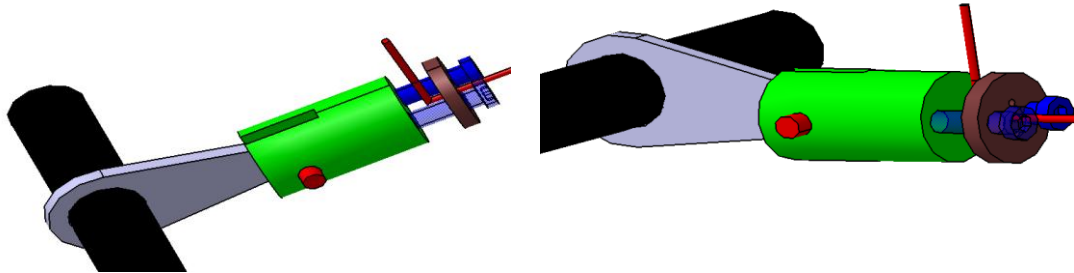
Figure 83: Jig for mounting the SMA actuator to the host structure

3.3.3 Fabrication of prototype

The various parts were fabricate and assembled together in order to form the two ribs of the prototype. In this section details about their design and fabrication are given.

The parts consisting the rib were fabricated as sandwich structures using glass fiber reinforced plastic (GFRP) (material: HexPly 1454/43%/664) for their skin and balsa wood as the core material. Each skin was made of 8 biaxial layers with thickness of 0.25mm while the balsa core had a thickness of 10mm. For the fabrication of the skin components, four GFRP square plates with dimensions of 550x410mm^2 were fabricated as shown in Figure 84. Then the skins for each rib's segment were extracted from the plates through hydro-cut process.
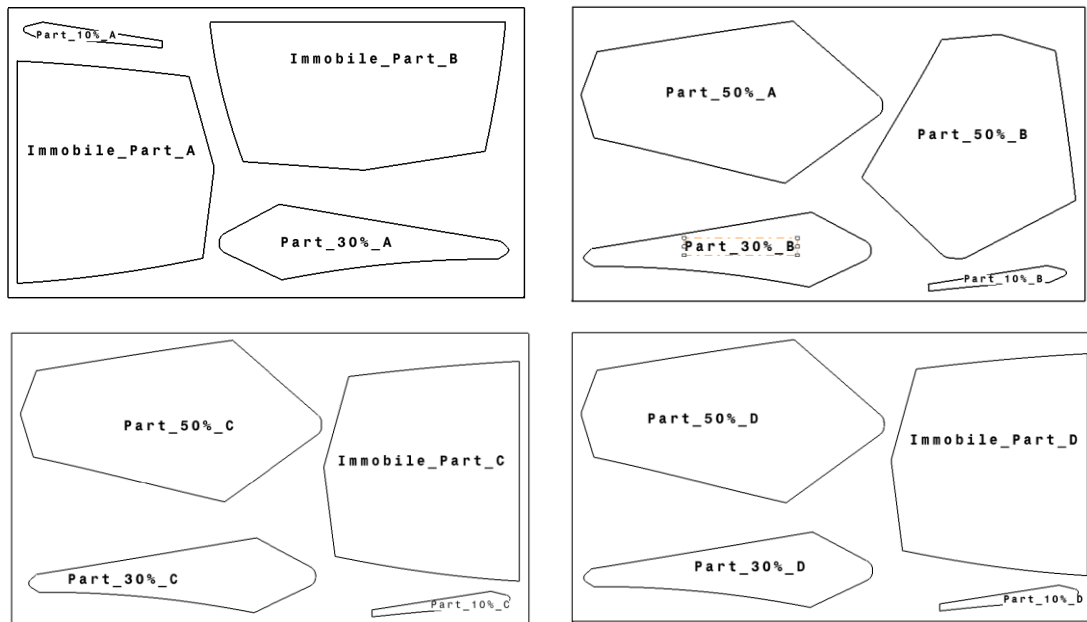
Figure 84: Illustration of four GFRP plates for the fabrication of skin components

Following the sandwich structures were formed by bonding the skins and the core material, using a two-component epoxy glue. In Figure 85 the parts consisting the two ribs are presented.

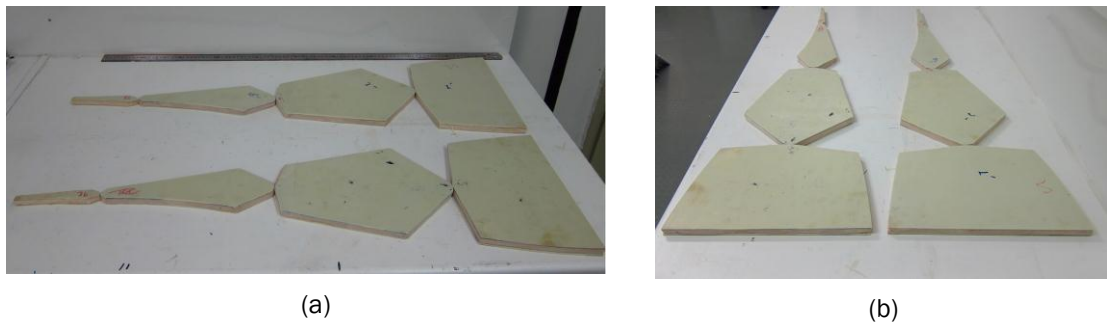(a)   (b)

Figure 85: Sandwich rib components; a) side view and b) fore-aft view

The remaining parts used for the assembly of the morphing section were fabricated in the university machine shop and are shown in Figure 85.

In Table 22 a summary of the number of the fabricated parts and the respective material is given.

Table 22: Summary of the fabricated parts

Part No	Number of pieces	Description	Material
1	4	Front lug connector for the actuator used for the 10% chord length segment	Aluminum
2	4	Front lug connector for the actuator used for the 50% chord length segment	Aluminum
3	4	Front lug connector for the actuator used for the 30% chord length segment	Aluminum
4	24	Jig for actuator mounting	Stainless steel
5	24	Locking head for actuator mounting	Stainless steel
6	4	Spacer intervening between rib components	Plastic
7	2	Rear lug connector for the actuator used for the 10% chord length segment	Aluminum
8	4	Rear lug connector for the actuator used for the 30% chord length segment	Aluminum
9	4	Rear lug connector for the actuator used for the 50% chord length segment	Aluminmum
10	4	Axle for mounting the 30% and 50% chord length rib components	Plastic
11	2	Axle for mounting the 10% chord length rib components	Plastic
12	2	Axle for mounting the immobile rib components	Plastic
13	2	Spacer intervening between 10% and	Plastic

|		30% chord length rib components	
14	12	Actuator spacers	Plastic
15	3	Axle for mounting the actuators	Plastic

The parts described in the previous paragraphs were assembled together in order to form the two morphing ribs. In each rib component two actuators were mounted, with the front end of each one attached in the current component and the rear end connected to the subsequent component, in order to move it to both directions. In Figure 86 details of the mounting system of the actuator are presented.

(a)

(b)
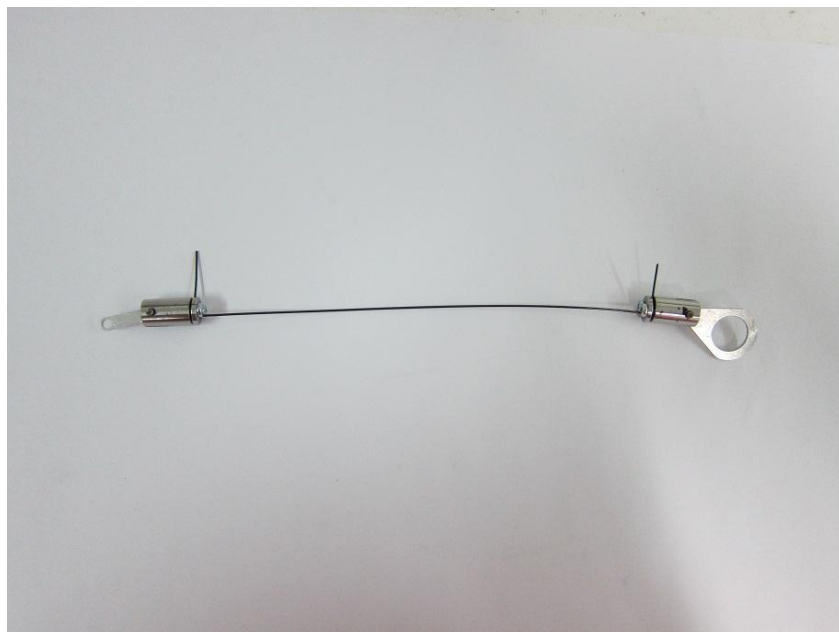
(c)

Figure 86: Details of jig for actuator mounting: a) actuator placed inside the jig, b) fastened jig assembly and c) complete assembly of the actuator mounting system.

Glass rods were used to connect the two morphing ribs and synchronize their movement. The assembled morphing section was mounted on a stiff and bulky test rig in order to be tested and characterize its functionality (Figure 87).

Figure 87: Morphing section prototype mounted on the test rig

3.4 Experimental setup for the prototype functionality tests

In order to perform the functionality tests of the scaled prototype and record its response, numerous devices were used to trigger the actuators and measure the response of the structure.

The temperature of the SMA actuators was elevated via Joule heating. To provide the required power a programmable power supply was used (Figure 143). Their temperature was monitored through thermocouples (Figure 149) while the displacement was measured through a Laser Doppler Vibrometer (LDV) presented in Figure a and a Laser triangulation displacement sensor (Figure 146b). In order to record the output of the temperature sensors and the LDV, the National Instrument (NI) chassis SCXI-1000 (Figure144a) equipped with signal conditioning modules NI SCXI-1120 (Figure144b) and SCXI-1140 (Figure144c) was used. The connection of the thermocouples to the respective module was realized through the NI SCXI-1320 (Figure a) terminal block while the out of LDV was connected via the NI SCXI-1305 (Figure 145b) terminal block. Subsequently, the chassis was connected to a Windows XP server through a PC-MIO-16XE-10 data acquisition card (DAQ) for simultaneous measurement of the displacement and temperature. The whole experimental process was monitored and controlled through a Virtual Instrument (VI) which was developed on NI Labview software (Figure 88). The developed VI was able to record the temperature and the displacement data and also to control the supplied power provided to the actuators by the power supply in order to increase their temperature.
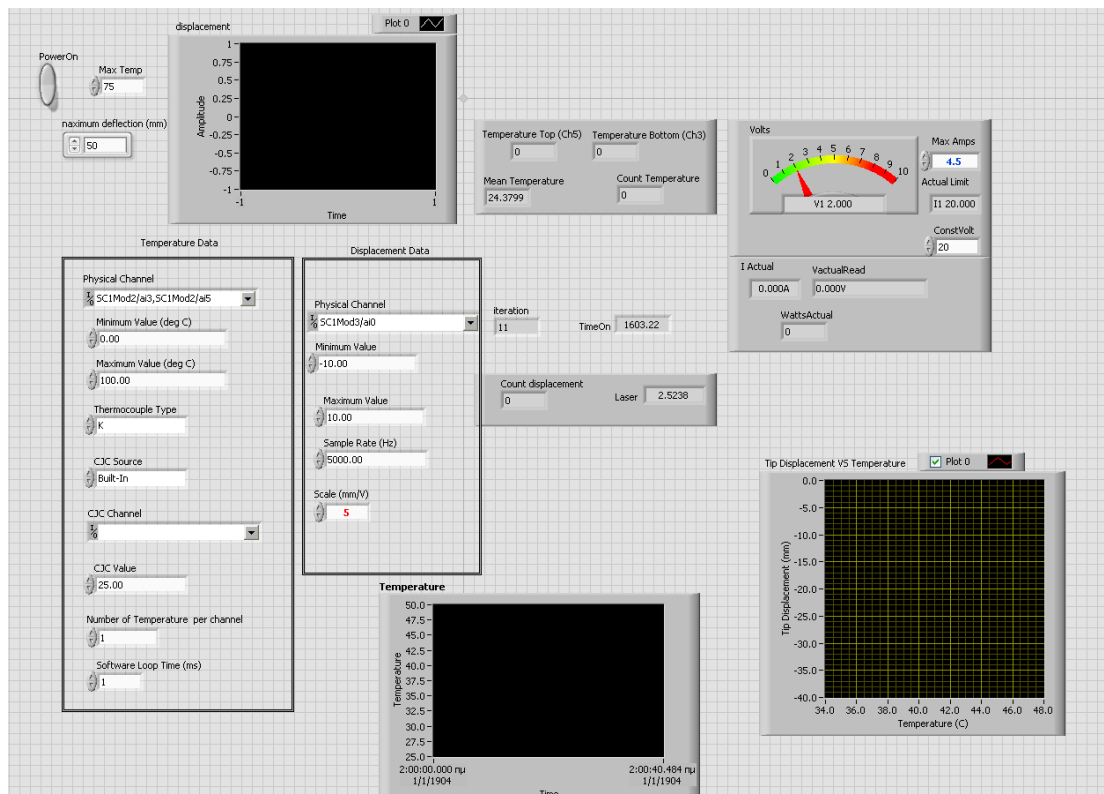

Figure 88: Virtual instrument graphical user interface

In Figure 89 a graphical representation of the testing setup for the characterization of the morphing concept response is presented.
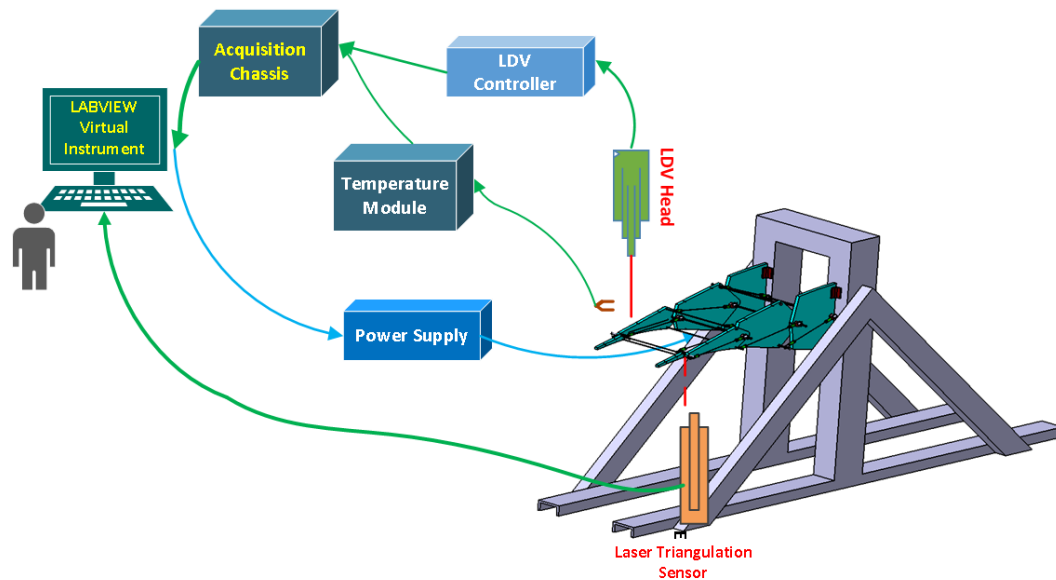

Figure 89: Graphical representation of the experimental setup for the characterization of the morphing section prototype

In Figure 90 the laboratory testing set up is presented including all the described instrumentation and the prototype.
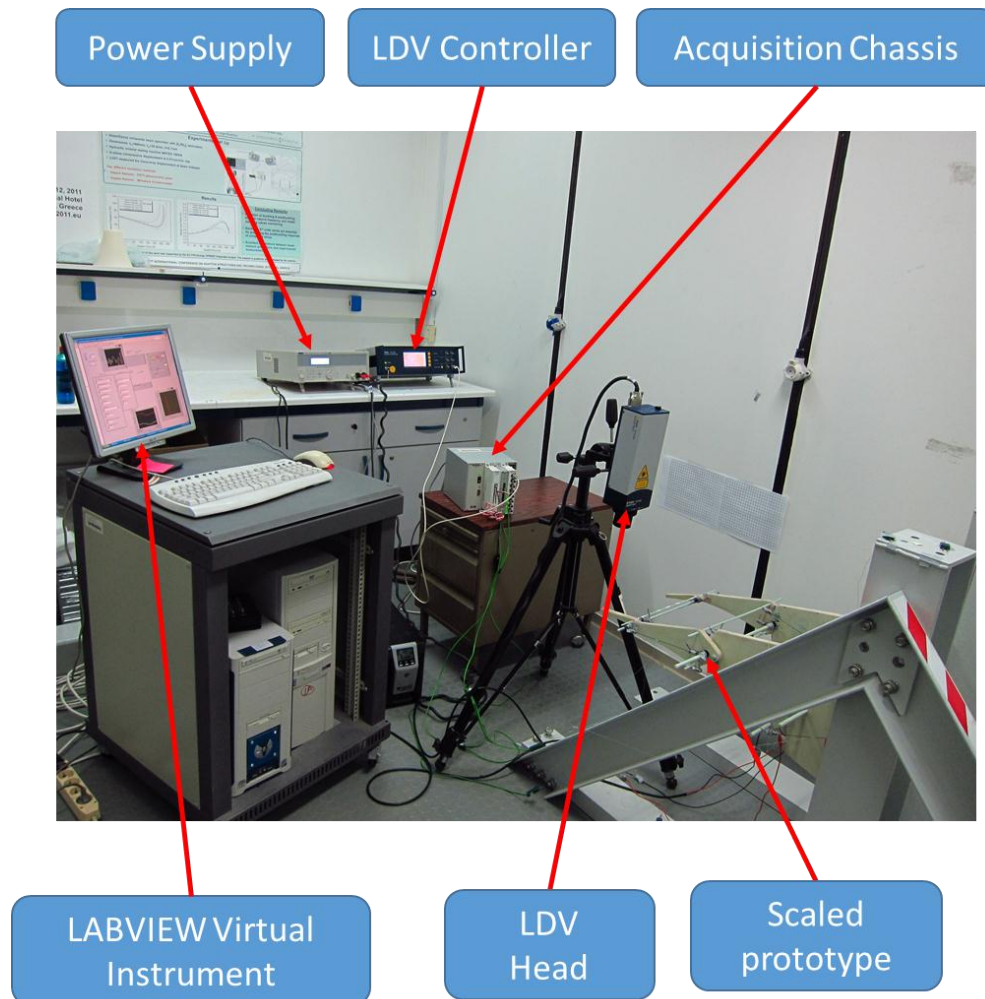
Figure 90: Laboratory testing set up

3.5 Test results

In this section the performed functionality tests of the fabricated scaled prototype and the acquired results are presented. Objective of the testing was to demonstrate the capability of the prototype to morph to predefined shapes. To this end, two sets of testing were performed; i) zero aerodynamic loading conditions and ii) representative aerodynamic loading conditions.

Initially the prototype was tested without any aerodynamic loading while subsequently tests were conducted under representative aerodynamic loads. The morphing capability of the prototype was evaluated by measuring the deflection at the tip of the trailing edge and at the rotation point of the 10% chordal length flap, whenever required (Figure 91). The deflection at the tip of the prototype was measured through the laser Doppler vibrometer (Figure a) while the displacement of the 10% rotation point was measured via the Laser Triangulation Sensor (Figure b). The flap rotation was then calculated using the achieved displacement and the dimensions of the flap in each case. Heating of the appropriate set of actuators resulted in either the clockwise (positive) or the counter clockwise (negative) rotation.
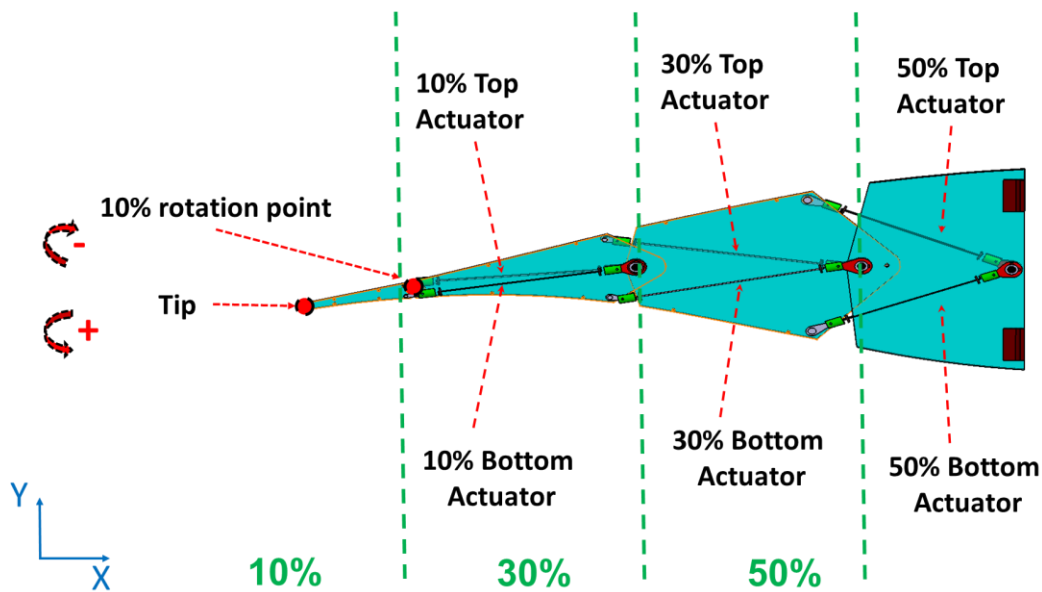

Figure 91: Representation of prototype configuration

3.5.1 Testing without aerodynamic loads

In this section the results acquired during the test campaign without the presence of representative aerodynamic loading on the prototype are presented.

Testing of 50% chord flap without loading

In this section the prototype is tested in order to evaluate its capability to rotate a flap of 50% of the chord length both clockwise (Figure 92a) and counter-clockwise (Figure 92b).
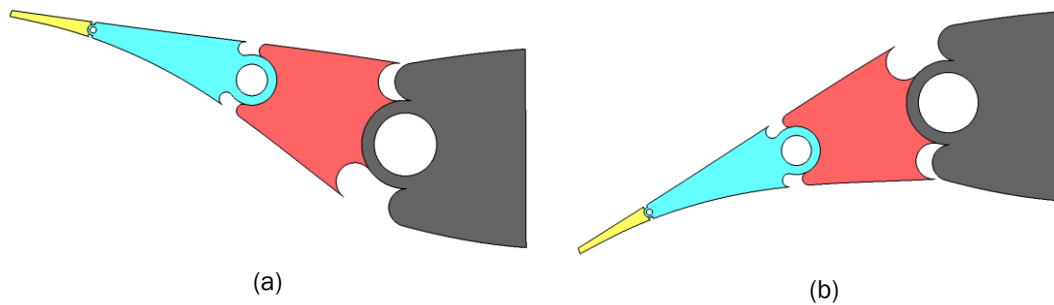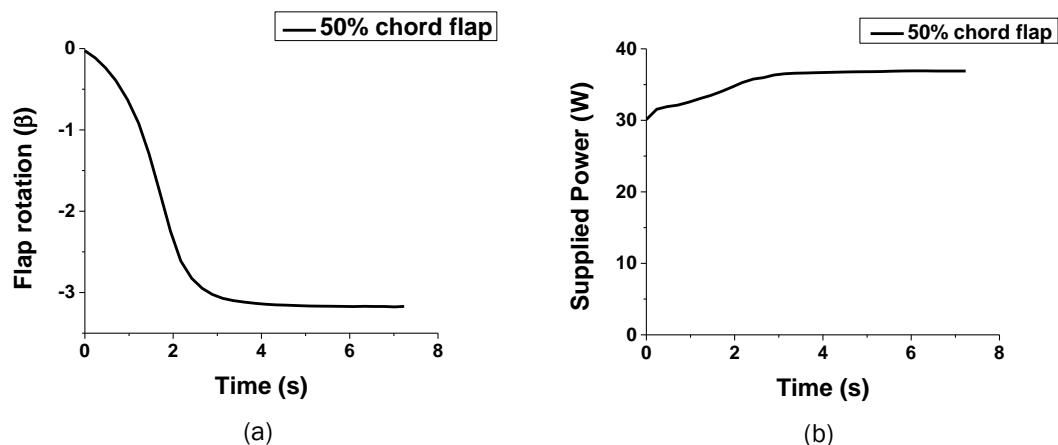

(a)	(b)

Figure 92: Flap of 50% chord length. A) Clockwise rotation and b) counter-clockwise rotation

Joule heating with constant voltage of 4.5V was applied initially at the top actuator to rotate clockwise the 50% chord flap. In Figure 93a the measured flap rotation evolution is depicted. According to the chart presented in Figure 76 the maximum achieved rotation (β=-3.17°) is able to achieve a change in lift coefficient greater than 0.3 ($\Delta C_L \geq 0.3$). In Figure 93b, the supplied power to the 50% top actuator is resented with a maximum value of 36.9 Watt, while in Figure 93c the temperature evolution of the actuator is presented. Finally, the association of the flap rotation and the temperature of the actuator is depicted in Figure 93d.
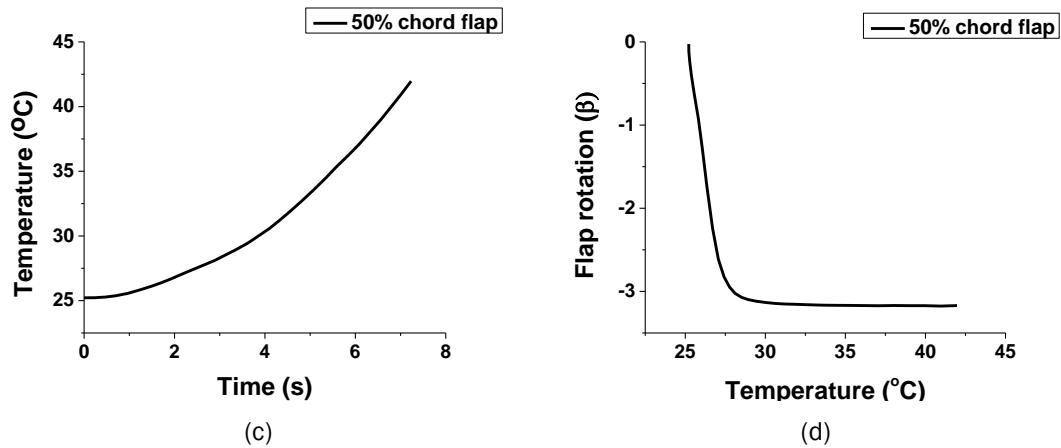

(a)	(b)

INNWIND.EU, Deliverable 2.24, Manufactured and laboratory tested scaled blades and parts of the blade

(c)   (d)

Figure 93: Measured response of 50% flap clockwise rotation; a) Rotation evolution, b) Supplied power, c) Temperature evolution and d) flap rotation versus actuator temperature

Similarly, a Joule heating with constant volt of 4.5V was applied to the 50% bottom actuator to increase its temperature and to rotate counter-clockwise the 50% flap. In Figure 94a the measured flap rotation evolution is depicted. According to the chart presented in Figure 76 the maximum rotation (β=1.95º) is able to achieve a change in lift coefficient greater than 0.2 ($\Delta C_L \geq 0.2$). In Figure 94b, the supplied power to the 50% bottom actuator is presented with a maximum value of 37.2 Watt, while in Figure 94c the temperature evolution of the actuator is presented. Finally, the association of the flap rotation and the temperature of the actuator is depicted in Figure 94d. Moving of the 50% moving segment can not achieve the maximum specified change in lift coefficient as the potential of the actuators is limited due to their small length that is not sufficient to provide the required stroke to rotate the flap to the maximum required angle. Therefore hereafter the flaps with length equal to 30% and 10% of the chord are considered for further investigation to assess the morphing capability of the scaled prototype.
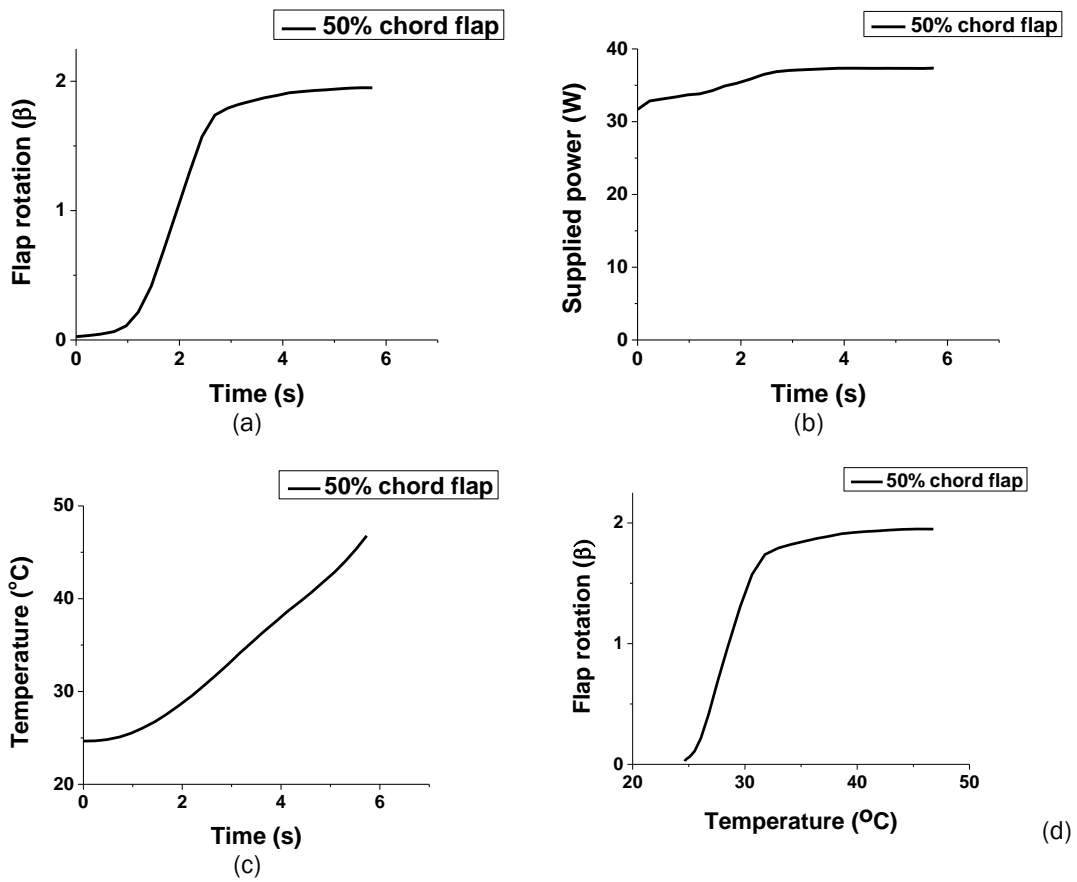
Figure 94: Measured response of 50% flap counter-clockwise rotation; a) Rotation evolution, b) Supplied power, c) Temperature evolution and d) flap rotation versus actuator temperature

In Figure 95 the undeformed and the deformed shape (clockwise rotation) of the 50% chord flap are presented.
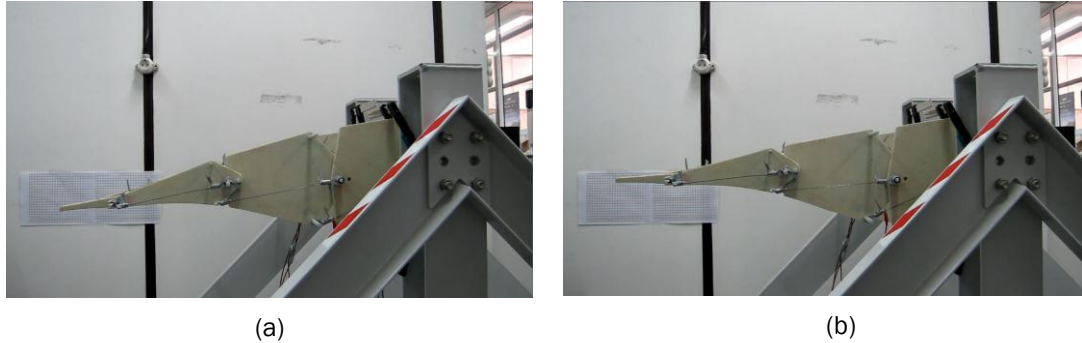
| (a) | (b) |

Figure 95: Testing of 50% chord moving flap without aerodynamic loading. a) unreformed configuration and b) clockwise rotation

Testing of 30% chord flap without loading

In this section the capability of the prototype to move a flap with length equal to 30% of the chord is assessed. To this end the SMA wire actuators responsible to move the respective section are enabled to rotate the flap clockwise and counter-clockwise (Figure 96).
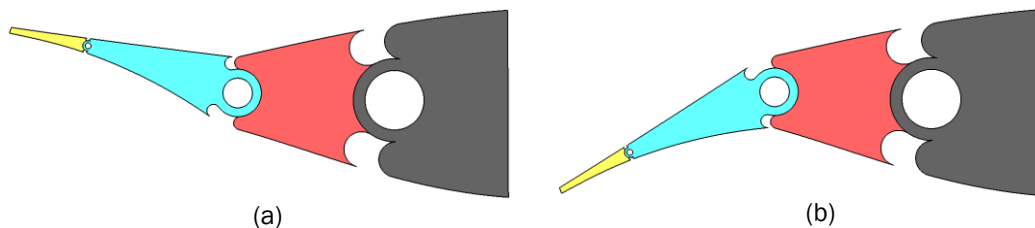

| (a) | (b) |

Figure 96: Flap of 30% chord length. A) Clockwise rotation and b) counter-clockwise rotation

In order to rotate clockwise the flap, Joule heating with constant current I=3.5A was applied to the 30% top actuator to rise its temperature while the bottom actuators remained at ambient temperature. In Figure 97a the measured flap rotation is depicted. According to the chart presented in Figure 76 the maximum achieved rotation (β=-4.2º) is able to achieve a change in lift coefficient greater than 0.3 ($\Delta C_L \geq 0.3$). In Figure 97b, the supplied power to the 30% top actuator is presented with maximum value of 11.7 Watts, while in Figure 97c the temperature evolution of the actuator is presented. In Figure 97d a correlation between the flap rotation and the actuator temperature is presented.
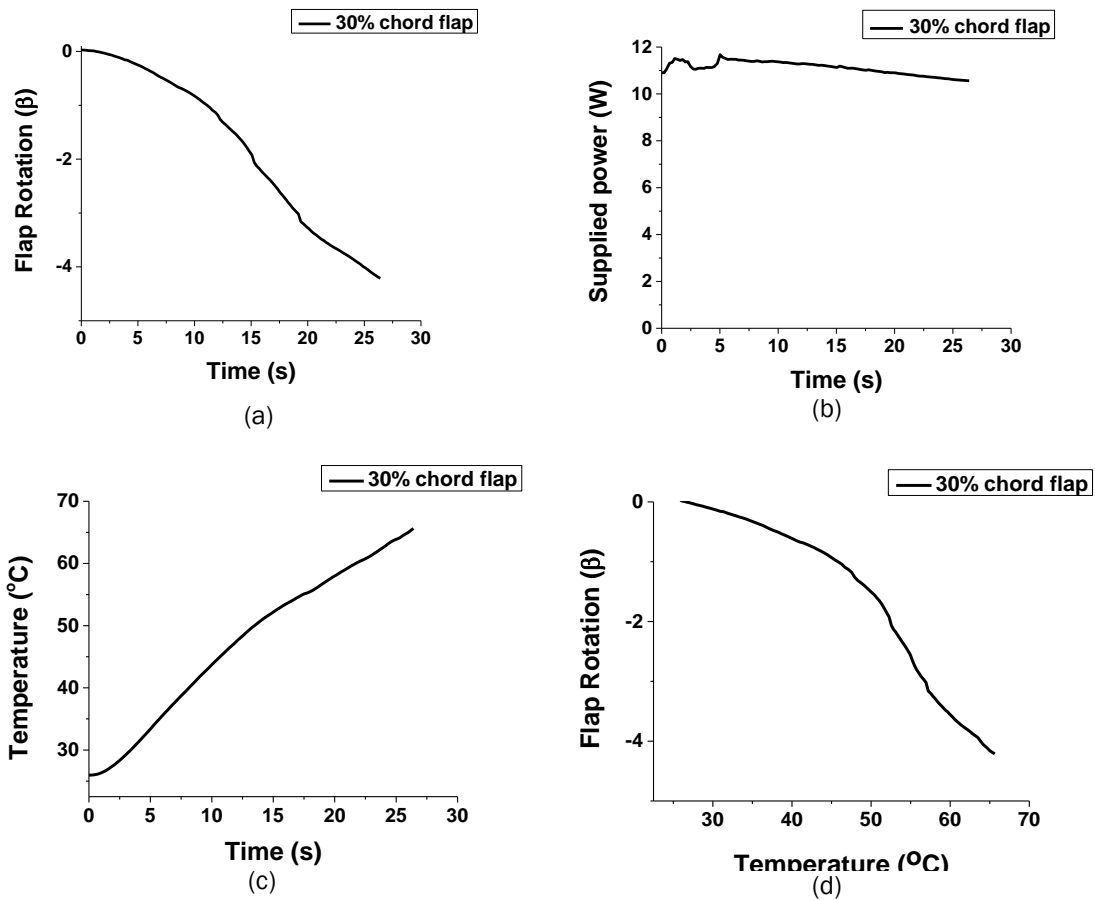
Figure 97: Measured response of 30% flap clockwise rotation; a) Rotation evolution, b) Supplied power, c) Temperature evolution and d) flap rotation versus actuator temperature.

To rotate the 30% of the chord length counter clockwise, Joule heating was applied at the 30% bottom actuators to increase their temperature, while the bottom actuators' temperature was kept constant to the ambient temperature. In Figure 98a the evolution of the flap rotation is depicted. According to the chart presented in Figure 76 the maximum achieved rotation (β=4.25°) is able to achieve a change in lift coefficient greater than 0.3 ($\Delta C_L \geq 0.3$). In Figure 98b, the supplied power to the 30% bottom actuator is presented with a maximum value of 10.7 Watts, while in Figure 98c the temperature evolution of the bottom actuator is presented. Figure 98d presents the correlation of the 30% bottom actuators' temperature and the flap rotation.
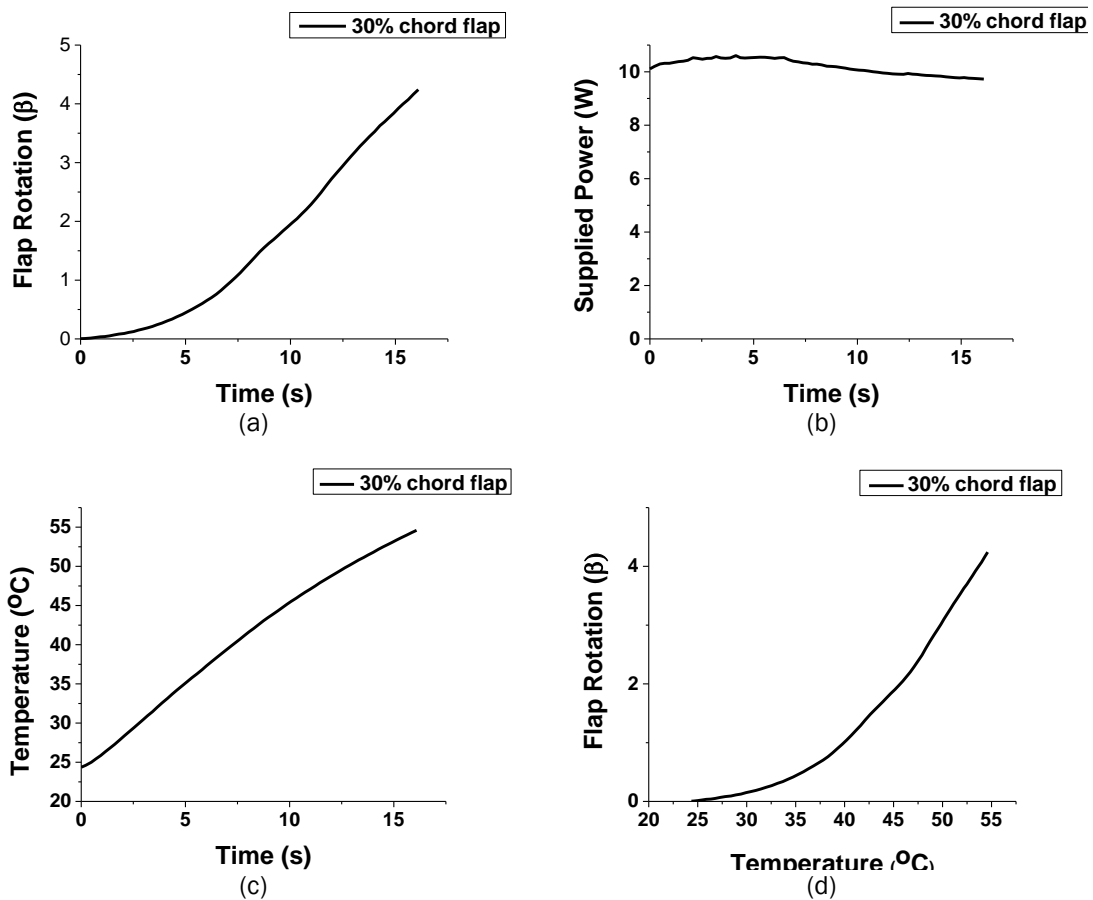
Figure 98: Measured response of 30% flap counter-clockwise rotation; a) Rotation evolution, b) Supplied power, c) Temperature evolution and d) flap rotation versus actuator temperature

In Figure 99 the undeformed and the deformed shape (clockwise rotation) of the 30% chord flap are presented.
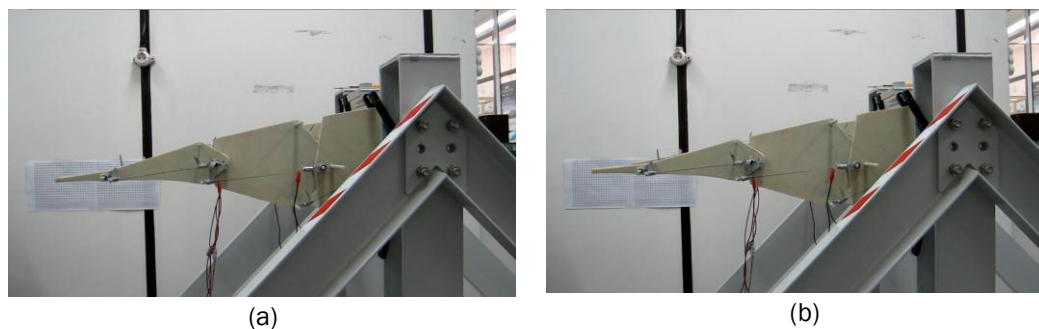

Figure 99: Testing of 30% chord moving flap without aerodynamic loading. a) undeformed configuration and b) clockwise rotation

In order to examine the capability of the prototype to rotate consecutively clockwise and counter-clockwise, from the extreme deflected positions, Joule heating was applied initially to the bottom actuators to rotate counter-clockwise the flap till the maximum angle was achieved. Then the

INNWIND.EU, Deliverable 2.24, Manufactured and laboratory tested scaled blades and parts of the blade

power was cut off and the antagonistic actuators were heated to rotate the flap clockwise. When the maximum deflection was achieved, the bottom actuators were again heated to retract the undeformed configuration of the flap. A Joule heating with a constant current I=3.5A was applied to elevate the temperature of the actuators each time. In Figure 100a the rotation of the flap is presented, while in Figure 100b the temperature of each actuator is depicted.
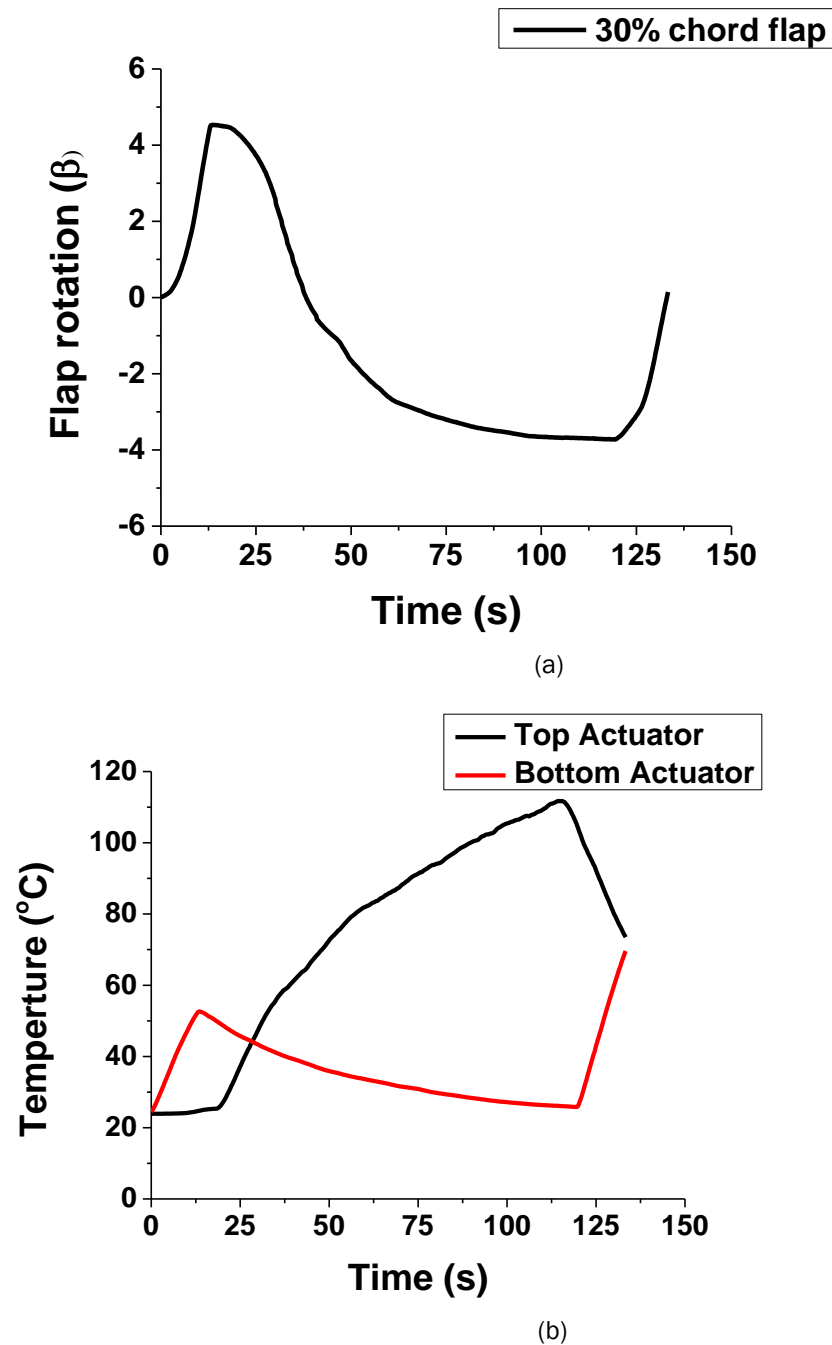

(a)

(b)

Figure 100: Measured response of 30% flap in consecutive actuation of antagonistic actuators. (a) Flap rotation and (b) Temperature of SMA actuators.

Testing of 10% chord flap without loading

In this paragraph the morphing capability of the flap with length equal to 10% of the chord is described.

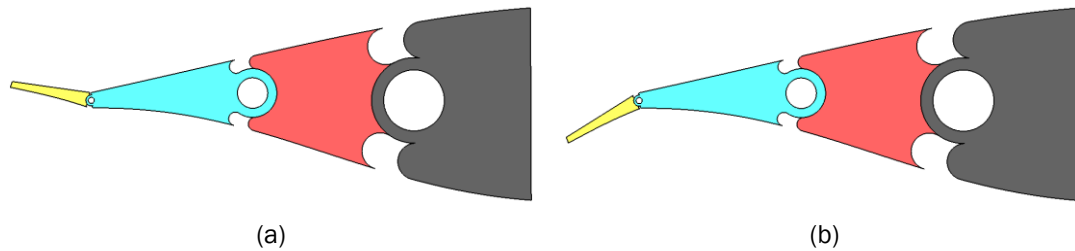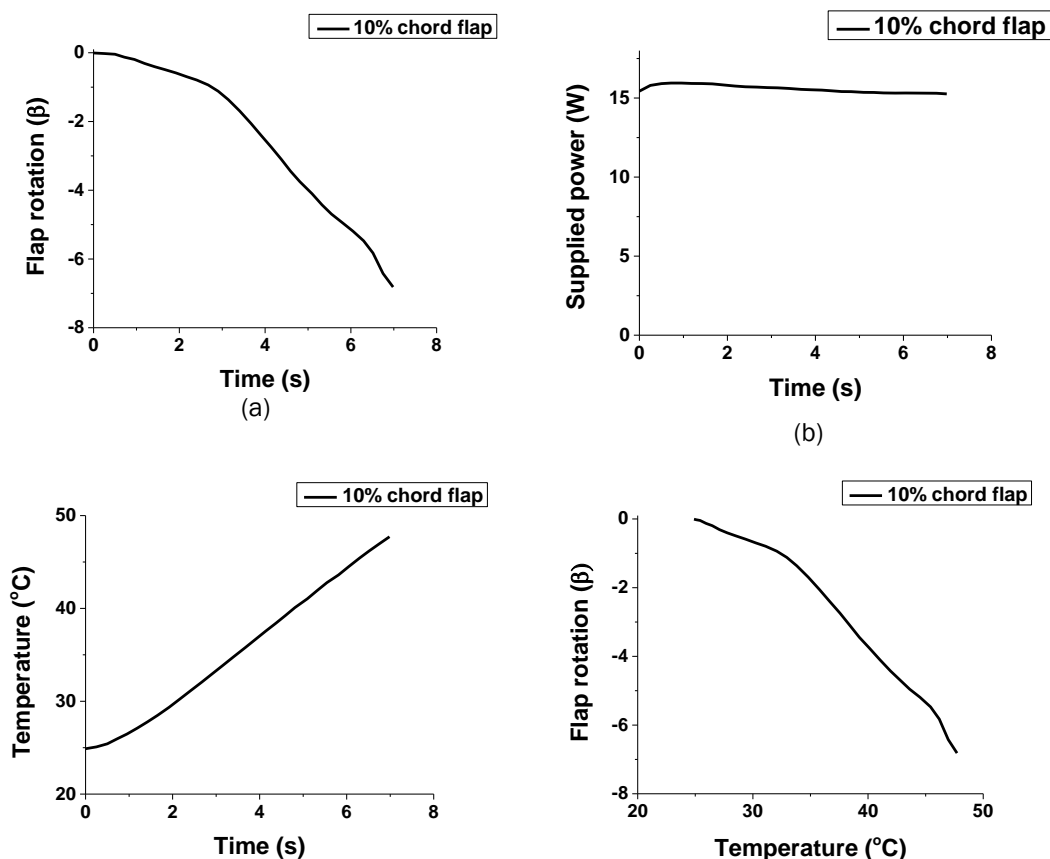(a)   (b)

Figure 101: Flap of 10% chord length. A) Clockwise rotation and b) counter-clockwise rotation

The clockwise rotation of the flap is achieved by applying a Joule heating with constant current of 4.5A to the 10% top actuators. In Figure 102a the evolution of the flap rotation is presented. The maximum achieved rotation of β=6.85˚ is able to offer a change in lift coefficient higher than 0.25 ($\Delta C_L \geq 0.25$) according to the chart presented in Figure 76. The maximum supplied power does not exceed the 16Watts (Figure 102b) while the maximum actuator temperature remains below 48°C (Figure 102c). In Figure 102d the correlation of the actuator temperature and the flap rotation is depicted.

(a)

(b)

INNWIND.EU, Deliverable 2.24, Manufactured and laboratory tested scaled blades and parts of the blade

Figure 102: Measured response of 10% flap clockwise rotation; a) Rotation evolution, b) Supplied power, c) Temperature evolution and d) flap rotation versus actuator temperature.

The counter-clockwise rotation of the 10% flap was feasible due to the heating of the 10% bottom actuators from ambient temperature through Joule heating up to 65˚C (Figure 103c). The maximum flap rotation β=6.28˚ (Figure 103a) is able to achieve and exceed the maximum change in lift coefficient $\Delta C_L \geq 0.25$ and the required power to achieve this rotation remains under 16.2 Watts (Figure 103b). Finally, the actuator temperature versus flap rotation diagram is presented in Figure 103d.
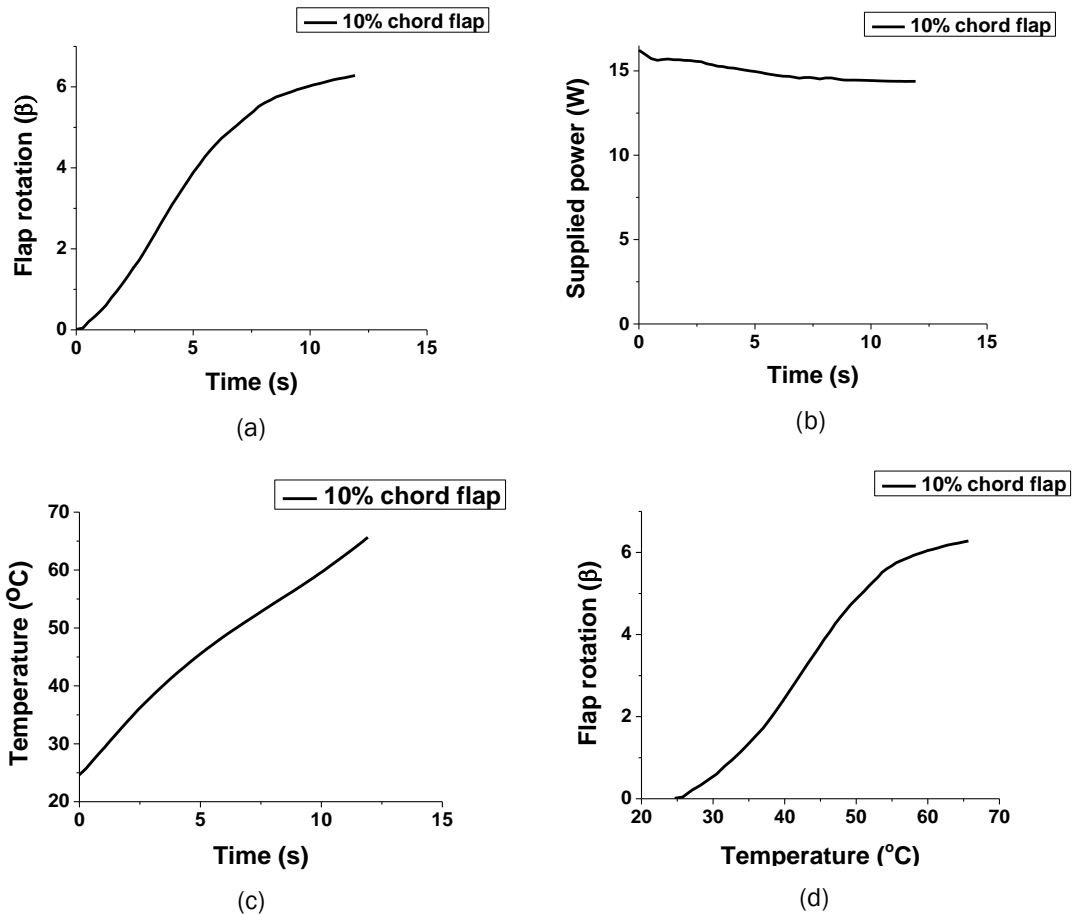

(a)

(b)

(c)

(d)

Figure 103: Measured response of 10% flap counter-clockwise rotation; a) Rotation evolution, b) Supplied power, c) Temperature evolution and d) flap rotation versus actuator temperature

In Figure 104 the undeformed and the deformed shape (clockwise rotation) of the 10% chord flap are presented.
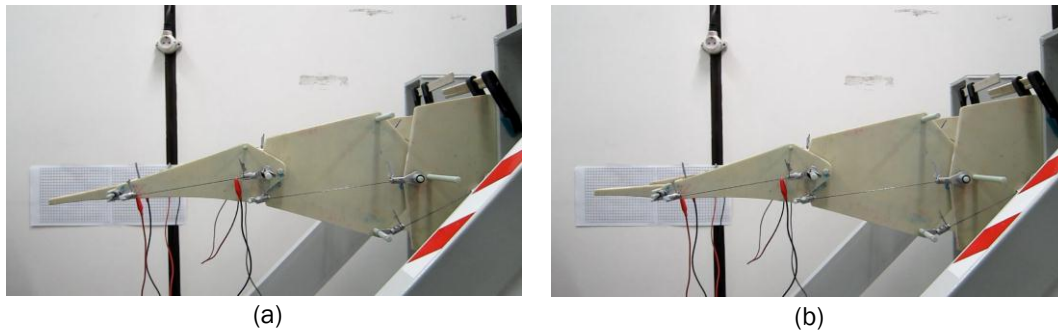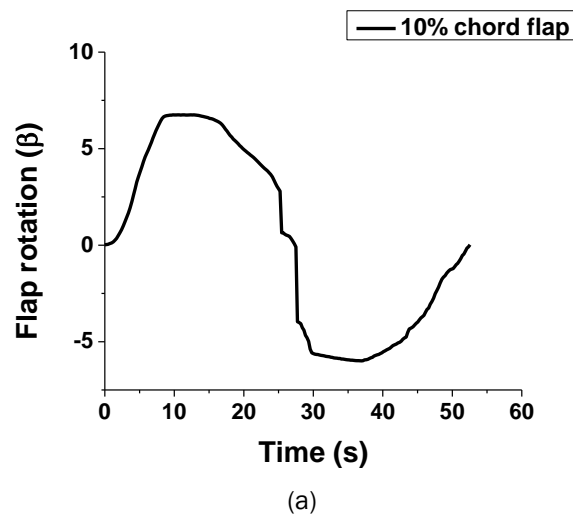
Figure 104: Testing of 10% chord moving flap without aerodynamic loading. a) undeformed configuration and b) clockwise rotation

The capability of the 10% chordal length flap to rotate consecutively clockwise and counter-clockwise was assessed by supplying power alternatively to the top and the bottom actuators. Joule heating with constant current I=4.5A was applied initially at the bottom actuators to rotate counter-clockwise the flap, then the circuit was switched to the top actuators and the flap was rotated clockwise and finally the bottom actuators were heated again to retract the initial configuration. The maximum supplied power remained under 16.5 Watts and the flap response is presented in Figure 105a while the SMA actuators temperature is depicted in Figure 105b.
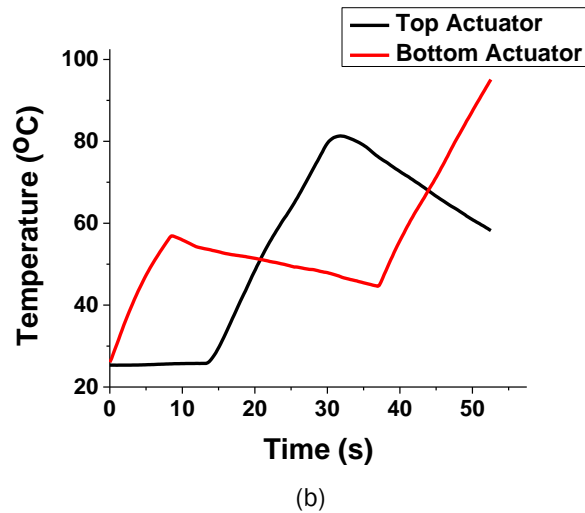

(a)

INNWIND.EU, Deliverable 2.24, Manufactured and laboratory tested scaled blades and parts of the blade

(b)

Figure 105: Measured response of the 10% flap in consecutive actuation of antagonistic actuators. (a) Flap rotation and (b) temperature of SMA actuators.

Combined movement of 30% chordal length flap and the 10% chordal length flap without loading

In order to achieve a smoother alteration on the profile of the morphing section as presented in Figure 77 the 30% chord flap and the 10% chord flap were activated simultaneously both to clockwise and to counter-clockwise direction (Figure 106).
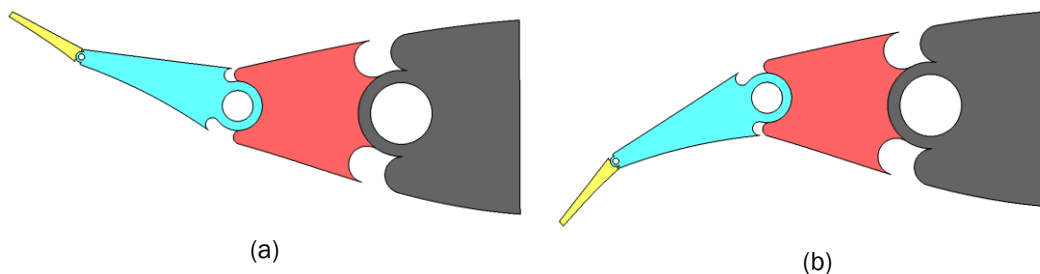

(a)   (b)

Figure 106: Smooth alteration of airfoil profile by activating simultaneously the 10% and 30% chord flap. A) clockwise rotation and b) counter-clockwise rotation

Initially the 30% and 10% top actuators were heated to morph the airfoil to the clockwise direction. The displacement at the trailing edge tip and the rotation point of the 10% flap (Figure 91) were recorded as well as the temperature of the respective actuators. The two actuators were serially connected and Joule heating was applied to both of them with constant current I=4.5A. In Figure 107a the displacement of the trailing edge tip and the rotation point of the 10% flap is presented, while Figure 107b presents the supplied power with a maximum of 35 Watts and in Figure 107c the temperature of the two actuators is presented.
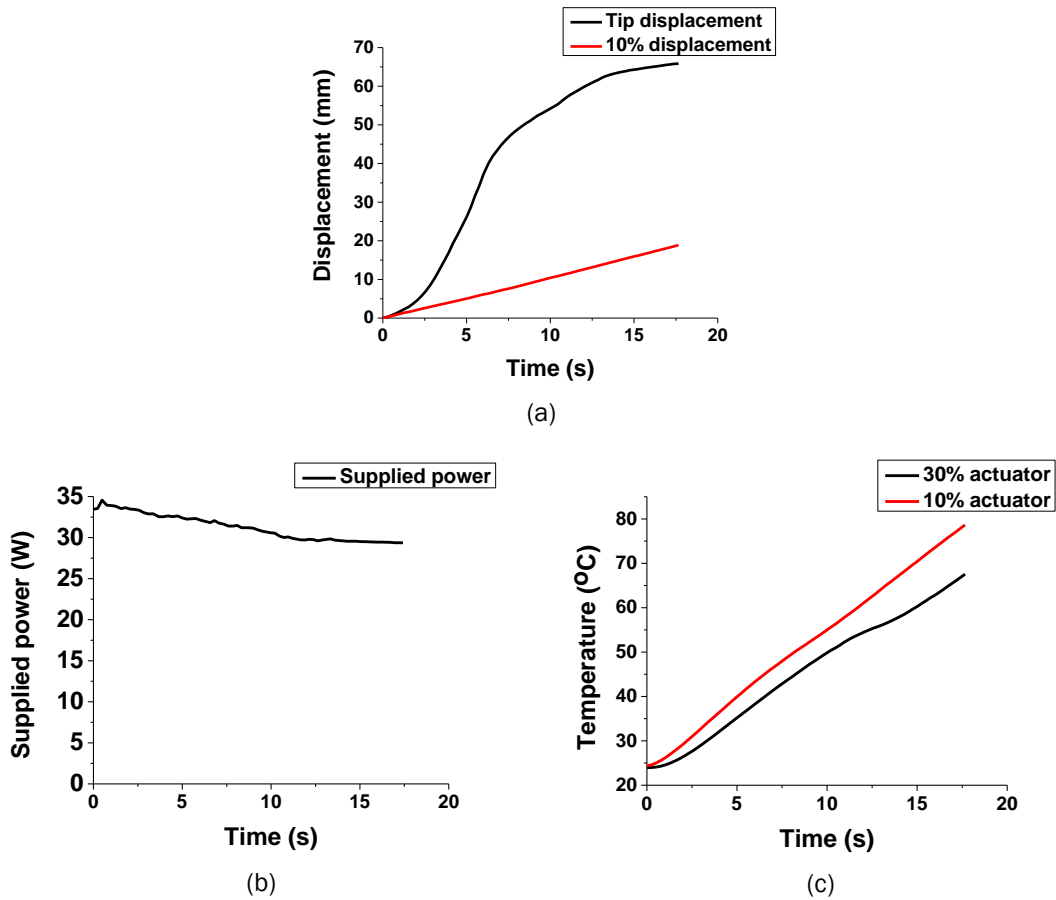
Figure 107: Clockwise rotation of the morphing section a) displacement of the two points, b) supplied power to the SMA actuators and c) temperature of the SMA actuators

Accordingly, the 10% and 30% bottom actuators were heated through Joule heating with constant current I=4.5A, to deflect the airfoil counter-clockwise. In Figure 108a the displacement of the trailing edge tip and the rotation point of the 10% flap is presented, while Figure 108b presents the supplied power with a maximum of 32 Watts and in Figure 108c the temperature of the two actuators is presented.
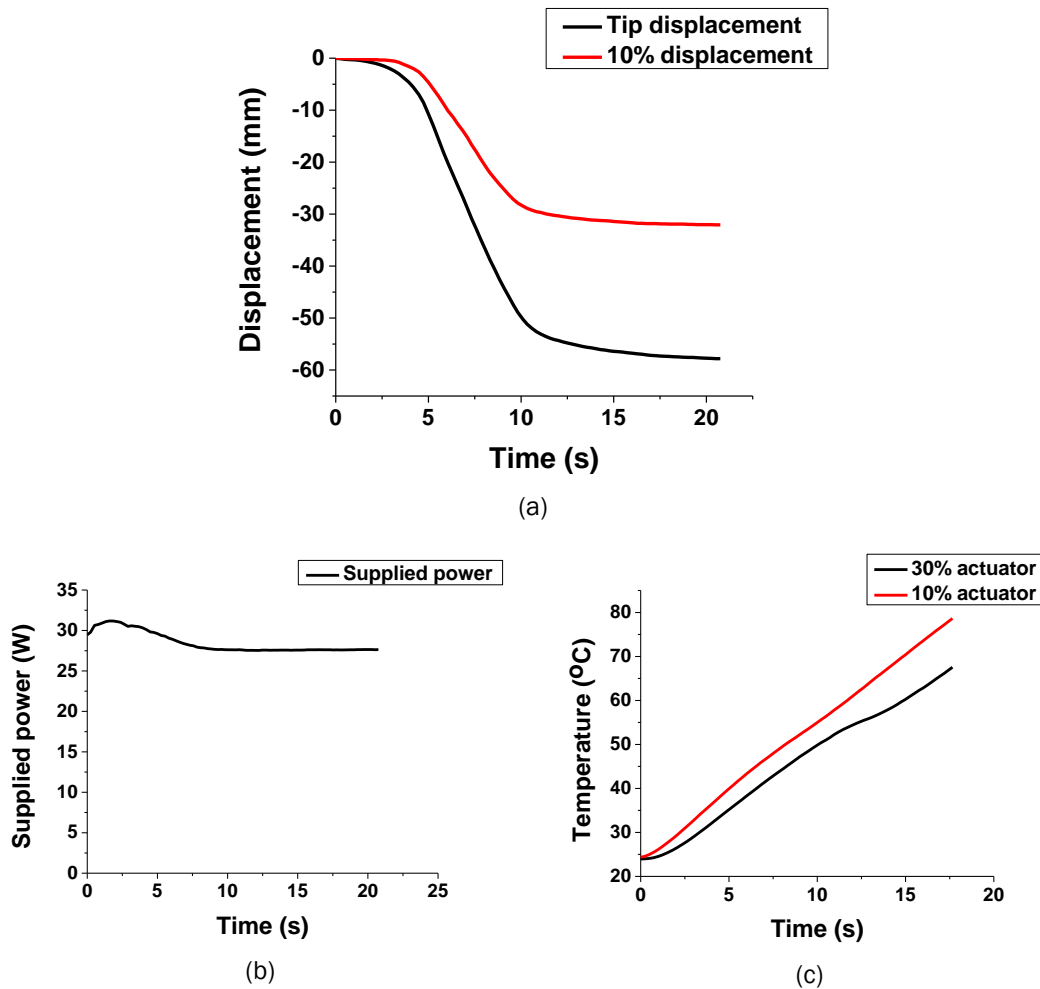
INNWIND.EU, Deliverable 2.24, Manufactured and laboratory tested scaled blades and parts of the blade

(a)

(b)

(c)

Figure 108: Counter-clockwise rotation of the morphing section a) displacement of the two points, b) supplied power to the SMA actuators and c) temperature of the SMA actuators.

In Figure 109 the position of the measured prototype is presented in association with the target camberline of the target morphed airfoil. The measured position of airfoil is depicted with black marks in Figure 109a for the clockwise rotation and in Figure 109b for the counter-clockwise rotation. As it can be seen the airfoil can achieve pretty well the target shape for the clockwise rotation with a target rotation angle of β= -10˚ while for the counter-clockwise deformation the prototype can achieve the trailing edge deflection for a target rotation angle of β=9˚ while the displacement of the 10% rotation point deviates from the target camberline for the same angle.

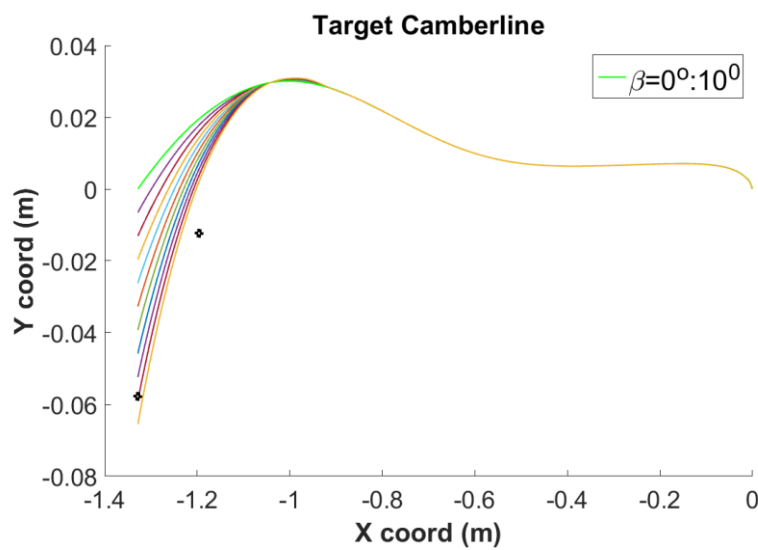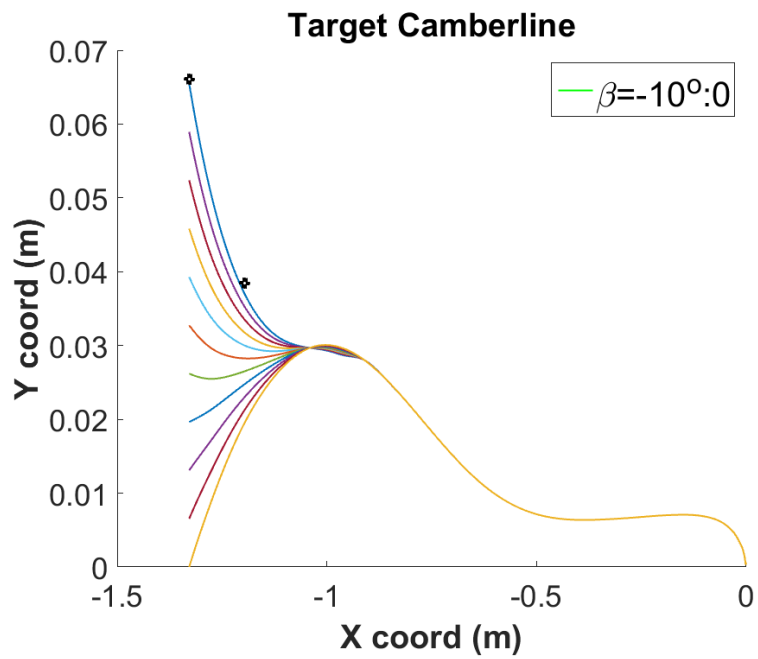*INNWIND.EU, Deliverable 2.24, Manufactured and laboratory tested scaled blades and parts of the blade*

Figure 109: Target camberline and maximum achieved deformation: a) clockwise rotation and b) counter-clockwise rotation

INNWIND.EU, Deliverable 2.24, Manufactured and laboratory tested scaled blades and parts of the blade

3.5.2 Testing under simulated aerodynamic loads

In this section the results of the prototype testing under representative aerodynamic loads are presented

Testing of 30% chord flap under simulated aerodynamic loading

In this section the testing of the 30% chord flap under representative aerodynamic loads is presented. Sandbags of appropriate weight were placed on the segment of the 10% and 30% chord flap to represent the aerodynamic loading as defined in Table 21. Joule heating with constant current I=4.5A was applied to the 30% top actuators to provoke the clockwise rotation while the bottom actuators remained at room temperature. In Figure 110a the evolution of the flap rotation is presented while the supplied power is depicted in Figure 110b. The temperature of the actuator is presented in Figure 110c and Figure 110d presents the correlation of the flap rotation to the actuator temperature. The maximum measured rotation exceeds the specified maximum rotation angle (β=-3.99°) therefore the flap is able to achieve the maximum change in lift coefficient $\Delta C_L \geq 0.30$ while the required power remains below 16.5 Watts.
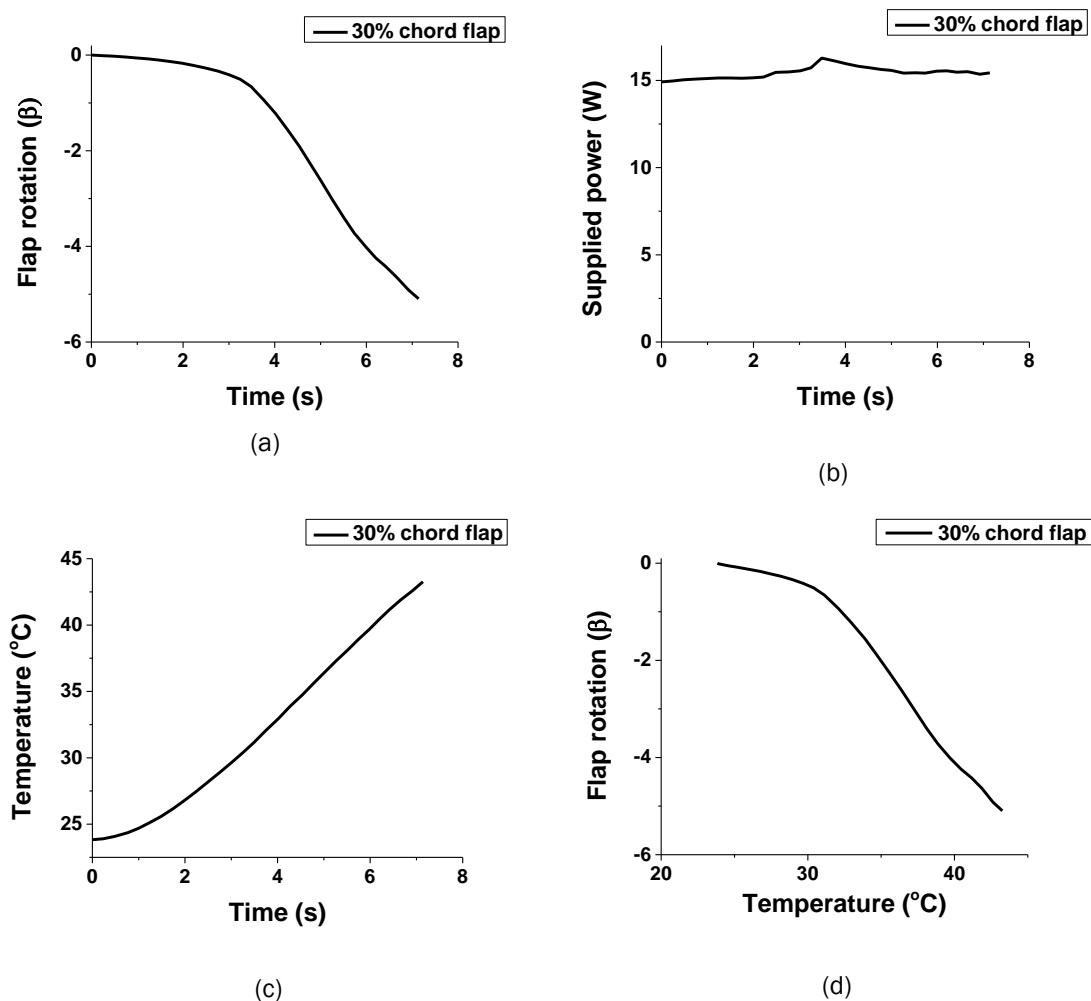

(a)

(b)

(c)

(d)

Figure 110: Measured response of 30% clockwise rotation under representative aerodynamic loading; a) Flap rotation, b) supplied power, c) temperature evolution and d) flap rotation versus actuator temperature.

To rotate counter-clockwise the flap, the temperature of the 30% bottom actuators is elevated from room temperature through Joule heating with constant current I=4.5A.Figure 111a presents the flap rotation and in Figure 111b the supplied power is given. The temperature of the actuator is presented in Figure 111c and the correlation of the flap rotation with the actuator temperature is depicted in Figure 111d. The maximum rotation (β=4.64˚) exceeds the maximum specified and therefore the maximum change in lift coefficient is achieved ($\Delta C_L \geq 0.30$) while the required power is still below 16.7 Watts.
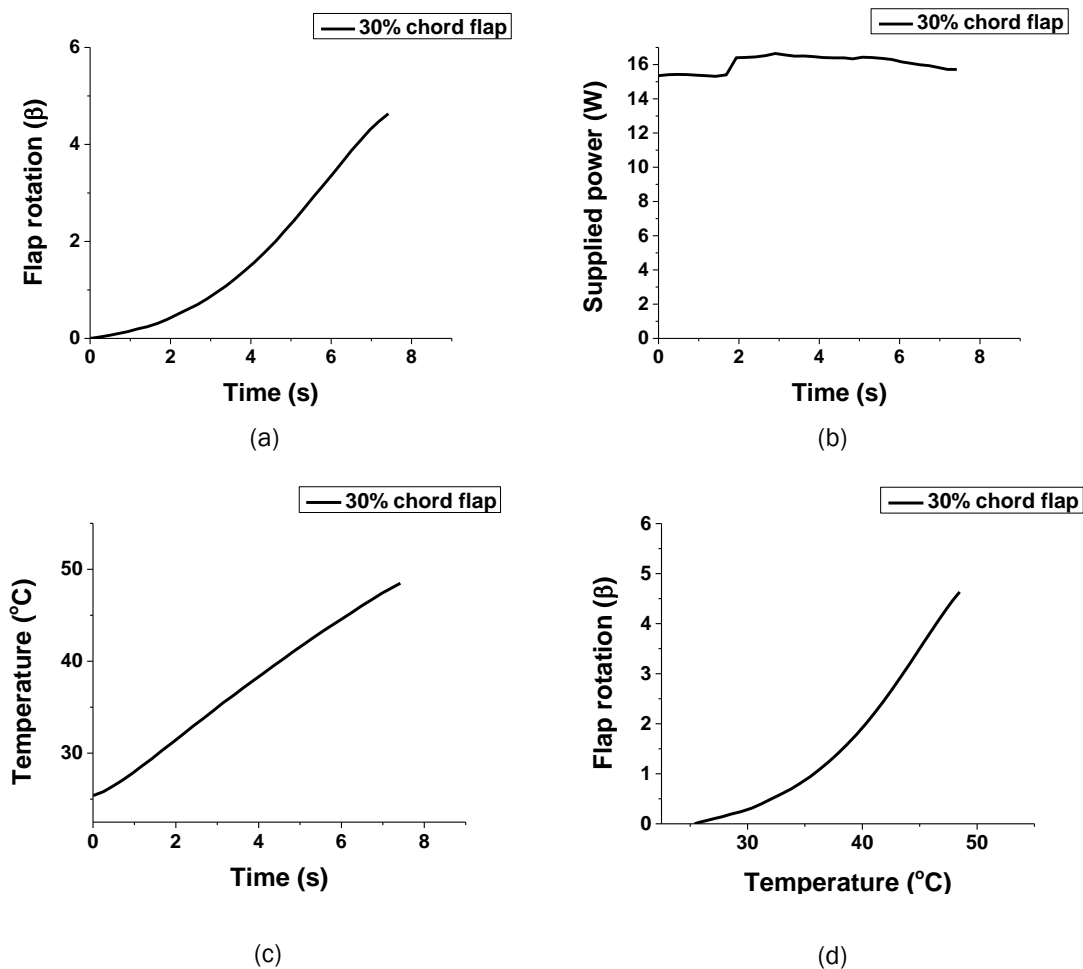

(a)

(b)

(c)

(d)

Figure 111: Measured response of 30% counter-clockwise rotation under representative aerodynamic loading; a) Flap rotation, b) supplied power, c) temperature evolution and d) flap rotation versus actuator temperature

In Figure 112 the undeformed and deformed shape (counter-clockwise rotation) of the 30% chord flap are presented.
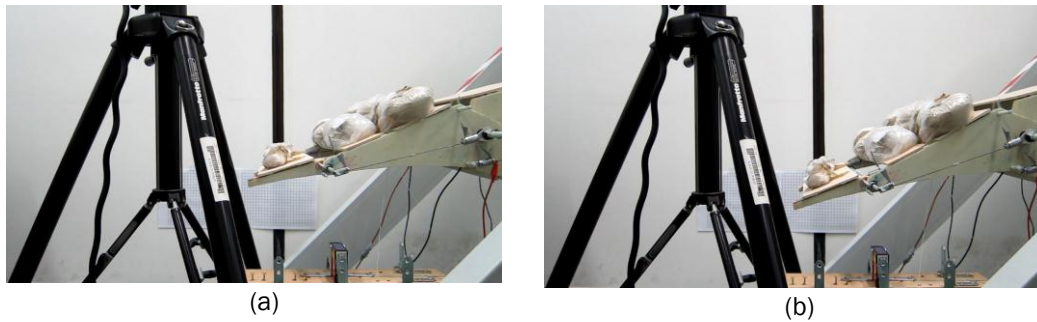
Figure 112: Testing of 30% chord moving flap with simulated aerodynamic loading. a) undeformed configuration and b) counter-clockwise rotation

Testing of 10% chord flap under simulated aerodynamic loading

Sandbags of appropriate weight were placed on the segment with 10% chordal length to represent the respective loading as specified in Table 21. Joule heating with constant current I=4.5A was supplied to the 10% top actuators for the clockwise rotation of the flap. The flap rotation is presented in Figure 113a and the required power for the heating of the actuators is depicted in Figure 113b. The Figure 113c presents the temperature of the top actuators while the association of the flap rotation and the actuator temperature is depicted in Figure 113d. The maximum achieved flap rotation β=-7.5˚ exceeds the specified angle (Table 18) that achieves the maximum change in the lift coefficient $\Delta C_L = 0.25$ while the required power is below 16 Watts.
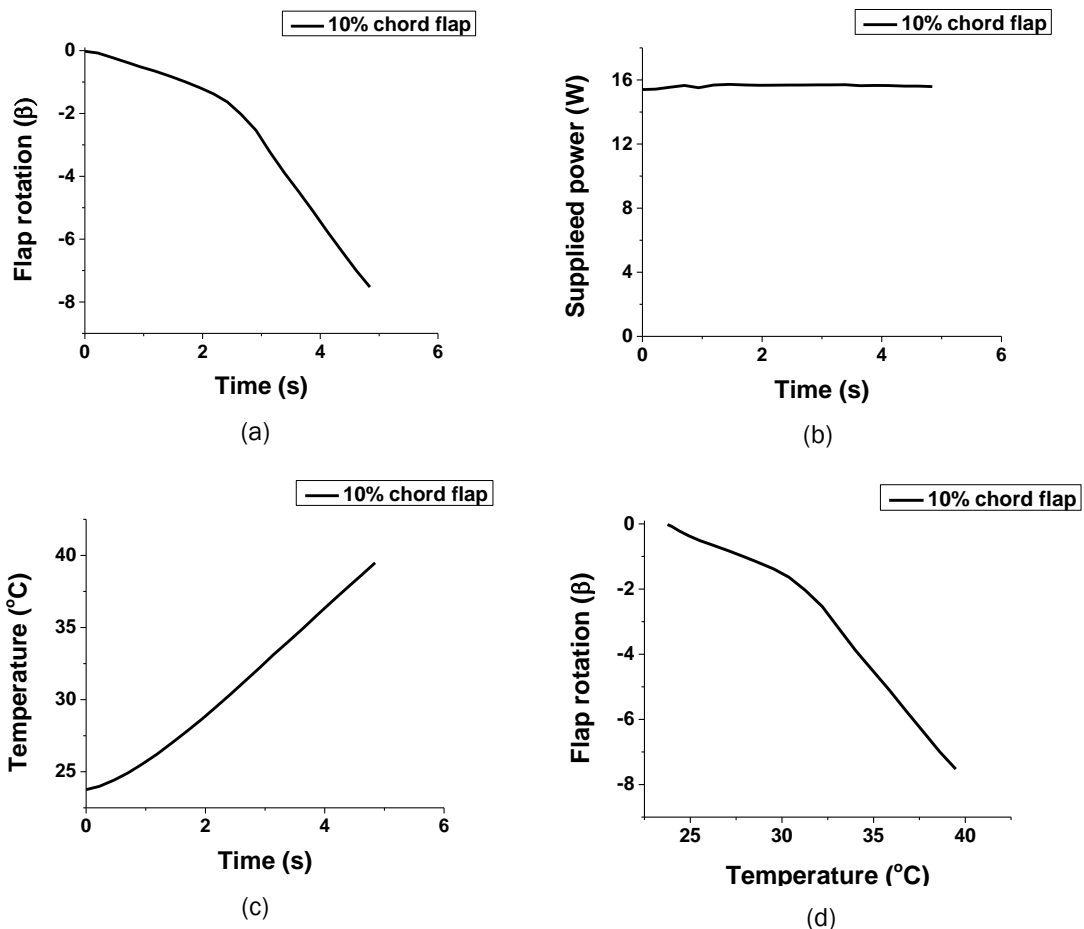

(a)

(b)

(c)

(d)

INNWIND.EU, Deliverable 2.24, Manufactured and laboratory tested scaled blades and parts of the blade

Figure 113: Measured response of 10% clockwise rotation under representative aerodynamic loading; a) Flap rotation, b) supplied power, c) temperature evolution and d) flap rotation versus actuator temperature

In order to rotate the flap counter-clockwise Joule heating with constant current I=4.5A was applied to the 10% bottom actuators. The flap rotation is presented in Figure 114a and the respective required power in Figure 114b while the actuator temperature is depicted in Figure 114c. The flap rotation versus temperature response is presented in Figure 114d. The maximum rotation β=6.1˚ is achieved when the temperature approaches 100˚C while the biggest portion of the rotation (β=5.5˚) has been achieved at the temperature of 55˚C. This is mainly due to the fact that the reverse transformation is approaching completion and further heating does not contribute significantly to the flap rotation. The maximum measured rotation is slightly below the maximum one required to achieve a change in lift coefficient equal to $\Delta C_L = 0.25$.
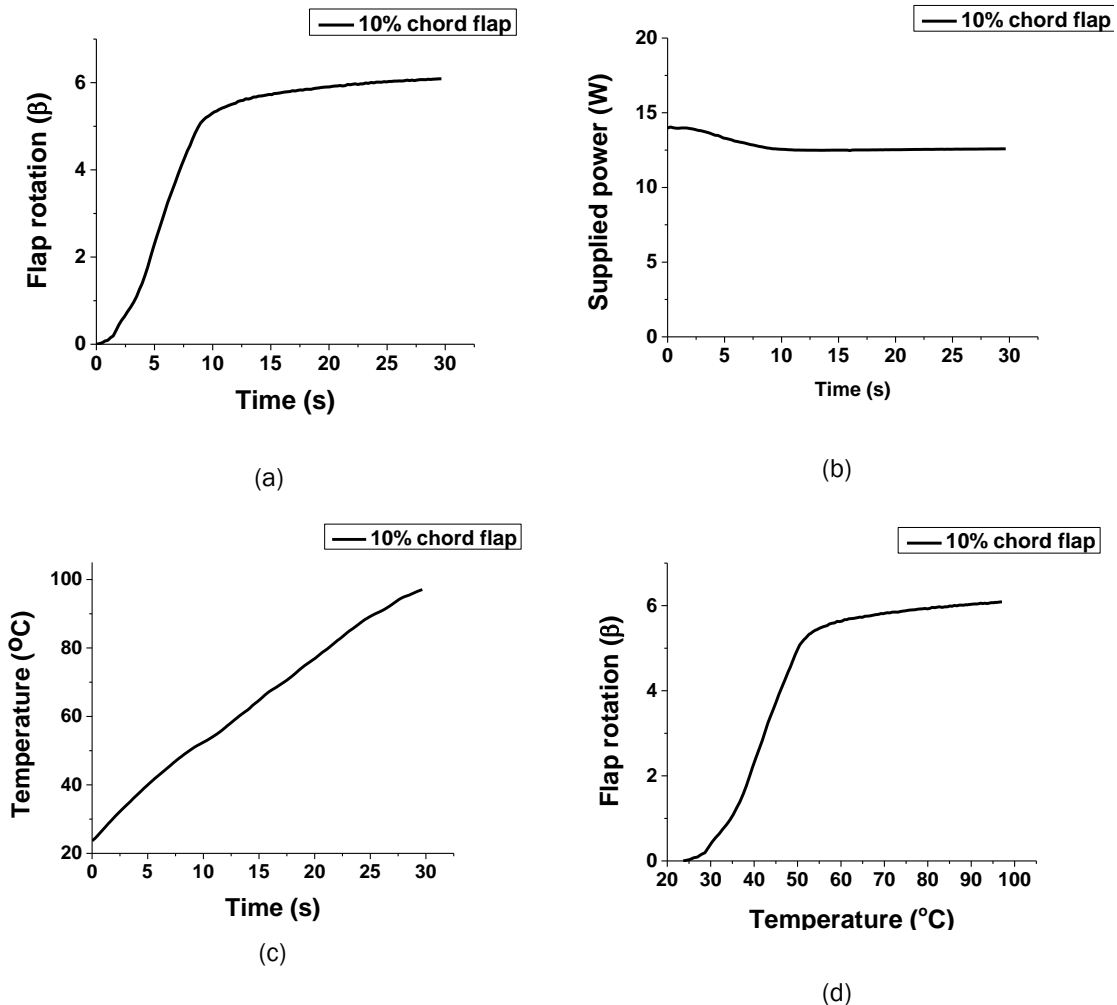

(a)

(b)

(c)

(d)

Figure 114: Measured response of 10% counter-clockwise rotation under representative aerodynamic loading; a) Flap rotation, b) supplied power, c) temperature evolution and d) flap rotation versus actuator temperatur

Combined movement of 30% chordal length flap and the 10% chordal length flap under simulated aerodynamic loading

In this test the 10% and 30% chord flap are activated simultaneously under representative aerodynamic loading to achieve a smoother deformation of the morphing airfoil. Initially the top actuators were heated to rotate clockwise the airfoil. The 10% and 30% top actuators were serially connected and Joule heating with constant current I=4.5A was applied to increase their temperature. The displacement at the trailing edge tip and the rotation point of the 10% flap were recorded and presented in Figure 115a while the supplied power is presented in Figure 115b and the temperature of each actuator in Figure 115c. The maximum displacement of the trailing edge is equal to $v_{TE} = 69.05mm$ while the maximum displacement of the 10% flap rotation point is equal to $v_{10RP} = 24.53mm$. The required power supplied to the actuators remains below 35 Watts. The small discrepancy between the temperature of the two actuators can be attributed to the different fraction of the reverse transformation each one has undergone and the latent heat absorbed that affects the temperature rise. The fraction of the reverse transformation each actuator has undergone, depends on the applied stress on it, and as they are attached to different segments of the airfoil their load is not equal.
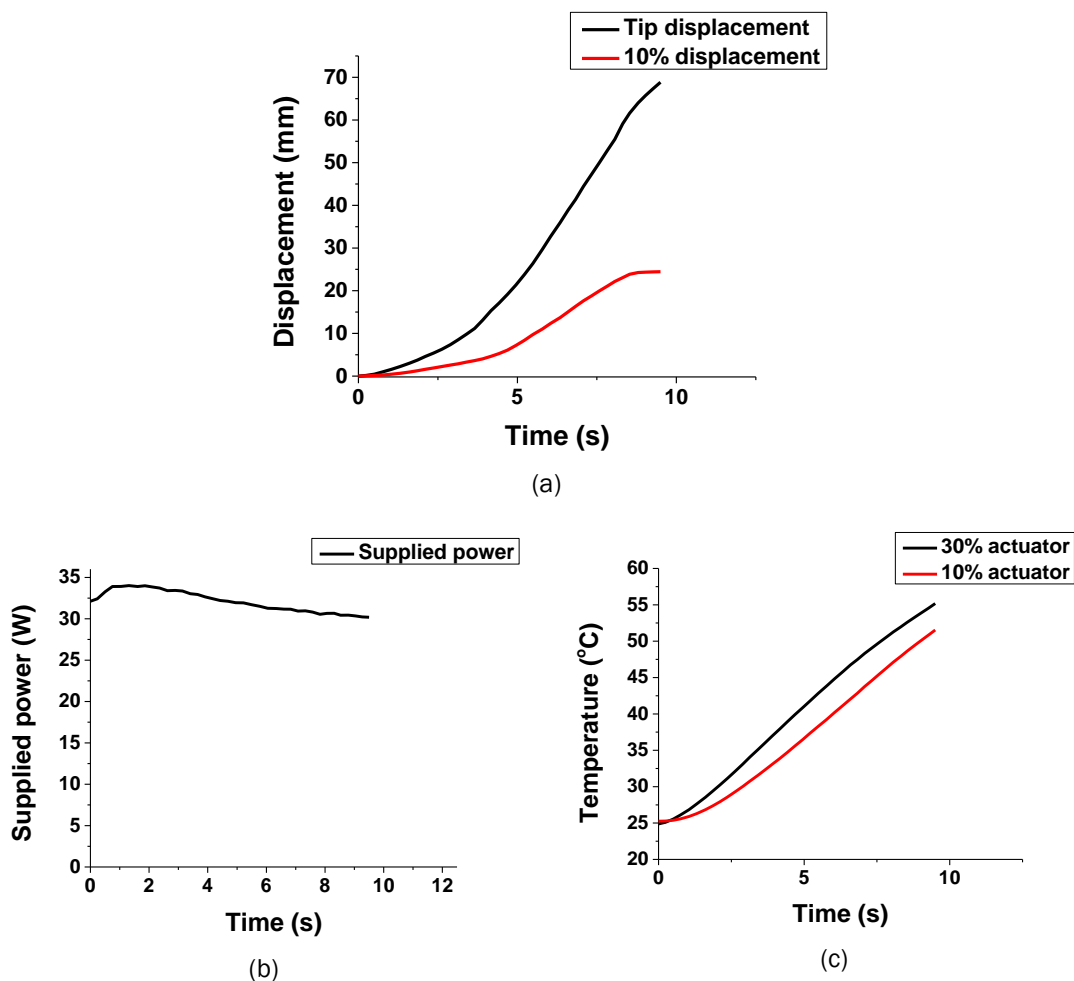

(a)

(b)

(c)

Figure 115: Clockwise rotation of the morphing section under representative aerodynamic loading a) displacement of the two points, b) supplied power to the SMA actuators and c) temperature of the SMA

actuators

Subsequently, the 10% and 30% bottom actuators were heated to rotate the airfoil to the counter-clockwise direction. In Figure 116a the displacement of the trailing edge tip and the rotation point of the 10% flap is presented, while Figure 116b presents the supplied power with a maximum of 32.5 Watts and in Figure 116c the temperature of the two actuators is presented.

(a)

(b)

(c)
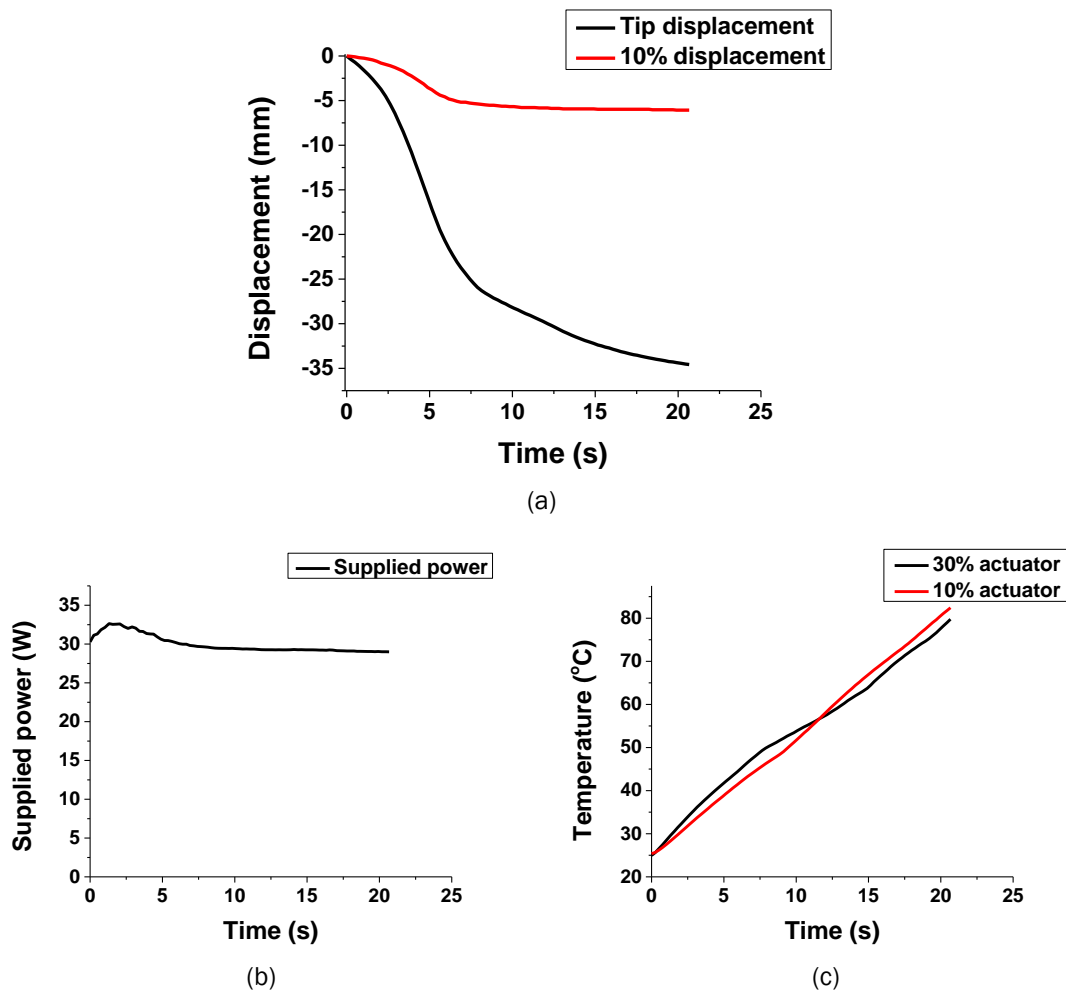
Figure 116: Counter-clockwise rotation of the morphing section under representative aerodynamic loading a) displacement of the two points, b) supplied power to the SMA actuators and c) temperature of the SMA actuators

In Figure 117 the position of the measured prototype is presented in association with the target camberline of the target morphed airfoil. The measured position of airfoil is depicted with black marks in Figure 117a for the clockwise rotation and in Figure 117b for the counter-clockwise rotation. As it can be seen the airfoil under representative loading can achieve the target trailing edge deflection of the target shape with rotation angle of β=-10˚ while the displacement of the 10% flap rotating point presents a small discrepancy from the target shape. During the counter-clockwise rotation under representative loading the prototype can achieve the trailing edge deflection for a target rotation angle of β=5˚ while the displacement of the 10% flap rotation point presents a small deviation from the respective target shape.

Target Camberline

$\beta=-10^o:0^0$

(a)

Target Camberline

$\beta=0^o:10^0$

(b)

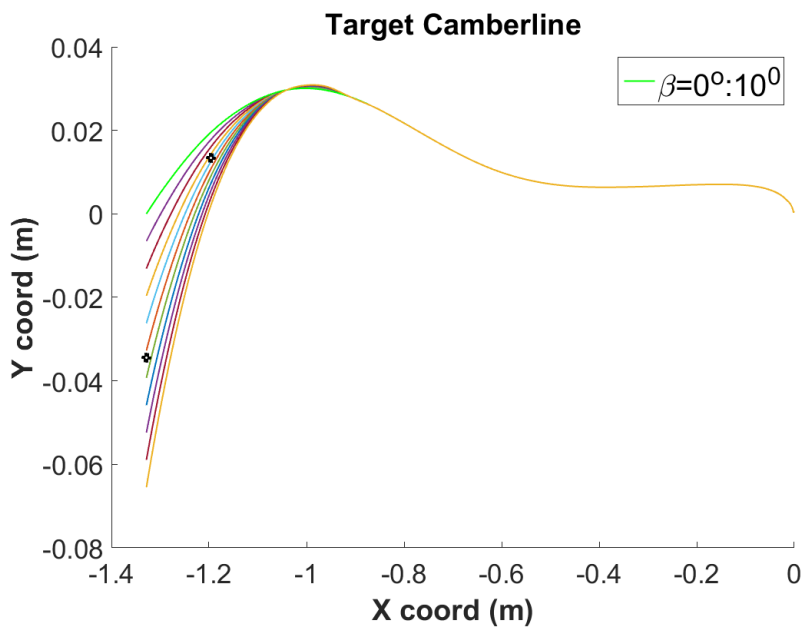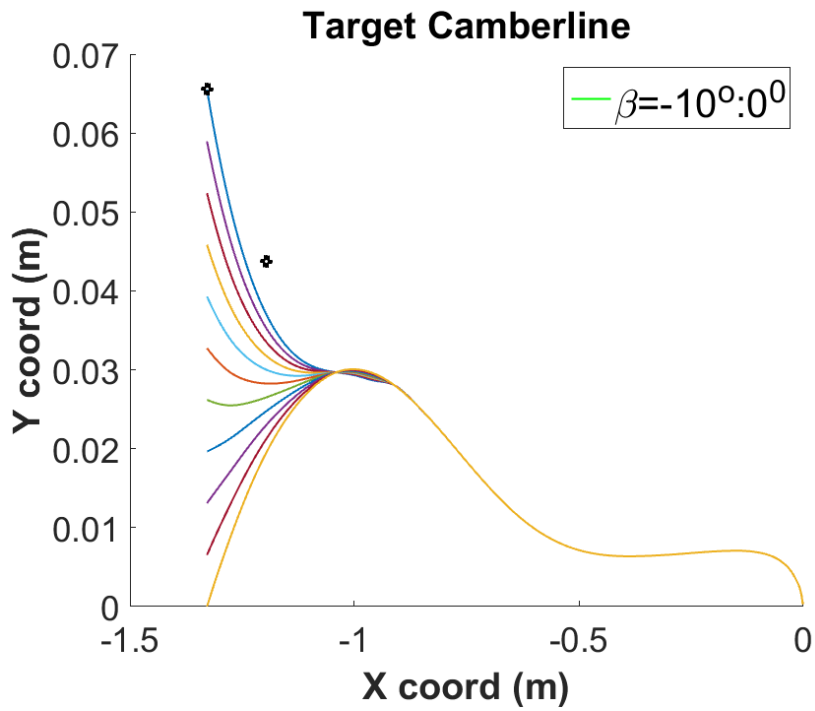**Figure 117:** Target camberline and maximum achieved deformation under representative aerodynamic loading: a) clockwise rotation and b) counter-clockwise rotation

In Figure 118 the deformed shape during clockwise rotation is presented for the combined movement of 10% and 30% chord length flaps.
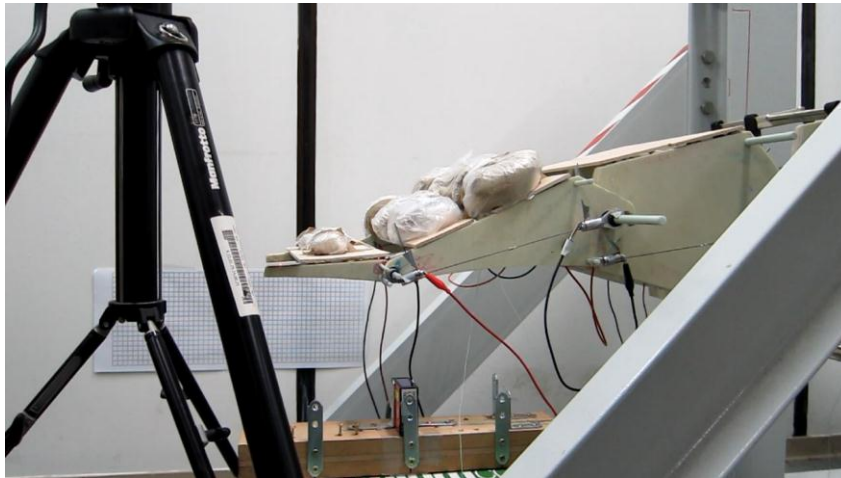
Figure 118: Deformed shape of combined movement of 30% and 10% flap

3.5.3 Comparison of flap testing with no loads and under simulated aerodynamic loading

In this section a correlation of the morphing flap's response without loading and under representative aerodynamic loading is presented. To this end the measured responses of the 10% and 30% chord flap are presented. To eliminate any interference due to the heating rate effect and to make feasible the comparison of the responses of the two cases, the temperature versus rotation response is presented. In Figure 119a the response of the 10% chord flap rotating clockwise is presented. The small amount of the added weight adds to the prestress of the top actuator that is already carrying the weight of the moving segment. The prestress affects the evolution of the reverse transformation which becomes more abrupt and therefore less temperature is needed to achieve the same rotation of the flap. Contrary the added weight does not affect significant the bottom actuator as the loads are being carried by the top actuator and the generated moment has a negligible effect due to the small dimensions of the 10% flap. Subsequently the temperature – rotation response remains almost unchanged (Figure 119b).

The 30% chord flap presents similar behavior with the 10% chord flap while rotating clockwise as the increased prestress due to the added weight on the moving segment makes the reverse transformation to require less temperature change on the actuator in order to provoke the same clockwise rotation (Figure 119c). Contrary during the counter-clockwise rotation the added weights create a significant larger moment in comparison to the 10% chord flap as both the forces and the distance from the rotation axis are larger. As a result, the counter-clockwise rotation is facilitated and therefore less transformation of the actuator is required to achieve the desired rotation.
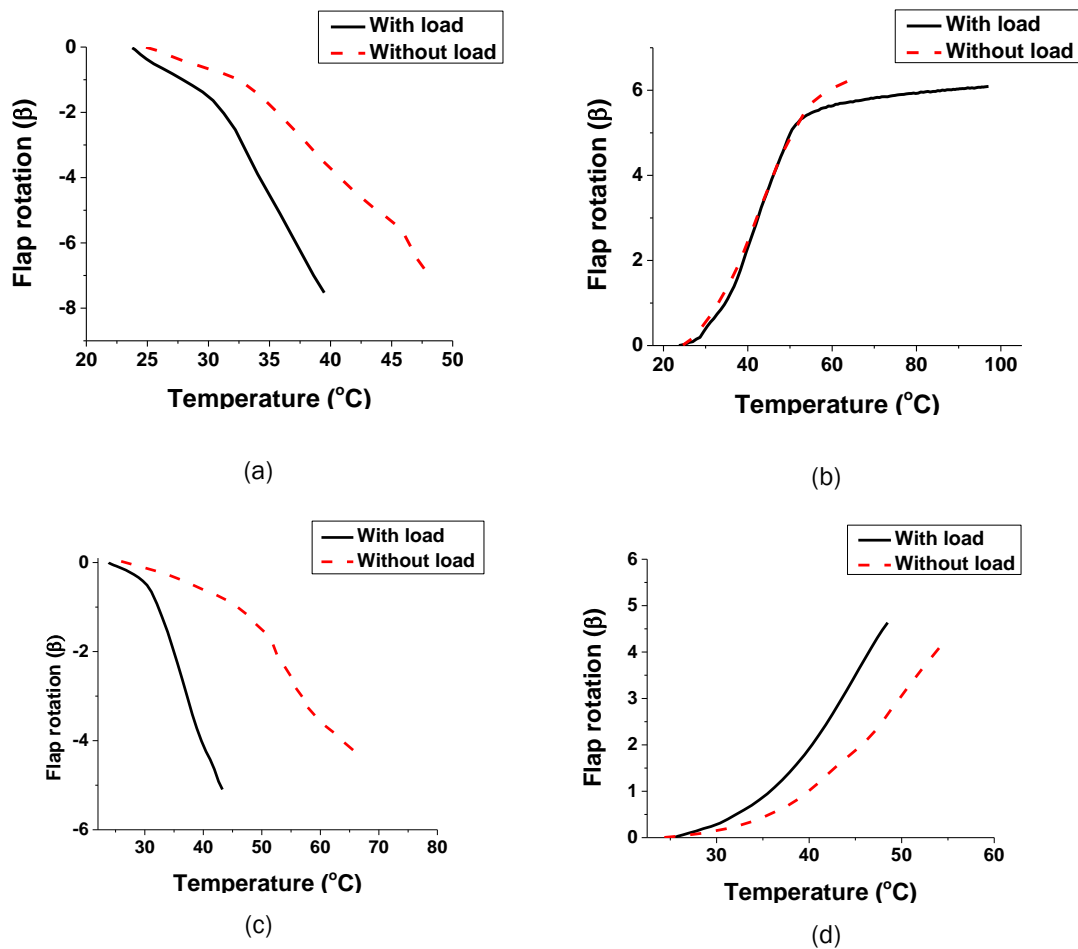
Figure 119: Comparison of temperature versus rotation responses without loading and under representative aerodynamic loading. a) Clockwise rotation of 10% chord flap, b) counter-clockwise rotation of 10% chord flap, c) clockwise rotation of 30% chord flap and d) counter-clockwise rotation of 30% chord flap.

3.6 Summary

In the preceding paragraphs the material characterization, fabrication and testing of a scaled morphing airfoil section prototype were described.

In the framework of this project NiTi equiatomic SMA material in wire form was used as actuator for morphing of an airfoil section. Due to the unique behaviour and complex thermomechanical response of SMAs their thermomechanical properties where properly obtained. First a determination of zero-stress transformation temperatures was performed using DSC results. These results were used to further determine the temperature values required for the design of the tests that followed, as they provide an indication regarding the transformation temperature thresholds. Based on the results of the DSC and on previous experience a new testing apparatus was designed to enhance testing capabilities, reduce cost of consumables and the required time for testing. Besides the design of the new apparatus new tools for processing the experimental results have been developed and used for acquiring material properties and useful information from the experimental data.

Ten SMA wire specimens of diameter of 1mm were trained to be used for further testing and twelve more were trained to be placed as actuators for the operation of the morphing prototype. Completion of training procedure required the specimens to be subjected to thermal cycles under constant mechanical load. The procedure was completed after the completion of 70-80 cycles. The new testing apparatus reduced the required time for training in less than the 1/3 of the time the existing device required.

Elastic properties of the co-existing phases of the material were extracted by performing isothermal tests at temperature below M_f and at temperature above A_f. The aforementioned isothermal tests led to the specification of the elastic modulus of Martensite and Austenite respectively. Moreover, isothermal tests were performed to create the phase diagram of the material by determination of the transformation temperatures at different stress levels. Additionally, the maximum transformation strain and developed stress relation was extracted.

The final step in the characterization process was the estimation of the fatigue life of the material. Determination of functional fatigue of SMAs was quite challenging due to the number of variables that had to be considered to properly account for it. Test performed by University of Patras indicated that the SMA wire actuators of 1 mm diameter can undergo approximately 1600 thermal cycles under mechanical load of 200MPa. This result agrees with the results found in international bibliography for similar materials.

The scaled morphing section prototype parts were designed, fabricated, assembled and tested in the facilities of the University of Patras. Functionality tests were performed to assess the capability of the trailing edge flap to operate without any loading and under simulated aerodynamic loads. The simulated aerodynamic loads were calculated using the pressure distribution provided by NTUA for a dimensionless airfoil and the geometry of the scaled prototype. The resulting loads were applied by distributing sandbags of proper weight on the prototype. Additionally, the morphing capability of the prototype trailing edge to achieve a smooth deformation of the airfoil profile was examined. The response of the morphing structure was recorded in terms of achieved rotation and deflection and actuator's temperature. Also the time response of the morphing structure was recorded. Additionally, the required power to provoke the required deflection of the morphing section was estimated. The performance of the prototype was evaluated via comparison with the target morphed configuration provided by NTUA. In all cases considering a single flap with length either equal to 10% or 30% the measured rotation, with and without representative loads, matched or exceeded the respective target rotation that resulted in the maximum change in lift coefficient (ΔC_L) according to the specifications.

The morphing capability of the trailing edge to provide a smooth airfoil deformation was assessed by actuating simultaneously the 10% and 30% chord flaps. The prototype performed well while tested without the presence of any loads, achieving the maximum target deflection in both the clockwise and counter-clockwise direction. The application of the simulated aerodynamic loads affected its performance and limited its morphing capability to achieve the target shapes.
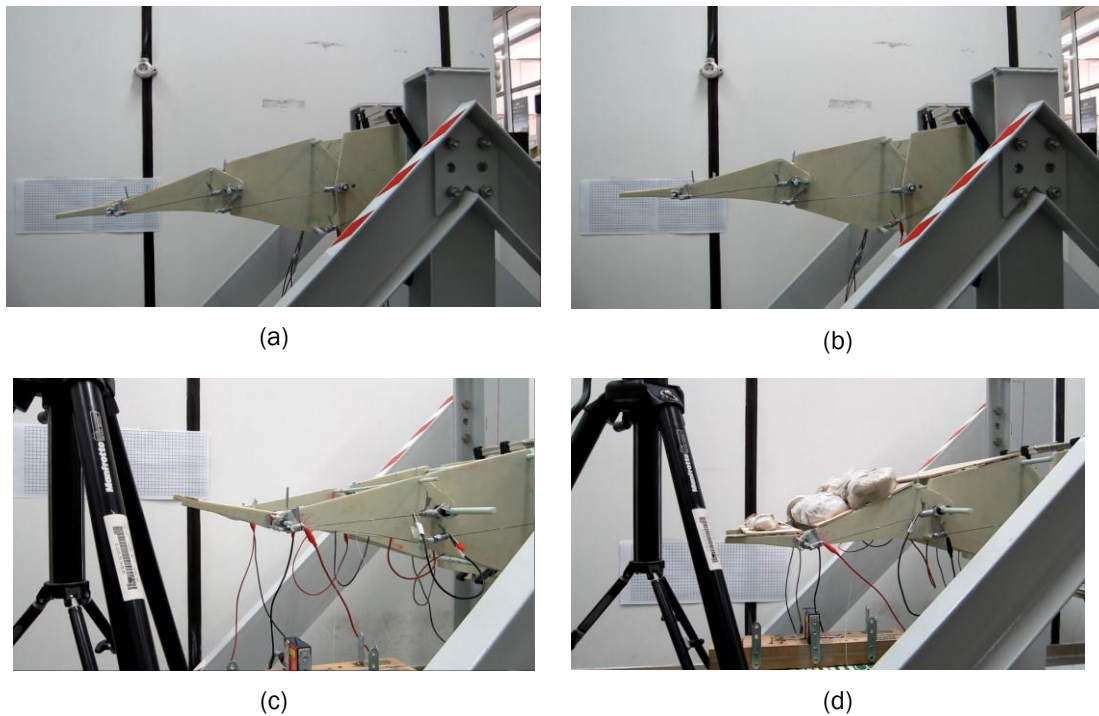
INNWIND.EU, Deliverable 2.24, Manufactured and laboratory tested scaled blades and parts of the blade

Figure 120: Testing of prototype. a) Undeformed configuration, b) flap of 30% chord length rotating clockwise without loads, c) combined clockwise rotation of flaps of 10% and 30% chordal length without loads and d) combined clockwise rotation of flaps of 10% and 30% chordal length under representative aerodynamic loads.

3.7 Conclusions and recommendations

The SMA material properties, used for actuating purposes, for the morphing section have been successfully extracted after a test campaign conducted by the University of Patras. Additionally the fatigue life of the material in the envisioned working stress level has been estimated. Furthermore, the scaled morphing section has been designed, fabricated and successfully tested in the laboratory to assess and demonstrate its morphing capabilities. The prototype proved its capability to morph its trailing edge to target shapes with and without the presence of simulated aerodynamic loads. To conclude, the experimental campaign proved that the morphing section prototype is capable to operate both as a single flap of length equal to 10% and 30% of the chord and as morphing trailing edge offering a smooth shape change, matching the specified target shapes that achieve the maximum change in lift coefficient in almost all of the considered cases.

The conducted fatigue tests provided an estimation of the functional fatigue life under continuous actuation, however further tests need to be performed to validate the results, account for the effect of the applied electrical current and provide a relation of the fatigue life to the developed stress levels. Thus, experimental fatigue testing is an ongoing process and more results and conclusions are pending.

Improvements on the design of the prototype can increase its performance especially in the case of the smooth airfoil variation concept. Design optimization can contribute to this scope while the consideration of more moving segments in the airfoil's trailing edge could result in smoother morphed shapes matching the specified target curvature profile. Furthermore, the realization of a

controller that will provide electric power on the actuators in accordance to the measured rotation of the morphing section can lead to a more realistic estimation of the prototype morphing capability. Additionally, the realization of a controller will provide the opportunity to assess the capability of the prototype to follow a given time trajectory. To this end, modifications on the experimental results will be required as well, in order to enable active cooling of the actuators. The respective acquired results could be the basis of correlation between numerical predictions and measured response. Lastly, the possibility of suppling different amount of power to each actuator must be considered in order to exploit adequately the potential of each SMA actuator that would lead to a better agreement between the achieved and the target morphed shapes

4 FABRICATION OF A PART OF THE BLADE USING THE GRID STIFFENED METHOD (TUD)

4.1 Introduction

Within the framework of this project, the Delft University of Technology has contributed towards a design and optimization tool that illustrated weight savings of up to 20% when traditional sandwich structure is replaced with the proposed grid stiffened structure solely in the trailing edge panel, of a particular stiffener height to skin thickness ratio [64]. All the design details and dimensions have been extracted from the same work reported in section 2.2 of Deliverable 2.22 *New lightweight structural blade designs and blade designs with build-in structural couplings*, for use in the current deliverable.

In the recent decade, the interest in the grid stiffened technology specially for aerospace applications has accelerated its development both in terms of design and manufacturing process. The traditionally produced grid stiffened structures were mainly focused on fuselage applications or conical payload adapters that were mostly wound on a mandrel using the filament winding technique [65]. This technique has serious limitations when it comes to non-geodesic paths and open structures, making it imperative to develop newer, cheaper and efficient processing options.

One of the most important characteristics of a grid stiffened structural strength is due to continuous fiber placed along the loading direction in the grid pattern. The continuous grids contribute to the maximum strength of the structure. This is a direct challenge for the manufacturing process, because the use of pre-impregnated tapes will lead to a height build up at the nodes where two or more grids cross each other, or when dry fiber is used and infusion is carried out, the fiber volume fraction at the nodes is too high. Although this may not be a problem in terms of strength theoretically, it may lead to very high resistance to resin flow at the nodes leaving it to be a void prone zone.

Depending upon the height of the grids, it may become necessary that a certain wall pressure must exist to compact the grid along its height during the curing process, to disallow it from spreading and causing undesired tolerances. This eliminates the use of metallic moulds with grooves in it to place grids inside it, because of its high co-efficient of thermal expansion mismatch leading to minimum or no compaction along grid height.

Reasonable choices must therefore be made to overcome the discussed challenges to select the right production process to get a good quality product. This process must have potential to be scaled up to produce larger parts to reduce the number of connections and hence the weight of the overall structure. It should also have a high production rate, and it goes without saying that it must be an economically efficient process.

As a contribution to the current WP, as described in the current chapter, TUDelft has used one among a few processes described here to fabricate a section of the wind turbine blade as designed using the optimization tool as an illustration of the manufacturing process and feasibility of production of a wind turbine blade with a complicated structure such as this one and the challenges associated with it. The contribution is limited to selection of a production process and fabrication of a section of the blade. The fabricated blade will not be tested within the framework of this project due to the limited involvement in man-months for the given work package.

4.2 Description of the work

Recent experimental work in grid stiffened structures made use of the vacuum infusion process to infuse continuously placed thick dry fiber grids in a flexible rubber mould [66]. The dry fiber grids are held in minimum tension and the complication lies in the infusion inlet and outlet designation along the length of the grids. The advantage of this process is that the dimensions of the grid are very well controlled and show minimum deviation along the grid lengths. The nodes are created very smoothly without any bumps or cut fibers along the length, however, the fiber volume fraction is higher than the surrounding areas. A destructive inspection reveals that minimum voids are present at these areas, provided that the width of the grid is not very high. The application was limited to fuselage structures with a repeated grid stiffened pattern of dense grids, where the grids were 2cm high, and 3mm wide throughout the fuselage skin.

The manufacturing method described is unsuitable for the current case of the wind turbine blade due to a number of reasons, with the size of the grids being the driving factor. Although a narrow width of 6.35mm is used for the grids, the height of the grids can go beyond 8cm at roughly 33m length of the blade from root location. Small-scale tests in infusion of large cross-section grids reveal that the process had to be optimized for several setups of inlets/outlets/pressure differences to produce parts that showed voids at nodal and near nodal locations. Another limitation with the current design is the varying height of the grids through the length of the blade. Placing loose dry fiber at certain heights to achieve the required grid height will be a great challenge, leave alone the making of the mould for such a part.

An alternative manufacturing method is the automated fiber placement process which is used in industry for large material deposition rates for layerwise composite laminate production. The most common process is the automated tape laying process, wherein extremely wide thermoset pre-impregnated composite UD tapes are laid down at a certain temperature and pressure at high speeds to create large sections by means of a ceiling mounted tape laying head. The use of narrow tapes, namely the fiber placement process is being recently developed to achieve steered fiber composite laminates with variable stiffness characteristics. This placement head is usually mounted on an agile 6-axis robot that can place varied curvatures, or on external axes or positioners with moulds mounted on it, and even rotating is it's a continuous section. Similar narrow tapes can be used to place grid stiffened structures with specialized multiple rollers that work in tandem to place multiple grids as demonstrated in small scale [67].

With the author's experience of this process of fiber placement, it is known that the prepreg tapes can be placed on top of each other at sufficiently high material deposition rate with a good tolerance to build up the height of the grid. The tapes already contain resin and hence no infusion would be required, leading to lower probability of void formation in the grids and nodes. The placed part can also be cured in an autoclave as is required by some high strength composite materials, although the finished part is perfectly capable of being cured in a regular oven, because a controlled process of tape placement, will ensure minimum voids in the part at ambient pressure curing. This method also overcomes the issue of dry fibers placed in the grooves, which may move, or sag and create waves within the part, leading to damage prone zones.

A prototype of a particular selected section of the wind turbine blade designed in the previous phase of the project is produced by hand-layup. The paraphernalia related to the automated fiber placement process is kept intact including the moulds, materials, and curing process. A person replaces the motion of the robot mounted tape placement head to produce this first prototype due to unavailability of the robot during this work phase. The speed of production and the subsequent quality of the part is expected only to be better by multiple folds when the entire process is automated. The production process is documented in the following section.

4.3 Project Plan

A representative section of the wind turbine blade had to be selected for the production demonstration. As a result of the optimization process, the section at blade length 62.393m from the root had the lowest stiffener height. To facilitate the hand-layup process to be fast and efficient, this section was most suitable because the tapes would have to be cut to length and placed by hand one on top of the other. The stiffener and skin dimensions were extracted from the previous deliverable [64] and the spar dimensions and locations were taken from the reference blade [68].

The blade section consists of the following parts:
1. upper and lower skin
2. upper and lower spar caps
3. upper and lower grid stiffening in the trailing panel section
4. front and back spars
5. leading edge piece

In the automated process, the skin, spar caps, stiffeners and upper/lower spar, depending on which panel it is, are laid down progressively. First the skin is laid down using widest tapes, followed by spar caps with widest possible tapes, and finally the grid stiffening with 6.35mm tapes same as the dimensions of the grid. The front and back spars are produced separately and the four parts are then assembled together as the final stage in the production process. Covering with the leading edge piece finishes off the upper and lower sections to form the final assembled blade section. It was decided to realize the blade in two parts – upper and lower stiffened skin and subsequently joined together at the tips – which required the production of two separate moulds for the upper and lower sections. The moulds are the most time consuming and design intensive parts of the production process in the current method.

Since a slower hand-layup process replaced the automated fiber placement process, the steps had to be adjusted slightly. The moulds however, would remain quite much the same for the final process as well. Taking the sizing into consideration, CAD models of the moulds were generated as shown in figures 121 and 122. The several parts of the assembled mould were produced by using the best possible means in terms of cost and time efficiency. The detailed step-by-step process is described in the following section.
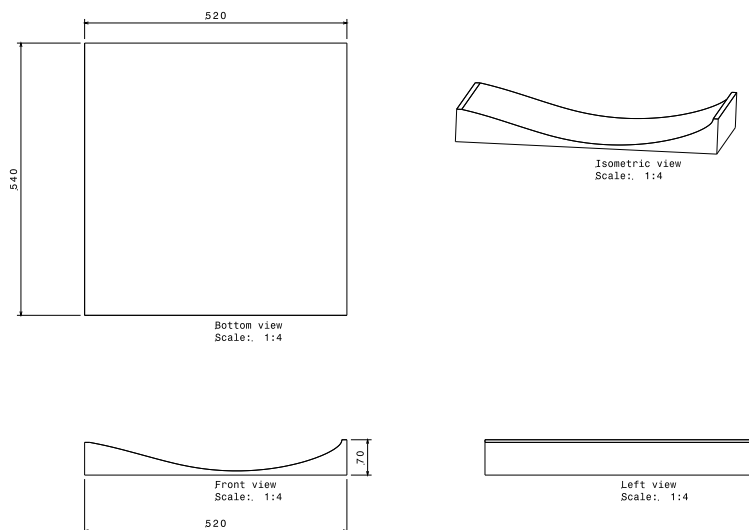

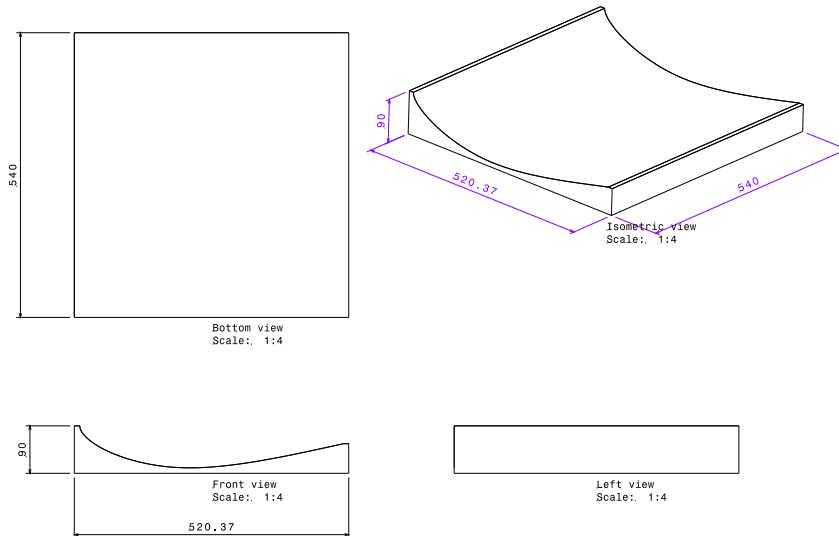**Figure 121:** Drawings of of Base Mould - Female

Bottom view
Scale: 1:4

Isometric view
Scale: 1:4

Front view
Scale: 1:4

Left view
Scale: 1:4

Figure 122: Drawings of Base Mould - Male

4.4 Production Process

In the current simplified approach for production, the skin and spar caps are produced first, followed by the grids and front and back spars, and finally the leading edge cover. The productions process is shown in form of flowcharts with supporting figures.

Skin and Spar caps

The moulds for the upper and lower skin were produced by milling of aluminum blocks. These moulds were cleaned and coated with anti stick agents to allow easy release of the product. The prepreg tapes are cut to size using the Gerber cutting machine and placed with the appropriate stacking sequence according to the design. The prepregs for both skin and spar are placed and then covered with Teflon film for protection. The complete prepreg assembly is then covered with a one-cm thick silicon rubber sheet for compaction pressure. The assembly is shown in figure 123(a). This assembly is vacuum bagged and placed in an oven for curing as per material specification. Finally the demoulded product is shown in the figure 123(b) and figure 123(c).
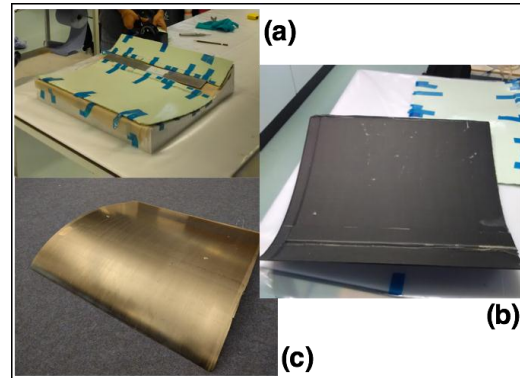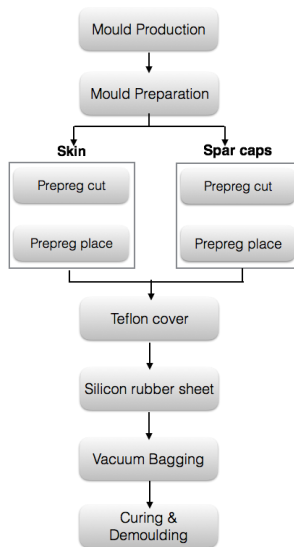
Figure 123: Flowchart of skin production process

Figure 123: (a) Mould assembly for skin production; (b) Cured inner section of skin;(c) Cured outer section of skin

Grids

The mould for the grids was the most complicated part to be produced. As pointed out earlier in the Introduction, the wall pressure of the grid mould is extremely important for a good quality and within tolerance limit finish. The mould material therefore selected is Silastic S Green silicon rubber, because of its excellent toughness and flexibility combination for an easy release of the product. Since silicon is a contaminating product, a cured block of silicon cannot be milled to produce the final part, therefore, a grid of the final shape and dimensions is first 3D printed using ABS plastic and placed on the Aluminum skin mould to pour in the silicon and cure it, to result in the grid mould as shown in the figure 125(c). It is therefore important that the 3D printed grid be very smooth for a good surface finish.

The cured silicon mould is now used to place the grid prepreg layer-by-layer into the grooves. The assembly of the silicon mould with the prepreg in the grooves, placed on the skin moulds is vacuum bagged and cured as per material specifications. The product is then demoulded and rough resin flow is sanded off for a proper finish. As a note to the reader, it must be stressed that the above two steps of skin, spar caps and grids production could be carried out in one single step as well to have an integral product which is much stronger than one that is bonded later.
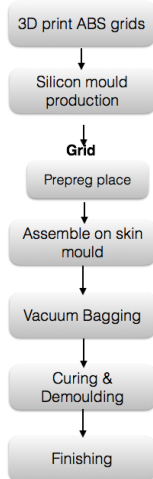
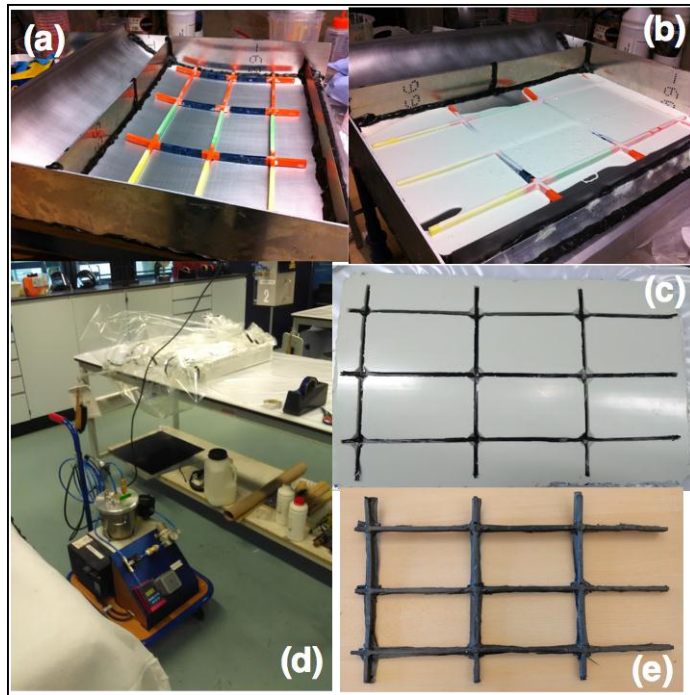Figure 124: Flowchart of grid production process

Figure 125: (a) 3D printed grid placed inside base skin mould; (b) Silicon Silastic S green poured into mould; (c) prepreg tapes placed in mould grooves; (d) vaccum bagged debulking; (e) cured and demoulded grid

Spars

The front and back spars are produced in a simple way with prepreg layered on an Aluminum moulds, vaccum bagged and cured.

Leading edge cap

About 10cm of the positive skin mould is 3D printed in ABS plastic to form a silicon mould similar to the one produced for the grids. This silicon mould is then used to layer a thin stack of prepreg on it to produce a section of the leading edge called the leading edge cap in this process. This cap is used to join the upper and lower skin sections from the inside. The mould and parts are shown in figure 126.
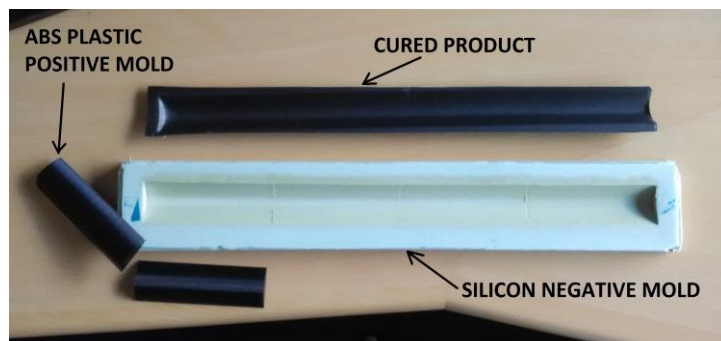

Figure 126: Mould for leading edge cap and demoulded leading edge cap

Assembly

After all the parts have been produced, a dry assembly is carried out to check for tolerances. Finally, the assembly is carried out with a quick curing epoxy adhesive in the steps provided below.

1. The two bottom skins are placed one at the side of the other and the overlapping part is glued while being kept in position with clamps
2. The bottom grids are glued to the bottom skins while being kept in position with clamps
3. The rear spar is glued to the bottom skins using clamps
4. The inferior side of the leading edge is glued at the specified position on the bottom skins using clamps
5. The two top skins are placed one at the side of the other and the overlapping part is glued while being kept in position with clamps
6. The top grids are glued to the top skins while being kept in position with clamps (figure 128)
7. A layer of glue is applied to the top of the back spar and to the superior side of the leading edge
8. The two top skins are placed in position on the top of the back spar and to the superior side of the leading edge, without applying pressure
9. A layer of glue is applied to the edges of the front and medium spars
10. The spars are slid from the sides to reach the correct position
11. The top skins are pressed towards the bottom skins by means of clamps
12. The bonded parts of the whole assembly are left to cure (figure 129)
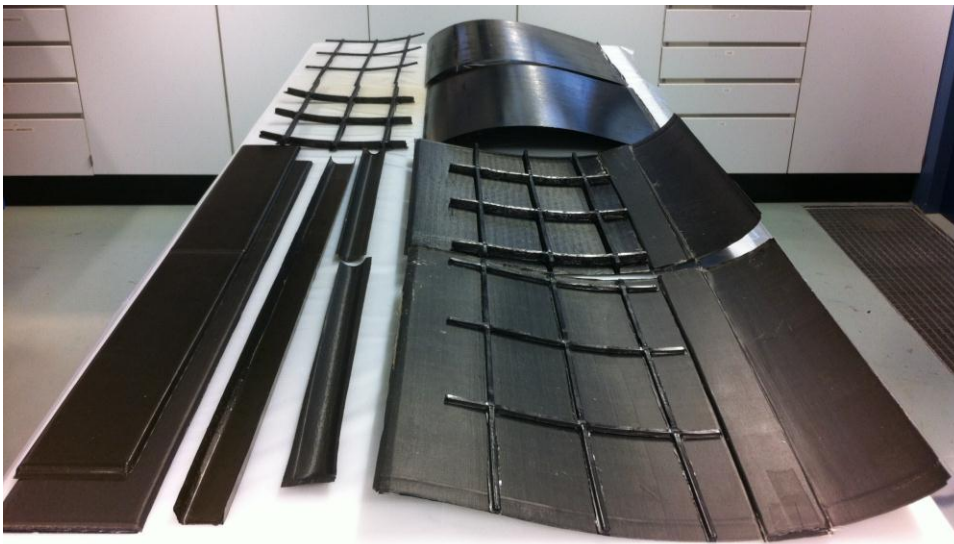

Figure 127: All parts ready to be assembled

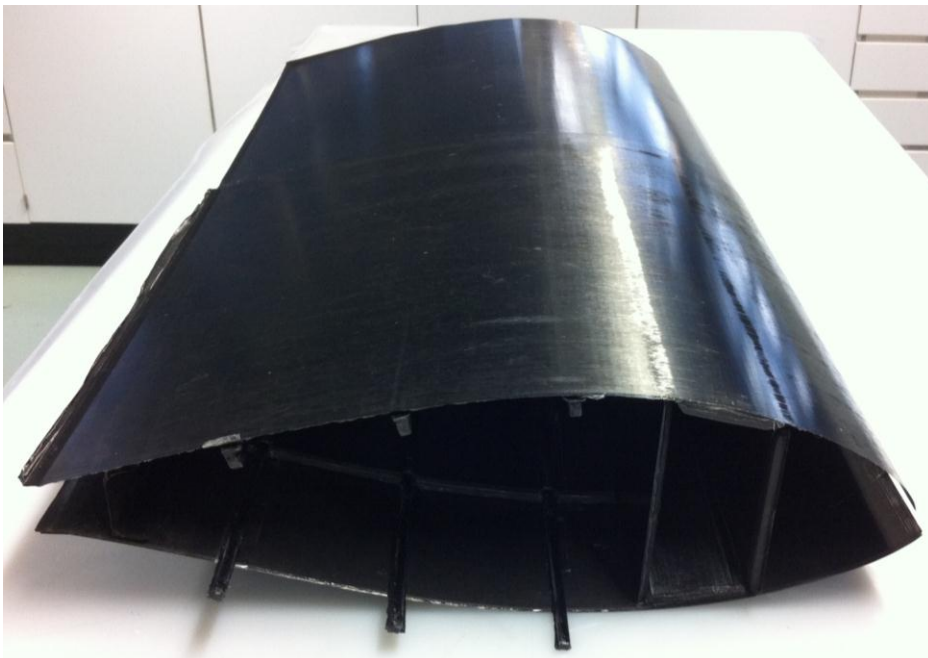**Figure 128:** Skins placed edge to edge and held together by clamps. Grids are glued to the skins

Figure 129: Final assembled blade section

INNWIND.EU, Deliverable 2.24, Manufactured and laboratory tested scaled blades and parts of the blade

4.5 Cost analysis

In the current work, the manufacturing demonstrator was produced for the section with the smallest possible grid height. All the parts dimensions and drawings are provided at the end of this report section for reference. The demonstrator as described before is 1m long and roughly 0.5m wide. The cost analysis is therefore, conservative, because the material used is minimal, however, since the material is ordered in small quantities, prices used from the quotation are higher than expected for bulk volumes. The same carbon-epoxy prepreg material is used for all the parts and yet show different prices, because of additional work carried out on the material – in our case, slitting in 6.35mm widths to lay down the designed grids. A general wastage amount is taken as 30% for complex regions which different layups and grids, and 10% for simpler sections such as spars where less wastage was observed during the layup process.

It should be observed that the costs for the grid material are very low. This is just based on volumetric calculations. The costs associated with the grids will be the highest overall considering the man-hours spent on producing these. In an automated process, these hours will be considerably reduced, reducing the process costs by a large amount.

Table 23 Cost breakdown

Part	Area (incl. wastage) (m²)	Cost (€/m²)	Cost (€)
Top Skin	6.8	40	272
Bottom Skin	2.86	40	114.4
Spar Caps	4.84	40	193.6
Front and Back Spars	10.736	40	430
Top Grid	0.73	52	38
Bottom Grid	0.26	52	13.5
Trailing edge spar	0.64	40	25.6
		Total	1087.10

The total number of hours spent in producing this part by hand-layup is roughly 110 hours. Translating into European standard labour cost of €30.00 per hour, would amount to €3300.00. Further, the equipment cost for vacuum and debulking and service charges for the autoclave and oven, which was used for a total of about 72 hours is estimated to be €2500.00.
A total cost of hand-layup production of this blade section therefore results in €6887.10 as an estimate.

4.6 Upscaling

The automated fiber placement process can be used to produce extremely large parts with the use of multiple robots with the fiber placement heads mounts on them in a bilinear track arrangement with minimum difficulty. The parts can be produced using alternative fiber types such as glass fibers that are more commonly used in the wind energy industry specifically for a cost benefit. The material deposition rate will guarantee a time and cost efficient production that can be highly automated both in material lay-down as well as for inspection purposes since the current trend in development of online inspection is rigorously underway. The limitation, however, comes in maximum size of the section that can be produced to oven or autoclave these parts, dictated by the size of the autoclave or oven itself. Various alternatives can be envisioned, although they are in fundamental research phase. In-situ consolidation thermoplastics are a favourite research topic at this stage, promising out of autoclave production and hence no limitation of sizing, as long as you have enough land to build a assembly line on. Another alternative is flexible autocaves, wherein blocks of autoclave parts can be joined together, much like lego blocks to extend the size of the autoclave. So in principle the autoclave can be built around the part itself.

Further, the moulds for the current demonstrated parts are simple to create, but when it comes to section continuity the design poses several challenges to be overcome. One, the grid has a varying height over various sections, which means that the amount of material laid down for the grids and skin will vary. A design initiative will be required to plan the ply addition and subsequent ply drops where needed. This will pose changes to the original design as well for strength and stiffness. Two, another foreseeable challenge is the connections or attachments between the sections and with other equipment that may be needed.

Further, repair and inspection holes will have to be planned and since each section is unique multiple moulds will be necessary to produce this blade for the design envisioned using the grid stiffened skins.

5 CONCLUSIONS

The efforts performed relevant to manufacture and test in laboratory scaled blades or parts of the new designs developed within WP2 were reported. Three promising concepts, the first one aiming for load alleviation using passive load control of the blade, the second one aiming for load alleviation using active load control and the last one aiming for weight reduction of the blade using an innovative fabrication technique, were manufactured and tested in laboratory.

Considering the scaled blade with the bend-twist coupling ad-hoc design and manufacturing processes have been set-up for the realization of scaled multi-megawatt blades with bend-twist coupling, testable in the wind tunnel. To evaluate the manufacturing, the blade was characterized at bench, by the use of static tests both at PoliMI and DTU and by modal tests with hammer at PoliMI and with a Scanning Laser Vibrometer at DTU. The modal analysis showed the modal frequencies and the Lock number remained close to design, with mismatches around 10%. The two experimental modal methods generally showed very good agreement for the lower Eigen frequencies, while the difference was larger for the higher Eigen frequencies. The static tests showed the twist-to-feather capability evaluated through the Kinematic Coupling Coefficient. The tests in the aeronautical section of GVPM showed little or no reduction in the power coefficient for the rotor with BTC blades if compared with the one with identical shape but without BTC. The main difference is the minimum collective pitch, which proved lower since the twist to feather causes a higher effective angle of attack to the airfoils.

A tests campaign for assessing the load reduction capability was performed in the boundary layer section of the GVPM. Several no wake/partial wake conditions were tested. The model was tested in three configurations: RGD, (i.e. with rigid blades), BTC, hybrid BTC+IPC (BTC blades and cyclic pitch controller). Looking at the shaft and tower base bending moments, the BTC seemed capable of mitigating the peaks within a bandwidth up to the first blade flapping frequency. The inertial loads were not affected by the BTC, therefore their contribute may increase the peak at the 1xRev, and hence the equivalent fatigue load the shaft bending moment. To conclude, the tests in the wind tunnel showed that the synergy of the BTC with IPC led to the most promising results for the load reduction on the blade.

The work performed by University of Patras was focused on the thermomechanical characterization of the selected SMA material in a wire form and the manufacture and testing of a scaled blade prototype equipped with a SMA morphing actuator.

The experimental campaign regarding the SMA technology proved that the morphing section prototype is capable to operate both as a single flap of length equal to 10% and 30% of the chord and as morphing trailing edge offering a smooth shape change, matching the specified target shapes that achieve the maximum increase of the lift coefficient in almost all of the considered cases.

Finally the conducted fatigue tests provided an estimation of the functional fatigue life under continuous actuation, however further tests need to be performed to validate the results, account for the effect of the applied electrical current and provide a relation of the fatigue life to the developed stress levels. Thus, experimental fatigue testing is a topic where future efforts should be focused.

TUD used an innovative manufacture technique to fabricate a scaled 2m section of a wind turbine blade. This section was designed using an optimization tool presented in D2.2.2, where weight savings of up to 20% were illustrated when the traditional sandwich structure is replaced with a proposed grid stiffened structure, of a particular height to thickness ratio, solely in the trailing edge panel. The contribution was limited to selection of the production process and fabrication of a section of the blade. The fabricated blade was not tested within the framework of this project due to the limited involvement in man-months for the given work package.

6 REFERENCES

[1]   Bak C, Zahle F, Bitsche R, Kim T, Yde A, Henriksen LC, Andersen PB, Natarajan A, Hansen MH, 2013, "Design and performance of a 10 MW wind turbine", submitted to J. Wind Energy.

[2]   ProfilPolaren für den Modellflug, Band 1. Institut für Aerodynamik und Gasdynamik der Universität Stuttgart, Necktar-Verlag, Vs-Villingen, 1998.

[3]   Anonymus: Evonik Corporation Rohacell® 71 WF High Heat Grade Polymethacrylimide (PMI) Foam, MatWeb, http://www.matweb.com.

[4]   Anonymous: Toray Company, Web Site: http://www.toraycompam.com

[5]   Anonymous: Standard Test Method for Tensile Properties of Polymer Matrix Composite Materials, Standard Designation D 3039/D 3039 M, Approved by agencies of the Department of Defense, 2000.

[6]   Anonymus: 3M Scotch-Weld Structural Adhesive Film AF 163-2, Technical Datasheet, Aerospace and Aircraft Maintenance Department 3M Center, Building 223-1N-14 St. Paul, MN 55144-1000, 1-800-235-2376, http://www.3M.com/aerospace/, 2009.

[7]   Anonymus: The Fastest, Solver Neutral CAE Environment for High Fidelity Modeling, HyperMesh, part of HyperWorks, Altair Engineering, Troy, MI, 2010.

[8]   Ashwill, T.: Passive load control for large wind turbines, 51-st SDM Conference, Orlando, FL, USA, 2010.

[9]   Bahaj ,A.S., Molland, A.F., Chaplin, J.R., Batten, W.M.J.: Power and thrust measurements of marine current turbines under various hydrodynamic flow conditions in a cavitation tunnel and a towing tank, Renewable Energy, 32/3, 407 – -426, 2007.

[10]   Bauchau, O.A. and Bottasso, C.L. and Nikishkov, Y.G.: Modeling rotorcraft dynamics with finite element multibody procedures, Journal of Mathematics and Computer Modeling, 33, 1113--1137, 2011.

[11]   Bernhard, A., and Chopra, I.: Hover test of a Mach-Scale Rotor Model with active blade tips, Journal of the american helicopter society, 47, 273--284, 2002.

[12]   Berring, P., Branner, K., Berggreen, C., and Knudsen, H.W.: Torsional performance of wind turbine Blades-Part I: Experimental investigation,16-th International Conference on composite materials, Kyoto, Japan, 2007.

[13]   Bossanyi, E.A.: Individual blade pitch control for load reduction, Wind Energy, 6/2, 119-128, 2003.

[14]   Bossanyi, E.A., Wright, A., and Fleming, P.: Further progress with field testing of individual pitch control, European Wind Energy Conference, Warsaw, Poland, 2010.

[15]   Bottasso, C.L., Croce, A.: *Cp-Lambda* User's Manual.
Dipartimento di Scienze e Tecnologie Aerospaziali, Politecnico di Milano, Milano, Italy, 2006--2015.

[16]   Bottasso, C.L., Campagnolo, F., and Croce, A.: Multi-Disciplinary Constrained Optimization of Wind Turbines, Multibody System Dynamics, 27/1, 21–53, doi: 10.1007/s11044-011-9271-x, 2011.

INNWIND.EU, Deliverable 2.24, Manufactured and laboratory tested scaled blades and parts of the blade

[17] Bottasso, C.L., Croce, A., Riboldi, C.E.D., Nam, Y.: Multi-Layer Control Architecture for the Reduction of Deterministic and Non-Deterministic Loads on Wind Turbines, Renewable Energy, 51, 159-169, 2013.

[18] Bottasso, C., Campagnolo, F., Croce, A., and Tibaldi, C.: Optimization-based study of bend–twist coupled rotor blades for passive and integrated passive/active load alleviation, Wind Energy, 16/8, 1149--66, 2013.

[19] Bottasso, C.L., Campagnolo, F., Croce, A., Dilli, S., Gualdoni, F., Nielsen, M.B.: Structural Optimization of Wind Turbine Rotor Blades by Multi-Level Sectional/Multibody/3DFEM Analysis, Multibody System Dynamics, doi: 10.1007/s11044-013-9394-3, 2013.

[20] Bottasso, C.L., Campagnolo, F., Petrovič, V.: Wind tunnel testing of scaled wind turbine models: Beyond aerodynamics, Journal of Wind Engineering and Industrial Aerodynamics, 127, 11–28, 2014.

[21] Branner, K., Berring, P., Berggreen, C., Knudsen, H.: Torsional Performance of Wind Turbine Blades: Part II: Numerical Validation, 16-th International Conference on Composite Materials, Kyoto, Japan, 2007.

[22] Capellaro, M., and Kühn, M.: Boundaries of bend twist coupling, In Proceedings of TORQUE 2010: The Science of Making Torque from Wind, June 28-30, Crete, Greece, 2010.

[23] Geyler, M. and Caselitz, P.: Individual blade pitch control design for load reduction on large wind turbines, Proceedings of the European Wind Energy Conference, Milan, Italy, 2007.

[24] Giavotto, V., Borri, M., Mantegazza, P., Ghiringhelli, G., Carmaschi, V., Maffioli, G.C., Mussi, F.: Anysotropic beam theory and applications, Computers and Structures, 16(1-4), 403--413, 1983.

[25] Jinsong B., Nagaraj V., Chopra I. and Bernhard A.: Wind Tunnel Test of Five Sets of Mach Scale Composite Tailored Rotor with Flap-Bending/Torsion Couplings for Vibration Reduction, Journal of the american helicopter society, 53, 215--225, 2008.

[26] Jonkman, J., Butterfield, S., Musial, W., and Scott, G.: Definition of a 5-MW Reference Wind Turbine for Offshore System Development. Technical Report NREL/TP-500-38060, http://www.nrel.gov/docs/fy09osti/38060.pdf, 2009.

[27] Kanev, S., and Van~Engelen, T.: Exploring the limits in individual pitch control, Wind Energy, 13, 18--35, 2010.

[28] Choosing nodes in parametric curve interpolation, Journal of Computer-Aided Design, 21, 363--370, 1989.

[29] Lobitz, D.W., Laino, D.J.: Load mitigation with twist-coupled HAWT blades, ASME Wind Energy Symposium, Reno, January 11–14, doi: 10.2514/6.1999-33, 1999.

[30] Lobitz D., Veers, P.S., Laino, D.: Performance of twist-coupled blades on variable speed rotors, ASME Wind Energy Symposium, Reno, January 10–13, doi: 10.2514/6.2000-62, 2000.

[31] Luczak, M., Manzato, S., Peeters, B., Branner, K., Berring, P., and Kahsin, M.: Dynamic investigation of twist-bend coupling in a wind turbine blade, Journal of theoretical and applied mechanics, 49, 765–789, 2011.

[32] Olesen, N.: Personal communication. Vestas Wind Systems. Aarhus, Denmark, 2009.

[33] Piegl, L., Tiller, W.: The NURBS Book (Monographs and Visual Communications), Springer, 2ns edition, 1996.

[34] Sala, G., Di Landro, L., Airoldi, A., Bettini, P.: Fiber optics health monitoring for aeronautical applications, Meccanica, 50/10, 2547–2567, 2015.

[35] Schubel, P.J., Crossley, R.J. , Boateng, E.K.G., Hutchinson, J.R.: Review of structural health and cure monitoring techniques for large wind turbine blades, Renewable Energy, 51, 113–123, doi:10.1016/8.2012-72, http://www.sciencedirect.com/science/article/pii/S0960148112005423, 2013.

[36] Bauchau, O.A., Flexible Multibody Dynamics, Solid Mechanics and its Applications, Vol. 176, Springer, Dordrecht Heidelberg London New York, 2011.

[37] Bottasso, C.L., Cacciola, S.: Estimation of wind turbine model properties – Towards the validation of comprehensive high-fidelity multibody models, Proceedings of the EWEA 2014 Annual Event, Barcelona, Spain, March 10 – 13, 2014.

[38] Barclay, A., Gill, P.E., Rosen, J.B., SQP methods and their application to numerical optimal control, Report NA 97-3, Department of Mathematics, University of California, San Diego, CA, 1997.

[39] Dimitris C. Lagoudas, Shape Memory Alloys: Modeling and Engineering Applications. 2008.

[40] K. Otsuka, "Shape Memory Materials," Corrosion, 1998.

[41] J. G. Boyd and D. C. Lagoudas, "A thermodynamical constitutive model for shape memory materials. Part I. The monolithic shape memory alloy," Int. J. Plast., vol. 12, no. 6, pp. 805–842, 1996.

[42] C. Calhoun, R. Wheeler, T. Baxevanis, and D. C. Lagoudas, "Actuation fatigue life prediction of shape memory alloys under the constant-stress loading condition," *Scr. Mater.*, vol. 95, no. 1, pp. 58–61, 2015.

[43] G. Eggeler, E. Hornbogen, A. Yawny, A. Heckmann, and M. Wagner, "Structural and functional fatigue of NiTi shape memory alloys," *Mater. Sci. Eng. A*, vol. 378, no. 1–2 SPEC. ISS., pp. 24–33, 2004.

[44] M. J. Bigeon and M. Morin, "Thermomechanical study of the stress assisted two way memory effect fatigue in TiNi and CuZnAl wires," *Scr. Mater.*, vol. 35, no. 12, pp. 1373–1378, 1996.

[45] E. Hornbogen, "Review Thermo-mechanical fatigue of shape memory alloys," *J. Mater. Sci.*, vol. 39, no. 2, pp. 385–399, 2004.

[46] O. W. Bertacchini, D. C. Lagoudas, and E. Patoor, "Thermomechanical transformation fatigue of TiNiCu SMA actuators under a corrosive environment - Part I: Experimental results," *Int. J. Fatigue*, vol. 31, no. 10, pp. 1571–1578, 2009.

INNWIND.EU, Deliverable 2.24, Manufactured and laboratory tested scaled blades and parts of the blade

[47] D. C. C. Lagoudas, D. A. A. Miller, L. Rong, and P. K. K. Kumar, "Thermomechanical fatigue of shape memory alloys," *Smart Mater. Struct.*, vol. 18, no. 8, p. 85021, 2009.

[48] J. L. McNichols, P. C. Brookes, and J. S. Cory, "NiTi fatigue behavior," *J. Appl. Phys.*, vol. 52, no. 12, pp. 7442–7444, 1981.

[49] S. Miyazaki, K. Mizukoshi, T. Ueki, T. Sakuma, and Y. Liu, "Fatigue life of Ti–50 at.% Ni and Ti–40Ni–10Cu (at.%) shape memory alloy wires," *Mater. Sci. Eng. A*, vol. 273–275, pp. 658–663, 1999.

[50] H. Tobushi, T. Hachisuka, S. Yamada, and P.-H. Lin, "Rotating-bending fatigue of a TiNi shape-memory alloy wire," *Mech. Mater.*, vol. 26, no. 1, pp. 35–42, 1997.

[51] D. C. Lagoudas, D. A. Miller, and L. Rong, "Thermomechanical Transformation Fatigue of {SMA} Actuators," *Proc. Adapt. Struct. Mater. Syst. Symp. ASME Int. Mech. Eng. Congr. Expo.*, vol. 60, pp. 1–6, 2000.

[52] D. J. Hartl and D. C. Lagoudas, "Characterization and 3-D modeling of Ni60Ti SMA for actuation of a variable geometry jet engine chevron," *SPIE 6529, Sensors Smart Struct. Technol. Civil, Mech. Aerosp. Syst.*, vol. 6529, p. 65293Z–65293Z–12, 2007.

[53] F. Trochu, N. Sacépé, O. Volkov, and S. Turenne, "Characterization of NiTi shape memory alloys using dual kriging interpolation," *Mater. Sci. Eng. A*, vol. 273–275, pp. 395–399, 1999.

[54] Z. Bo, D. C. Lagoudas, and D. Miller, "Material Characterization of SMA Actuators Under Nonproportional Thermomechanical Loading," *J. Eng. Mater. Technol.*, vol. 121, no. 1, p. 75, 1999.

[55] D. Roy, V. Buravalla, P. D. Mangalgiri, S. Allegavi, and U. Ramamurty, "Mechanical characterization of NiTi SMA wires using a dynamic mechanical analyzer," *Mater. Sci. Eng. A*, vol. 494, no. 1–2, pp. 429–435, 2008.

[56] D. a Miller and D. C. Lagoudas, "Thermomechanical characterization of NiTiCu and NiTi SMA actuators: influence of plastic strains," *Smart Mater. Struct.*, vol. 9, no. 5, pp. 640–652, 2000.

[57] J. A. Shaw, C. B. Churchill, and M. A. Iadicola, "Tips and tricks for characterizing shape memory alloy wire: Part 1-differential scanning calorimetry and basic phenomena," *Exp. Tech.*, vol. 32, no. 5, pp. 55–62, 2008.

[58] C. B. Churchill, J. A. Shaw, and M. A. Iadicola, "Tips and tricks for characterizing shape memory alloy wire: Part 2 - Fundamental isothermal responses," *Exp. Tech.*, vol. 33, no. 1, pp. 51–62, 2009.

[59] C. B. Churchill, J. A. Shaw, and M. A. Iadicola, "Tips and tricks for characterizing shape memory alloy wire: Part 3-localization and propagation phenomena," *Exp. Tech.*, vol. 33, no. 5, pp. 70–78, 2009.

[60] C. B. Churchill, J. A. Shaw, and M. A. Iadicola, "Tips and tricks for characterizing shape memory alloy wire: Part 4 - Thermo-mechanical coupling: Experimental characterization of active materials series," *Exp. Tech.*, vol. 34, no. 2, pp. 63–80, 2010.

[61] A. F2004-05, "Standard test method for transformation temperature of nickel-titanium alloys by thermal analysis," *F04*, pp. 5–8, 2010.

INNWIND.EU, Deliverable 2.24, Manufactured and laboratory tested scaled blades and parts of the blade

[62]   D. C. Lagoudas, *Shape Memory Alloys: Modeling and Engineering Applications*. 2008.

[63]   D. J. Hartl, D. C. Lagoudas, F. T. Calkins, and J. H. Mabe, "Use of a Ni60Ti shape memory alloy for active jet engine chevron application: I. Thermomechanical characterization," *Smart Mater. Struct.*, vol. 19, no. 1, p. 15020, 2010.

[64]   Lekou D. J., Bacharoudis K., Markis A., Dekker J.P., de Winkel G.D., Croce A., Wang D., Brinkmeyer A., Buckney N., Capuzzi M., Weaver P., Philipidis T.P., Roukis G.A., Branner K., Montejo R. and Nuin I., 2015, "New lightweight structural blade designs and blade designs with build-in structural couplings", section 2.2 in Deliverable D2.22.

[65]   Huybrechts S.M., Meink T.E., Wegner P.M. and Ganley J.M., "Manufacturing theory for advanced grid stiffened structures", Composites part A: Applied Science and Manufacturing, vol. 33, n0. 2, pp. 155-161, 2002

[66]   Shroff S., "Design, analysis, fabrication and testing of composite grid stiffened structures for fuselage applications", PhD thesis Delft University of technology, ISBN: 978-94-6259-479-1, 2014

[67]   (2011)   Isogrid   Composites   Canada   Inc.   [Online].   Available: http://www.isogridinc.com/Applications/

[68]   Bak C., Zahle F., Bitsche R., Kim T., Yde A., Henriksen L. C., Natarajan A. and Hansen M., "Description of the DTU 10MW Reference Wind Turbine, Report number DTU Wind Energy Report-I-0092, Sponsorship EUDP 2010-I, 2013

INNWIND.EU, Deliverable 2.24, Manufactured and laboratory tested scaled blades and parts of the blade

APPENDIX A: CAD DRAWINGS OF THE SCALED PROTOTYPE (TUD)
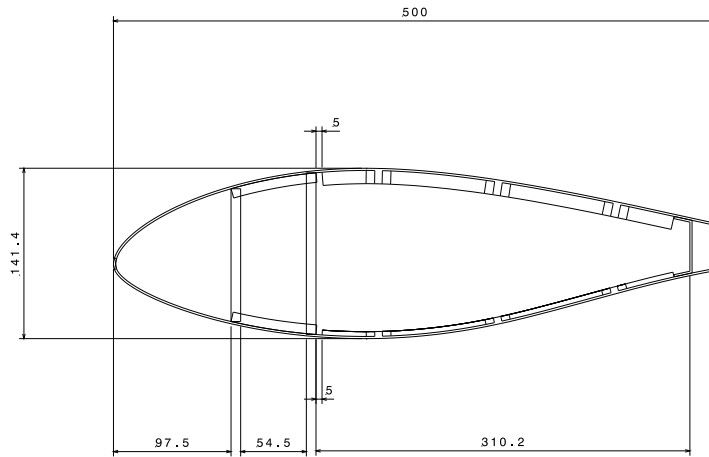
Figure 130: Assembly side view

Front view
Scale:. 1:4

Left view
Scale:. 1:4

Figure 131: Front Spar

Right view
Scale:. 1:4

Front view
Scale:. 1:4

Figure 132: Middle Spar

INNWIND.EU, Deliverable 2.24, Manufactured and laboratory tested scaled blades and parts of the blade

.1000

77.7°

14.7

43.6

1.8

Front view
Scale:. 1:4

Left view
Scale:. 1:4

Figure 133: Rear Spar

6.3

.11

1.8

216 .100 98

SIDE VIEW
Scale:. 1:4

500

.157

.170

.170

R7

.170

.170

1000

BOTTOM VIEW
Scale:. 1:4
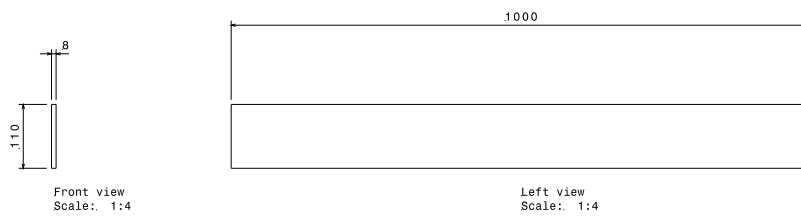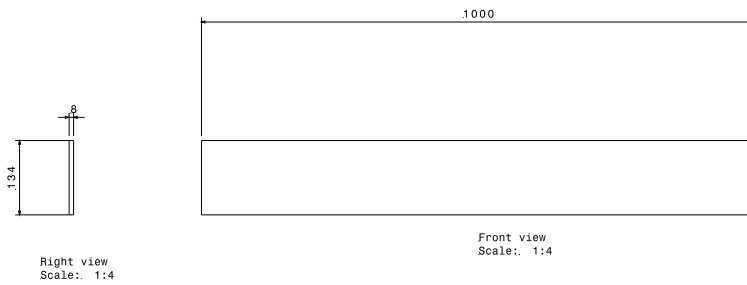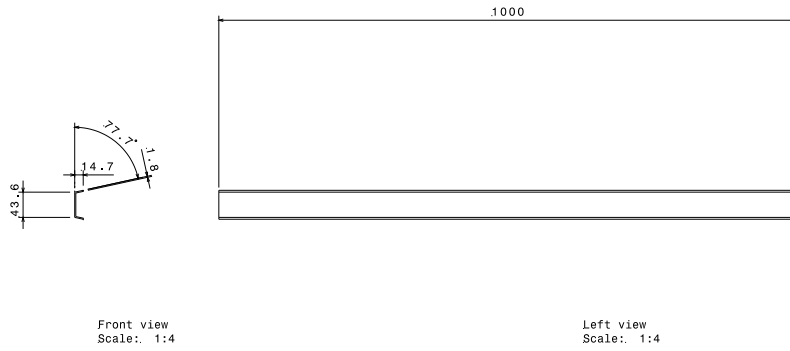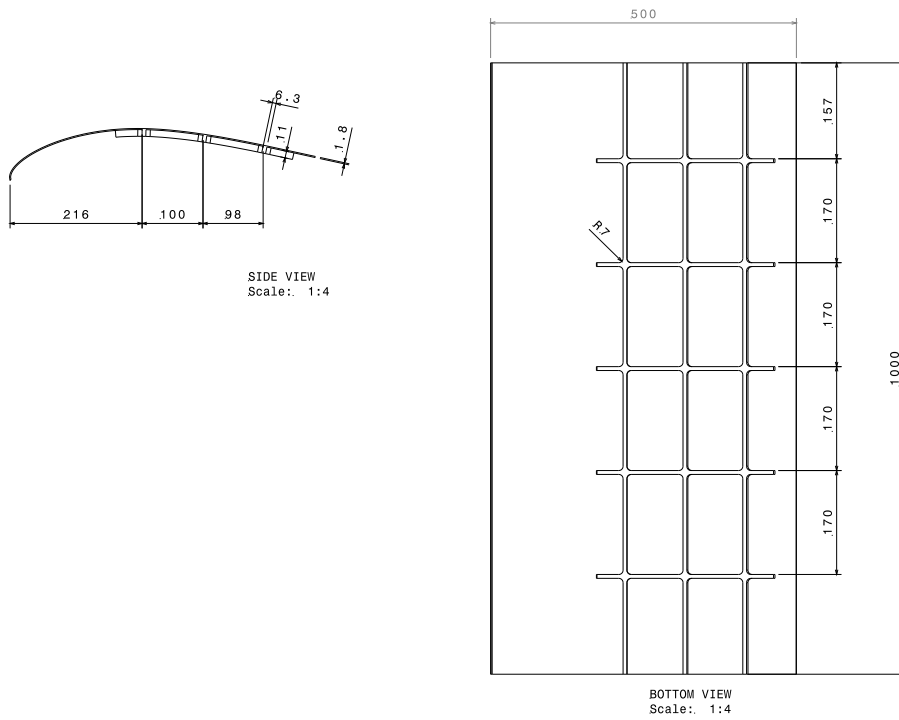
Figure 134: Upper Surface and grid
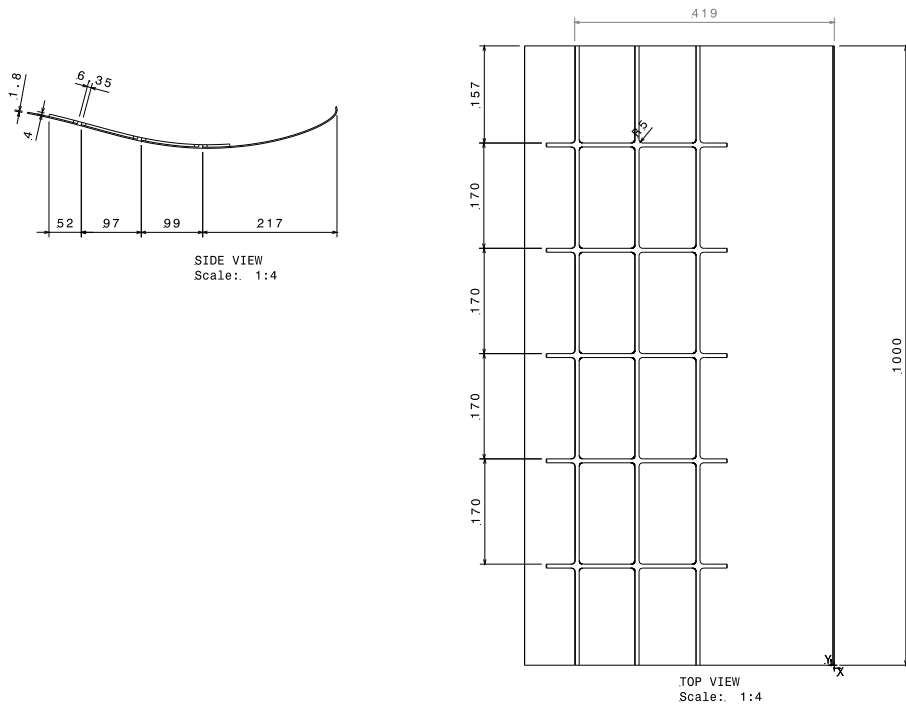
SIDE VIEW
Scale:. 1:4

TOP VIEW
Scale:. 1:4

Figure 135: Lower surface and grid

APPENDIX B: EXPERIMENTAL TESTING EQUIPEMENT   (UPATRAS)

In order to perform the material characterization and test the morphing section, numerous devices were used. The instrumentation, entails devices for triggering the actuators and record their response as well as the response of the morphing section. Hereafter a brief description of each device is presented.

Testing machines

A MTS universal testing machine with maximum load capacity of 100kN.

Testing chambers

Rectangular chamber

The rectangular chamber is constructed out of a metal skeleton that holds the insulation material. Insulation is achieved by using rock mineral wool, a material that is nonflammable (Class 1 reaction to fire). The main advantages of rock mineral wool as an insulation material are the stability and compactness, resistance to fire, ease of handling and low price. This chamber can be positioned both horizontally and vertically (depending on the specimen length and experimental setup). Inside the chamber there is space provided for placing the extensometer. Furthermore, cables for the electrical resistance, cooling pipe and airways for the placement of grips are placed through the insulation.
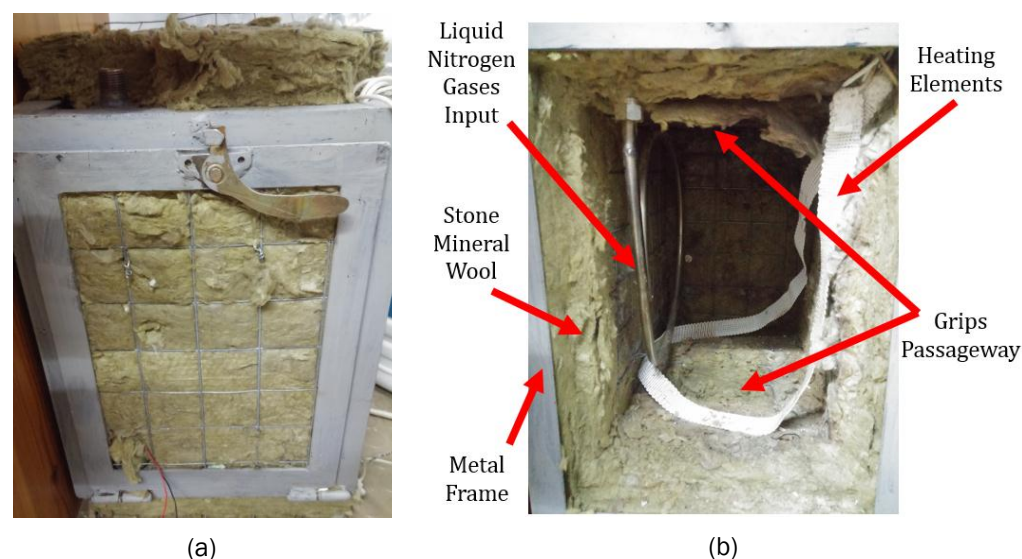

(a)   (b)

Figure 136: Rectangular Chamber (a) exterior and (b) interior view.

The main capabilities and limitations of the setup of this chamber are summarized below:

- only one specimen can be processed
- the volume of the chamber permit usage of extensometers and other measuring equipment
- efficient room for handling the specimen
- upright position of the chamber leads to high temperature variation while level position reduces the possible specimen length
- heating and cooling of the specimen are indirect
- the control volume is large compared to the specimen

INNWIND.EU, Deliverable 2.24, Manufactured and laboratory tested scaled blades and parts of the blade

- operational costs are large
- fatigue testing can be challenging due to the amounts of consumables required

Cylindrical chamber plexiglass

The cylindrical chamber is manufactured out of a plexiglass pipe that is split in half. On the upper part of the chamber there are holes to provide input for nitrogen gases flow during cooling and holes for electrical wiring that will deliver current through the specimens for Joule heating. On the lower part of the chamber there are also some holes for placing the thermocouples and attaching them on the specimen. On the edges of the two chamber parts proper strip insulation has been placed to reduce the losses during cooling procedure. Apart from the thermocouples there is no other device inside the chamber.
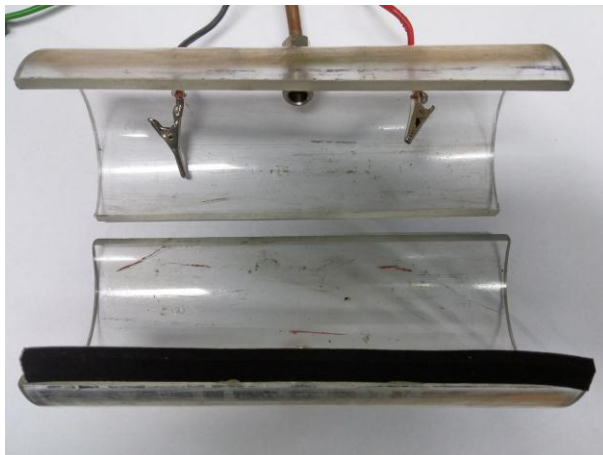

Figure 137: The Two Part Cylindrical Plexiglass Chamber

The main capabilities and limitations of the setup of this chamber are summarized below:

- enables use of Joule heating
- simultaneous training or testing of up to 4 wire specimens
- adjustable specimen length (up to 560 mm net length)
- increased speed and reduced operational cost
- suitable for fatigue testing
- displacement measurements can only be obtained through telemetry methods
- small control volume
- restricted space for specimen handling

Custom made specimen grips

Due to the different configuration of the testing chambers used there were two sets of custom made grips that hold the specimens without letting them slip.

Rectangular chamber grips

The main body of the grips for the rectangular chamber is like a cube which is split in two parts. The wire specimen is placed between these parts and gets bended when the screws are fastened. Apart from the cubic shape, each of the two grips has a different configuration. The upper grip has an extended plate that helps for fixing the grip on the frame of the device while the lower grip has a threaded hole for fitting the axle that holds the dead weights (in case of isobaric loading). These grips can hold up to one specimen and are manufactured out of hard steel.

(a)

(b)

Figure 138: Grips of Rectangular Chamber: (a) upper and (b) lower grip.

Cylindrical chamber grips

The grips for the specimens of the cylindrical chamber are identical. Each grip has holes in a specific configuration in order to get the wire specimens through them. The specimens are bended inside the grip and hold tightly when the screws are fastened. These grips are much lighter although they are also manufactured using hard steel and can hold up to for specimens.
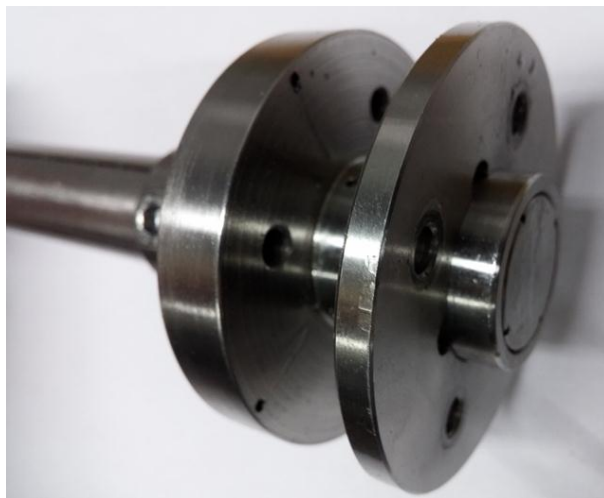

Figure 139: Grip of Cylindrical Chamber

Liquid Nitrogen storage and handling

Liquid nitrogen is the main consumable material for wire SMA testing as it is used for cooling the specimens below ambient temperature. Being a cryogenic fluid, liquid nitrogen requires special equipment for storage and handling.

Storage unit

A TP35 aluminium vessel manufactured by Air Liquide is used for storing up to 35 litres of liquid nitrogen. The vessel is equipped with an operating head which is used to manipulate the flow according to the operational state. When there is no experimental procedure the liquid nitrogen

gases are relieved through the vent valve. Otherwise, before starting experimental procedure the vent valve is closed and the pressure is adjusted to increase the flow of liquid nitrogen. The inside pressure of the unit is monitored using the pressure gauge. For safety reasons the maximum allowed pressure is set to 0.5 bar and it is automatically regulated through the safety valves.
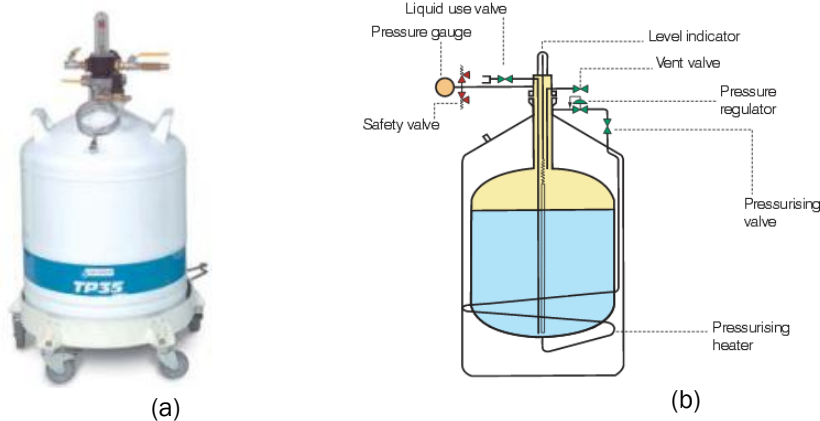

(a)   (b)

Figure 140: The storage unit with the regulated valve attached: (a) photo of the equipment and (b) schematic representation of its components

Electrical & electronic equipment

In this section all the electrical and electronic equipment for testing is descried.

Programmable Logic Controller – PLC

A FATEC series FB controller with a LCD screen is used for controlling the heating and cooling procedures during thermal/thermomechanical testing. The controller offers a lot of different features such as implementation of P, I, D control, timing of the procedure (On and Off times), number of cycles to perform e.t.c.

(a)   (b)

Figure 141: The Programmable Controller (a) unit and (b) the LCD screen.

Digital controllers

Along with the PLC there two SR1, SR3 series digital controller for setting the temperature limits – specifications for the operations of heating and cooling.

Figure 142: The SR1, SR3 series Digital Controller

Power supply

The temperature rise of the SMA actuators during the test of the morphing section was achieved through Joule heating. To this end an adjustable programmable power supply was used, able to provide up to 60 Volts and 50 Amperes. The model QPX 1200 SP from Aim & Thurlby Thandar Instruments was used.
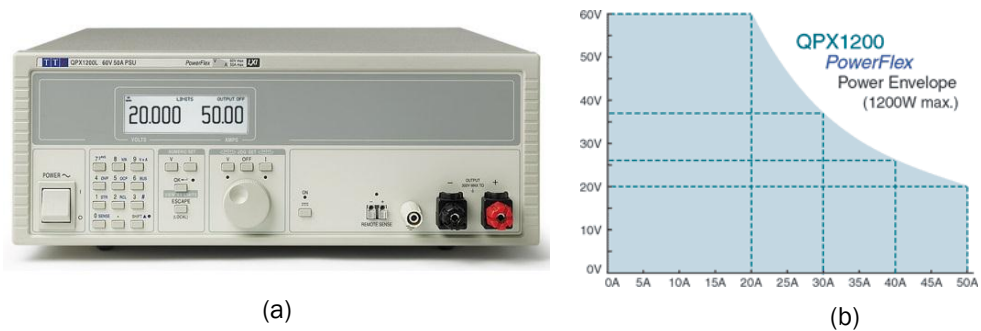

(a)   (b)

Figure 143: Power Supply (a) Device and (b) Power Envelope

Measurements & Data Acquisition devices

In this section all the measuring devices and data acquisition equipment is described.

In order to record the actuator's temperature and the displacement of the morphing structure the National Instrument (NI) chassis SCXI-1000 equipped with the signal conditioning modules, NI SCXI-1120 and SCXI-1140 is used.

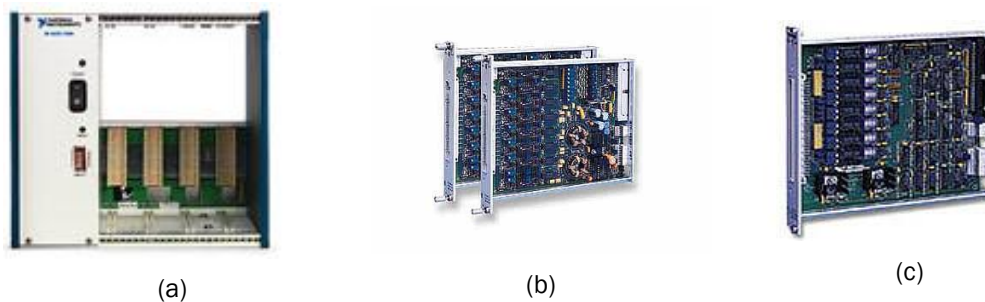(a)   (b)   (c)

Figure 144: Recording devices: (a) Chassis SCXI-1000, (b) Module SCXI-1120, (c) Module SCXI-1140

The first module was used to record the temperature of the actuators, acquired by thermocouples. The connection of the thermocouples to the respective module was realized through the NI SCXI-1320 terminal block. The second module was used to collect the output of the displacement sensor. To this end a Laser Doppler Vibrometer unit was connected to a NI SCXI-1305 terminal block to enable the communication with the respective module. Subsequently, the chassis was connected on a Windows XP server through a PC-MIO-16XE-10 data acquisition card (DAQ) for simultaneous measurement of temperature and displacement. The whole process was monitored and controlled through a Virtual Instrument (VI) which was developed on a NI LabVIEW platform. The developed VI was able to record the temperature and displacement data and also to mandate the supplied power provided to the actuators by the programmable power supply unit in order to increase their temperature.
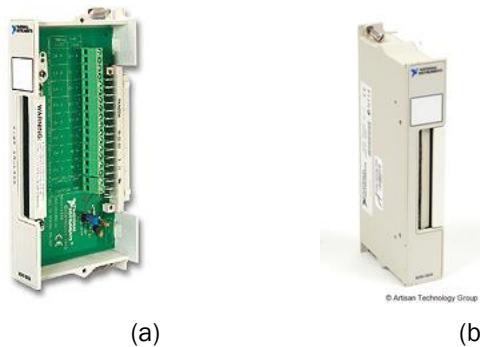

(a)   (b)

Figure 145: Terminal blocks: (a) SCXI-1320 and (b) SCXI-1305

Measuring displacement

In order to measure displacement a Laser Doppler Vibrometer and a Laser Triangulation displacement sensor were used. The Laser Doppler Vibrometer unit consisted of the laser head (Polytec OFV-505) and the controller (Polytec OFV-5000) able to measure deflections on the level of nanometers. The model of Laser Triangulation is optoNCDT 1302 ILD with accuracy of 100μm. The sensor is equipped with a dedicated power supply and a USB converter for communication with a Windows 7 server.

(a)   (b)

Figure 146: Displacement Sensors: (a) Laser Doppler Vibrometer and (b) Laser Triangulation Sensor

Figure 147: Laser Vibrometer Controller

Measuring strain

Inside rectangular chamber an Epsilon Axial Extensometer Model 3542-025M-025-LHT is placed. Its gauge length is 25 mm, can measure up to ±25% strain and operational temperature range is -265 to +175˚C.

Figure 148: Epsilon Axial Extensometer

Measuring temperature

K-type thermocouples acquired from OMEGA Engineering LTD are able to measure temperatures in a range from -250°C up to 1100°C. This range covers the ranges considered in the experiments in the framework of this project, thus they were selected.

Figure 149: Omega Thermocouples of Type K

INNWIND.EU, Deliverable 2.24, Manufactured and laboratory tested scaled blades and parts of the blade

APPENDIX C: MECHANICAL DRAWINGS AND FABRICATED PARTS OF THE SCALED PROTOTYPE (UPATRAS)
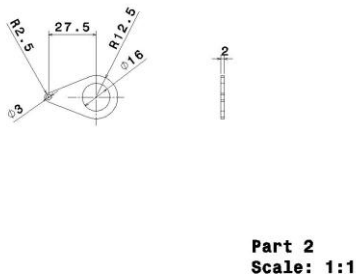
In the following figures the mechanical drawings and the respective fabricated parts of the morphing section prototype are presented.
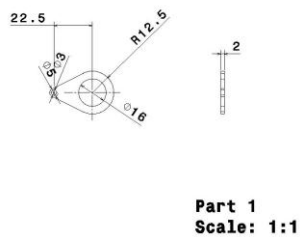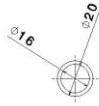

(a)   (b)

Figure 150: Front lug connector for the actuator used for the 10% chord length segment (Part 1): a) mechanical drawing and b) fabricated part

(a)   (b)

Figure 151: Front lug connector for the actuator used for the 50% chord length segment (Part 2): a) mechanical drawing and b) fabricated part

INNWIND.EU, Deliverable 2.24, Manufactured and laboratory tested scaled blades and parts of the blade
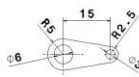
(a)   (b)

Figure 152: Front lug connector for the actuator used for the 30% chord length segment (Part 3): a) mechanical drawing and b) fabricated part


(a)   (b)

Figure 153: Jig for actuator mounting (Part 4): a) mechanical drawing and b) fabricated part

(a)   (b)

Figure 154: Locking head for actuator mounting (Part 5): a) mechanical drawing and b) fabricated part

INNWIND.EU, Deliverable 2.24, Manufactured and laboratory tested scaled blades and parts of the blade

(a)   (b)

Figure 155: Spacer intervening between rib components (Part 6): a) mechanical drawing and b) fabricated part
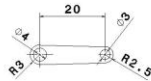
(a)   (b)

Figure 156: Rear lug connector for the actuator used for the 10% chord length segment (Part 7): a) mechanical drawing and b) fabricated part
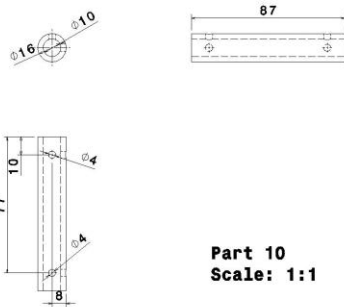

(a)   (b)

Figure 157: Rear lug connector for the actuator used for the 30% chord length segment (Part 8): a) mechanical drawing and b) fabricated part
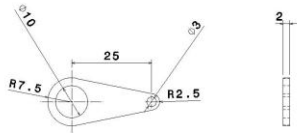
Figure 158: Rear lug connector for the actuator used for the 50% chord length segment (Part 9): a) mechanical drawing and b) fabricated part

Figure 159: Axle for mounting the 30% and 50% chord length rib components (Part 10): a) mechanical drawing and b) fabricated part
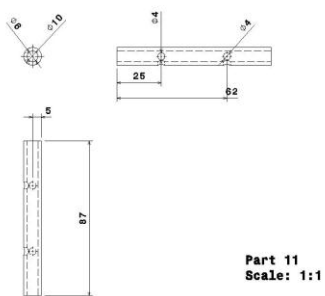
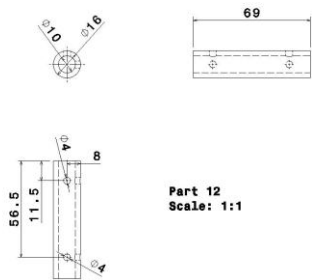**Figure 160:** Axle for mounting the 10% chord length rib components (Part 11): a) mechanical drawing and b) fabricated part
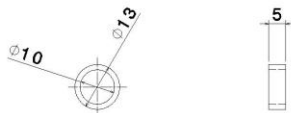
(a)

(b)

Figure 161: Axle for mounting the immobile rib components (Part 12): a) mechanical drawing and b) fabricated part

(a)

(b)

Figure 162: Spacer intervening between 10% and 30% chord length rib components (Part 13): a) mechanical drawing and b) fabricated part
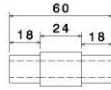

(a)

(b)

Figure 163: Actuator spacers (Part 14): a) mechanical drawing and b) fabricated part

INNWIND.EU, Deliverable 2.24, Manufactured and laboratory tested scaled blades and parts of the blade

Figure 164: Axle for mounting the actuators (Part 15): a) mechanical drawing and b) fabricated part

The jigs for the actuator mounting were made of stainless steel in order to provide tough surfaces for the wire clamp. The lug connectors were made of aluminum in order to confine the weight and provide adequate stiffness to transmit the moment to the moving parts. On the other hand, the spacers and the mounting axles were made of plastic material to keep the weight in reasonable levels.

INNWIND.EU, Deliverable 2.24, Manufactured and laboratory tested scaled blades and parts of the blade